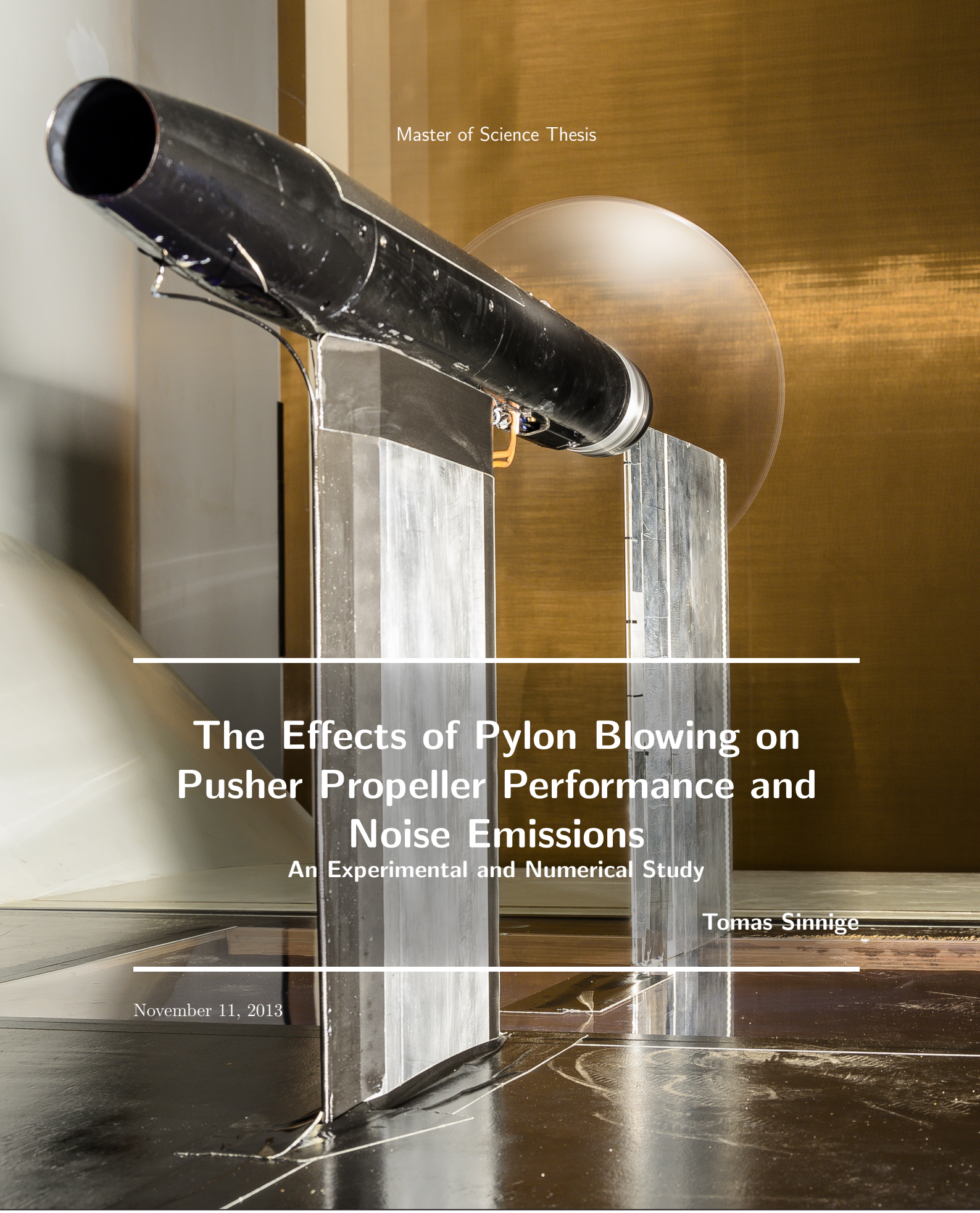

Master of Science Thesis

The Effects of Pylon Blowing on Pusher Propeller Performance and Noise Emissions

An Experimental and Numerical Study

Tomas Sinnige

November 11, 2013

Aerodynamics

TU Delft

Faculty of Aerospace Engineering

Delft University of Technology

The Effects of Pylon Blowing on Pusher Propeller Performance and Noise Emissions

An Experimental and Numerical Study

Master of Science Thesis

For obtaining the degree of Master of Science in Aerospace Engineering
at Delft University of Technology

Tomas Sinnige

November 11, 2013

Faculty of Aerospace Engineering · Delft University of Technology

Delft University of Technology

DELFT UNIVERSITY OF TECHNOLOGY
DEPARTMENT OF AERODYNAMICS

The undersigned hereby certify that they have read and recommend to the Faculty of Aerospace Engineering for acceptance the thesis entitled **"The Effects of Pylon Blowing on Pusher Propeller Performance and Noise Emissions"** by **Tomas Sinnige** in fulfillment of the requirements for the degree of **Master of Science**.

Dated: November 11, 2013

Exam committee:

prof. dr. ir. L.L.M. Veldhuis

prof. Dr.-Ing. G. Eitelberg

ir. C.S. Potma

dr. H.H. Brouwer

Preface

Delft – November 11, 2013

This document is written as the final deliverable of the MSc thesis of the Aerodynamics and Wind Energy track of Delft University of Technology's Aerospace Engineering Master. Twelve months of hard work have finally resulted in this report, which marks the end of my Aerospace Engineering curriculum - a wonderful time on which I look back with great memories. From studying die-hard mathematics to performing internships at the greatest aircraft manufacturers in the world, from my first ever pilot experience in a Cessna 172 to parabolic flights in the university's Cessna Citation II, from performing basic airfoil measurements in the world-famous Low Turbulence Tunnel to conducting my own wind tunnel experiments in the mighty Open Jet Facility, it has been a mix of uncountable unforgettable experiences.

At this point I would like to express my gratitude to a number of people who have helped me during my thesis, or during my Aerospace Engineering studies as a whole.

Leo, thank you very much for the guidance during my thesis work. Your in-depth knowledge and impressive experience have greatly contributed to the successful completion of this thesis.

Georg, thank you for the advice during my wind tunnel tests, but also for your courier services when parts needed to be transported back and forth between TU Delft and DNW.

Christian, thanks for the efforts you put into the design of the Uniform Blowing Rod, a device which was essential for the experimental test campaigns performed during my thesis.

Harry, thank you for taking the time to discuss the experimental and numerical noise data and to verify the surprising results I obtained for the isolated propeller at low velocities.

Frits, Henk-Jan, Nico, and Peter, thanks for the excellent support during my wind tunnel test campaigns. Henk-Jan, special thanks for your never ending support on getting the Propeller Test Rig to work properly, and thereby in the end rescuing my thesis work!

Moreover, also many thanks to my close friends in Delft; whether discussing university related subjects or drinking Belgian beers in the city center, you made this whole journey so much more enjoyable! Regarding my thesis work special thanks to Biem, Bryan, Erik, Lennart, Lisanne, and Rian for your invaluable assistance during the wind tunnel tests.

Last but certainly not least I would like to thank my family; without your never ending love and support I would have never reached this point!

Tomas Sinnige

Summary

This report discusses the potential of pylon trailing edge blowing to reduce the adverse effects of airframe installation on the performance and noise emissions of pusher propellers. Both experimental and numerical analyses were performed, focusing on the pylon wake profiles, the propeller performance, and the propeller noise emissions. The experiments were executed in Delft University of Technology's Open Jet Facility using a scale model pylon and two propeller models (one powered and one windmilling). The numerical analysis combined an existing propeller lifting line code with analytic methods suited to predict the effects of installation on the propeller performance and noise emissions.

The pylon wake measurements showed that the application of the pylon blowing system reduced the absolute values of the velocity deficit in the pylon wake compared to the unblown configuration. For the right combinations of freestream velocity and blowing rate a reduction of up to 60% was achieved in the integral wake velocity deficit. However, no full mixing of the external flow and the flow blown into the pylon wake was obtained. As a result, the application of blowing did not completely eliminate the pylon wake, but instead led to a velocity overshoot in the wake center and two local minima left and right of the wake centerline.

From the experimental and numerical studies of the propeller performance it was concluded that the effects of installation on the time-averaged performance are small compared to the steady-state results. The measured changes in the time-averaged thrust and torque coefficients resulting from the installation effects were equal to at maximum several percent. The results obtained at the three considered freestream velocities however were not consistent, which is explained by considering the low signal quality of the used rotating shaft balance. The numerical data showed differences between the time-averaged isolated and installed thrust and torque coefficients of less than 2% for advance ratios below 1.4. The peak-to-peak variations in the time-accurate installed signals equaled at most 4% for the same advance ratio range. In the blown configuration the computed differences between the isolated and installed data became even smaller. A comparison of the experimental and numerical data showed that for the isolated propeller performance excellent agreement was obtained for advance ratios above 0.7, with differences between the computed and measured thrust coefficients of at maximum 1%. The experimental and numerical results for the installed and blown configurations could not be successfully compared considering the low signal quality of the experimental data.

The measurements of the powered propeller noise emissions showed that the effects of installation strongly increase the sound pressure level (SPL) of the propeller tones, with noise penalties of up to 10 to 25 dB for the first six tones occurring at integer multiples of the blade passage frequency (BPF). Broadband levels on the other hand were unaffected by the presence of the upstream pylon. The application of blowing resulted in significant noise reductions

when compared to the unblown installed case. Depending on the advance ratio, at the highest blowing rate considered an SPL reduction of up to 4 dB was observed for the 1BPF tone. For the 2BPF and 3BPF tones the maximum reductions were even larger at 8 and 12 dB, respectively. Finally, the higher BPF tones (4BPF and above) were practically eliminated by the application of blowing. The evolution of the tonal noise reduction due to blowing as a function of the advance ratio followed the trend in the noise penalty due to installation, thereby confirming that the application of blowing indeed successfully opposes the adverse installation effects. Although the trends in the experimental and numerical noise emission data were comparable, the absolute levels differed. The experimental data was characterized by relatively large SPL variations between measurements performed at successive advance ratios, while the numerical method clearly underpredicted the isolated propeller noise emissions for low freestream velocities. The latter is likely the result of an overprediction of the decrease in radiation efficiency with increasing blade number at low tip Mach numbers. Directivity analyses performed using the numerical method showed that the effects of installation are particularly pronounced for axial directivity angles near the propeller axis. Furthermore, as a result of the installation effects clear lobes are introduced into the circumferential directivity pattern, with the highest sound pressure levels observed perpendicular to the pylon plane.

The experimental and numerical evaluations of the potential of pylon trailing edge blowing to reduce the adverse installation effects experienced by pusher propellers have shown that the application of pylon blowing can result in clear noise reductions. Considering the significant fuel savings promised by future engine concepts employing propellers in a pusher configuration, this is an important result which can be used to develop potential solutions for the relatively high noise emissions associated with such propulsion systems. Follow-up research using additional computational and measurement techniques is required to increase the understanding of the working principles of the blowing system and its effects on the propeller performance and noise emissions.

Table of Contents

Nomenclature

List of Symbols

Symbol	Description	Unit
a	Speed of sound	m/s
A	Area	m^2
AR	RSB calibration matrix	N(m)/V
b	Span	m
BPF	Blade Passage Frequency	Hz
B	Number of propeller blades	-
c	Chord	m
c_d	Drag coefficient	-
c_l	Lift coefficient	-
c_{l_α}	Lift gradient	1/rad
$\Delta c_{l_{\text{stall}}}$	Lift coefficient increment to stall	-
CG	Coherent gain	-
C_p	Pressure coefficient	-
C_Q	Torque coefficient, $C_Q = Q/\rho n^2 D^5$	-
C_T	Thrust coefficient, $C_T = T/\rho n^2 D^4$	-
D	Diameter	m
	Doppler factor	-
	Drag	N
f	Non-dimensional chordwise lift/drag distribution function	-
	Force per unit area	N/m^2
	Frequency	Hz
	Raw analog output	V
	Reynolds number scaling exponent	-
Δf	Frequency bin width	Hz
F	Force	N
FA	Distance from the blade section normal to the blade planform	m
G	Green's function	-
h	Height	m
H	Non-dimensional thickness distribution function	-
i	Index	-
I	Modified periodogram	-

Continued on next page

Continued from previous page

Symbol	Description	Unit
j	Index	-
J	Advance Ratio, $J = U_\infty/nD$	-
J_n	n^{th} order Bessel function of the first kind	-
k	Harmonic order	-
	Index	-
	Wave number	-
K	Calibration factor	-
	Correction factor	-
	Average factor Welch's method	-
L	Length	m
m	Harmonic number (noise harmonics)	-
$\dot{m}$	Mass flow	kg/s
M	Mach number	-
MCA	Distance between the local mid-chord point and the pitch change axis	m
n	Rotational velocity	rev/s
N	Number	-
NG	Noise gain	-
p	Pressure	Pa
P	Harmonic component	-
	Power	dB
Q	Torque	Nm
	Volumetric flow rate	m^3/s
r	Radial coordinate	m
R	Distance	m
	Propeller radius	m
Re	Reynolds number	-
RPM	Propeller RPM	rev/min
SPL	Sound Pressure Level	dB
s	Spacing	m
S	Sears function	-
t	Thickness	m
	Time	s
T	Period	s
	Thrust	N
$\overline{T}$	Aerodynamic transfer function	-
$T_{i,j}$	Lighthill's stress tensor	N/m^2
u	Induced velocity	m/s
Δu	Velocity deficit	m/s
U	Velocity	m/s
W	Effective advance velocity	m/s
	Window function	-
X	X-coordinate	m
y	Sideline distance	m

Continued on next page

Continued from previous page

Symbol	Description	Unit
Y	Y-coordinate	m
Y_n	n^{th} order Bessel function of the second kind	-
Z	Z-coordinate	m
α	Angle of attack	rad
α_0	Zero-lift angle of attack	rad
β	Blade pitch angle	deg
	Prandtl-Glauert compressibility factor, $\beta = \sqrt{(1 - M^2)}$	-
	Empirical constant Schlichting Wake Model, $\beta = 0.18$	-
Γ	Circulation	m^2/s
ζ	Argument of Bessel function used in propeller noise computations $\zeta = mB\eta M_{\text{t}} \sin\theta$	-
η	Propeller efficiency, $\eta = \frac{J}{2\pi}\frac{C_T}{C_Q}$	-
	Non-dimensional radial coordinate r/R	-
$\Delta\eta$	Non-dimensional spanwise extent of radial segment	-
θ	Axial directivity angle	deg
λ	Taper ratio	-
Λ	Sweep angle	deg
ξ	Integral wake velocity deficit	-
ρ	Density	kg/m^3
σ	Reduced frequency	-
ϕ	Circumferential directivity angle	deg
	Polar angle	deg
φ	Advance angle	deg
	Phase shift	rad
ψ	Frequency domain distribution function	-
Ω	Angular Velocity	rad/s

Sub- and Superscripts

Symbol	Description
0	Initial
	Outside flow
1B	Single blade
3/4	75% chord
a	Axial
	Apparent
add	Additional
air	Air
b	(propeller) Blade
blow	Blowing
bp	Back pressure
cal	Calibrated

Symbol	Description
mic	Microphone
min	Minimum
n	Normal
non-ind	Non-induced
non-lin	Non-linear
o	Offset
obs	Observer
out	Outlet
p	Propulsive
prop	Propeller
r	Radial
ref	Reference

Continued on next page

Continued from previous page

Symbol	Description
cor	Corrected
crit	Critical
cut	Cut-off
D	Doppler
	Drag
des	Design
e	Exit
ext	Extended
flat	Flattened
g	Gust
H	Helical
hub	(propeller) Hub
i	Index
in	Inlet
ind	Induced
inst	Installed
iso	Isolated
j	Jet
L	Lift
lin	Linear
m	Measurement
M	Compressible
max	Maximum
meas	Measurement
req	Required
rms	Root mean square
rot	Rotational
RPM	RPM
RSB	Rotating shaft balance
s	Static
	Sweep
	Sample/sampling
shp	Sharp
SS	Steady-state
stall	Stall
t	Tangential
	Total
	(wind) Tunnel
	Tip
TE	Trailing edge
UBR	Uniform blowing rod
US	Unsteady
v	Vane
V	Volume
w	Wake
x	Chordwise
ϕ	Polar angle
∞	Freestream

Abbreviations and Acronyms

Abbreviation	Description
ACARE	Advisory Council for Aeronautics Research in Europe
BBN	Broadband Noise
BPF	Blade Passage Frequency
DAQ	Data Acquisition
DNW	German-Dutch Wind Tunnels
NLR	National Aerospace Laboratory of the Netherlands
OJF	Open Jet Facility
PCA	Pitch Change Axis
PSD	Power Spectral Density
RPM	Revolutions Per Minute
RSB	Rotating Shaft Balance
SLS	Selective Laser Sintering
UBR	Uniform Blowing Rod
UDF	Unducted Fan

Chapter 1

Introduction

Growing concerns about the environmental impact of aircraft operations and increasing fuel prices have led to the demand for more fuel-efficient aircraft. One of the technologies with the potential to offer a significant reduction in fuel burn is the open rotor engine. When compared to current generation turbofans, open rotor engines allow the bypass ratio to be increased to values unattainable by turbofans, thereby increasing the engines' propulsive efficiency.

This chapter first presents an overview of the history of the open rotor engine concept in Section 1.1, followed by Section 1.2 which discusses the opportunities and challenges related to this engine concept. Then, an overview of open rotor noise sources is presented in Section 1.3, after which Section 1.4 elaborates on the potential of pylon blowing to reduce the adverse pylon - propeller interaction effects. Having introduced the open rotor engine concept, the thesis' research aim and objectives are stated in Section 1.5 and the structure of this report is presented in Section 1.6.

1.1 History of the Open Rotor Engine Concept

The history of the open rotor engine concept shows a clear correlation with trends in the demand for more fuel-efficient aircraft. Development started in the 1970s following the major oil crisis in 1973 (Subsection 1.1.1). After a decade of little interest, increases in fuel prices and growth of air traffic volume have led to the resurrection of the open rotor engine starting in the first years of the current millennium (Subsection 1.1.2).

1.1.1 Development of the Propfan – the First Open Rotor Engine (1975-1990)

The development of the open rotor engine (also known as unducted fan engine) started by a collaboration of NASA and Hamilton Standard in the years following the 1973 oil crisis. Driven by record high fuel prices, ways were sought to increase the efficiency of aircraft. The very high bypass ratios achievable by open rotor engines promised a step change in propulsive efficiency compared to turbofan engines. As a result, the open rotor was considered as a very interesting option for an efficient aircraft propulsion system.

The resulting open rotor engine concept was first presented to the public in 1975, under the name of 'propfan' [1]. In subsequent years the concept was further developed by NASA and a continuously increasing number of industry and university partners in the *Advanced Turboprop Project*, which initially focused on single-rotating propfans but gradually moved

towards contra-rotating designs in later years. Finally, full-scale contra-rotating propfan designs from General Electric (GE36 UDF) and a joint-venture of Pratt & Whitney and Allison (578-DX) were successfully flight tested in 1987 on Boeing 727 and McDonnell Douglas MD-80 test aircraft [2].

Despite the propfan's positive reception by various aircraft manufacturers such as Boeing, Lockheed, and McDonnell Douglas, the reduction of fuel prices in the late 1980s made the propfan lose its potential market in the aircraft industry. As such the incentive for further developments disappeared and the *Advanced Turboprop Project* was halted in 1987 [3]. However, with fuel prices back to record highs in recent years, a renewed interest in the open rotor engine concept is observed in the aircraft community.

1.1.2 Renewed Interest in the Open Rotor Engine (2005-present)

Starting from the first years of the 21st century increasing fuel prices and growing air traffic volume combined with concerns about the environmental impact of aircraft operations have been identified as new drivers for the development of more fuel-efficient aircraft. Ambitious targets have been set by the Advisory Council for Aeronautics Research in Europe (ACARE), which aim for a 50% reduction in fuel consumption (thus CO_2 emissions) per passenger kilometer and a 50% reduction in perceived noise levels for aircraft entering service in 2020 when compared to those entering service in 2000 [4]. Similar targets have been set in the United States by NASA [5]. There is a general consensus that game-changing technologies are required to achieve these challenging goals.

In the area of aircraft propulsion the open rotor engine is considered as one of the technologies with the potential to offer the required increase in efficiency. Starting from around 2005, extensive research studies in the field of open rotor engine technology have been performed by the industry and academic institutions in both Europe and the United States, leading to a further optimization and maturation of the technology. On the European side, several projects funded by the European Commission (NACRE, DREAM, Clean Sky) are or have been performed, involving contributions from Rolls-Royce, Snecma, Airbus, and many other influential institutions [6]. In the United States, NASA's SFW and ERA projects and the FAA's CLEEN program all (partly) focus on open rotor engine technology [7]. In particular, NASA and GE Aviation have been collaborating on open rotor noise developments since 2009 [5, 8]. Both numerical and experimental research is performed, mainly focused on reducing the noise emissions from open rotor engines.

A rendering of a modern geared open rotor engine currently under conceptual development at Rolls-Royce is shown in Figure 1.1. Figure 1.2 displays an example of a typical aircraft configuration with rear-mounted contra-rotating open rotor engines in a pusher configuration.

1.2 Opportunities and Challenges Related to the Open Rotor Engine Concept

The open rotor engine concept offers a major opportunity in terms of the potential reduction in aircraft fuel consumption when compared to aircraft equipped with turbofans. However, also a number of challenges remain which have to be overcome before open rotor technology can successfully be applied on next-generation aircraft. Both opportunities and challenges related to the open rotor engine concept are discussed separately in the following two subsections.

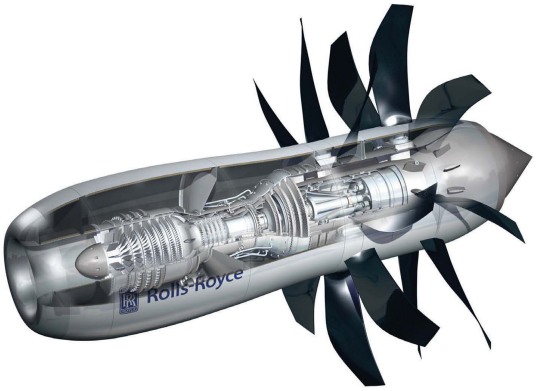

Figure 1.1: Rendering of Rolls-Royce geared open rotor concept engine. Reproduced from [9].

Figure 1.2: Typical aircraft configuration with rear-mounted contra-rotating open rotor engines. Reproduced from [10].

1.2.1 Opportunities Related to the Open Rotor Engine Concept

The major advantage of the open rotor engine is that it offers a step change in propulsive efficiency when compared to current generation turbofan engines, with estimations for the possible reduction in fuel burn at around 25-30% [5, 11, 12]. The high efficiency of the open rotor engine is the result of the high bypass ratios achievable with this type of engine. The corresponding beneficial effect on the propulsive efficiency can be explained by considering the equations for the thrust and propulsive efficiency of jet engines:

$$T = \dot{m}\,(U_\mathrm{j} - U_\infty) \tag{1.1}$$

$$\eta_\mathrm{p} = \frac{2}{1 + \frac{U_\mathrm{j}}{U_\infty}} \tag{1.2}$$

with $\dot{m}$ the air mass flow, T the net thrust, U_j the jet velocity, U_∞ the freestream velocity, and η_p the propulsive efficiency.

From Equation (1.2) it follows that the propulsive efficiency η_p increases when the difference between the jet velocity U_j and the freestream velocity U_∞ decreases. Combination with Equation (1.1) shows that for a given thrust T this implies that from a propulsive efficiency point of view it is more efficient to give a small acceleration (i.e. a small difference between U_j and U_∞) to a large amount of air (i.e. a large mass flow $\dot{m}$) than vice versa. Correspondingly, higher propulsive efficiencies are achieved by increasing the bypass ratio. For turbofans a limit exists on the maximum feasible bypass ratio since with increasing bypass ratio the nacelle diameter increases, leading to increased nacelle weight and drag. This limitation is eliminated by open rotor engines, for which the propeller blades operate without a nacelle thus making it possible to achieve very high bypass ratios.

1.2.2 Challenges Related to the Open Rotor Engine Concept

The high propulsive efficiency offered by open rotor engines comes at the cost of a number of disadvantages compared to turbofans, thereby presenting challenges for the successful implementation of open rotor engines on next-generation aircraft. The two most important

challenges are discussed here, after which a number of additional complications in open rotor design and integration are briefly mentioned.

The major disadvantage of the open rotor engine is its associated high level of noise emissions. The open rotor's most significant noise sources are the propeller blades, of which the emitted noise is not shielded by a casing as is the case for turbofans. Assuming a contra-rotating configuration, tonal noise is generated by each rotor individually as well as by the aerodynamic interactions between the two rotors. These interactions are strong and exist up to high frequencies. Furthermore, installation effects lead to unsteady blade loading and associated additional tonal noise emissions. Broadband noise is generally considered as less important, although significant reductions in the tonal noise levels have increased the contribution of broadband noise to the overall perceived noise levels [13]. Optimization of the aeroacoustic properties of open rotor engines have led to open rotor designs with a cumulative noise margin relative to the current ICAO Chapter 4 Noise Certification Standard. However, despite the advancements made in open rotor engine noise emissions it is unlikely that noise levels emitted by open rotor engines will be comparable to (or less than) those emitted by next-generation turbofans [5, 12]. A more detailed discussion of the open rotor noise sources is provided in Section 1.3, which also discusses the corresponding link to the current research project.

A second challenge is the fact that the open rotor's propellers impose limitations on the aircraft's flight speed. To prevent excessive losses in the propeller efficiency and increases in the noise emissions it has to be made sure that the propeller's helical tip speed is kept below acceptable Mach numbers. Practically, this means that aircraft equipped with open rotor engines are limited to cruise speeds below approximately 0.80, with a typical value for latest-generation open rotor technology equal to 0.78 [7]. For short-haul aircraft this is comparable with the cruise performance of current generation aircraft, while long-range aircraft typically cruise at higher Mach numbers of around 0.82-0.85 [14]. For long-range aircraft the associated increase in travel time might impose a limitation on the willingness of airlines to adopt aircraft equipped with open rotor engines.

Furthermore, a number of additional technological challenges are identified in the development of open rotor engines. The absence of a casing around the open rotor's propeller blades imposes certification challenges concerning blade failures. Furthermore, the open rotor requires a complex and heavy blade pitch control system and the integration of the open rotor on the airframe is not straightforward. However, it is expected that these challenges can be solved by using advanced design methods and multi-disciplinary optimization techniques and thus will not be critical with respect to the further development of the open rotor engine. [15]

1.3 Open Rotor Noise Sources

As mentioned, the relatively high noise emissions associated with open rotor engines currently form the main challenge for their widespread commercial introduction. Open rotor engines have a tone-dominated noise signature, with broadband noise (BBN) only becoming significant at higher frequencies [13]. A schematic overview of contra-rotating open rotor noise sources is presented in Figure 1.3.

From Figure 1.3 it is seen that the open rotor noise sources can be divided into two categories: rotor sources and other sources. For overview reasons, a breakdown of the open rotor noise sources is given in Figure 1.4.

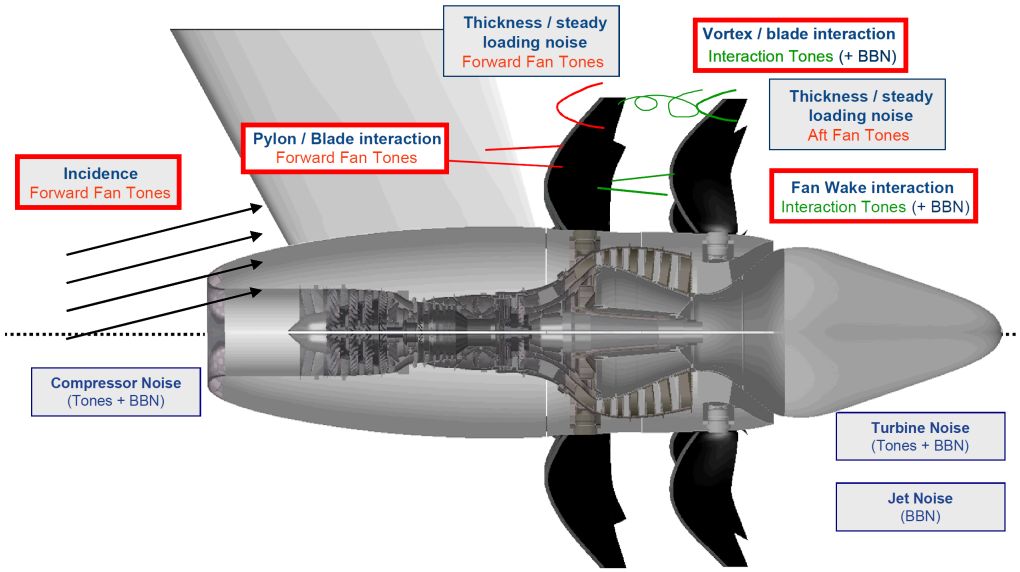

Figure 1.3: Overview of contra-rotating open rotor noise sources. Reproduced from [11].

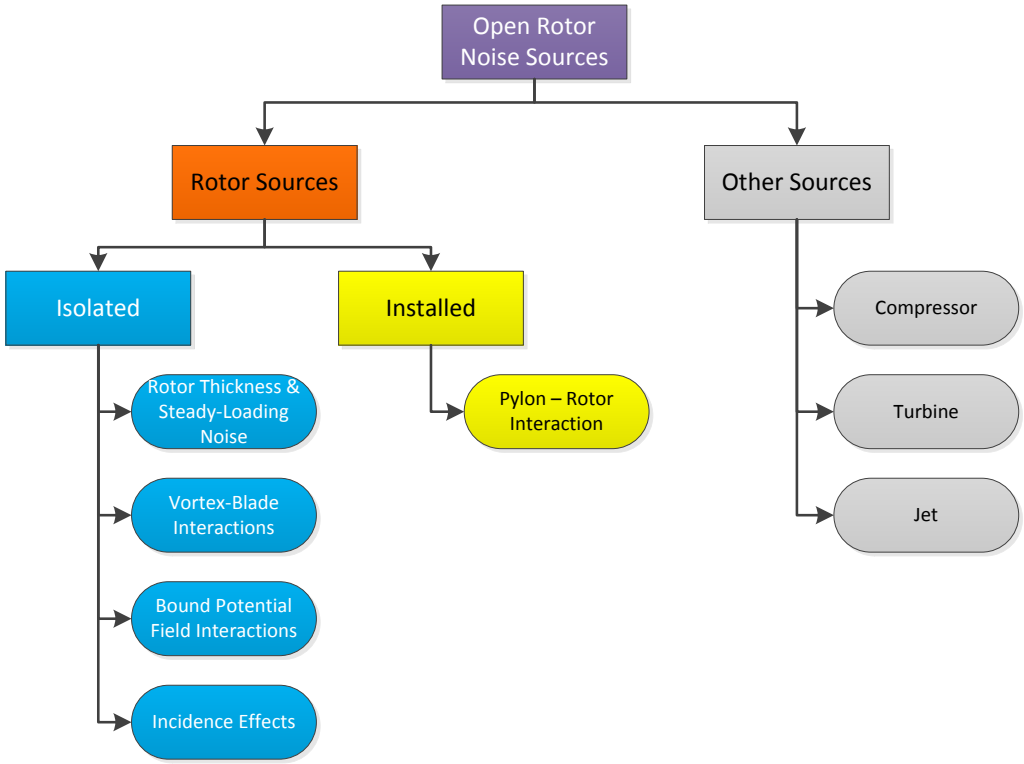

Figure 1.4: Breakdown of contra-rotating open rotor noise sources.

The noise sources indicated as other sources in Figure 1.4 are of limited interest to the current research project, and thus are not further considered here. Regarding the rotor noise sources a distinction is made between isolated and installed rotor noise sources, which are treated separately in Subsections 1.3.1 and 1.3.2, respectively. In both subsections the attention is focused on tonal noise; a brief discussion of broadband noise sources is given in Subsection 1.3.3 which deals with both the isolated and installed cases.

1.3.1 Isolated Tonal Noise Sources

The isolated open rotor generates tonal noise at multiples of the Blade Passage Frequency[1] (BPF) due to thickness and steady-loading noise radiated from the front and rear rotors. Furthermore, aerodynamic interaction effects result in interaction noise due to the wake and tip vortices from the front rotor impinging on the rear rotor, and the bound potential fields of the front and rear rotors interacting with the blades of the adjacent rotor. These interactions result in interaction tones at frequencies equal to $n_1 \cdot BPF_{\text{front}} + n_2 \cdot BPF_{\text{rear}}$. Finally, incidence effects result in additional noise radiation from the front rotor. [11, 13]

1.3.2 Installed Tonal Noise Sources: Pylon Installation Effect

In addition to the isolated noise sources, installation of the open rotor on the aircraft introduces another noise generating mechanism. Interior noise and ground clearance reasons dictate a pylon-mounted placement at the aft end of the fuselage, as illustrated before in Figure 1.2. As a result, the wake shed from the upstream pylon impinges on the front rotor, resulting in unsteady blade loading and associated noise emissions [11, 16–21]. Note that apart from the impact on the propeller noise emissions the fluctuating loads also affect the propeller performance.

The pylon - open rotor interaction mainly affects the noise levels associated with the front rotor tones, while the rear rotor tones show some effect and the interaction tones remain unaffected [20–23]. Furthermore, the noise emissions in the installed configuration display a clear axial directivity. Experimental results obtained by Ricouard et al. and Block showed that the pylon interaction noise has maxima towards the propeller axis (i.e. in the upstream and downstream directions), while minimum additional noise levels are experienced in the plane of the propeller at an axial directivity angle of around $\theta = 90°$ [16, 17, 20, 21, 24]. Furthermore, lobes are introduced in the circumferential directivity pattern with maximum noise levels experienced over the circumferential angle range approximately perpendicular to the pylon plane [20, 24].

1.3.3 Broadband Noise Sources

It should be noted that advancements in the design of open rotor engines for reduced tonal noise emissions have made broadband noise increasingly important. First investigations of the broadband noise emissions of uninstalled contra-rotating open rotors have identified the broadband rotor-wake/rotor interaction noise and the broadband rotor trailing edge noise as the two most significant contributors to the overall broadband noise levels. For installed open rotor engines it is expected that additional broadband noise emissions result from the impingement of the turbulent wake shed from the upstream pylon onto the leading edge of the front rotor blade, and from the ingestion of turbulence from various sources (atmospheric, fuselage boundary layer, etc.). [25] Experimental investigations by Rolls-Royce showed that the broadband noise emissions dominate the open rotor noise at mid to high frequencies and high blade speeds. At lower frequencies the tonal noise components still clearly dominate the total noise emissions, at absolute values higher than the broadband emissions in the higher frequency range. [13] It is clear that broadband noise emissions contribute to the open rotor noise emissions. However, to limit the scope of the current research project it is decided to only focus on tonal noise emissions in the following.

[1] The n^{th} Blade Passage Frequency $n \cdot BPF$ is defined as $n \cdot BPF = nB\Omega/(2\pi)$ [Hz], with B the number of blades and Ω the angular velocity of the rotor in radians per second.

1.4 The Potential of Pylon Blowing to Reduce Installation Effects

The pylon installation effects originate from the impingement of the pylon wake on the propeller. The resulting non-uniform propeller inflow leads to unsteady blade loading with associated performance and noise emission penalties. Based on the identified interaction mechanism (see Subsection 1.3.2) it can be expected that the installation effects can be reduced or even completely removed by eliminating the pylon wake. The flow control techniques that could be used for this purpose can be divided into active and passive techniques. From the literature it is concluded that especially the active technique of pylon blowing can be very effective in reducing the pylon - propeller interaction effects, and has indeed been successfully applied in a number of independent numerical and experimental studies [19–21, 26–28].

The outlet of the pylon blowing system can be positioned in the trailing edge of the pylon or along the pylon chord at the aft part of the pylon. The former approach leads to the most straightforward integration of the blowing outlet in the pylon model and was adopted in experimental studies by Airbus, Boeing, and DLR [19–21]. The approach in which the blowing outlet is positioned along the pylon chord on the other hand provides additional length for the blown flow to mix with the undisturbed external flow, and was used in experimental investigations performed by NASA [27]. Numerical studies performed by ONERA showed that chordwise injection results in the most uniform wake profiles [26].

As an example of the possible reductions in the pylon wake velocity deficit due to the application of pylon blowing, Figure 1.5 presents a number of wake profiles measured during NASA's investigations (see reference [27]) of the effects of blowing on the propeller performance.

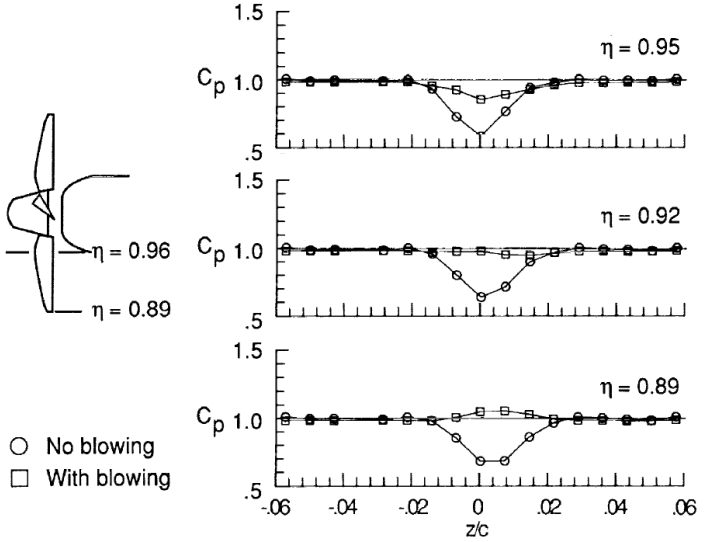

Figure 1.5: Pylon wake profiles with and without blowing using a blowing system with its outlets at 80% of the pylon chord (z = lateral coordinate, η = radial coordinate). Reproduced (in modified form) from [27].

Figure 1.5 shows that the application of pylon blowing can indeed successfully fill up the pylon wake. During the same experiments the propeller performance was measured in the isolated, installed, and blown configurations. The results that were obtained for the time-averaged thrust coefficient as a function of the advance ratio[2] are plotted in Figure 1.6. The installed and blown configurations were characterized by the wake profiles presented in Figure 1.5.

[2]The advance ratio J is defined as the ratio of the freestream velocity U_∞ and rotational component nD.

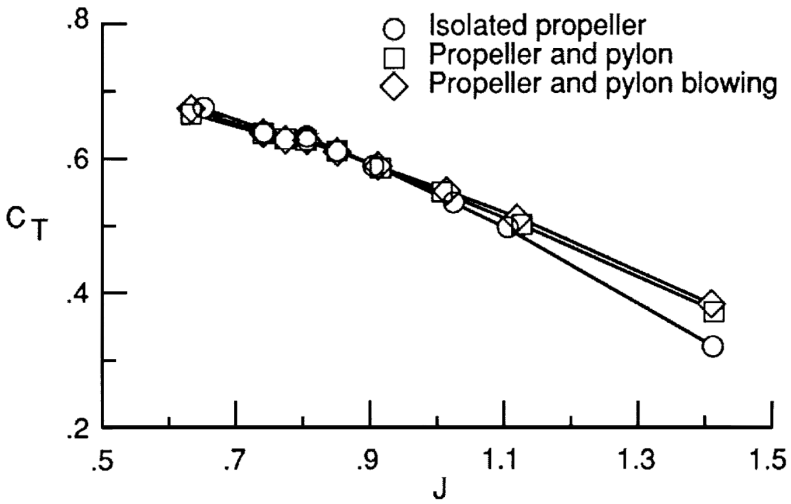

Figure 1.6: Thrust coefficient C_T versus advance ratio J for a pusher propeller in isolated, installed, and blown configurations ($U_\infty = 48.4$ m/s, $\beta_{3/4} = 40°$). Reproduced from [27].

Figure 1.6 shows that for advance ratios below 1.0 the effects of installation were found small, indicating that the time-averaged propeller performance was dominated by steady-state effects. For advance ratios above 1.0 on the other hand the results measured in the three configurations started to deviate, with the isolated propeller generating the lowest thrust and the propeller in the blown configuration producing the highest thrust. Note that considering the wake profiles presented in Figure 1.5 it would be expected that the blown propeller thrust would fall in between the results measured in the isolated and installed configurations, since the velocity deficit in the blown pylon wake is reduced as compared to the unblown case. Reference [27] however does not provide any reasons for this unexpected behavior.

An example of the beneficial effects of pylon blowing on the noise spectrum of a contra-rotating open rotor engine (scale model) as obtained by Ricouard et al. in DNW's LLF low-speed wind tunnel is presented in Figure 1.7.

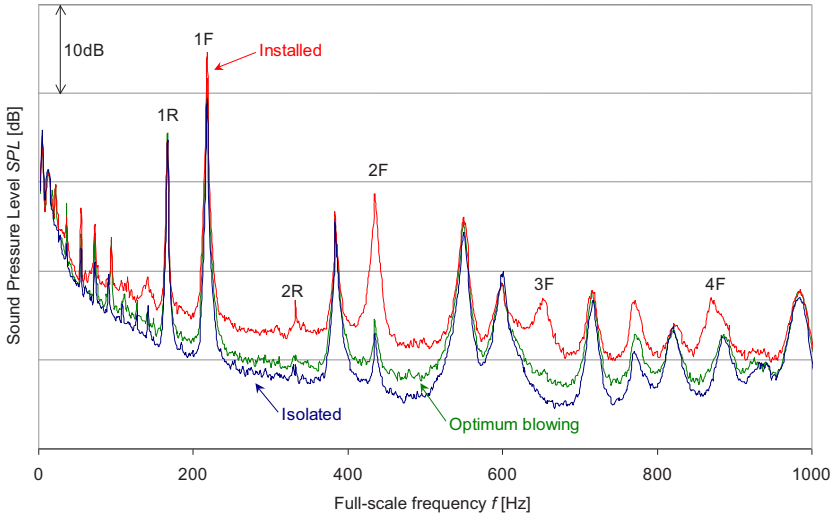

Figure 1.7: Effects of pylon blowing on the noise spectrum of a typical contra-rotating open rotor engine. The n^{th} front and rear blade passage frequencies are indicated by nF and nR, respectively. Reproduced from [20].

From Figure 1.7 it is seen that the application of pylon blowing indeed successfully reduced the propeller noise levels. Whereas for the 1BPF tone emitted by the front rotor (1F) the effects of installation resulted in an increase in the SPL of 5 dB compared to the isolated configuration, the application of blowing reduced the noise penalty to 2 dB (hence corresponding to a noise reduction due to blowing of 3 dB). For the front rotor's 2BPF tone (2F) the presence of the upstream pylon resulted in an increase in SPL of 16 dB compared to the isolated propeller noise emissions, while the application of blowing reduced the noise levels to a level only 2 dB above that measured in the isolated configuration. Figure 1.7 also shows that the measured effects of installation on the rear rotor tones were much less pronounced than for the tonal noise emitted by the front rotor. Considering the 1BPF tone of the rear rotor (1R) the noise levels are within 1 dB for the isolated, installed, and blown configurations. The SPL of the rear rotor's 2BPF tone (2R) increased by 7 dB due to installation, however at an absolute level about 20 dB lower than the SPL of the 1BPF tone of the rear rotor.

1.5 Research Aim and Objectives

The potential of pylon trailing edge blowing to reduce the adverse installation effects experienced by rear-fuselage mounted open rotor engines forms the main topic of this thesis. Both experimental and numerical investigations are to be performed, which leads to the definition of the following research aim:

> *The aim of this research project is to experimentally and numerically analyze the performance and noise emissions of a pylon - pusher propeller combination, with and without pylon trailing edge blowing.*

It should be noted that available experimental apparatus limit the current project to single-rotating propeller applications, in contrast to the contra-rotating technology typically projected for future applications of open rotor engines on next-generation passenger aircraft.

The project's aim is planned to be achieved by satisfying the following major research objectives:

- To perform scale model wind tunnel experiments for various operating conditions in which quantitative measurements are performed of:
  - the effect of the presence of an upstream pylon on the pusher propeller performance and noise emissions
  - the effect of pylon blowing on the wake profile of a generic pylon design
  - the effect of pylon blowing on the pusher propeller performance and noise emissions
- To develop and apply a numerical tool capable of quantifying the effects of the presence of an upstream pylon on the performance and noise emissions of a single-rotating pusher propeller.

1.6 Thesis Outline

The body of this report consists of the current introduction followed by three separate parts consisting of in total eleven chapters, which are ordered as shown in the thesis roadmap presented in Figure 1.8.

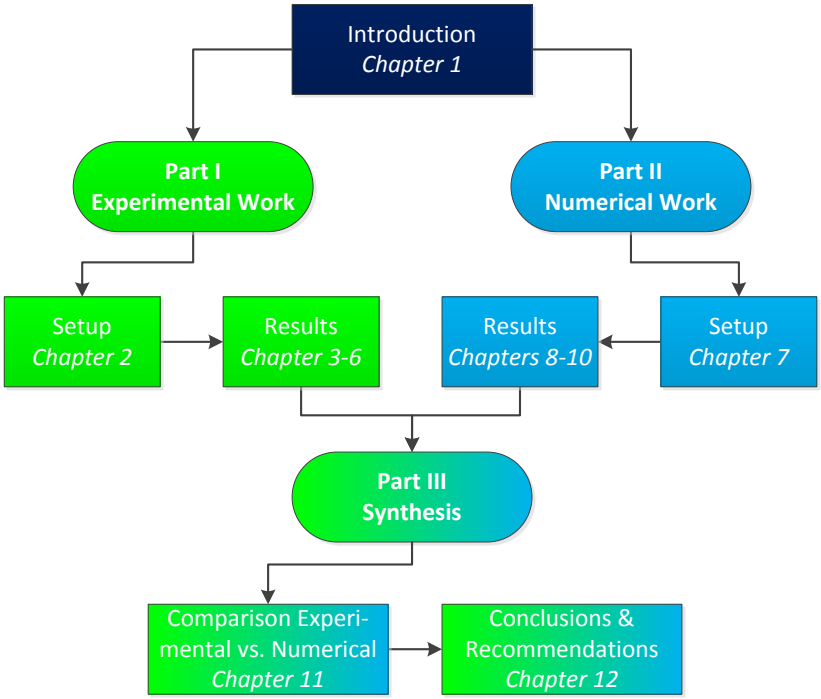

Figure 1.8: Thesis roadmap.

Following this introduction, Part I presents all experimental work. First, a detailed description of the experimental setup is given in Chapter 2. Thereafter, the experimental results are presented in four separate chapters. The pylon wake profile measurements in the unblown and blown configurations are treated in Chapter 3, followed by Chapter 4 which presents the results obtained from the initial noise measurements performed using an unpowered propeller model. Finally, the results obtained using the powered propeller model are discussed in Chapters 5 and 6, discussing the propeller performance and noise emissions, respectively.

Having completed the experimental part, the report continues with Part II which deals with the numerical evaluations of the effects of pylon blowing on pusher propeller performance and noise emissions. Following the same structure as used in Part I, first the setup of the numerical methods is treated in Chapter 7. Subsequently, the numerical results are presented in three separate chapters. The computed pylon wake profiles in the unblown configuration are discussed in Chapter 8, followed by the propeller performance results in Chapter 9. Finally, the results obtained from the numerical analysis of the propeller noise emissions are presented in Chapter 10.

After the separate treatment of the experimental and numerical results, a synthesis of all data is the topic of discussion of Part III. First, the computed and measured results for the pylon wake profiles, propeller performance, and noise emissions are compared in Chapter 11. Finally, the conclusions drawn from the work presented in this report are stated in Chapter 12, including recommendations for future research.

Part I

Experimental Work

"The true method of knowledge is experiment."
William Blake

Part I of this report focuses on the experimental work performed to investigate the effects of pylon trailing edge blowing on pusher propeller performance and noise emissions. Following an overview of the setup of the wind tunnel experiments, the measured pylon wake profiles, the unpowered propeller noise emissions, the powered propeller performance, and the powered propeller noise emissions are discussed in separate chapters.

Chapter 2

Experimental Setup

This chapter describes the setup of the wind tunnel experiments performed to study the effects of pylon trailing edge blowing on pusher propeller installation effects. First, an overview of the test campaign is given in Section 2.1. Subsequently, Section 2.2 introduces the coordinate systems used throughout the discussion of the experimental setup and results. Thereafter, the wind tunnel in which the experiments were performed is described in Section 2.3. Then, Section 2.4 presents the wind tunnel models used, followed by a discussion of the pylon blowing system in Section 2.5. Subsequently, the measurement techniques are elaborated upon in Section 2.6, followed by Section 2.7 which introduces the techniques used to post-process the measurement results. A detailed description of the post-processing of the experimental data is given in Appendix A, which also includes an overview of the measurement corrections.

2.1 Test Campaign Overview

The experimental analysis focused on pusher propeller performance and noise emissions in isolated, installed (with pylon upstream), and blown (with blown pylon upstream) conditions. The test campaign was started with a set of pylon wake measurements in unblown and blown conditions. Subsequently, an unpowered (windmilling) propeller was used to perform initial noise measurements in isolated, installed, and blown configurations. Finally, a powered propeller was used to measure the isolated, installed, and blown propeller performance and noise emissions. An overview of the elements of the test campaign is given in Figure 2.1.

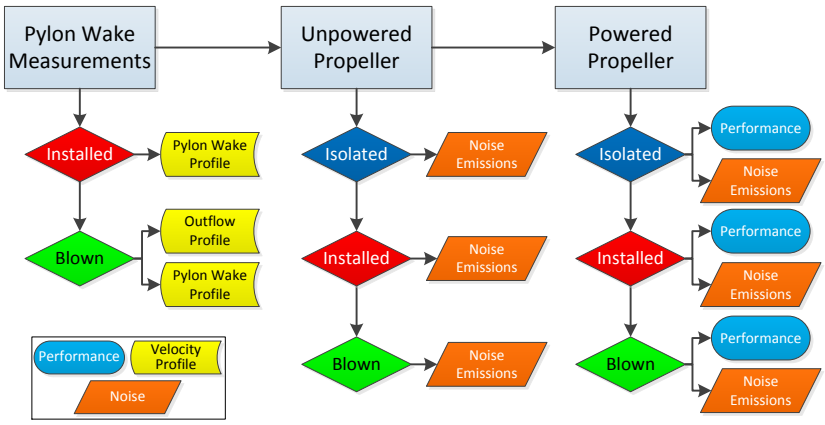

Figure 2.1: Overview of the different elements of the wind tunnel test campaign.

The pylon wake measurements were performed to obtain insight in the wake profile behind the pylon which would impinge on the propeller during the subsequent measurements. Also, the effectiveness of the blowing system was assessed. A range of blowing rates was considered and the measurements were performed at a range of wind tunnel velocities, including zero velocity to assess the uniformity of the blowing system's outflow profile.

The unpowered propeller measurements served as an initial test for the effectiveness of the blowing system in reducing the noise penalty due to the installation effects. Initially, four different wind tunnel velocities were considered. Subsequently, an analysis of the noise directivity pattern was performed for two freestream velocities.

The final part of the test campaign involved the powered propeller model. First, measurements were performed at a range of freestream velocities and a sweep of advance ratios to assess the effects of installation on the propeller performance. Thereafter, noise measurements were done to quantify the effects of installation and blowing on the emitted noise levels.

2.2 Coordinate Systems

Throughout the discussion of the experimental setup and results three different coordinate systems are used: the wake-based coordinate system, the propeller disk coordinate system, and the microphone axial directivity coordinate system. Note that the numerical analysis discussed in Part II of this report uses the same coordinate systems as presented here.

An illustration of the definition of the wake-based coordinate system $\mathbf{X}_\mathrm{w}$ is presented in Figure 2.2. The system is a standard Cartesian coordinate system with its origin defined at the intersection of the pylon's chord line and the trailing edge at the root of the pylon model.

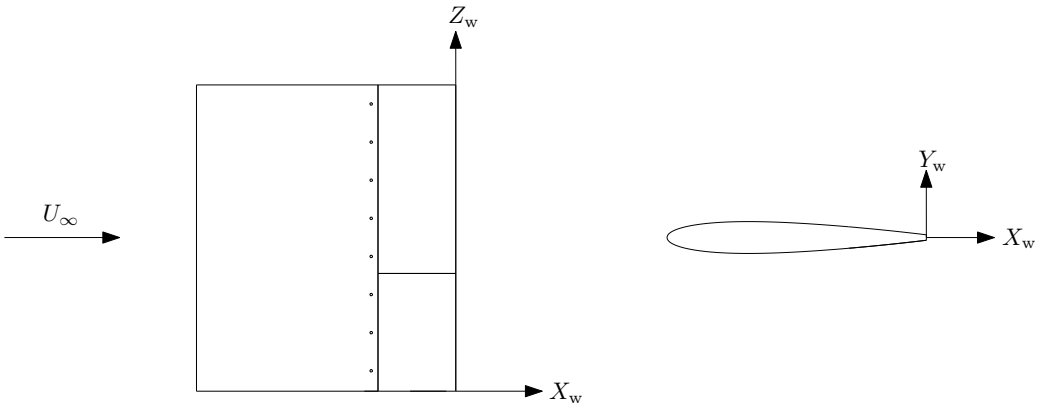

Figure 2.2: Wake based coordinate system: side view (l) and top view (r).

The propeller disk coordinate system shown in Figure 2.3 is characterized by a polar coordinate system with its origin in the center of the propeller disk. The blade section position is defined by the non-dimensional radial coordinate η and the polar angle ϕ. The polar angle ϕ is also used to define the circumferential directivity angle of the propeller noise emissions.

The microphone axial directivity coordinate system depicted in Figure 2.4 is used to define the axial directivity characteristics of the propeller noise emissions. The axial directivity angle θ is defined to be zero along the propeller axis in the upstream direction, while it equals 90 degrees in the propeller plane. All noise emission results are defined relative to an observer distance R, which is also included in Figure 2.4.

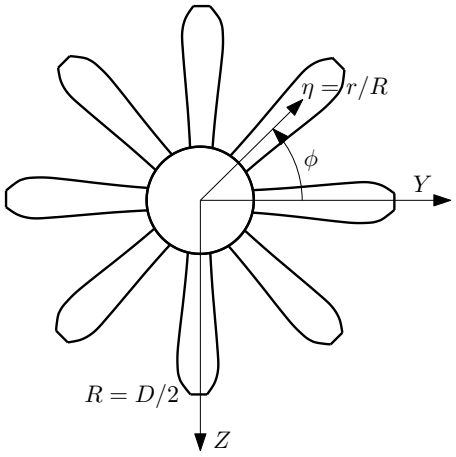

Figure 2.3: Propeller disk coordinate system.

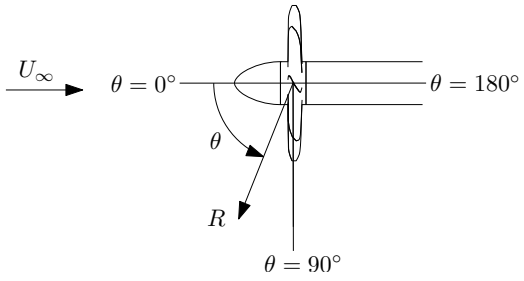

Figure 2.4: Microphone axial directivity coordinate system.

2.3 Wind Tunnel Facility

All experiments were performed in Delft University of Technology's Open Jet Facility (OJF). This closed circuit wind tunnel with open test section and an equivalent exit jet diameter of 3.1 m has a maximum wind velocity of 30 m/s. The test section is 6.0 m wide, at a height of 6.5 m and a length of 13.5 m. To remove spatial velocity deviations and to reduce the flow's turbulence level, the settling chamber is equipped with a honeycomb flow rectifier and five screens. This results in velocity deviations smaller than 0.5% in the vertical plane at two meters from the outlet, with a longitudinal turbulence intensity level lower than 0.24%. To reduce noise levels, the inside of the entire tunnel is covered with perforated plates installed on mineral wood and sound absorbing foam. The fan however does not feature any special noise reduction measures. [29] A cutaway drawing of the OJF is depicted in Figure 2.5.

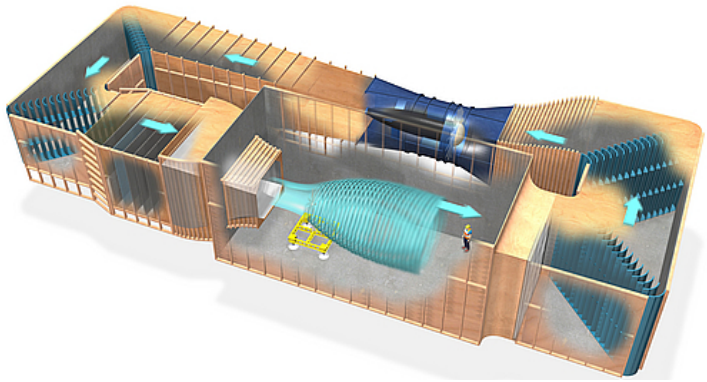

Figure 2.5: Cutaway drawing of Delft University of Technology's Open Jet Facility (OJF). Reproduced from [29].

2.4 Wind Tunnel Models

The wind tunnel tests involved the use of three scale models: the pylon (Subsection 2.4.1), the unpowered propeller (Subsection 2.4.2), and the powered propeller (Subsection 2.4.3). To simulate a pusher configuration the tractor propeller models were placed behind the pylon. Therefore, compared to a 'real' pusher configuration the nacelle was positioned at the wrong side of the pylon. No additional nacelle was installed upstream of the propeller. The pylon blowing system is integrated in the pylon, but discussed separately in Section 2.5.

2.4.1 Pylon

The pylon was designed based on typical pylon characteristics used in comparable pylon - propeller interaction studies (see for example references [16, 17, 21, 23, 24, 27, 30]) and taking into account the minimum dimensions required for a successful integration of the blowing system in the trailing edge region of the pylon. As a result, the pylon had a straight, untapered planform with chord equal to 1.25 times the propeller diameter. The span of the pylon was selected based on the available space in the test setup, resulting in a span of 0.450 m. Zigzag tape was attached to both sides of the pylon at 25% of the chord from the leading edge. A NACA 0012 profile was used, modified to have a trailing edge thickness of 2.1% of the chord.

Note that the large trailing edge thickness of the pylon model was required because of scaling issues related to the minimum feasible outlet height of the blowing system. Constraints were imposed on the minimum acceptable wall thickness at both sides of the blowing outlet and the minimum acceptable vane spacing. The increase in the pylon's trailing edge thickness will increase the size of the wake, thereby aggravating the adverse pylon - propeller interaction phenomena. For full-scale applications such problems are not expected, thus not requiring the large pylon trailing edge thickness. Two alternative pylon model configurations were used to assess the adverse effects of the large trailing edge thickness of the default model. For the 'extended' model two straight metal plates were taped to the aft end of the upper and lower surfaces of the original pylon model. Attachment of the extensions reduced the pylon trailing edge thickness to 4.5 mm, while the chord length increased by 25 mm. The 'sharp' pylon model was built by connecting a solid metal trailing edge extension to the original trailing edge of the default pylon model, resulting in a trailing edge thickness of 0.3 mm at a total pylon chord of 412 mm.

The integration of the pylon blowing system in the aft part of the pylon required the pylon (without trailing edge extension) to be manufactured in three separate parts. The solid front part of the pylon was milled out of aluminum, while the other two parts (the blowing system inlet and the Uniform Blowing Rod, see Section 2.5) were produced out of polyamide using Selective Laser Sintering (SLS). The front part of the pylon was designed with a straightforward connection system to which the other elements were connected in a reversible fashion.

An overview of the pylon characteristics is given in Table 2.1, followed by Figure 2.6 depicting technical drawings of the pylon models.

Table 2.1: Pylon model characteristics.

Parameter		**Symbol**	**Value**	
Chord	Default	c	381 mm	$1.25/D_{\text{prop}}$
	Extended	c_{ext}	406 mm	$1.33/D_{\text{prop}}$
	Sharp	c_{shp}	412 mm	$1.35/D_{\text{prop}}$
Span		b	450 mm	$1.48/D_{\text{prop}}$
Sweep angle		Λ	0 deg	-
Taper ratio		λ	1.0	-
Airfoil		-	NACA 0012 (modified)	-
Trailing edge thickness	Default	t_{TE}	8.0 mm	$0.021/c$
	Extended	$t_{\text{TE}_{\text{ext}}}$	4.5 mm	$0.011/c$
	Sharp	$t_{\text{TE}_{\text{shp}}}$	0.3 mm	$7.3 \cdot 10^{-4}/c$

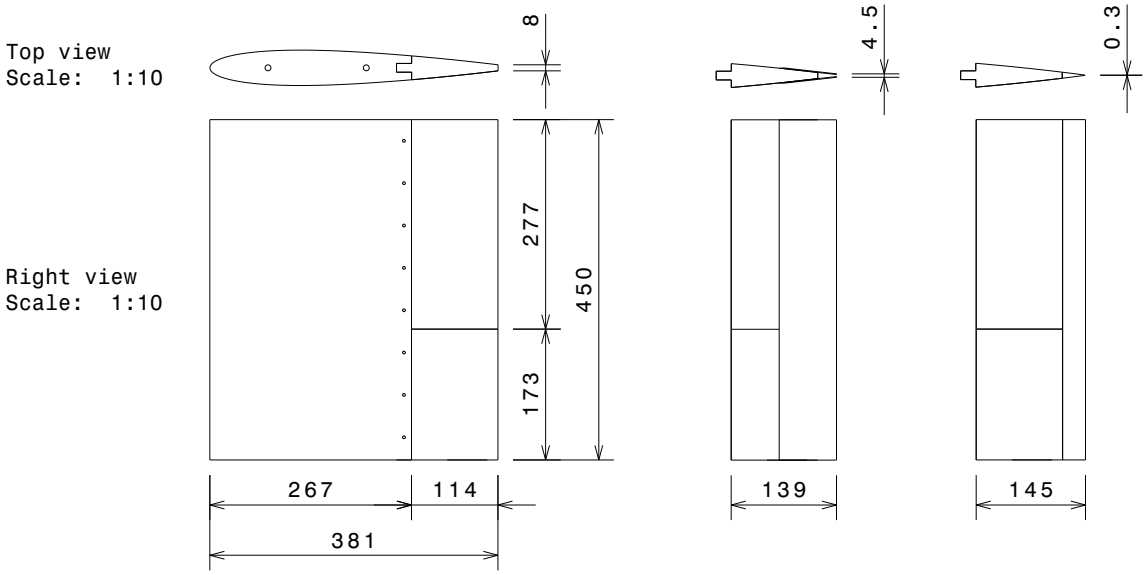

Figure 2.6: Technical drawing of the pylon scale model in the default configuration (left) and the aft parts of the extended (center) and sharp (right) models; dimensions in millimeters.

2.4.2 Unpowered Propeller

Initial noise measurements were performed using a two-bladed unpowered propeller, referred to as 'unpowered propeller' in the remainder of this report. The unpowered propeller has a diameter of 0.28 m and a blade angle at the 75% radial station of about 20 degrees. During the measurements in installed and blown conditions the unpowered propeller was positioned at 30% of the (default) pylon chord behind the pylon. Note that this is a relatively large value, which was selected to match the geometry of the installed powered test setup discussed in Subsection 2.4.3. The unpowered propeller is connected to a single ball bearing installed in a small housing fixed to the top of a straight support strut. The strut has a span of 583 mm and a cross-section formed by a NACA 0012 profile with a chord of 80 mm. An overview of the characteristics of the unpowered propeller is given in Table 2.2; photographs of the model in the isolated and installed configurations are presented in Figure 2.7.

Table 2.2: Characteristics of the *unpowered* propeller model.

Parameter	Symbol	Value	Unit
Number of blades	B	2	-
Diameter	D_{prop}	0.28	m
Hub diameter	D_{hub}	0.053	m
Blade angle at $r/R = 0.75$	$\beta_{3/4}$	20	deg

2.4.3 Powered Propeller

The powered single-rotating propeller scale model used during the wind tunnel tests was made by Fokker during the development of the conceptual Fokker F−29. The model has a diameter of 0.3043 m and is equipped with up to eight blades, which can be removed independently. In the current study the eight-bladed configuration was selected. The blade angle at 75% of the blade span can be adjusted as desired, and was set to 41 degrees. A four-component Rotating Shaft Balance (RSB) is integrated in the propeller model to measure the propeller forces and moments, as discussed in more detail in Subsection 2.6.3.

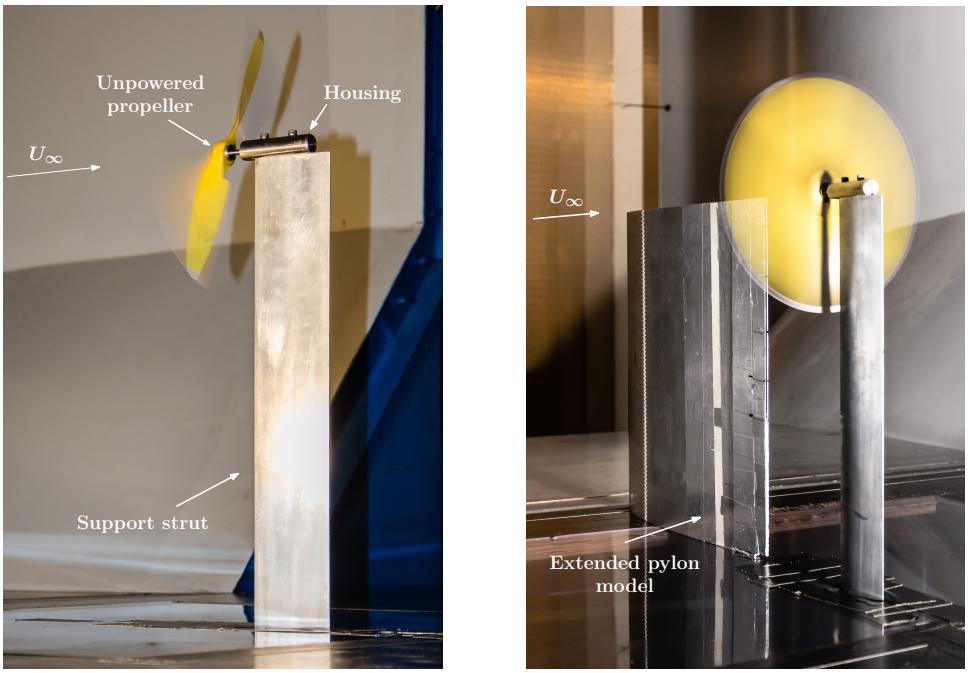

Figure 2.7: *Unpowered* propeller scale model in the isolated (left) and installed (right) configurations.

The powered propeller is driven by a Tech Development (TDI) 1999A pneumatic motor, with the air supply obtained from the central air supply system of Delft University of Technology's High Speed Wind Tunnel Laboratory. For a detailed description of the setup and operating procedures of the pneumatic motor the reader is referred to reference [31]. An overview of the most relevant characteristics of the powered propeller is given in Table 2.3. A technical drawing of the powered propeller test setup including the pneumatic motor and the integrated RSB as well as the support structure housing the air supply lines and RSB data transmission cables is presented in Figure 2.8.

Table 2.3: Characteristics of the *powered* propeller model.

Parameter	Symbol	Value	Unit
Number of blades	B	8	-
Diameter	D_{prop}	0.3043	m
Hub diameter	D_{hub}	0.084	m
Blade angle at $r/R = 0.75$	$\beta_{3/4}$	41	deg

The powered propeller model was positioned at 30% of the (default) pylon chord behind the pylon during the measurements performed in the installed and blown configurations. Note that this spacing is at the high end of the spectrum of pylon - propeller spacings considered during comparable pylon - propeller interaction studies available in the literature[1]. However, taking into account the geometry of the powered propeller model it was not possible to position the propeller any closer to the pylon. A technical drawing of the complete setup of the powered propeller in the installed configuration is presented in Figure 2.9. A photograph of the isolated powered propeller in its test setup in the OJF wind tunnel is depicted in Figure 2.10.

[1] See for example references [16, 17, 21, 23, 24, 27, 30].

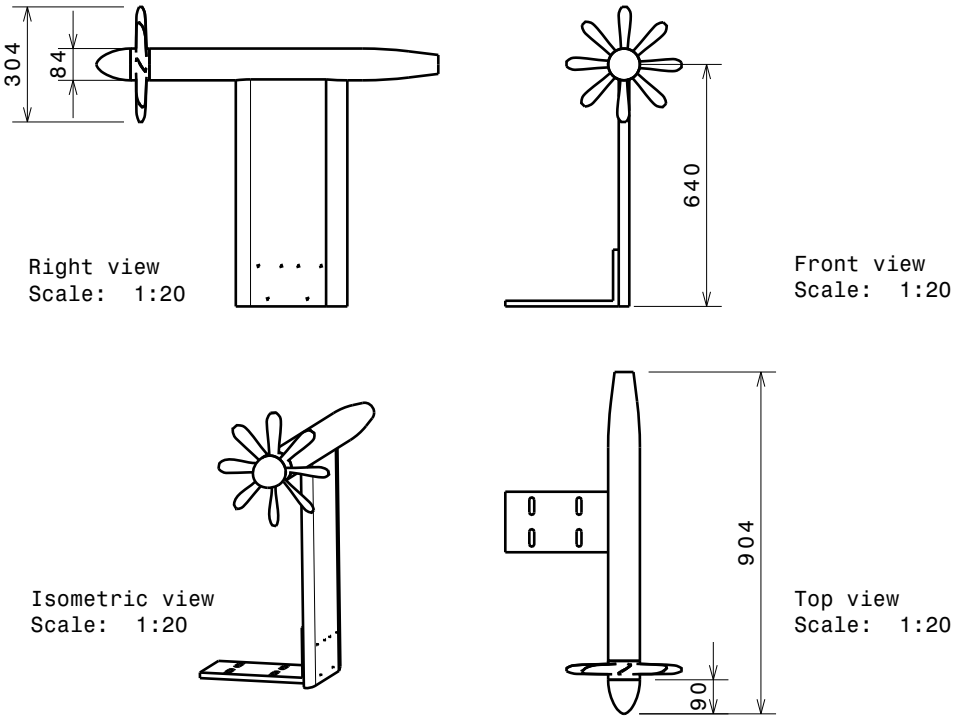

Figure 2.8: Technical drawing of the eight-bladed powered propeller scale model in isolated configuration; dimensions in millimeters. Based on [32].

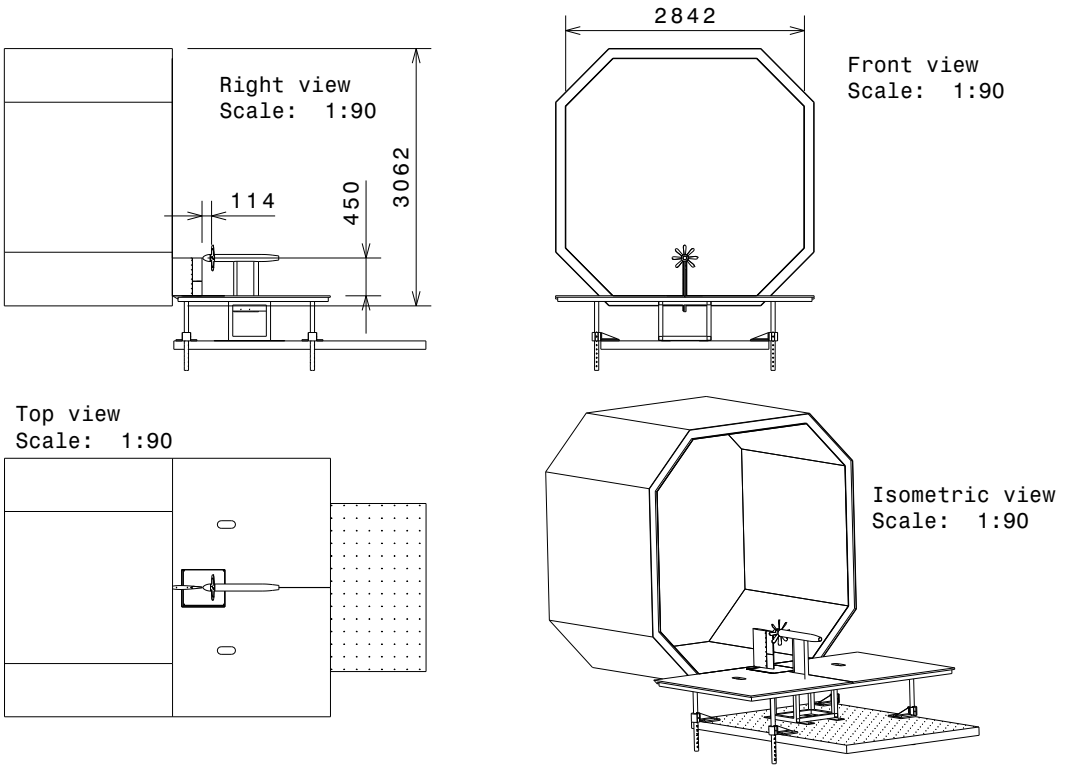

Figure 2.9: Technical drawing of the installed powered propeller setup; dimensions in millimeters. Based on [32].

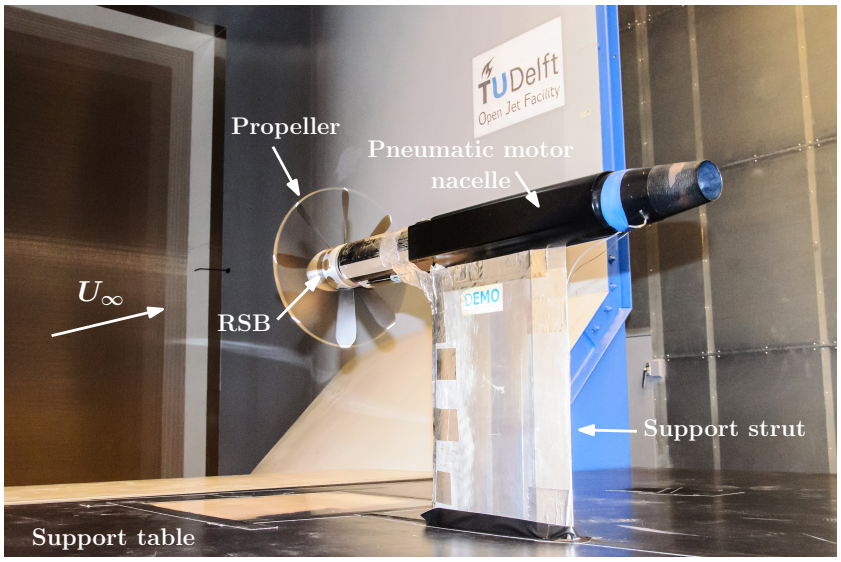

Figure 2.10: Photograph of the isolated powered propeller setup inside the OJF.

2.5 Pylon Blowing System

The goal of the pylon blowing system is to fill up the wake shed by the pylon, thereby reducing the adverse pylon - propeller interaction effects. To successfully fill up the pylon wake it is desirable to have a uniform outflow from the aft region of the pylon over the spanwise part of the pylon which is located in front of the propeller disk. For simplicity, it was decided to use a blowing system with its outlet integrated in the pylon's trailing edge. This reduced the blowing system design problem to three steps:

1. Defining the overall system dimensions and required flow rate (Subsection 2.5.1).
2. Determining the optimal cross-sectional geometry and spanwise distribution which meets all of these requirements and results in the most uniform outflow as possible (Subsection 2.5.2).
3. Designing an inlet which connects the blowing device to the air supply system (Subsection 2.5.3).

The air required to run the pylon blowing system was obtained from an external air supply connected to the blowing system's inlet via a combination of pipes and tubes (Subsection 2.5.4).

2.5.1 Blowing System Design Requirements

The blowing system design requirements followed directly from the goal of filling up the pylon wake to reduce the pylon - propeller interaction effects. Requirements were imposed based on both geometric and flow rate considerations.

2.5.1.1 Geometric Requirements

Geometric requirements were set on the blowing system's span, chordwise extent, and outlet thickness.

To make sure the blowing system covers the entire part of the propeller disk immersed in the pylon wake, the blowing system's outflow span b_{blow} should at least equal the propeller radius. However, to be on the safe side the blowing system was required to have an outflow span of 1.75 times the propeller radius, or 266 mm.

The upper limit on the chordwise extent of the blowing system c_{blow} was selected to equal 30% of the pylon chord, this to prevent potential interference problems with the rear spar of the pylon in a full-scale installation of the system. Note that this is an upper limit only; the actual chordwise extent could be selected to be smaller than this value.

The outlet thickness of the blowing system t_{out} is constrained by the trailing edge thickness of the pylon. As shown in Table 2.1, this thickness equals 8.0 mm. Assuming a minimum skin thickness of 1.0 mm on both sides of the blowing outlet, this results in an available outlet thickness of 6.0 mm.

An overview of the geometric requirements imposed on the blowing system design is given in Table 2.4.

Table 2.4: Geometric requirements imposed on the pylon blowing system.

Parameter	Symbol	Value	Unit
Chord	c_{blow}	$\leq 0.30 c_{\text{pylon}}$ ≤ 114	mm
Span	b_{blow}	$1.75 R_{\text{prop}}$ 266	mm
Outlet Thickness	t_{out}	6.0	mm

2.5.1.2 Flow Rate Requirements

The design mass flow of the blowing system was computed based on the velocity deficit expected in the pylon wake. This velocity deficit was predicted using the analytic Schlichting wake model, which expresses the velocity deficit Δu at any point $(X_{\text{w}}, Y_{\text{w}})$ in the pylon wake as a function of the pylon characteristics as follows: [33]

$$\frac{\Delta u}{U_\infty}(X_{\text{w}}, Y_{\text{w}}) = \frac{\sqrt{10}}{18\beta}\sqrt{\frac{c_d c}{X_{\text{w}}}}\left[1 - \left|\frac{Y_{\text{w}}}{b_{\text{w}}}\right|^{\frac{3}{2}}\right]^2 \tag{2.1}$$

with b_{w} the wake semi-width, c the pylon chord, c_d the pylon 2D drag coefficient, and β an empirical constant set to $\beta = 0.18$ based on experiments performed by Schlichting and Reichardt [33, 34]. The wake-based coordinate system $\mathbf{X}_{\text{w}}$ is defined as illustrated in Figure 2.2. The X_{w}-axis is fixed to the pylon chord line and points in the downstream direction, with the origin defined at the trailing edge of the pylon.

The wake semi-width b_{w} was computed using: [33]

$$b_{\text{w}}(X_{\text{w}}) = \beta\sqrt{10 c_d c X_{\text{w}}} \tag{2.2}$$

To compute the volumetric flow rate required to be blown into the pylon wake per unit span of the blowing device, the pylon wake velocity deficit defined by Equation (2.1) was integrated over the total pylon wake width:

$$\frac{Q_{\text{req}}}{b_{\text{blow}}} = \int_{-b_{\text{w}}}^{b_{\text{w}}} \Delta u \mathrm{d}Y_{\text{w}} = 2b_{\text{w}} \int_0^1 \Delta u \mathrm{d}\left(\frac{Y_{\text{w}}}{b_{\text{w}}}\right) = \frac{9}{10} U_\infty b_{\text{w}} \frac{\sqrt{10}}{18\beta}\sqrt{\frac{c_d c}{X_{\text{w}}}} = \frac{1}{2} U_\infty c_d c \tag{2.3}$$

where the expression for the wake semi-width b_w defined by Equation (2.2) has already been substituted. Note that the result obtained from Equation (2.3) is independent of the longitudinal position X_w, which is as expected since the Schlichting wake model satisfies conservation of momentum.

With the required volumetric flow rate known from Equation (2.3), the design mass flow was computed by:

$$\dot{m}_{des} = \rho_\infty Q_{req} = \frac{1}{2}\rho_\infty U_\infty b_{blow} c_d c \tag{2.4}$$

The (default) pylon section drag coefficient was computed using XFOIL at an angle of attack of $\alpha = 0°$ and a Reynolds number referenced to the pylon chord of $Re_c = 5.2 \cdot 10^5$. This corresponds to a freestream velocity of $U_\infty = 20\,\text{m/s}$, which is the approximate velocity at which the wind tunnel experiments were planned to be performed. The position of the transition point was fixed at the location of the zigzag tape on the pylon models. The resulting drag coefficient equaled 0.0120, which was substituted into Equation (2.4) together with the pylon chord given in Table 2.1, the span of the blowing device given in Table 2.4, a freestream velocity of $U_\infty = 20\,\text{m/s}$, and the density of air at standard atmospheric conditions at sea-level to obtain:

$$\dot{m}_{des} = 1.5 \cdot 10^{-2}\,\text{kg/s} \tag{2.5}$$

2.5.2 Blowing System Design: the Uniform Blowing Rod

The core of the pylon blowing system is formed by a Uniform Blowing Rod (UBR). Developed by FlowMotion[2], the UBR is designed to provide a uniform outflow from its outlet. The UBR basically consists of two components: an interior air channel with a variable cross-sectional shape along the span of the UBR, and an outlet channel with a constant cross-section and vanes placed at constant spacing to align the flow which exits the UBR. A sketch showing a side view of an example UBR design is presented in Figure 2.11.

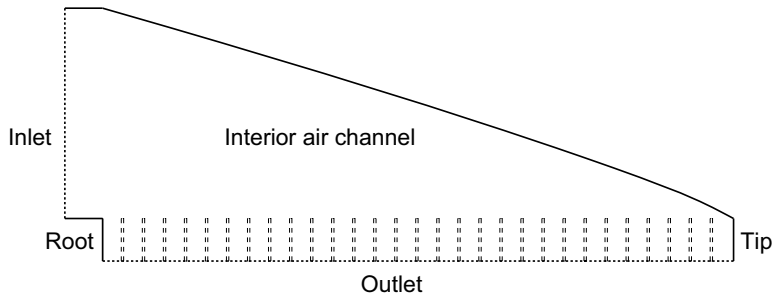

Figure 2.11: Schematic side view of an example Uniform Blowing Rod.

The UBR design is characterized by the geometry of the initial cross-section (at the inlet plane, i.e. the UBR's root), after which the shape of the cross-sections of the interior air channel in spanwise direction towards the UBR's tip are computed such that in theory a uniform outflow profile is obtained. This is done by taking into account the boundary layer development along the UBR's interior air channel in determining the optimal local cross-sections. Although the theory behind the UBR's design process is based on circular cross-sections, corrections are implemented such that the cross-section at the root of the UBR can have any desired shape. For the current application a simple rectangle was chosen. Vanes are placed in the outlet

[2]FlowMotion - Consultancy for Heat Transfer and Fluid Dynamics: www.flowmotion.nl.

segment to align the flow before it exits the UBR. Note that when straight vanes are used it is likely that the flow will separate from the vanes' leading edges. More involved vane shapes were used in the final UBR design presented in this report to prevent this undesired separation.

UBR Design

All design work related to the UBR was performed by FlowMotion. The final UBR design was the result of a manual optimization process, of which the main goal was to achieve a uniform outflow profile and to minimize flow separation at the outlet vanes.

During all iterations ANSYS Fluent was used to analyze the UBR's performance based on RANS simulations of the internal geometry of the UBR. For the analyses, a straight channel was modeled ahead of the inlet of the UBR, at the inlet of which a suitable boundary condition was specified. In the final steps of the optimization process the actual inlet geometry (discussed in Subsection 2.5.3) was included in the CFD analyses, thereby providing a more complete picture of the actual UBR performance which could be expected in its fully installed configuration. Note that for all analyses a design mass flow of $1.25 \cdot 10^{-2}$ kg/s was used (as opposed to the value of $1.5 \cdot 10^{-2}$ kg/s given by Equation (2.5)), since at the start of the design process the effects of forced transition were not taken into account in the computation of the pylon drag coefficient and a freestream velocity of 30 m/s was assumed.

Beginning with an initial design based on experience obtained with previously developed UBRs for different applications, a number of manual design iterations were performed. The main changes made between the different iterations were related to the vane shape and spacing, as well as the cross-sectional geometry at the root of the UBR. Starting with straight vanes with relatively large spacing, the quest for a minimization of flow separation from the vanes' leading edges gradually drove the design towards more involved, airfoil-like vane shapes with a much smaller spacing. Also, the consideration of the inlet shape resulted in a decrease in chord of the cross-section at the root.

In the final design iteration convergence issues prevented a completely successful numerical analysis of the UBR. Therefore, it was decided to manufacture a first test specimen (both UBR and corresponding inlet) using SLS. The performance of this test object was then evaluated outside of the wind tunnel to verify the uniformity of the outflow velocity profile. Although the outflow velocity profile of the test specimen showed a reduction in the velocity at the root and tip of the UBR, it was decided that the design was sufficiently successful to pursue.

The characteristic dimensions and specifications of the final UBR are given in Table 2.5, while a technical drawing of the design is presented in Figure 2.12.

Table 2.5: Uniform Blowing Rod design: characteristic dimensions and specifications.

Parameter	Symbol	Value	Unit
Outflow Span	b_{UBR}	266	mm
Outlet Thickness	t_{out}	6.0	mm
Design Mass Flow	$\dot{m}_{\mathrm{des}}$	$1.25 \cdot 10^{-2}$	kg/s
Number of Vanes	N_{v}	59	-
Vane Spacing	s_{v}	4.45	mm
Vane Thickness	t_{v}	1.0	mm

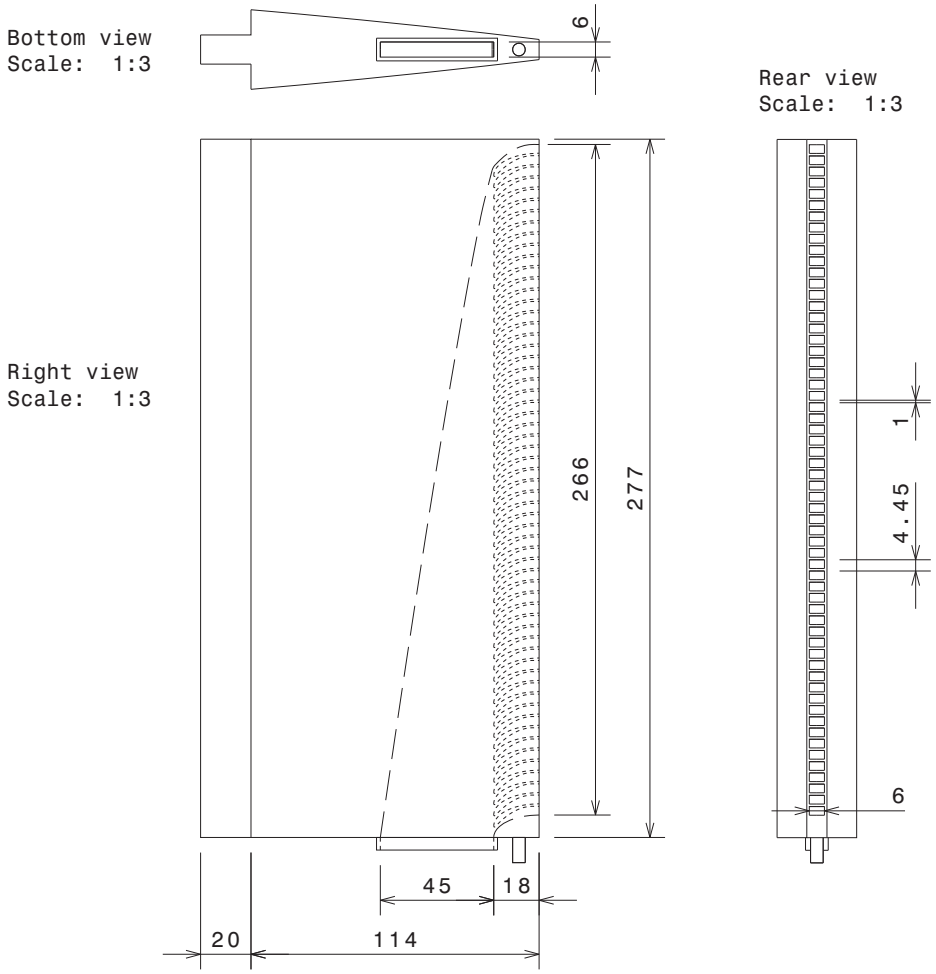

Figure 2.12: Technical drawing of the Uniform Blowing Rod design integrated in the aft part of the pylon; dimensions in millimeters.

2.5.3 Blowing System Inlet

To connect the UBR to its air supply system an inlet was required of which the shape changes from the UBR's root cross-section to the cross-section of the air supply's outlet. For the current blowing system, the inlet was designed for an (outside) air supply outlet diameter of $D = 19.05$ mm.

The available span for the UBR inlet was limited and set by the space remaining between the pylon root and the start of the UBR: $b_{\text{in}} = b - b_{\text{UBR}} - t_{\text{add}} = 0.450 - 0.266 - 0.011 = 0.173\,[\text{m}]$, with t_{add} the total additional material thickness at the tip and root of the UBR. However, when designing the inlet to fit this limited span, the required change in cross-sectional shape from circular at the bottom of the inlet (to which the air supply tube is attached) to rectangular at the UBR's root cross-section would result in a relatively large divergence angle. This would then lead to flow separation in the inlet channel and correspondingly a non-uniform velocity profile at the inlet of the UBR.

To solve this problem the inlet was partly positioned outside of the pylon. A rectangular channel with a cross-section equal to that of the UBR's root was designed inside the trailing edge geometry of the pylon. The span of this channel was set equal to the remaining span in

the pylon below the UBR: 173 mm. A separate circular-to-rectangular inlet channel of span 213 mm was then added below the straight channel to allow for the attachment of a circular air supply tube. A technical drawing of the UBR inlet assembly is shown in Figure 2.13.

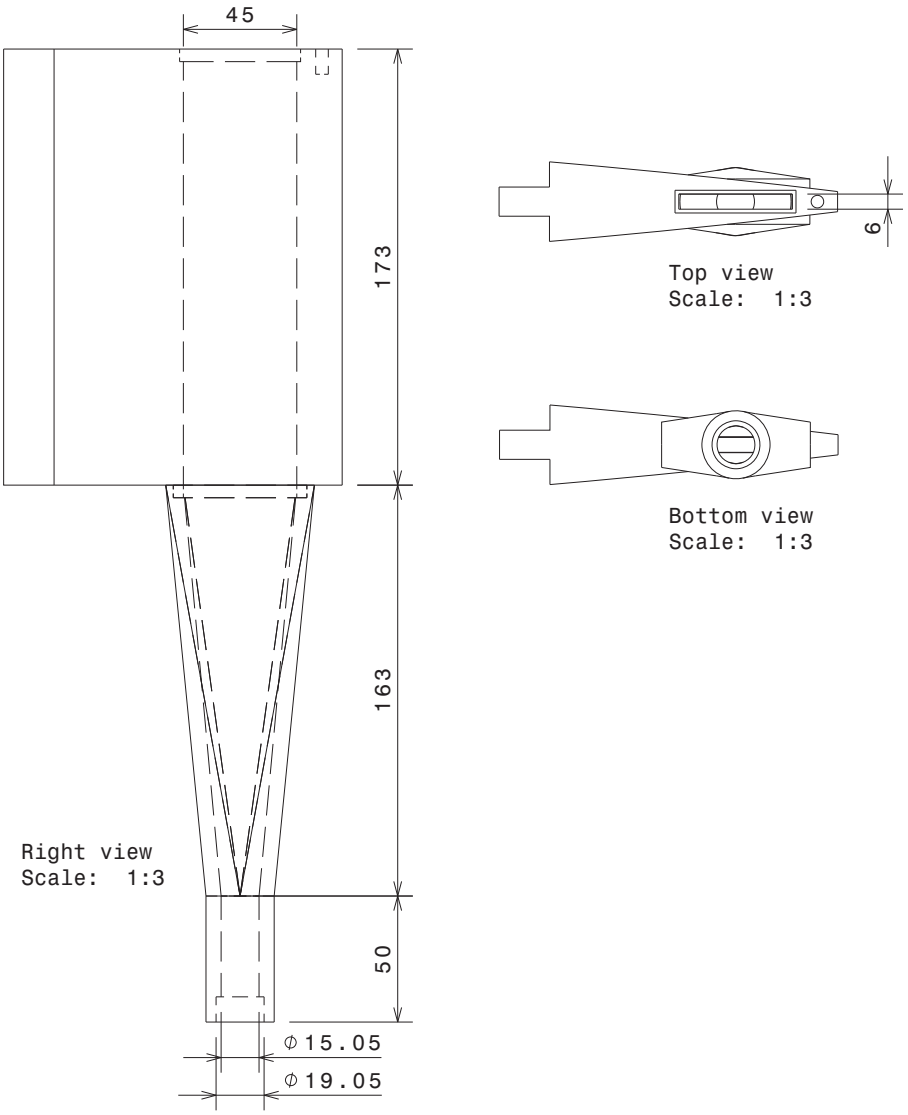

Figure 2.13: Technical drawing of the inlet assembly of the Uniform Blowing Rod (partially integrated in the aft part of the pylon); dimensions in millimeters.

2.5.4 Blowing System Air Supply System

The UBR was supplied with air obtained from the pressurized air supply system installed in the OJF wind tunnel. A combination of pipes and tubes was used to connect the UBR to the air supply system. To control the mass flow going through the UBR a pressure regulator was used. Subsequently, a straight pipe was installed to stabilize the flow before it entered the flow meter, which was used to read the current mass flow. The outlet of the flow meter was then connected to the inlet of the UBR by means of a tube.

2.6 Measurement Techniques

To obtain quantitative data from the wind tunnel experiments a number of different measurement techniques were employed. This section describes all techniques used; note that the post-processing techniques applied to the measurement data are discussed in Section 2.7.

During all blown measurements the amount of air supplied to the pylon blowing system was measured using a flow meter (Subsection 2.6.1). The wake profiles behind the pylon (unblown and blown) were derived from measurements performed using total and static pressure tubes (Subsection 2.6.2). The forces and moments produced by the powered propeller were measured using a Rotating Shaft Balance (Subsection 2.6.3). Finally, the propeller's noise emissions were measured using two out-of-flow microphones (Subsection 2.6.4).

2.6.1 Pylon Blowing System Air Supply Measurements

A VPinstruments VPF-R200-M100 flow meter was used to determine the mass flow provided to the pylon blowing system during the measurements with the blowing system enabled. The flow meter has a measurement range of $0.88 - 200$ m^3/h, at an accuracy of smaller than 0.5% of the full scale [35]. Considering the final design flow rate of $1.5 \cdot 10^{-2}$ kg/s $= 44$ m^3/hr, the flow meter's measurement range is more than sufficient for the projected test matrix. A photograph of the flow meter is depicted in Figure 2.14.

Figure 2.14: Photograph of the VPinstruments VPF-R200-M100 flow meter. Reproduced from [36].

2.6.2 Pylon Wake Profile Measurements

The wake profiles behind the unblown and blown pylons were measured by traversing a total and a static pressure tube over a range of lateral positions Y_w at an axial position X_w behind the pylon, with the centerline of the trailing edge of the pylon positioned at $Y_w = 0$ mm. During all measurements the pylon was set to zero degrees angle of attack.

The desired high spatial resolution in the pylon wake region imposed the requirement of pressure tubes with a small tube diameter. Since the available pitot-static tubes were considered too thick, separate total and static pressure tubes were used. As a result, the total pressure and static pressure measurements were performed separately, with the reference pressure input in both cases connected to a pressure tube positioned outside of the flow close to the pylon model. The tubes were installed on a traversing system which could translate in all three directions. The lateral and longitudinal directions were controlled automatically using a Galil DMC-2162 motion controller, while the vertical direction was set manually.

To minimize pressure disturbances an airfoil-shaped rod was used to provide a means of attachment for the static and total pressure tubes. To further minimize potential disturbances the pressure tubes were positioned such that the distance between the rod and the pressure holes was maximized. A photograph of the two pressure tubes installed on the airfoil-shaped rod is depicted in Figure 2.15.

To obtain the local pressures in the pylon wake region the pressure tubes were connected to a Mensor Digital Pressure Gauge 2101. The DPG 2101 features a suitable minimum gauge pressure range of $0 - 2,500$ Pa, at an accuracy of 0.010% full-scale. The raw pressure data was obtained during a measurement time of three seconds at a sampling frequency of 10 Hz, after which the average was taken for each measurement point. A photograph of the Mensor DPG 2101 is presented in Figure 2.16.

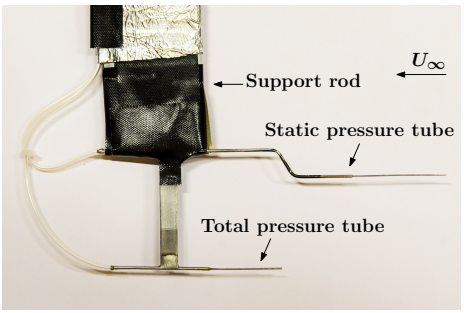

Figure 2.15: Photograph of the static and total pressure tubes attached to the airfoil-shaped rod which is installed on the traversing system.

Figure 2.16: Photograph of the Mensor DPG 2101 pressure transducer used to obtain the total and static pressures in the pylon wake region. Reproduced from [37].

2.6.3 Propeller Performance Measurements

A four-component Rotating Shaft Balance (RSB) was integrated in the propeller test setup and was used to measure the propeller forces and moments. Developed and provided by the National Aerospace Laboratory of the Netherlands (NLR), the RSB features a 'spokewheel'-type design with two pairs of three spokes connecting an inner and outer ring. The inner ring is directly installed on the drive shaft of the pneumatic motor, while the outer ring serves as mount for the propeller hub. A photograph of the RSB used in the wind tunnel experiments is depicted in Figure 2.17.

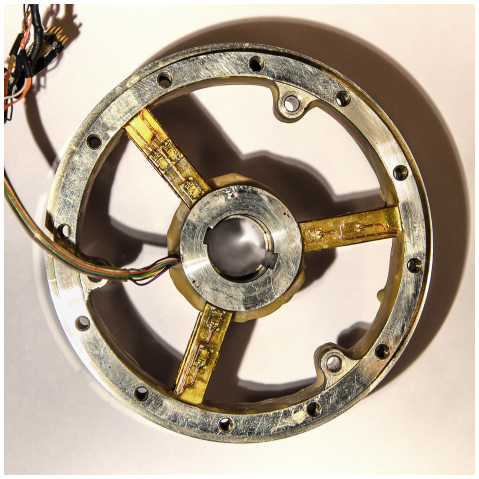

Figure 2.17: Photograph of the Rotating Shaft Balance.

The RSB determines the propeller forces and moments by measuring strains in the spokes between the inner and outer rings. Four separate strain gauge bridges are installed on the spokes, with each bridge sensing one of the four force/moment components (two on-axis, two off-axis). Furthermore, a trigger pulse is generated at every rotation of the RSB, thereby indicating the angular position of the RSB at each sampling point. All RSB measurements were performed at a sampling frequency of 50 kHz and a measurement time of five seconds.

Using the known angular position of the RSB the two off-axis components can be decomposed into four components, hence effectively making the RSB a full six-component balance. The three spoke design results in a large sensitivity to axial loading (thrust and torque) combined with the desired stiffness in the plane of the balance (which needs to be sufficiently high since the propeller hub is attached to the RSB). This in-plane stiffness however limits the sensitivity to the off-axis force and moment components. The target accuracies of the RSB used in the wind tunnel experiments equal $\pm 0.5\%$ of the measurement range for the on-axis components and $\pm 2.5\%$ of the measurement range for the off-axis components [38]. The measurement range for the on-axis force (thrust) equals $0 - 400\,\mathrm{N}$, while for the off-axis force it is $0 - 250\,\mathrm{N}$. For the on- and off-axis moments the measurement range equals $0 - 40\,\mathrm{Nm}$ and $0 - 30\,\mathrm{Nm}$, respectively. Validation studies performed by NLR using an RSB with slightly different dimensions than those of the RSB used in the current research project, but designed following the same principles, showed accuracies of 0.2% on torque and 0.3% on thrust (with respect to the full measurement range). The off-axis components were found accurate up to 1.8% and 1.5 % of the full measurement range for the off-axis force and moment, respectively. [38]

2.6.4 Propeller Noise Measurements

Two LinearX M51 high performance low voltage electret condenser microphones (see Figure 2.18) were used to measure the acoustic pressures induced during the experiments. Both microphones were positioned outside the open-jet stream, at a lateral distance of 2.25 m from the centerline of the propeller. By changing the position of the microphones along the sideline measurements could be performed at a range of axial directivity angles.

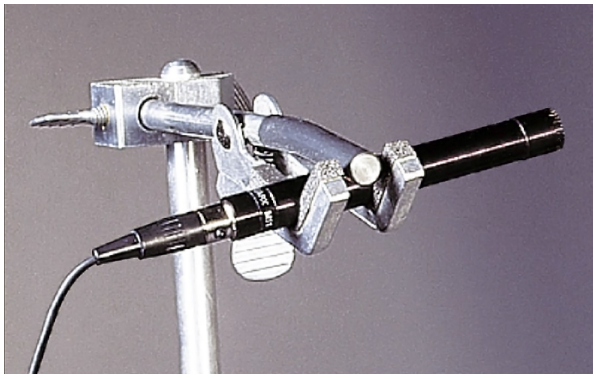

Figure 2.18: Photograph of a LinearX M51 microphone. Reproduced from [39].

The microphones are characterized by a maximum sound pressure level of 150 dB and operate in the frequency range of 10 Hz up to 40 kHz. The directivity pattern is fully omni-directional (directivity $D = 0$ dB) for frequencies up to 5 kHz, while the directivity increases from $D = 1.2$ dB at 10 kHz to $D = 4.0$ dB at 20 kHz. The frequency response of the microphones is practically flat in the 50-2,000 Hz range; for the response at lower and higher

frequencies calibrated correction factors provided by LinearX were used to correct the microphone response. [39] The microphone measurements were performed at the same sampling frequency as used for the RSB measurements: 50 kHz. To convert the raw microphone signals into sound pressure levels, the microphones were calibrated every measurement day using a G.R.A.S. Pistonphone 42AA.

Comparison of the frequency range of the microphones with the main frequencies of interest expected in the wind tunnel measurements showed that the microphones' frequency range is adequate. The main frequencies of interest were expected to be centered around integer multiples of the propeller's BPF. For the current propeller model (in eight-bladed configuration) these multiples are given by:

$$n \cdot BPF = \frac{nB\Omega}{2\pi} = n\frac{B}{D}\frac{U_\infty}{J} = n \cdot 26.2\frac{U_\infty}{J} \tag{2.6}$$

with J the propeller advance ratio and U_∞ the freestream velocity. For a freestream velocity of $U_\infty = 20\,\mathrm{m/s}$ and an advance ratio range of $0.5 \leq J \leq 1.8$, Equation (2.6) evaluates to:

$$n \cdot 292\,[\mathrm{Hz}] \leq n \cdot BPF \leq n \cdot 1050\,[\mathrm{Hz}] \tag{2.7}$$

with the upper limit corresponding to $J = 0.5$ (high rotational velocity) and the lower limit to $J = 1.8$ (low rotational velocity). From Equation (2.7) it is clear that a sufficient number of propeller tones can be measured using the selected microphones.

2.7 Measurement Data Post-Processing Techniques

The data obtained during the experimental test campaign was post-processed to obtain the final experimental results. This section briefly introduces the post-processing techniques used, for a detailed discussion of the procedures the reader is referred to Appendix A.

The pressure measurements in the pylon wake region were converted into velocities following Bernoulli's principle. The freestream air density was obtained from the wind tunnel's diagnostics data acquisition system every time a pressure measurement was performed. Since the static and total pressure measurements were not performed at the exact same time, small differences in air density occurred between the total and static pressure measurements corresponding to the same position in the pylon wake. This was accounted for by averaging the two available values of the air densities at each measurement position in the wake domain.

The RSB returns analog output voltages from the four channels corresponding to the four force/moment components. To convert the measured voltages into actual forces and moments, a number of calibration steps were performed. Following the determination of the zero loading offset of the RSB, predefined calibration matrices (see Appendix B) were applied to convert the measurement data to forces and moments. In this process the data was directly corrected for RPM effects. Finally, the effects of the propeller hub back pressure were corrected for by subtracting the effective drag term resulting from the pressure acting on the hub.

The microphone data was calibrated using calibration factors determined using a pistonphone. Subsequently, Welch's method (see reference [40]) was used to convert the data to the frequency domain and to obtain the sound pressure levels as a function of the frequency. Zero overlap was used together with a rectangular window of which the length was selected such that a frequency resolution Δf of about 1 to 2 Hz was obtained. The final step in the post-processing of the microphone data was to correct the sound pressure levels for the microphones' uneven frequency response and wind tunnel shear layer refraction effects.

Chapter 3

Experimental Results: Pylon Wake Profiles

The pylon wake profile measurements were performed to obtain insight in the wake profiles behind the pylon which would govern the inflow velocity profiles at the propeller disk during the measurements of the propeller performance and noise emissions. Also, the effectiveness of the blowing system in filling up the pylon wake was assessed. In this chapter first an overview of the wake measurements is presented in Section 3.1. Subsequently, Section 3.2 discusses the wake profiles of the pylon model in unblown conditions. Then, the outflow profiles of the UBR for zero wind tunnel velocity are shown in Section 3.3. Finally, the wake measurements behind the blown pylon model are treated in Section 3.4.

3.1 Measurement Overview

An overview of the characteristics of the pylon wake profile measurements is presented in Table 3.1. For a detailed description of the setup of the pressure measurements and the post-processing of the resulting data the reader is referred to Chapter 2.

Table 3.1: Overview of the characteristics of the pylon wake profile measurements.

Parameter	**Symbol**	**Value**	**Unit**
Freestream velocity	U_∞	[10,19,26][1]	m/s
Blowing rate	Q	[0,400,500,600,680]	L/min
Axial position	X_w	[50,114]	mm
Lateral position	Y_w	$-35 < Y_\mathrm{w} < 50$	mm
Vertical position	Z_w	320	mm
Pylon angle of attack	α	0	deg
Sampling frequency	f_s	10	Hz
Measurement time	t_m	3.0	s

All pylon wake measurements were performed for the isolated pylon model, i.e. no measurements were performed with the rotating propeller model present behind the pylon. This is expected not to have a significant effect on the (non-dimensional) results since experimental studies using comparable configurations have shown that the effect of the presence of the propeller on the pylon wake profile is small [41, 42]. For the results obtained in the blown

[1]The freestream velocity of 10 m/s was only used for measurements with the default pylon model.

configuration it should however be noted that the rotating propeller does result in a local increase in the flow velocity, thereby changing the interactions between the external flow and the flow blown into the pylon wake by the blowing system. Additional measurements using for example PIV would be required to obtain insight in the actual flow patterns in these cases.

Throughout this chapter static and total pressure coefficients are used, which are defined as follows:

$$C_{p_s} = \frac{p_s - p_{ref}}{q_\infty} \tag{3.1}$$

$$C_{p_t} = \frac{p_t - p_{ref}}{q_\infty} \tag{3.2}$$

with p_s and p_t the measured static and total pressures, p_{ref} the reference pressure used during the pressure measurements, and q_∞ the undisturbed dynamic pressure obtained from the wind tunnel diagnostics data.

3.2 Unblown Pylon Wake Profile Measurements

The unblown pylon wake measurements were performed for the default, extended, and sharp pylon models. A comparison of the non-dimensional velocity profiles measured in the wakes of the three pylons at a freestream velocity of 26 m/s is shown in Figure 3.1. Additional velocity and pressure profiles measured at different freestream velocities are presented and discussed in Appendix C.1 for the three pylon models separately.

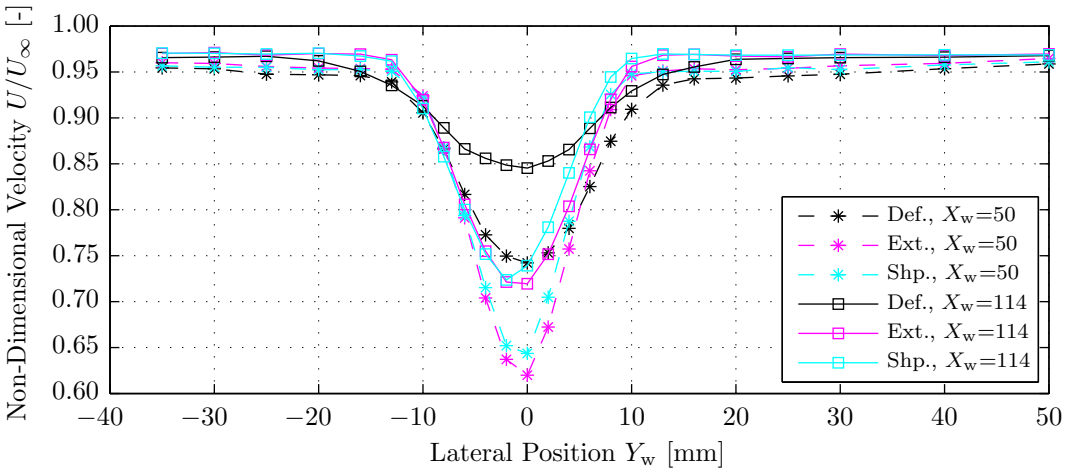

Figure 3.1: Non-dimensional velocity profiles in the wakes of the default (Def.), extended (Ext.), and sharp (Shp.) pylon models. $U_\infty = 26$ m/s, $X_w = [50, 114]$ mm.

From Figure 3.1 it is observed that for all pylon models the wake depth decreases and the wake width increases with increasing axial distance from the pylon trailing edge (X_w). Furthermore, it is noticed that the wake profiles are not exactly symmetrical, which is attributed to a small misalignment of the pylon and/or the traversing system. Also, the non-dimensional velocity ratio is not equal to unity outside the wake region. This is explained by the fact that the measurements are performed relatively close to the pylon and hence are influenced by the presence of the pylon. Computations performed using XFOIL confirmed that at the axial positions considered the local velocities outside of the wake region were unequal to that of the freestream.

A comparison of the wake profiles behind the three pylon models shows that the default pylon's wake profile is wider and less deep than those of the extended and sharp pylons. The depth and width of the wake profile at 50 mm behind the default pylon are of the same order as those measured at 114 mm behind the extended and sharp pylon models. Furthermore, it is also seen that the wake profile behind the extended pylon is wider than that of the sharp pylon, at approximately equal wake depth. This observation is as expected considering the thicker trailing edge of the extended pylon model.

To obtain additional insight in the reasons for the differences between the velocity distributions measured behind the three pylon models the profiles of the total and static pressure coefficients (defined according to Equations (3.1) and (3.2)) are presented in Figure 3.2. For overview reasons only the results measured at $X_w = 114$ mm are shown.

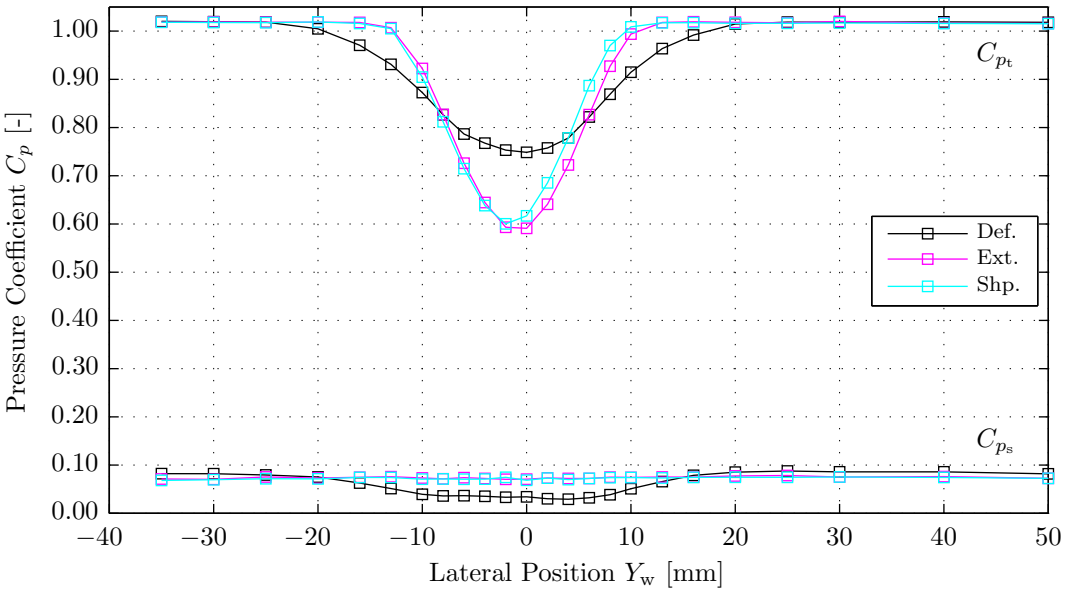

Figure 3.2: Total and static pressure coefficient profiles in the wakes of the default (Def.), extended (Ext.), and sharp (Shp.) pylon models. $U_\infty = 26$ m/s, $X_w = 114$ mm.

The total pressure profiles shown in Figure 3.2 follow the velocity profiles displayed in Figure 3.1. The static pressure profiles on the other hand show a large drop in the static pressure in the wake region for the default pylon model which does not occur for the extended and sharp pylons. This is explained by considering the thick trailing edge of the default pylon model, which leads to flow separation from the model's trailing edge. This results in a complex vortex pattern in the wake region and a relatively low pressure in the near wake [43–46]. The presence of the vortices promotes mixing between the flow inside and outside of the wake, thereby increasing the wake decay rate compared to the situation in which the flow remains attached as for the extended and sharp pylon models. To test this hypothesis better insight in the flow structure behind the pylon models is required, which could for example be obtained by time-accurate velocity measurements or flow visualization techniques.

Note that the value of the total pressure coefficient is larger than one outside of the wake region. This could be the result of a difference between the reference pressure used for the local measurements of the total pressure and the freestream value used by the wind tunnel diagnostics data. Furthermore, the value of the static pressure coefficient is not equal to zero outside of the wake region, which is the result of the presence of the pylon as discussed before.

3.3 Uniform Blowing Rod Outflow Profiles

To assess the uniformity of the outflow profile of the UBR, total pressure measurements were performed at axial positions of $X_w = 20$ mm and $X_w = 50$ mm centered behind the pylon's trailing edge ($Y_w = 0$), at a freestream velocity equal to zero. Three different blowing rates were considered: $Q = 400$ L/min, $Q = 600$ L/min (corresponding to the UBR's design point), and $Q = 680$ L/min. Note that the latter value corresponds to the maximum blowing rate that could be obtained from the used air supply system.

The outflow velocities measured at 20 mm from the UBR's trailing edge are presented in Figure 3.3, followed by Figure 3.4 displaying the velocities measured at $X_w = 50$ mm. The measured total pressures were converted into velocities assuming standard atmospheric conditions at sea-level. In both figures the solid black lines indicate central moving averages with a span of nine, while the dashed vertical lines indicate the position of the propeller blade behind the UBR in the installed and blown propeller measurements.

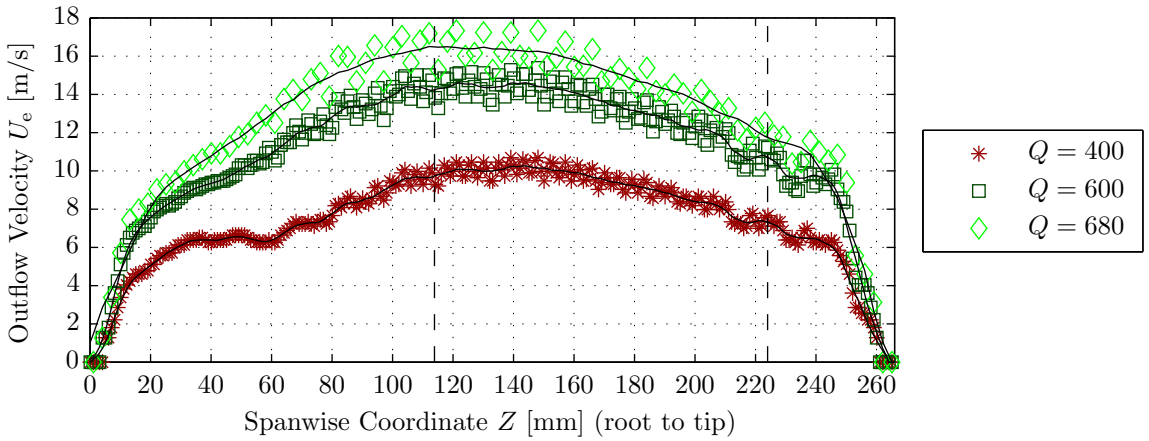

Figure 3.3: Outflow velocity profiles at $X_w = 20$ mm behind the Uniform Blowing Rod.

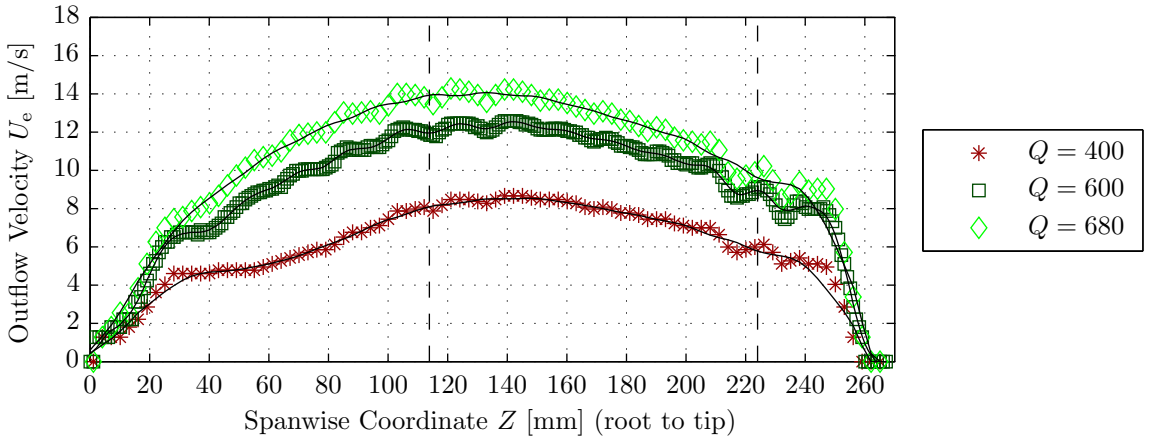

Figure 3.4: Outflow velocity profiles at $X_w = 50$ mm behind the Uniform Blowing Rod.

Figures 3.3 and 3.4 show that the UBR's outflow profile is not uniform over the entire span: at the tip and root the outflow velocity is clearly lower than in the middle. The differences in uniformity of the velocity profiles at the three different blowing rates are small. Based on measurements of the inflow profile at the UBR's inlet it is concluded that the non-uniform spanwise outflow profile is likely the result of non-uniform inflow. The inflow velocity profile

showed a clear increase in velocity towards the center of the inlet. Since the UBR's outflow velocity profile can be predicted by mapping the inlet velocity profile on the UBR's outlet geometry, the outflow velocity in the middle part of the UBR is expected to be higher than at the root and tip. This corresponds to the results shown in Figures 3.3 and 3.4. The non-uniform velocity profile at the UBR's inlet is likely the result of the large divergence angle in the inlet geometry (discussed in Subsection 2.5.3). The resulting separation at the start of the diverging channel results in a jet-like flow in the first part of the inlet. The straight part of the inlet channel then does not provide sufficient length for the jet to spread over the entire channel's width, hence resulting in a non-uniform velocity profile at the inlet of the UBR.

Furthermore, it is observed that at $X_w = 20$ mm the wakes shed from the vanes are clearly visible in the velocity profile behind the UBR, while at $X_w = 50$ mm the wakes have largely disappeared. Therefore, it is expected that at the propeller position in the tests performed in the installed configuration ($X_w = 114$ mm) the effect of the vane wakes is negligible.

3.4 Blown Pylon Wake Profile Measurements

The pylon models in the default and extended configurations were used to perform blown wake profile measurements at a range of different blowing rates. First, the results obtained for the two pylon models are discussed separately (Subsections 3.4.1 and 3.4.2), followed by a comparison (Subsection 3.4.3).

3.4.1 Default Pylon Model

The non-dimensional velocity profiles in the default pylon's wake are presented in Figure 3.5 for a freestream velocity of 26 m/s and blowing rates of 0, 600, and 680 L/min. The corresponding total and static pressure profiles are depicted in Figure 3.6. The blowing rate of 680 L/min was considered for measurements at both axial positions (50 mm and 114 mm), while the blowing rate of 600 L/min was only used for the measurements at $X_w = 50$ mm.

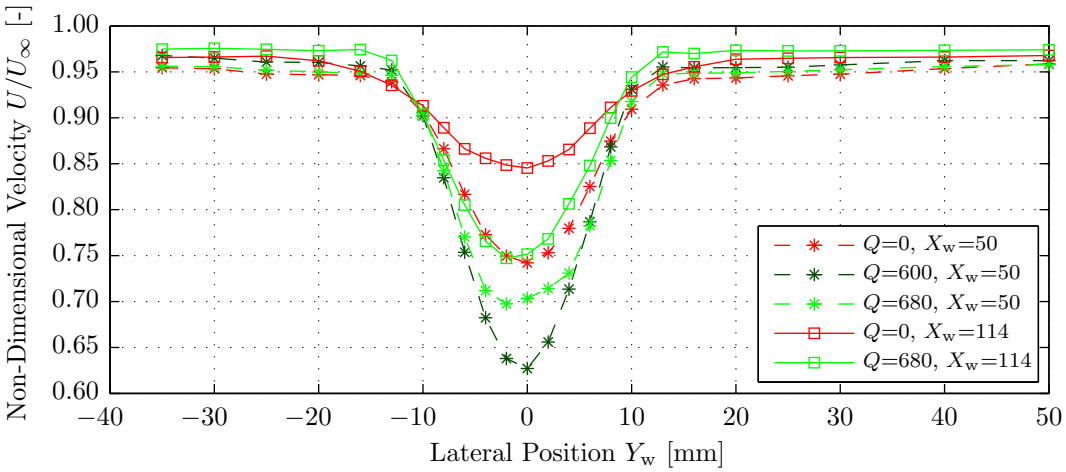

Figure 3.5: Non-dimensional velocity profiles in the wake of the default pylon model. $U_\infty = 26$ m/s, $X_w = [50, 114]$ mm, $Q = [0, 600, 680]$ L/min.

Figure 3.5 shows that for a freestream velocity of 26 m/s the application of blowing with blowing rates of 600 L/min and 680 L/min increases the default's pylon wake depth at both axial distances considered. At an axial distance of 50 mm from the pylon's trailing edge the wake width remains unchanged by the application of blowing, while at the larger distance of 114 mm the blowing reduces the wake width by approximately 25%.

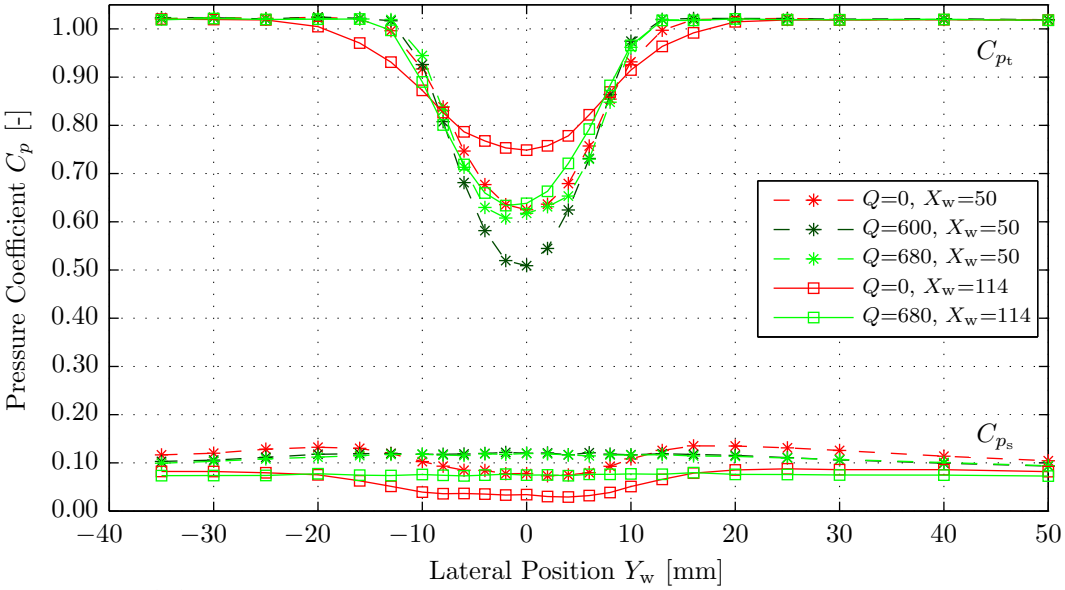

Figure 3.6: Total and static pressure profiles in the wake of the default pylon model. $U_\infty = 26$ m/s, $X_w = [50, 114]$ mm, $Q = [0, 600, 680]$ L/min.

The total pressure coefficient data displayed in Figure 3.6 follows the trends observed in the velocity data. For the static pressure coefficient it is observed that the application of blowing eliminates the pressure drop in the wake region observed in the unblown results. Note also that the static pressure coefficients outside of the wake region are not the same for the blown and unblown cases. Therefore, it is concluded that the application of blowing from the default pylon's trailing edge affects the entire flow field around the pylon, and not only that in the wake region.

From Figure 3.5 it was concluded that at a freestream velocity of 26 m/s the application of blowing increased the velocity deficit in the pylon wake compared to the unblown case. Additional measurements were performed at 10 m/s and 19 m/s to assess the effects of the freestream velocity on the effectiveness of the blowing system in the default configuration. The corresponding velocity and pressure profiles are presented and discussed in Appendix C.1.4. The results showed that at a wind tunnel velocity of 10 m/s the blowing system easily manages to fill up the wake, while at a freestream velocity of 19 m/s the application of blowing actually increased the wake depth while reducing the wake width. Since the outflow velocity from the UBR equals around 18 m/s for a blowing rate of 600 L/min and 21 m/s at 680 L/min, it is concluded that the blowing system outflow velocity needs to be sufficiently high compared to the freestream velocity for the blowing system to be effective.

If the outflow velocity is relatively low compared to the freestream velocity, the flow pattern behind the default pylon corresponds to that of a blunt airfoil with base bleed air injection. Experimental studies performed by Wood and Bearman showed that such base flows with bleed air feature an increase in base pressure, a downstream displacement of the formation region of the vortices, and lower vortex strength when compared to the same base flow without bleed [47, 48]. As a result the mixing of the flow inside and outside of the wake is reduced, which is indeed recognized in the results obtained for UBR outflow velocities lower than the freestream value. Flow visualization of the wake behind the default pylon with and without blowing is required to further confirm this hypothesis.

3.4.2 Extended Pylon Model

The non-dimensional velocity profiles in the extended pylon wake are presented in Figure 3.7 for a freestream velocity of 19 m/s and blowing rates of 0, 400, 500, 600, and 680 L/min. Since the total and static pressure profiles did not return any unexpected results these are not further discussed here; for reference they are presented in Appendix C.1.5.

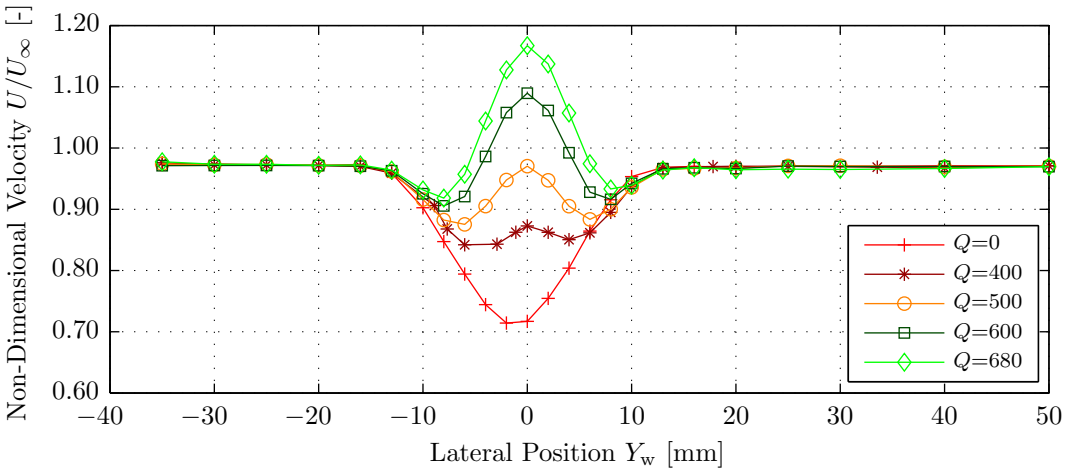

Figure 3.7: Non-dimensional velocity profiles in the wake of the extended pylon model. $U_\infty = 19$ m/s, $X_w = 114$ mm, $Q = [0, 400, 500, 600, 680]$ L/min.

The non-dimensional wake velocity profiles displayed in Figure 3.7 show a continuously increasing reduction in wake depth with increasing blowing rate. At a blowing rate of 500 L/min the velocity on the centerline of the wake reaches the freestream value, while it increases to values beyond the freestream velocity for even higher blowing rates. The application of blowing from the extended pylon's trailing edge does not have an appreciable effect on the total wake width. Furthermore, it is observed that the influence of blowing is confined to lateral positions between $Y_w = -12$ mm and $Y_w = 12$ mm. This indicates that the the jet blown into the flow from the UBR's outlet does not fully mix with the external flow before reaching the axial position of $X_w = 114$ mm. As a result, the velocity profiles measured at this position are not uniform but instead display a profile with one local maximum on the wake's centerline and two local minima left and right of the centerline.

The influence of the freestream velocity on the effectiveness of the extended pylon's blowing system was assessed by performing additional wake measurements at a freestream velocity of 26 m/s. The corresponding non-dimensional velocity profiles for blowing rates of 0, 400, 500, 600, and 680 L/min are presented in Figure 3.8. Again the corresponding pressure profiles are presented in Appendix C.1.5 and not further discussed here.

Figure 3.8 shows that at a freestream velocity of 26 m/s the application of blowing from the extended pylon model's trailing edge again successfully reduces the wake depth. However, at a given blowing rate the increase in the non-dimensional velocity on the wake centerline is smaller compared to the measurements performed at a freestream velocity of 19 m/s. At the highest considered blowing rate of 680 L/min the velocity on the wake centerline becomes approximately equal to that of the freestream. This once more indicates the importance of the ratio between the UBR outflow velocity and the freestream velocity.

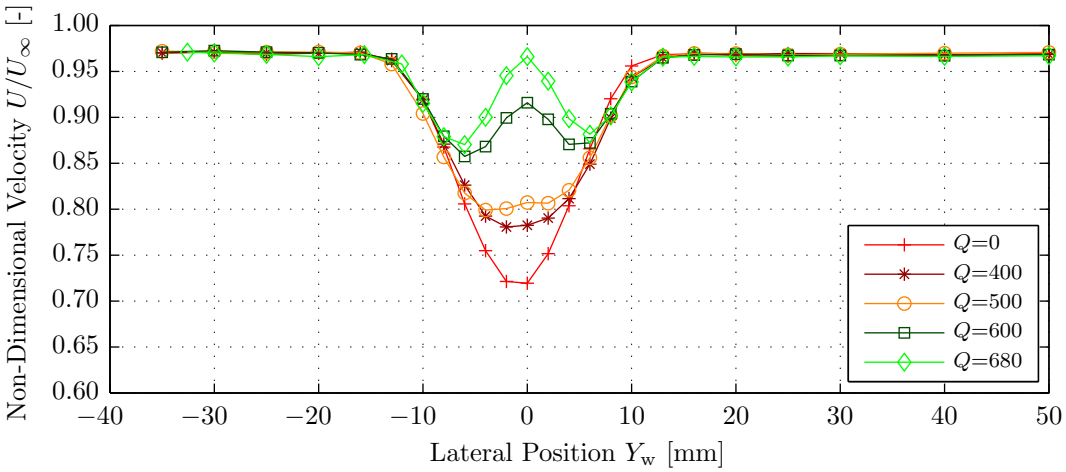

Figure 3.8: Non-dimensional velocity profiles in the wake of the extended pylon model. $U_\infty = 26$ m/s, $X_w = 114$ mm, $Q = [0, 400, 500, 600, 680]$ L/min.

3.4.3 Comparison of the Default and Extended Pylon Wakes

The blown wake profile results for the default and extended pylon models presented in Subsections 3.4.1 and 3.4.2 show significant differences. For comparison reasons, the blown non-dimensional wake velocity profiles discussed previously were used to compute integral values of the non-dimensional wake velocity deficit, denoted ξ:

$$\xi = \frac{1}{Y_{max} - Y_{min}} \int_{-b_w}^{b_w} \left| \frac{U(Y_w)}{U_\infty} - 1 \right| dY_w \tag{3.3}$$

with Y_{min} and Y_{max} the lateral limits of the measurement domain and the velocity profiles scaled such that outside of the wake the non-dimensional velocity ratio became equal to one.

The values of the non-dimensional integral wake velocity deficit parameter ξ are plotted versus the blowing rate in Figure 3.9. The results are presented for both the default and extended pylon models, for all considered freestream velocities and an axial position of $X_w = 114$ mm.

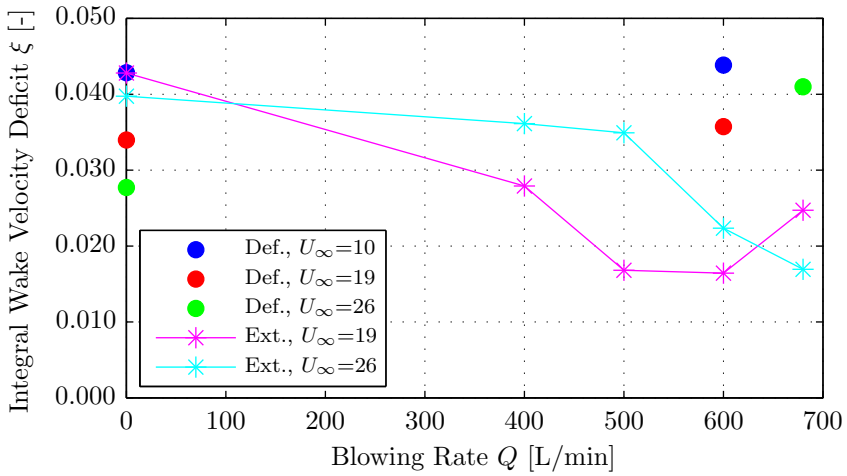

Figure 3.9: Non-dimensional integral wake velocity deficit parameter ξ versus the blowing rate for the default (Def.) and the extended (Ext.) pylon models. $U_\infty = [10, 19, 26]$ m/s, $X_w = 114$ mm, $Q = [0, 400, 500, 600, 680]$ L/min.

Figure 3.9 shows that for the default pylon the value of the integral wake velocity deficit parameter increases with increasing blowing rate. At a freestream velocity of 10 m/s this is the case because the blowing rate of 600 L/min results in an overshoot in the wake profile. At the velocities of 19 and 26 m/s the velocity deficit parameter increases because the application of blowing increases the wake depth. This is a result of the fact that for these freestream velocities the outflow velocities blown into the pylon wake were smaller than the freestream velocity, as discussed in Subsection 3.4.1.

The extended pylon with its thinner trailing edge, hence higher outflow velocity, on the other hand shows much more favorable blown results. Although the jet injected by the UBR does not fully mix with the external flow, hence not resulting in a uniform wake velocity profile, the wake depth can be reduced significantly by the application of blowing. Depending on the freestream velocity and selected blowing rate, blowing from the extended pylon's trailing edge results in a reduction of up to 60% in the integral wake velocity deficit parameter.

The blown pylon wake measurements showed that the default pylon model is not effective in reducing the wake velocity deficit behind the pylon. The extended pylon model on the other hand performed much better and displayed clear reductions in wake depth at the higher blowing rates. Therefore, it was decided to only use the extended pylon model for the propeller measurements in the installed and blown configurations discussed in the following chapters.

Chapter 4

Experimental Results: Unpowered Propeller Noise Emissions

The unpowered propeller noise measurements served as an initial test for the effectiveness of the blowing system in reducing the noise penalty due to the pylon installation effects. The measurements were mainly performed to become familiar with the microphone setup and acoustic testing of propellers. It should be noted that the propeller blade loads could not be measured and as such are unknown, thereby making it difficult to draw conclusions about the exact noise generating mechanisms occurring at the various measurement points. This chapter first gives an overview of the characteristics of the unpowered propeller noise measurements in Section 4.1. Then, the signal quality and reproducibility of the measurements is discussed in Section 4.2. Subsequently, the results obtained using the isolated unpowered propeller model are detailed in Section 4.3. Thereafter, Sections 4.4 and 4.5 elaborate on the measurements performed in the installed and blown configurations, respectively.

4.1 Measurement Overview

An overview of the characteristics of the unpowered propeller noise measurements is presented in Table 4.1. A detailed description of the setup of the noise measurements and the post-processing of the resulting data is presented in Chapter 2.

Table 4.1: Overview of the characteristics of the unpowered propeller noise measurements.

Parameter	**Symbol**	**Value**	**Unit**
Freestream velocity	U_∞	[15,19,24,30]	m/s
Propeller RPM[1]	RPM	[4200,5600,6900,8600]	-
Blowing rate	Q	[0,400,500,600,680]	L/min
Pylon-propeller spacing	ΔX	114	mm
Pylon angle of attack	α	0	deg
Microphone sideline distance	y	2.2	m
Microphone directivity angle	θ_{mic}	[90,110,130]	deg
Sampling frequency	f_{s}	50	kHz
Measurement time	t_{m}	30	s
Average factor Welch's method	K	90	-

[1]Corresponding to freestream velocities of 15, 19, 24, and 30 m/s, respectively.

Except for the sound spectra all data presented in this chapter is corrected for shear layer refraction effects using the method outlined in Appendix A.1.2.2, and scaled to a constant observer radius of 1.0 m. The RPM of the unpowered propeller could not be controlled, and hence followed directly from the selected freestream velocity.

4.2 Signal Quality and Reproducibility of the Results

The signal quality of the microphone data was evaluated by assessing the reproducibility of the noise measurements. For this purpose four measurements were performed directly after each other during a single run, where a run is defined as a sequence of measurements performed at constant wind tunnel settings and without interruptions in the operation of the propeller (i.e. the motor is not switched off during a run). The resulting sound pressure levels of the first six propeller tones (occurring at integer multiples of the BPF) as recorded during these four measurements are plotted in Figure 4.1. Subsequently, Figure 4.2 presents the differences between the individual results obtained from the four measurements and the corresponding mean value (averaged over the four measurements) for each propeller tone considered.

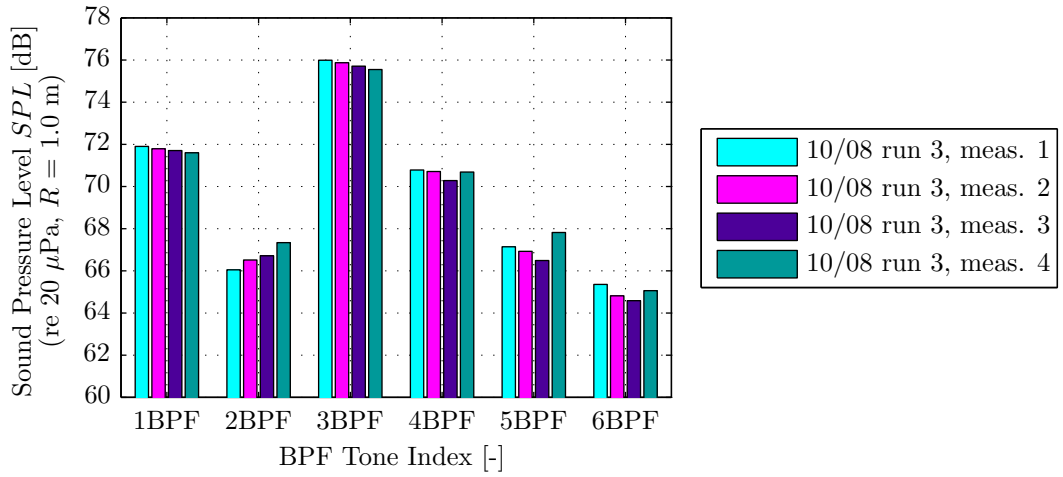

Figure 4.1: Reproducibility of consecutive unpowered propeller noise measurements. Installed configuration, $U_\infty = 24$ m/s, $\theta_{\text{mic}} = 110°$, $K = 90$.

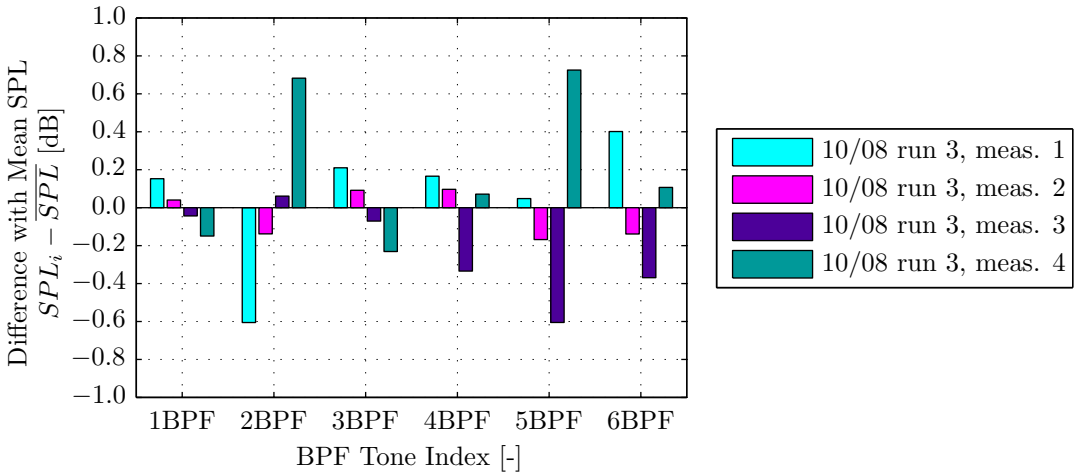

Figure 4.2: Variability of consecutive unpowered propeller noise measurements. Installed configuration, $U_\infty = 24$ m/s, $\theta_{\text{mic}} = 110°$, $K = 90$.

From Figures 4.1 and 4.2 it is concluded that the reproducibility of unpowered propeller noise measurements performed in direct succession at constant wind tunnel setting is good. For the first six fundamental propeller tones the maximum variability observed in the sound pressure levels is within -0.6 dB to $+0.7$ dB. Therefore, it is concluded that the variability of the SPL for consecutive measurements performed at constant wind tunnel setting is of the order of ± 1 dB. The largest differences are observed for the propeller tones with a relatively low intensity (in this case the 2BPF, 5BPF, and 6BPF tones). This is explained from the fact that a lower sound pressure level for a given tone corresponds to a lower signal-to-noise ratio of the microphone signal than for a tone with a high SPL. Hence, the reproducibility is best for tones with a relatively high sound pressure level.

To further assess the reproducibility of the unpowered propeller noise measurements, Figures 4.3 and 4.4 present the SPL of the first six propeller tones obtained during measurements *not* performed consecutively. All measurements were performed at the same freestream velocity of 24 m/s and a microphone angle of 110 degrees, but during four different runs divided over two days. Note that the y-axis of Figure 4.4 has a different scale than used in Figure 4.2.

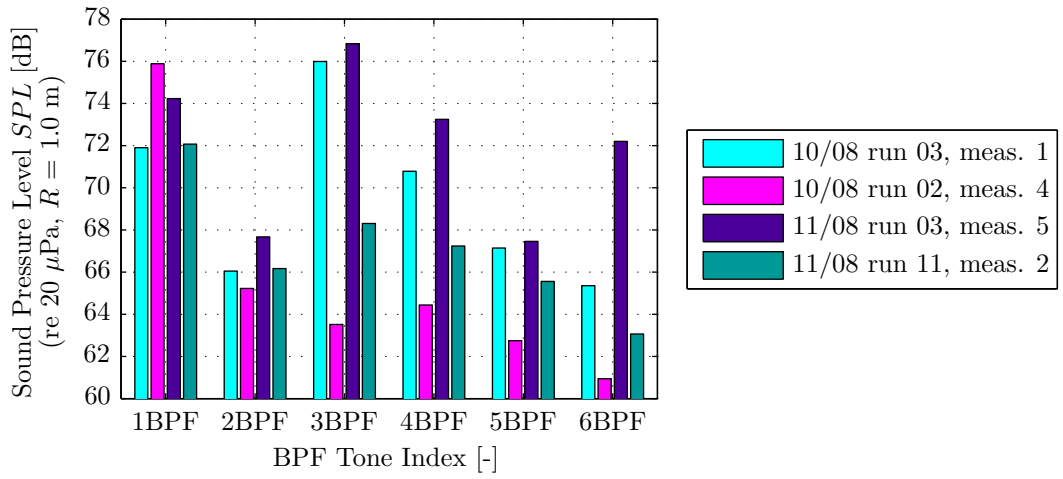

Figure 4.3: Reproducibility of nonconsecutive unpowered propeller noise measurements. Installed configuration, $U_\infty = 24$ m/s, $\theta_{\text{mic}} = 110°$, $K = 90$.

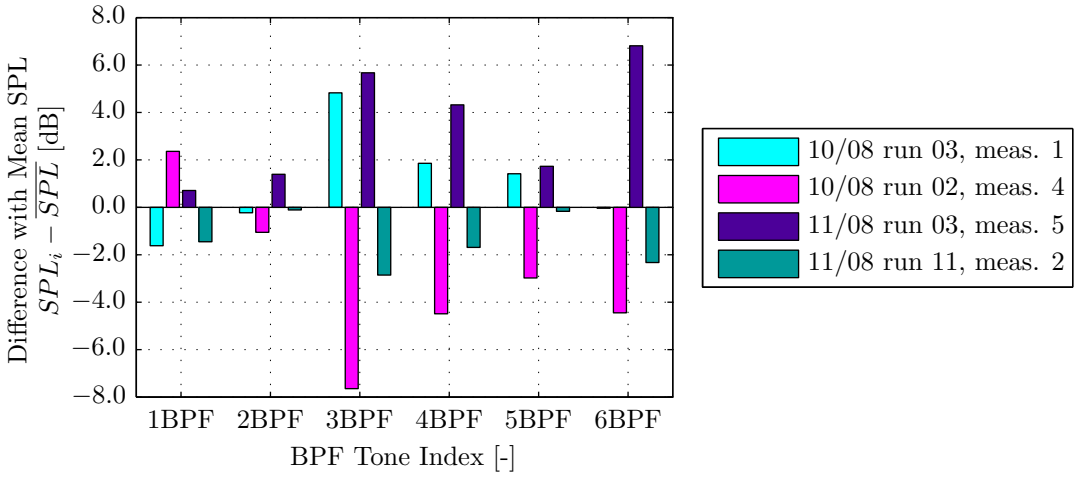

Figure 4.4: Variability of nonconsecutive unpowered propeller noise measurements. Installed configuration, $U_\infty = 24$ m/s, $\theta_{\text{mic}} = 110°$, $K = 90$.

Figures 4.3 and 4.4 show that the reproducibility of nonconsecutive measurements is much worse than that observed for measurements performed consecutively during a single run. Whereas for the 1BPF tone the difference between the first and forth measurement points is almost zero, the other two runs returned sound pressure levels of about 2 dB and 4 dB higher. For the 3BPF tone and the higher BPF multiples the differences are even more pronounced, with variations between the four measurements of up to ±8 dB.

The results presented in Figures 4.1 through 4.4 show that unpowered propeller noise measurements performed in direct succession show a good reproducibility. Measurements performed nonconsecutively on the other hand show too large variations to provide data sufficiently accurate for comparisons. Possible explanations for the variations between the different measurements are interference effects with varying wind tunnel fan noise, non-constant propeller RPM, and variable (signal) noise in the raw microphone signals due to interference with the wind tunnel fan. The effect of reflections due to the reverberant test section seems to be small considering the good reproducibility of consecutive measurements.

Considering the bad reproducibility of nonconsecutive measurements it was decided to obtain the installed and blown noise emissions during single runs performed at constant tunnel velocity. Both the blowing rate and the microphone directivity angle were varied with running wind tunnel. The isolated measurements on the other hand had to be performed separately, thereby reducing the accuracy of comparisons between the isolated and installed noise levels.

4.3 Isolated Configuration

The isolated propeller produces noise due to the periodic pressure fluctuations resulting from the passing of the propeller blades. The noise emissions of the isolated propeller were used as baseline for comparison with the installed and blown noise levels discussed in the subsequent sections.

The isolated propeller noise measurements were performed at a constant microphone directivity angle of 110 degrees and freestream velocities of 15, 19, 24, and 30 m/s. Using the recorded data noise frequency spectra (Subsection 4.3.1) and tonal noise levels (Subsection 4.3.2) were computed as a function of the freestream velocity.

4.3.1 Propeller Noise Spectrum

An example noise spectrum corresponding to the unpowered propeller model in isolated conditions is depicted in Figure 4.5. The sound pressure level is indicated by the blue line, with the asterisks indicating the maximum tonal noise levels at integer multiples of the propeller's BPF. The frequencies corresponding to these BPF tones are indicated by the black dashed vertical lines, while the magenta dashed lines represent the first two BPF tones corresponding to the wind tunnel fan. The data depicted in Figure 4.5 was obtained at a freestream velocity of 19 m/s and a microphone angle of 110 degrees. Note that the data plotted in Figure 4.5 is not corrected for shear layer refraction effects. This correction can only be applied to the individual propeller noise, while Figure 4.5 also contains wind tunnel induced noise.

The noise spectrum displayed in Figure 4.5 shows that the unpowered propeller model's noise emissions are largely of tonal nature. The first six BPF tones clearly stand out from the background noise level. The 1BPF and 3BPF tones are dominant with sound pressure levels of about 60 dB, while the SPL of the other tones is much lower at about 50 dB.

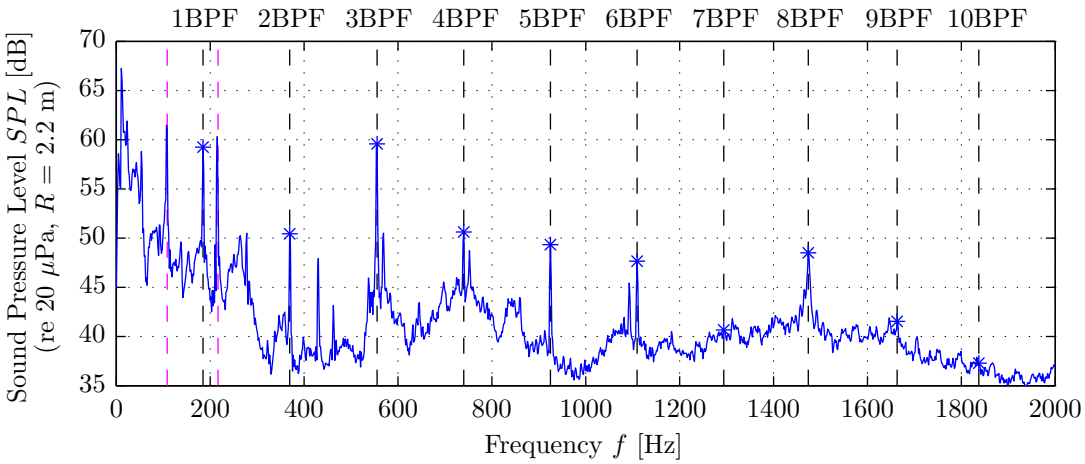

Figure 4.5: Unpowered propeller noise spectrum.
Isolated configuration, $U_\infty = 19$ m/s, $\theta_{\text{mic}} = 110°$, $K = 90$.

The noise emitted by the wind tunnel fan is also recognized with two dominant tones present at frequencies of 108 Hz and 216 Hz, corresponding to the first and second BPF multiples of the wind tunnel fan. Note that the maximum sound pressure levels of the propeller tones are of the same order as those corresponding to the wind tunnel fan noise. This is observed for all freestream velocities considered, as both the wind tunnel fan tones and the propeller tones become louder with increasing velocity.

4.3.2 Propeller Tonal Noise Levels

From the noise spectrum shown in Figure 4.5 it was concluded that the unpowered propeller noise emissions are dominated by tonal components. Figure 4.6 presents the sound pressure levels of the first six BPF tones for freestream velocities of 15, 19, 24, and 30 m/s. The data was corrected for shear layer refraction effects and scaled to a constant radius of 1.0 m. Note that therefore the sound pressure levels displayed for the measurement performed at 19 m/s are different from those shown in Figure 4.5 which did not include the shear layer correction.

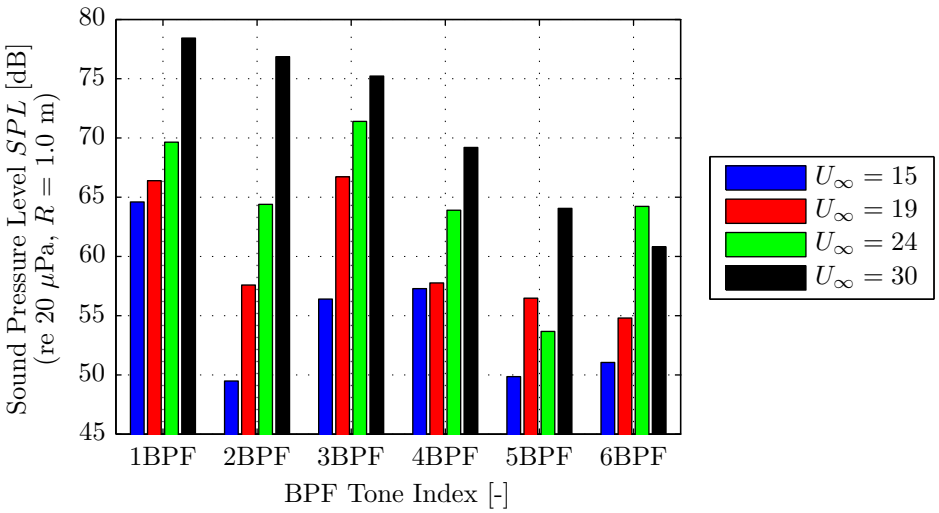

Figure 4.6: Unpowered propeller tonal noise levels.
Isolated configuration, $U_\infty = [15, 19, 24, 30]$ m/s, $\theta_{\text{mic}} = 110°$, $K = 90$.

The data depicted in Figure 4.6 shows that the SPL of the propeller tones increases with increasing freestream velocity, as expected considering the increase in RPM accompanied with the increase in velocity. Furthermore, it is observed that for freestream velocities of 19 m/s and 24 m/s the 1BPF and 3BPF tones are dominant. At 30 m/s on the other hand the second BPF multiple has increased to a level in between the first and third BPF tones.

The high SPL of the 3BPF tone at velocities of 19 and 24 m/s is an unexpected result. It is likely that it is the result of interaction effects, possibly resulting from the propeller support strut which was positioned relatively close to the propeller plane. It should however be noted that since the blade operating conditions are unknown it is difficult to draw exact conclusions about the sound generating mechanisms occurring at the different velocities considered.

4.4 Installed Configuration

With the pylon present in front of the unpowered propeller model, it is expected that the noise emissions will increase compared to the isolated case. The wake shed by the pylon results in non-uniform inflow conditions at the propeller plane which lead to additional pressure fluctuations due to varying blade loads, hence additional noise. This subsection first compares the propeller noise spectra measured in the installed and isolated configurations (Subsection 4.4.1). Thereafter, a more detailed analysis is presented of the tonal noise penalty due to the installation effects (Subsection 4.4.2).

4.4.1 Propeller Noise Spectrum

A comparison between the propeller noise spectra obtained in installed and isolated conditions is depicted in Figure 4.7. The presented data was obtained at a freestream velocity of 19 m/s and a microphone angle of 110 degrees, and was not corrected for shear layer refraction effects. The sound spectrum of the isolated propeller is the same as plotted before in Figure 4.5. It should be noted that the RPM in installed conditions was slightly lower than in the isolated configuration, hence shifting the BPF tones towards a lower frequency. Depending on the velocity, the RPM in the installed configuration was about 50-100 RPM lower than during the isolated measurements. The dashed black lines indicate integer multiples of the BPF based on the average RPM of the isolated and installed measurements.

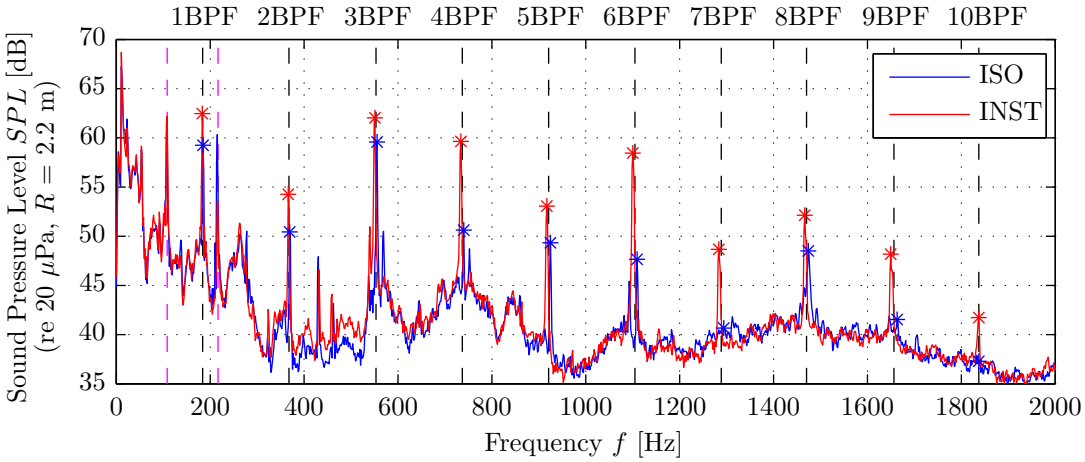

Figure 4.7: Unpowered propeller noise spectrum: effects of installation. Isolated and installed configurations, $U_\infty = 19$ m/s, $\theta_{\text{mic}} = 110°$, $K = 90$.

From Figure 4.7 it is concluded that the propeller noise emissions increase in the installed configuration. The 1BPF tone displays a noise penalty due to installation effects of about 3 dB, while the 3BPF tone becomes 2 dB louder. For the displayed measurement point the increases for the even multiples of the BPF are larger, with noise penalties of 4 dB at 2BPF, 9 dB at 4 BPF, and 10 dB at 6 BPF. The broadband levels seem to be largely unaffected by the presence of the pylon, except for a small increase between the 2BPF and 3BPF tones.

It should be stressed once more that the reproducibility of nonconsecutive unpowered propeller noise measurements was not good. This is also illustrated by Figure 4.7 when considering the SPL of the 2BPF tone of the wind tunnel fan. Although the installed and isolated measurements were performed at the same freestream velocity (hence the same wind tunnel setting), the measured SPL for this tone was about 6 dB lower during the installed measurement.

4.4.2 Propeller Tonal Noise Levels

The sound spectrum depicted in Figure 4.7 showed that the installed noise levels are higher than the corresponding isolated values. To further assess this observation, the installed tonal noise levels at freestream velocities of 15, 19, 24, and 30 m/s and microphone directivity angles of 90, 110, and 130 degrees were extracted from the measured sound spectra. To reduce the variability in the installed noise measurement data the measurements were repeated several times during different runs and the data was subsequently averaged per measurement point over all available runs. The differences between the installed and isolated tonal noise emissions are presented in Figures 4.8, 4.9, and 4.10, displaying the results obtained at microphone angles of 90, 110, and 130 degrees, respectively. For reference, dashed orange lines are added indicating the variability of *consecutive* measurements. Note that the nonconsecutive measurements presented here can show a larger variability as discussed in Section 4.2.

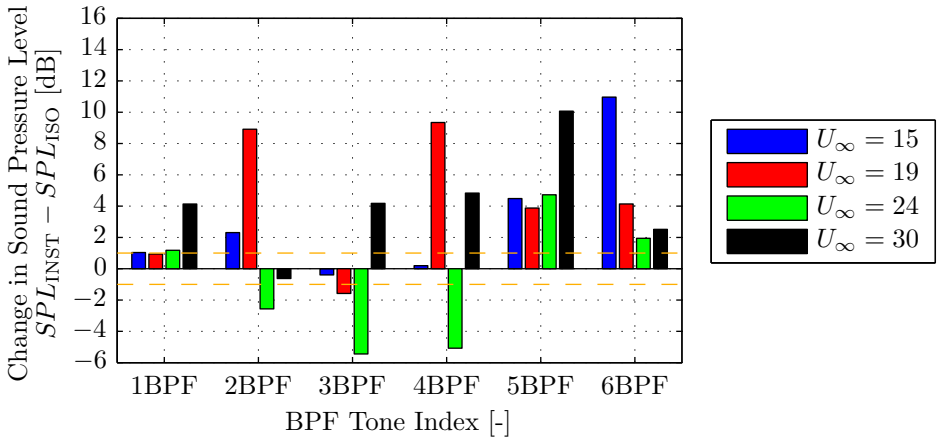

Figure 4.8: Differences between the installed and isolated unpowered propeller tonal noise levels. Isolated and installed configurations, $U_\infty = [15, 19, 24, 30]$ m/s, $\theta_{\text{mic}} = 90°$, $K = 90$.

Figures 4.8 through 4.10 show that in general the installed tonal noise levels are higher than the corresponding isolated values. The increases become larger with increasing microphone angle, indicating that the noise due to the installation effects mainly radiates towards the propeller axis. This agrees with experimental data for powered propellers presented in the literature [17, 20, 21, 24]. Furthermore, it is also recognized that the largest noise penalties occur for the tones corresponding to the higher BPF multiples. For the isolated propeller the SPL of these tones in general was found comparatively low, but for the installed propeller the sound pressure levels become close to those of the dominant 1BPF and 3BPF tones.

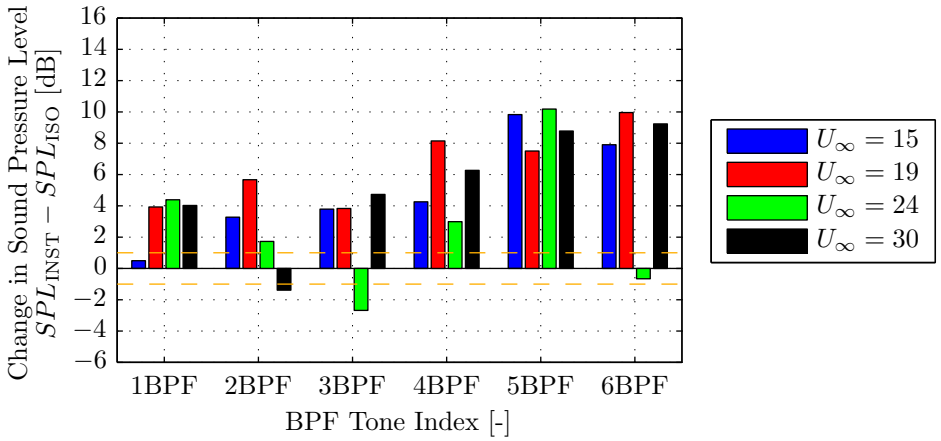

Figure 4.9: Differences between the installed and isolated unpowered propeller tonal noise levels. Isolated and installed configurations, $U_\infty = [15, 19, 24, 30]$ m/s, $\theta_{\text{mic}} = 110°$, $K = 90$.

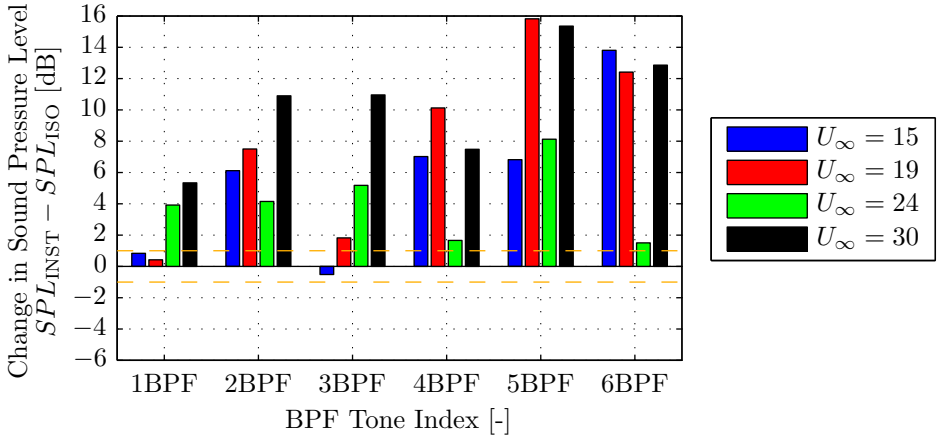

Figure 4.10: Differences between the installed and isolated unpowered propeller tonal noise levels. Isolated and installed configurations, $U_\infty = [15, 19, 24, 30]$ m/s, $\theta_{\text{mic}} = 130°$, $K = 90$.

The data presented in Figures 4.8, 4.9, and 4.10 however also contains a number of unexpected results. From Figure 4.8 it is seen that for a freestream velocity of 24 m/s and a microphone angle of 90 degrees the installed noise levels of the 2BPF, 3BPF, and 4BPF tones are lower than the corresponding isolated values. The same is observed at a microphone angle of 110 degrees for the 3BPF tone. It is unsure whether these measured reductions in SPL due to installation are indeed correct (which is possible if the additional interaction noise would cancel the isolated contributions for the combination of freestream velocity and microphone angle considered), or should be attributed to measurement errors.

It is also recognized that the results presented in Figures 4.8, 4.9, and 4.10 do not show clear trends between the data sets obtained at the different freestream velocities. Considering for example the SPLs of the 6BPF tone depicted in Figure 4.9, an increase of about 8 to 10 dB is observed for the measurements performed at 15, 19, and 30 m/s, while at 24 m/s a 1 dB reduction is observed. Again it is unsure whether this actually is a correctly measured phenomenon, or that this specific result is dominated by measurement errors. However, inspection of the isolated noise levels presented before in Figure 4.6 showed that the SPL of the 6BPF tone at 24 m/s was much higher than those measured at the other three freestream velocities. As a result, it is concluded that it is also possible that the isolated reference value is inaccurate, thereby directly affecting the measured noise penalty due to installation effects.

In short, it is concluded that the comparison of the isolated and installed data indicates that the effects of installation indeed increase the noise emissions. However, a large variability is present in the measured data, thereby making it unsuitable for accurate comparisons.

4.5 Blown Configuration

The pylon blowing system is targeted at reducing the velocity deficit in the pylon wake, thereby decreasing the noise penalty due to the installation effects. The blown measurements were performed consecutively with the installed measurements to achieve the lowest possible measurement variability as discussed in Section 4.2. This section first presents an example noise spectrum obtained with the blowing system enabled (Subsection 4.5.1) and compares it to the spectra measured in the isolated and installed configurations. Subsequently the effect of the blowing rate on the tonal noise emissions is assessed for a range of freestream velocities (Subsection 4.5.2). Finally, a directivity analysis is given of the first three propeller tones measured with and without the pylon blowing system enabled (Subsection 4.5.3).

4.5.1 Propeller Noise Spectrum

The propeller noise spectrum measured in the blown configuration is presented in Figure 4.11, together with the isolated and installed spectra shown before in Figures 4.5 and 4.7. The data recorded in the blown configuration was obtained at a freestream velocity of 19 m/s, a blowing rate of $Q = 680$ L/min, and a microphone angle of 110 degrees. Again, no correction was performed to account for shear layer refraction effects. Note that the propeller RPM in the blown configuration falls in between the RPMs obtained in the isolated and installed configurations.

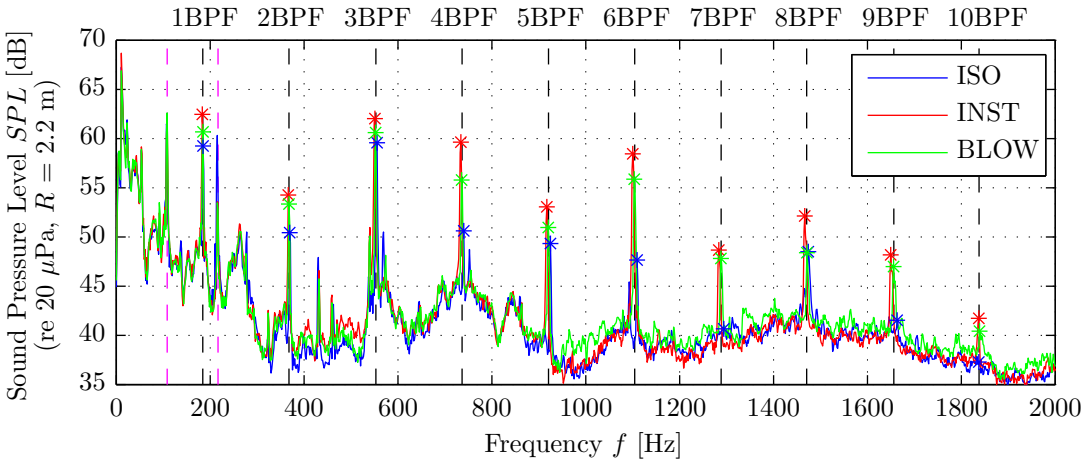

Figure 4.11: Unpowered propeller noise spectrum: effects of blowing. Isolated, installed, and blown configurations, $U_\infty = 19$ m/s, $Q = 680$ L/min, $\theta_{\text{mic}} = 110°$, $K = 90$.

Figure 4.11 shows that application of the pylon blowing system at a blowing rate of 680 L/min indeed reduces the propeller noise emissions compared to the installed case. For all tones considered the SPL decreases by blowing, with reductions in the order of about 2 to 5 dB. The isolated noise levels are still lower than those recorded in the blown configuration, indicating that the installation effects are not fully eliminated by the blowing system. This is as expected considering the wake profiles presented before in Chapter 3, which showed that the blown pylon wake does not become completely uniform.

4.5.2 Propeller Tonal Noise Levels

The noise spectrum displayed in Figure 4.11 showed that at $U_\infty = 19$ m/s and $Q = 680$ L/min the application of blowing reduced the tonal noise emissions. To quantify the effect of the blowing rate on the noise levels, measurements were also performed at blowing rates of 400, 500, and 600 L/min. Figure 4.12 presents the sound pressure levels of the first six BPF tones at $U_\infty = 19$ m/s for all blowing rates considered. The installed results are also added.

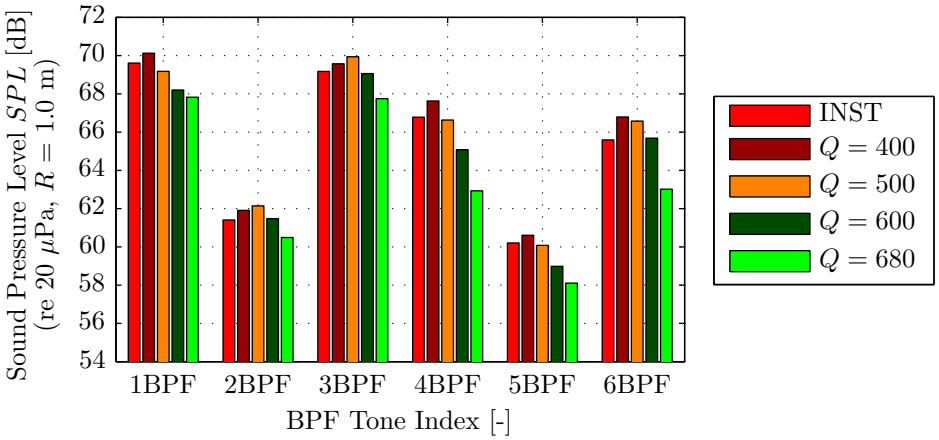

Figure 4.12: Unpowered propeller tonal noise levels: effects of blowing. Installed and blown configurations, $U_\infty = 19$ m/s, $\theta_{\text{mic}} = 110°$, $K = 90$.

Figure 4.12 shows that the tonal noise levels are lowest at the highest blowing rate. Furthermore, it is seen that at blowing rates of 400 and 500 L/min the noise levels are higher than in the installed configuration. However, it should be noted that at these two blowing rates for all BPF multiples the SPL increase falls within the ±1 dB range considered as the measurement variability. Based on the measured pylon wake profiles it is concluded that the reduction in tonal noise likely results from a reduced blade loading in the wake region. At $U_\infty = 19$ m/s for the higher blowing rates wake profiles were obtained with a negative velocity deficit in the center of the wake. When the blade passes through this region of increased inflow velocity the effective axial velocity increases compared to the undisturbed case, in this case apparently leading to reduced blade loads. This then results in reduced loading noise emissions.

So far, results of the measurements performed in the blown configuration have only been presented for a freestream velocity of 19 m/s. Since it was observed before during the pylon wake profile measurements that the freestream velocity has a strong effect on the blown wake profiles, blown noise measurements were also performed at freestream velocities of 15, 24, and 30 m/s. The reductions in the tonal noise levels at all considered velocities are plotted as a function of the blowing rate in Figure 4.13. The measured reductions in the SPL for the first six BPF tones were averaged for each freestream velocity. The dashed orange lines indicate the expected variability of the consecutively performed noise measurements (±1 dB).

Figure 4.13 shows that the effectiveness of the blowing system reduces with increasing freestream velocity. At 15 m/s an average tonal noise reduction of 7 dB is observed at the maximum blowing rate of 680 L/min, while at $Q = 400$ L/min already a noise reduction of approximately 1 dB is obtained. At 19 and 24 m/s on the other hand the effect of blowing at a rate of 400 L/min is negligible. Upon increasing the blowing rate for both velocities the noise penalty due to the installation effects starts to decrease around $Q = 600$ L/min, with a 2 dB reduction in the average tonal SPL observed for $U = 19$ m/s at $Q = 680$ L/min. At a

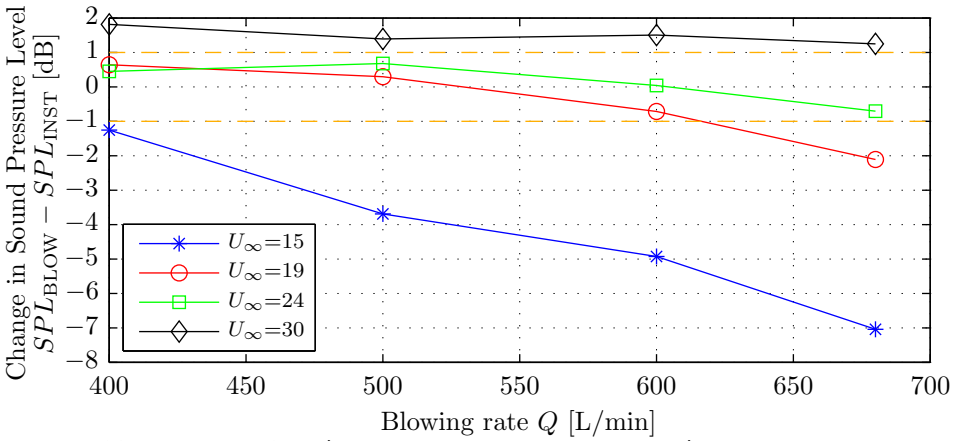

Figure 4.13: Change in SPL (average over first six BPF tones) versus blowing rate and freestream velocity. Blown configuration, $U_\infty = [15, 19, 24, 30]$ m/s, $\theta_{\mathrm{mic}} = 110°$, $K = 90$.

freestream velocity of 30 m/s increases in the noise levels are measured at all blowing rates considered. Based on the results discussed in Chapter 3 for the default pylon it is assumed that the outflow velocities from the blown extended pylon are too low at 30 m/s. The resulting interaction between the external flow and the flow blown into the pylon wake can result in an increased velocity deficit in the pylon wake and hence increased noise emissions.

Based on the data depicted in Figure 4.13 it is concluded that for the blowing rates considered the blowing system is very effective at 15 m/s, slightly effective at 19 m/s, and not effective at freestream velocities of 24 and 30 m/s. It is expected that at all velocities the blowing system should be able to reduce the noise levels to a similar extent as at 15 m/s, however higher blowing rates would be required to achieve this. This expectation could however not be verified since the test setup did not allow for blowing rates higher than 680 L/min.

To obtain additional insight in the noise reductions achievable by blowing the differences between the tonal noise levels in the installed and blown configurations were analyzed for the individual BPF tones. Considering that the blowing system only turned out to be effective at freestream velocities of 15 and 19 m/s, results are only given for these velocities. The corresponding data is presented in Figures 4.14 and 4.15, which display the change in the SPL as a result of blowing for the first six BPF tones and the same range of blowing rates as considered before. The dashed orange lines again represent the measurement variability.

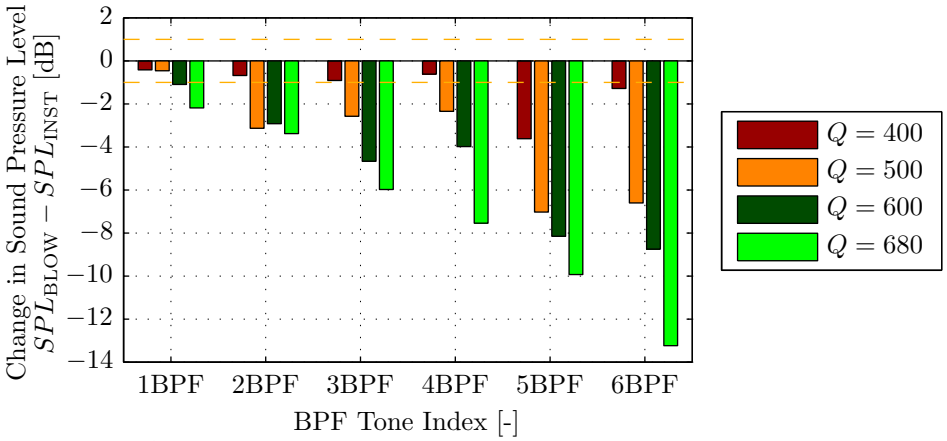

Figure 4.14: Tonal noise reductions due to blowing: effects of the blowing rate. Blown configuration, $U_\infty = 15$ m/s, $\theta_{\mathrm{mic}} = 110°$, $K = 90$.

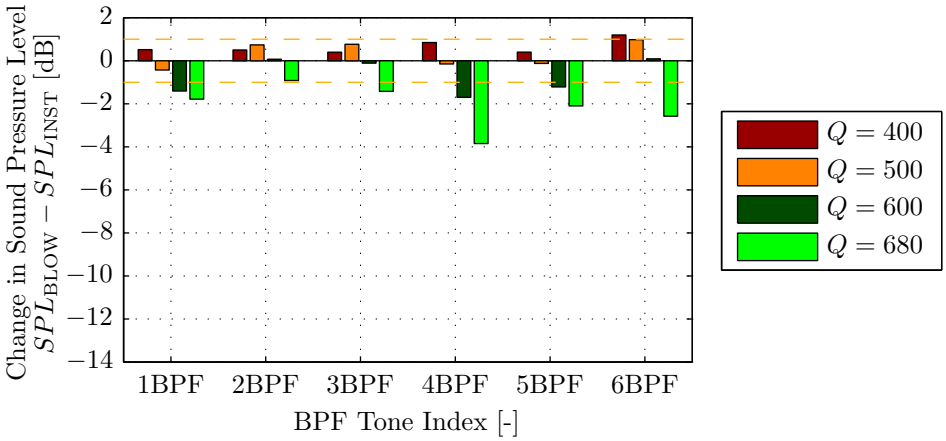

Figure 4.15: Tonal noise reductions due to blowing: effects of the blowing rate.
Blown configuration, $U_\infty = 19$ m/s, $\theta_{\text{mic}} = 110°$, $K = 90$.

Figures 4.14 and 4.15 confirm the previous findings. The reductions in the tonal noise levels due to blowing are much larger at a freestream velocity of 15 m/s than at 19 m/s. While at 15 m/s the SPL reductions at a blowing rate of 680 L/min range from 2 to 13 dB, at 19 m/s this has decreased to 1 to 4 dB. Furthermore, it is observed that at 15 m/s the SPL reductions are most pronounced for the tonal components corresponding to the higher BPF multiples. This confirms the observation made before that the noise penalty due to the installation effects is especially large for the tones with frequencies equal to higher BPF multiples.

4.5.3 Directivity Analysis

The measurements of the unpowered propeller noise emissions in the blown configuration presented so far were all obtained at a microphone angle of 110 degrees. To determine the directivity pattern of the noise emissions in the installed and blown configurations, measurements were also performed at microphone angles of 90 and 130 degrees. The resulting sound pressure levels of the 1BPF, 2BPF, and 3BPF tones obtained at a freestream velocity of 19 m/s are presented versus the emission angle in Figures 4.16, 4.17, and 4.18, respectively.

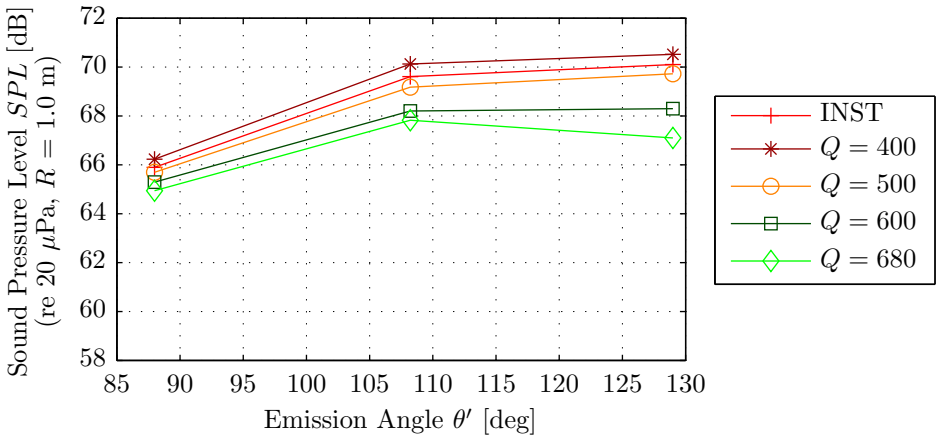

Figure 4.16: Directivity of the 1BPF tone for various blowing rates.
Installed and blown configurations, $U_\infty = 19$ m/s, $\theta_{\text{mic}} = [90, 110, 130]°$, $K = 90$.

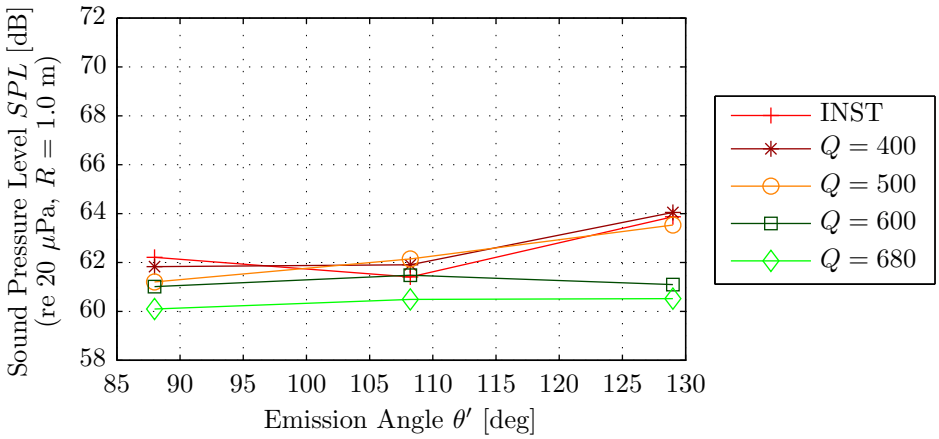

Figure 4.17: Directivity of the 2BPF tone for various blowing rates.
Installed and blown configurations, $U_\infty = 19$ m/s, $\theta_{\text{mic}} = [90, 110, 130]°$, $K = 90$.

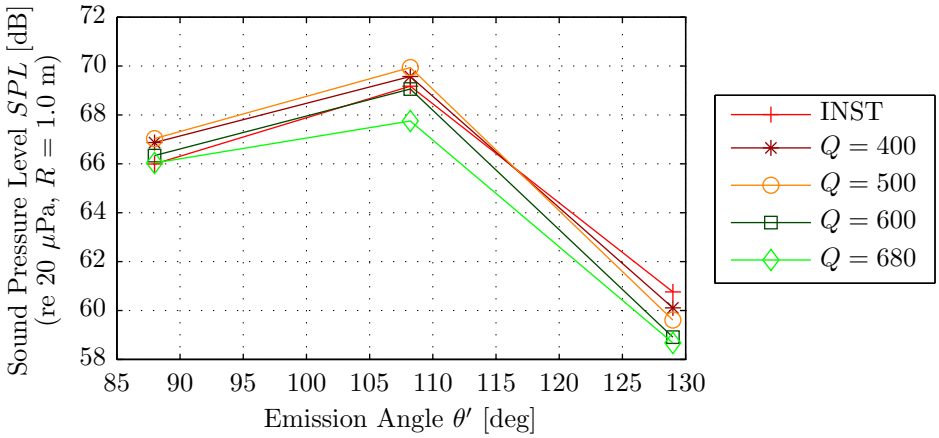

Figure 4.18: Directivity of the 3BPF tone for various blowing rates.
Installed and blown configurations, $U_\infty = 19$ m/s, $\theta_{\text{mic}} = [90, 110, 130]°$, $K = 90$.

Figure 4.16 shows that the SPL of the 1BPF tone increases towards the rear arc in the installed configuration, while application of blowing gradually shifts the point of maximum SPL forward. The reduction in SPL obtained at $Q = 680$ L/min increases with increasing directivity angle, hence indicating that the effect of installation on the 1BPF tone's SPL is strongest at directivity angles towards the propeller axis. It is expected that at blowing rates higher than 680 L/min the SPL of the 1BPF tone would further decrease in the rearward arc. The data obtained at a freestream velocity of 15 m/s (not presented here) confirmed this hypothesis.

The tonal noise levels corresponding to a frequency of two times the BPF plotted in Figure 4.17 are about 4 to 6 dB lower than the SPL of the 1BPF tone. In the installed configuration the directivity of the 2BPF tone shows a slight increase towards the rear arc with a noise increase of about 2 dB at $\theta' = 130°$ when compared to the SPL at $\theta' = 90°$. When blowing at a rate of 680 L/min the SPL remains approximately constant with the emission angle, indicating that again the largest noise reductions are obtained at the higher emission angles.

The directivity of the 3BPF tone depicted in Figure 4.18 shows a distinct increase in the SPL of about 3 dB when going from an emission angle of 90 to 110 degrees. Further towards the

rear arc the SPL drops rapidly, with sound pressure levels about 9 dB lower at an emission angle of around 130 degrees than at 110 degrees. The application of blowing results in noise reductions at all considered emissions angles, with the largest decrease in noise equal to about 2 dB at 110 degrees. Therefore, it is concluded that for the 3BPF tone the installation effect is largest around directivity angles of 110 degrees.

Chapter 5

Experimental Results: Powered Propeller Performance

The powered propeller performance measurements were used to quantify the effects of pylon installation on the propeller performance. This chapter starts by giving an overview of the measurements in Section 5.1. Then, the RSB signal quality and the reproducibility of the results are discussed in Section 5.2. Subsequently, Section 5.3 treats the isolated propeller performance. Thereafter, the measurements performed in the installed and blown configurations are compared to the isolated results in Sections 5.4 and 5.5.

5.1 Measurement Overview

An overview of the characteristics of the powered propeller performance measurements is given in Table 5.1. A detailed description of the applied measurement techniques and corresponding post-processing is presented in Chapter 2. All data presented in this chapter was corrected for RPM effects and the apparent back pressure drag term acting on the propeller hub.

Table 5.1: Characteristics of the powered propeller performance measurements.

Parameter	**Symbol**	**Value**	**Unit**
Freestream velocity	U_∞	[15,19,26,30][1]	m/s
Advance ratio	J	$[0.5 \leq J \leq 1.8]$[2]	-
Blowing rate	Q	[0,400,500,600,680]	L/min
Pylon-propeller spacing	ΔX	114	mm
Pylon angle of attack	α	0	deg
Sampling frequency	f_s	50	kHz
Measurement time	t_m	5	s
Cut-off frequency	f_cut	2,500	Hz

5.2 Signal Quality and Reproducibility of the Results

The RSB used for the propeller performance measurements provides time-accurate measurements of the propeller forces and moments. Since the pylon installation effects are expected

[1] The freestream velocity of 30 m/s was only used for measurements in isolated conditions.
[2] At 26 m/s and 30 m/s the lowest considered advance ratios equaled 0.55 and 0.65, respectively.

to be a strong function of time (or blade position to be more precise) the possibility of time-accurate comparisons is very interesting. Therefore, at this point the signal quality of the time-accurate RSB data is analyzed, including a discussion of the reproducibility of the measurements.

Time histories of the thrust and torque signals obtained at a freestream velocity of 19 m/s and an advance ratio of 0.5 are displayed in Figures 5.1 and 5.2. The raw data is plotted together with filtered data computed using three cut-off frequencies (25, 250, and 2,500 Hz).

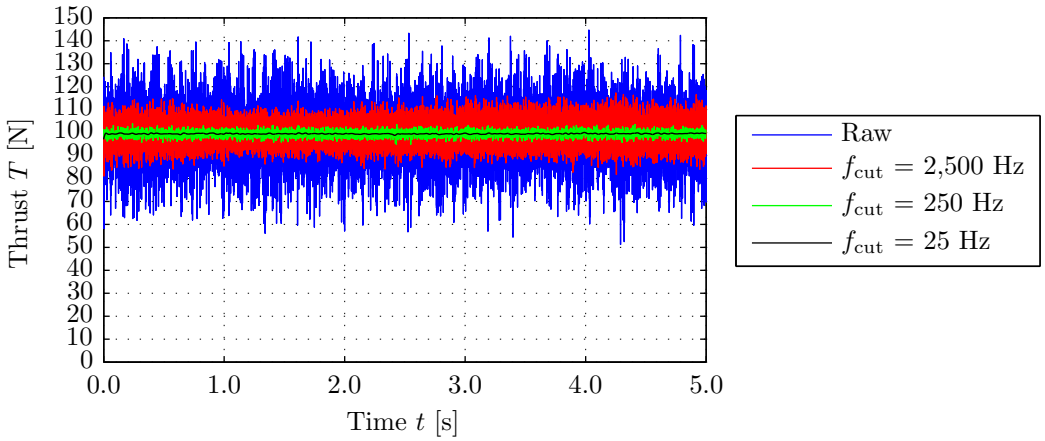

Figure 5.1: Thrust signal time history for a range of cut-off frequencies. Isolated configuration, $U_\infty = 19$ m/s, $J = 0.5$, $\overline{T} = 100$ N, $\overline{C_T} = 0.62$.

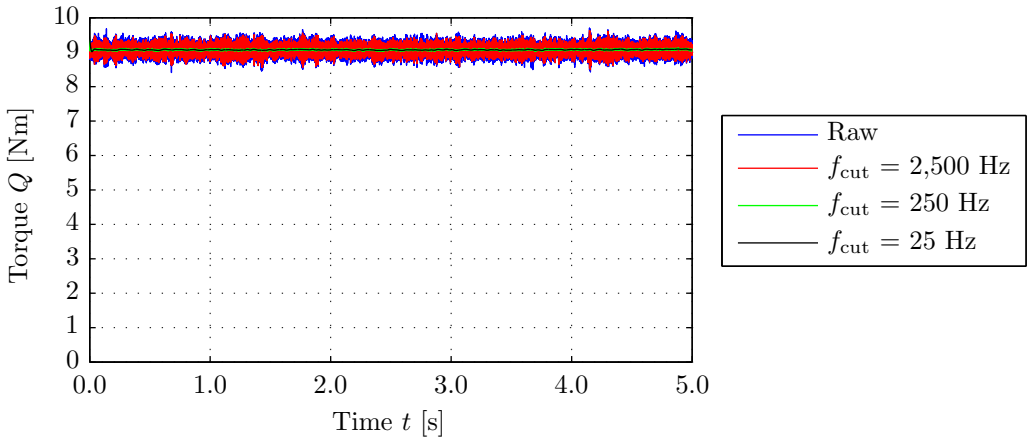

Figure 5.2: Torque signal time history for a range of cut-off frequencies. Isolated configuration, $U_\infty = 19$ m/s, $J = 0.5$, $\overline{Q} = 9.1$ Nm, $\overline{C_Q} = 0.19$.

From Figure 5.1 it is concluded that the signal quality of the raw thrust data at low advance ratio is low. While the average thrust for the measurement point displayed in Figure 5.1 equals 100 N, the raw time-accurate data fluctuates between about 60 N and 140 N. Figure 5.2 shows that the signal quality of the torque data is higher than that of the thrust data. The average torque recorded for the measurement point displayed in Figure 5.2 equals 9.1 Nm, while the time-dependent signal fluctuates between approximately 8.6 Nm and 9.6 Nm.

The time histories displayed in Figure 5.1 and 5.2 were obtained at an advance ratio of 0.5, hence the resulting thrust and torque signals were relatively strong. To assess whether the signal quality reduces further at higher advance ratios the thrust and torque time histories

obtained at an advance ratio of 1.8 are shown in Figures 5.3 and 5.4. Note that the y-axes of Figures 5.3 and 5.4 have different scales than used before in Figures 5.1 and 5.2.

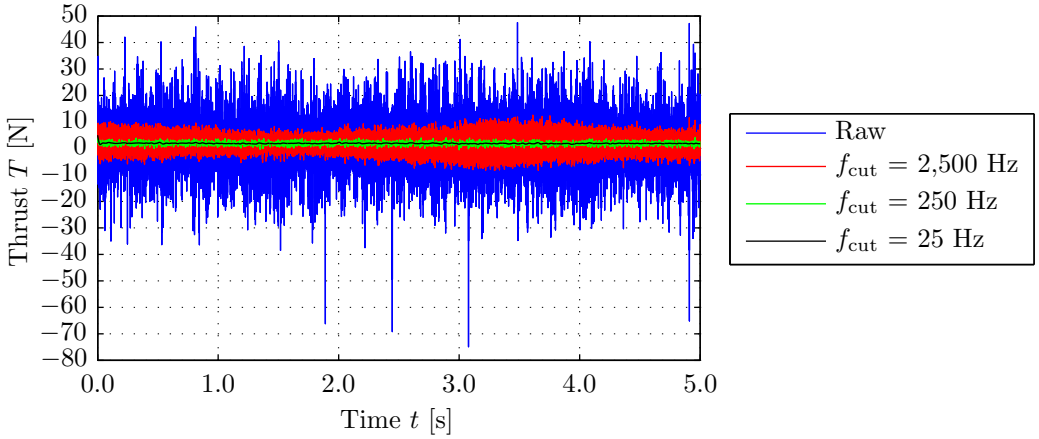

Figure 5.3: Thrust signal time history for a range of cut-off frequencies. Isolated configuration, $U_\infty = 19$ m/s, $J = 1.8$, $\overline{T} = 1.9$ N, $\overline{C_T} = 0.14$.

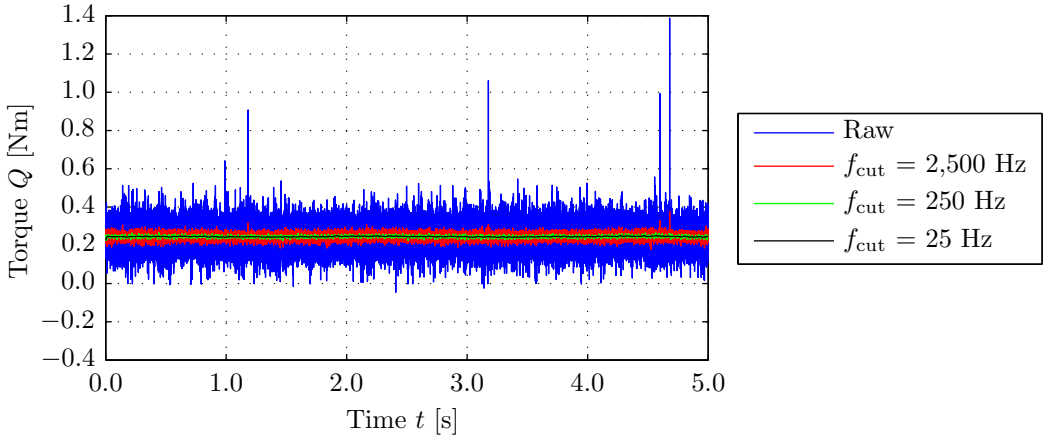

Figure 5.4: Torque signal time history for a range of cut-off frequencies. Isolated configuration, $U_\infty = 19$ m/s, $J = 1.8$, $\overline{Q} = 0.2$ Nm, $\overline{C_Q} = 0.06$.

Figure 5.3 shows that the quality of the thrust signal indeed becomes worse at high advance ratios. While the average thrust obtained at the measurement point displayed in Figure 5.3 equals 1.9 N, the peak-to-peak noise amplitude equals approximately 70 N. The torque time history displayed in Figure 5.4 confirms the previous findings. The average torque equals approximately 0.2 Nm while the peak-to-peak noise level is around 0.5 Nm.

The strong fluctuations in the measured thrust and (to a lesser extent) torque signals are expected to be the result of interference between the RSB signals and electromagnetic radiation emitted by the wind tunnel motor. Since the voltages transmitted from the RSB to the data acquisition (DAQ) system are very low (in the order of 1 mV), relatively low amplitude noise superimposed on the raw data directly results in large fluctuations in the measured thrust and torque signals. Application of a filter with increasingly low cut-off frequency gradually removes the noise from the measured data, hence smoothing the signal. However, the filtering process possibly also removes 'real' time-dependent phenomena from the signals, thereby making the data increasingly less useful for time-accurate comparisons when the cut-off frequency is reduced.

From the time histories presented in Figures 5.1 through 5.4 it was observed that the signal quality of the raw RSB data is low: both for low and high advance ratios a lot of noise is present in the data. Therefore, it was concluded that the quality of the RSB signals is insufficient for time-*accurate* comparisons. Analysis of the time-*averaged* results for various cut-off frequencies showed that the noise present in the data sets is random and averages out to zero. Therefore, it was decided that time-averaged evaluations could still be performed using the data measured using the RSB. This is discussed in more detail in Appendix C.2.1.1. In all data sets a number of distinct high frequency noise peaks were found which could be traced back to noise introduced into the signals by the DAQ system. To make sure these peaks would not influence the frequency spectrum analyses discussed later on, it was decided to filter all data using a cut-off frequency of $f_{\text{cut}} = 2,500$ Hz. This frequency is low enough to eliminate the first strong noise peak introduced by the DAQ system, while it is high enough to not remove any possibly relevant data from the RSB signals.

As a final step in the verification of the signal quality of the RSB the reproducibility of the measured results is considered. Figure 5.5 displays a comparison of the time-averaged propeller performance (in terms of the thrust coefficient C_T, torque coefficient C_Q, and propeller efficiency η) obtained at a freestream velocity of 19 m/s during measurement runs performed on two different days (15 August 2013 and 16 August 2013). The results presented so far in this section correspond to the measurement run labeled '15/08' in Figure 5.5.

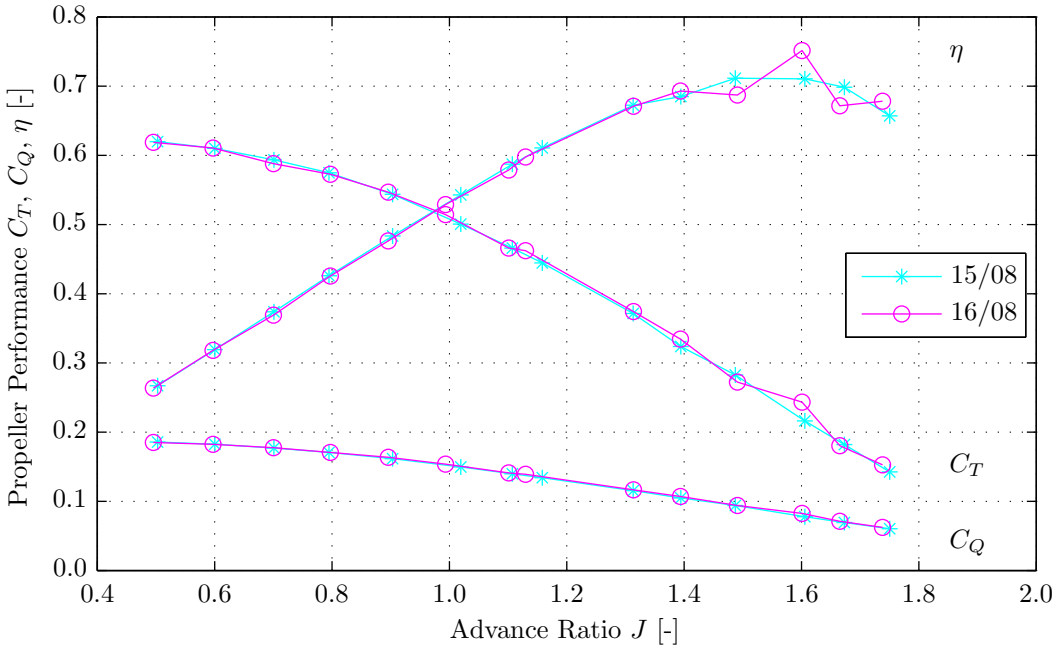

Figure 5.5: Reproducibility of time-averaged propeller performance measurements. Isolated configuration, $U_\infty = 19$ m/s, $0.5 \leq J \leq 1.8$, $f_{\text{cut}} = 2,500$ Hz.

The results depicted in Figure 5.5 show that in general the repeatability of the time-averaged RSB measurements is acceptable, with the largest differences occurring at high advance ratios for which the signal quality is lowest. To gain additional insight in the repeatability of the RSB measurements the relative differences between the repeated measurements were computed. Interpolation was performed to make sure that the differences were computed at equal advance ratios. Figure 5.6 presents the results for the thrust coefficient, while the

torque coefficient is considered in Figure 5.7. For reference, the approximate variability in the measurements as a function of the advance ratio is indicated by the dashed black lines. Results are presented for freestream velocities of 19 and 26 m/s. The data for $U_\infty = 19$ m/s was shown in Figure 5.5, while that for $U_\infty = 26$ m/s is presented in Appendix C.2.1.2.

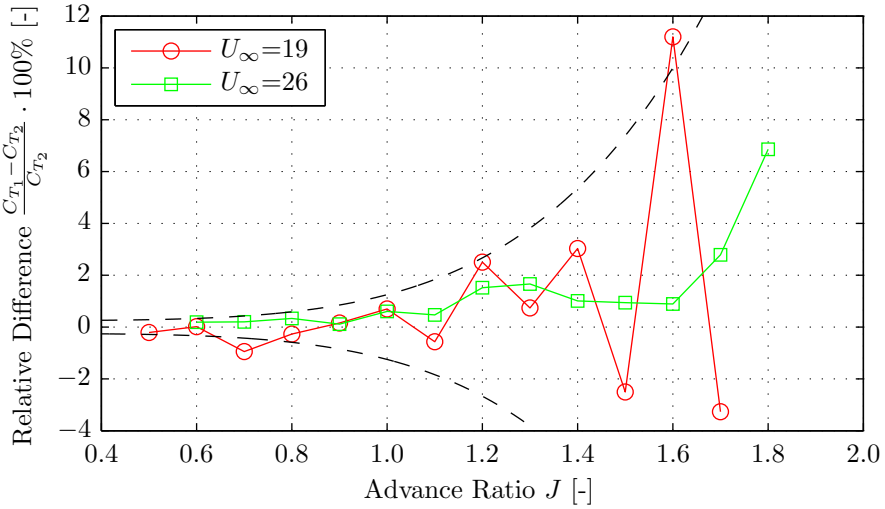

Figure 5.6: Relative differences between repeated thrust coefficient measurements. Isolated configuration, $U_\infty = [19, 26]$ m/s, $0.5 \leq J \leq 1.8$, $f_{\text{cut}} = 2,500$ Hz.

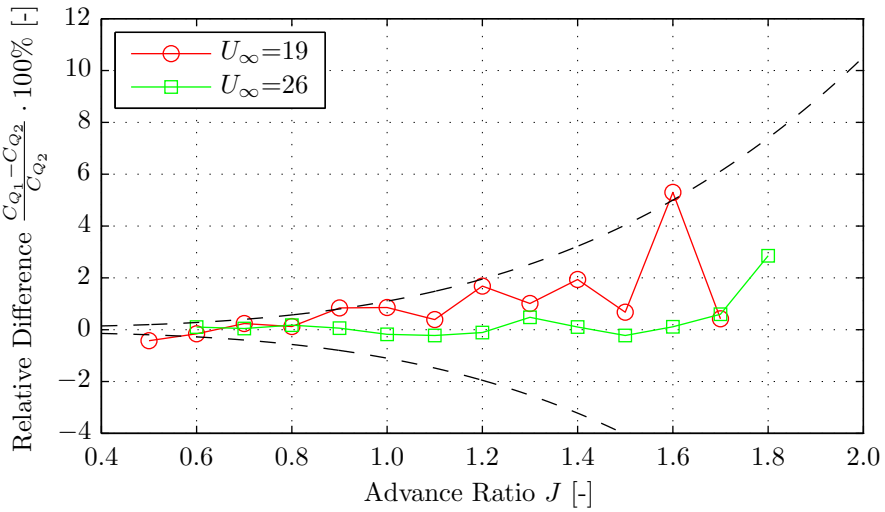

Figure 5.7: Relative differences between repeated torque coefficient measurements. Isolated configuration, $U_\infty = [19, 26]$ m/s, $0.5 \leq J \leq 1.8$, $f_{\text{cut}} = 2,500$ Hz.

Analysis of the data presented in Figures 5.6 and 5.7 learns that the reproducibility of the time-averaged RSB measurements is good for advance ratios below approximately $J = 1.1$. For this advance ratio range the measurements performed at 19 m/s and 26 m/s show a variability of $\pm 1\%$ between the thrust and torque coefficients obtained at the two measurement days. For $J > 1.1$ the reproducibility is worse with differences between repeated measurements of up to approximately 12% for the thrust coefficient. This is the result of the lower signal-to-noise ratio of the signals at high advance ratios. Note that at the highest advance ratios the repeatability of the torque coefficient measurements is better than for the thrust coefficient data, with a maximum relative difference between repeated measurements of around 5%.

5.3 Isolated Configuration

The isolated propeller performance measurements were performed to obtain a reference data set to which the installed and blown results could be compared later on. This section first presents the measured time-averaged propeller performance (Subsection 5.3.1). Subsequently, a frequency spectrum analysis of the thrust and torque signals is discussed (Subsection 5.3.2).

5.3.1 Time-Averaged Propeller Performance

The isolated propeller performance in terms of the thrust coefficient C_T, torque coefficient C_Q, and propeller efficiency η is plotted versus the advance ratio in Figure 5.8 for freestream velocities of 15, 19, 26, and 30 m/s.

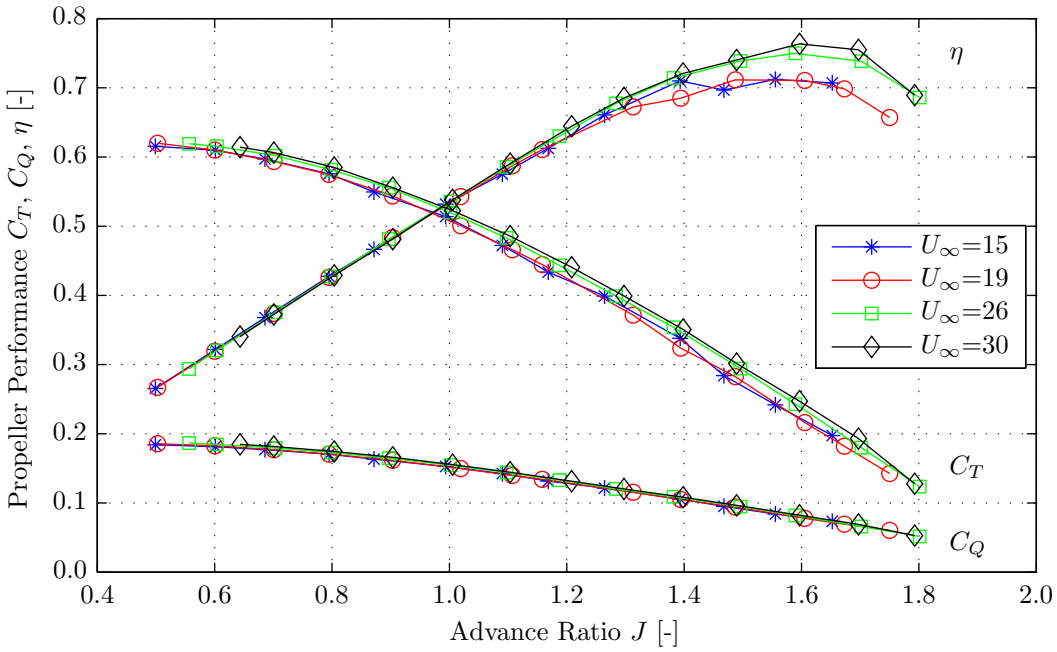

Figure 5.8: Propeller performance diagram.
Isolated configuration, $U_\infty = [15, 19, 26, 30]$ m/s, $0.5 \leq J \leq 1.8$, $f_{\text{cut}} = 2,500$ Hz.

From Figure 5.8 it is concluded that for all considered freestream velocities the thrust coefficient shows the expected behavior. For advance ratios above $J = 1.0$ the thrust coefficient is a quasi-linear function of the advance ratio, while at lower advance ratios the thrust coefficient curve gradually flattens due to the onset of non-linear effects in the lift response of the propeller blades. The torque coefficient data displays a similar trend, as expected. The propeller efficiency increases with increasing advance ratio up to approximately $J = 1.6$, reaching a maximum value of around 0.70 to 0.75 depending on the freestream velocity. Further increases in the advance ratio result in a gradual drop in propeller efficiency.

Furthermore, Figure 5.8 shows that at constant advance ratio the thrust coefficient increases with increasing freestream velocity. This is explained by the effect of the Reynolds number on the lift production of the propeller blades. If the advance ratio is kept constant an increase in freestream velocity results in an increase in the effective velocities experienced by the propeller blades, thereby increasing the local Reynolds numbers. Consequently, the boundary layers

on the propeller blades become thinner, resulting in a larger effective camber hence larger overspeeds and thus higher lift production at a given angle of attack. This increase in lift coefficient directly translates into an increase in the thrust coefficient measured at a given advance ratio. Inspection of Figure 5.8 shows that at a constant advance ratio the measured thrust coefficient is about 2% to 10% higher (for low and high advance ratios, respectively) at a freestream velocity of 30 m/s than at 15 m/s.

Apart from the increase in lift, the increase in Reynolds number also results in a decrease in propeller blade drag. However, based on the results presented in Figure 5.8 it is concluded that for the current propeller this decrease in drag is insufficient to reduce the torque coefficient with increasing freestream velocity. Apparently the increase in the magnitude of the contribution of the blade lift to the torque coefficient is larger than the decrease in the magnitude of the contribution of the blade drag. For $J > 1.1$ it is however observed that the relative increase of the torque coefficient is smaller than the relative increase in thrust coefficient, resulting in an increase in propeller efficiency with increasing freestream velocity.

The thrust coefficient data displayed in Figure 5.8 was corrected for RPM effects and the apparent drag due to the propeller hub back pressure. For all measurement points the effect of the RPM correction turned out to be negligible, hence not resulting in any changes in the computed thrust and torque coefficients. The back pressure correction on the other hand did affect the final values of the thrust coefficient. The magnitude of the effective drag term increased with decreasing advance ratio, leading to a change in thrust coefficient of up to 2% at the lowest advance ratio considered ($J = 0.5$). For a detailed analysis of the back pressure data the reader is referred to Appendix C.2.2.1.

5.3.2 Frequency Spectrum Analysis of the Thrust and Torque Signals

In Section 5.2 it was concluded that the signal quality of the RSB data is insufficient for time-accurate comparisons between the results measured in the isolated, installed, and blown configurations. However, at this point it should be noted again that the pusher propeller installation effects are governed by the pylon wake, hence confining the effects of installation to a limited region behind the pylon. As a result, in the installed configuration the rotating blades only experience a change in inflow conditions over a limited radial segment of the propeller disk. Therefore, the frequency content of the installed thrust and torque signals is expected to display a 'peaky' pattern, with the peaks located at frequencies equal to multiples of the propeller's BPF. Based on this observation it is concluded that, if the noise in the RSB signals is either broadband or centered in frequency bands which do not overlap with multiples of the BPF, frequency spectrum analysis of the RSB signals might be useful as an addition to the time-averaged evaluations.

To assess the potential of frequency spectrum analysis of the RSB signals for comparisons between the propeller performance in the isolated, installed, and blown configurations, the power levels of the isolated propeller thrust and torque signals were computed. Welch's method was used, following the same procedure as applied in the post-processing of the microphone data discussed in Appendix A.2.3. An average factor of fifteen was selected, resulting in a frequency resolution of 1.5 Hz. For overview reasons, this paragraph only presents the results obtained using the data measured at a freestream velocity of 19 m/s. The results computed from the data obtained at 15 and 26 m/s displayed similar trends.

The resulting power levels of the thrust data are plotted in Figure 5.9 for advance ratios of 0.5, 1.1, and 1.8. For the same measurement points the torque power levels are shown in Figure 5.10. The black dashed lines in Figures 5.9 and 5.10 indicate integer multiples of the BPF corresponding to the freestream velocity and advance ratio for which the plot is generated. The red asterisks mark the positions of the maximum power in the signals.

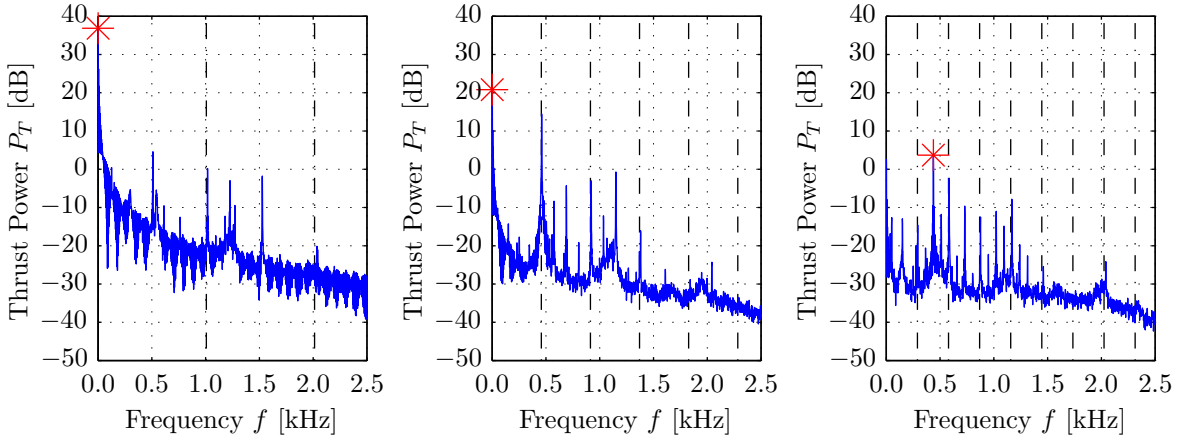

Figure 5.9: Power spectra of the thrust signal for $J = 0.5$ (l), $J = 1.1$ (c), and $J = 1.8$ (r). Isolated configuration, $U_\infty = 19$ m/s, $f_{\text{cut}} = 2,500$ Hz.

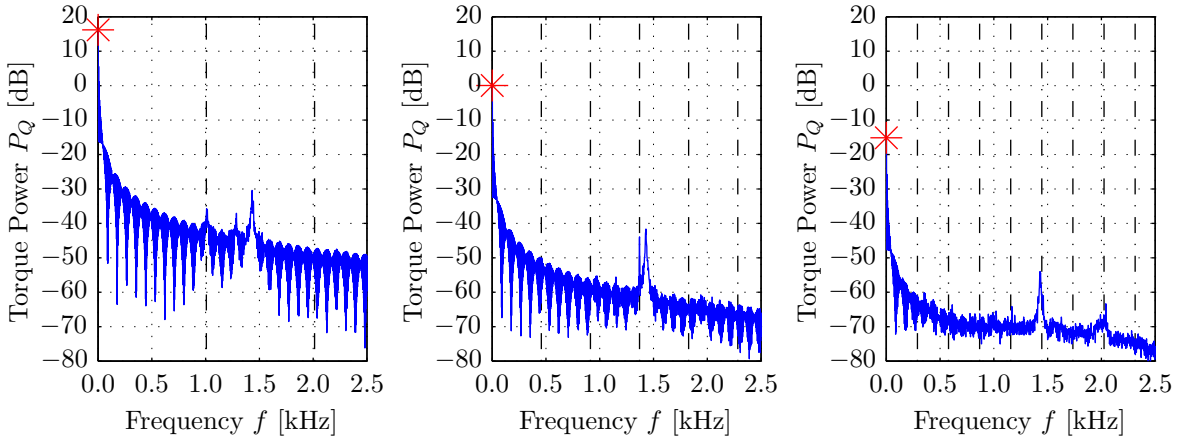

Figure 5.10: Power spectra of the torque signal for $J = 0.5$ (l), $J = 1.1$ (c), and $J = 1.8$ (r). Isolated configuration, $U_\infty = 19$ m/s, $f_{\text{cut}} = 2,500$ Hz.

Figure 5.9 shows that the maximum power in the thrust signal decreases with increasing advance ratio. The zero frequency component (labeled DC, corresponding to the average thrust) dominates at the advance ratios of 0.5 and 1.1, which is expected based on the relatively large steady-state thrust generated in these operating conditions. It is also observed that at all three advance ratios the largest power peaks at non-zero frequency occur at integer multiples of half the BPF ($n \cdot 0.5BPF$) which are close to approximately 500 Hz. For $J = 1.1$ and $J = 1.8$ the power of the corresponding peak is of the same order as the peak at zero frequency. This is an unexpected result considering the fact that the data presented in Figure 5.9 was obtained using the isolated propeller. In the ideal case the power spectrum for all measurements performed in isolated conditions should only show a peak at a frequency of zero, since the thrust should be constant in time. Although small deviations might occur due to for example unbalance or blade angle variations, for the isolated propeller the power of all peaks at non-zero frequency should be much smaller than that of the DC component.

Apart from the decrease in zero frequency power level with increasing advance ratio, the torque signal frequency contents displayed in Figure 5.10 show a clearly different pattern than observed in the thrust frequency spectra. For all three advance ratios the zero frequency component completely dominates the torque frequency spectrum. No peaks are visible at multiples of the BPF, indicating that the torque signal is stationary in time.

To gain more insight in the evolution of the peaks in the thrust power spectrum with the advance ratio the power levels for different integer multiples of half the BPF are plotted versus the advance ratio in Figure 5.11. Since Figure 5.10 showed that the torque frequency spectra did not display any significant peaks these are not further discussed here. Appendix C.2.2.2 presents a similar plot as Figure 5.11 but then for the torque power levels.

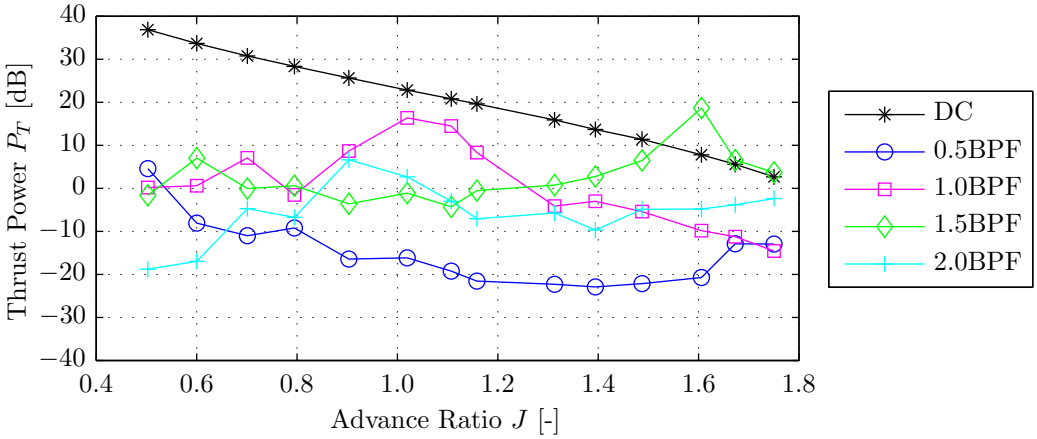

Figure 5.11: Thrust signal power levels for multiples of half the BPF versus the advance ratio. Isolated configuration, $U_\infty = 19$ m/s, $0.5 \leq J \leq 1.8$, $f_{\text{cut}} = 2,500$ Hz.

Figure 5.11 confirms that the zero frequency component of the thrust power decreases with increasing advance ratio, corresponding to the decrease in average thrust with decreasing RPM. The power levels of the multiples of half the BPF show a strong dependence on the advance ratio. At high advance ratios ($1.4 \leq J \leq 1.8$) the peaks corresponding to 1.5 times the BPF are dominant, with power levels of the same order as the DC level. Upon decreasing the advance ratio, gradually the 1.0BPF peak becomes most powerful, until it reaches its maximum around $J = 1.0$. The level of the maximum 1.0BPF peak is approximately equal to that of the maximum peak corresponding to 1.5BPF, and again is of the same order as the DC component. A further reduction of the advance ratio leads to a more varied frequency content, until the peak corresponding to 0.5BPF starts to become dominant at $J = 0.5$.

A more detailed analysis of the frequency contents of the thrust signal at all measured advance ratios showed that for all measurement points the maximum power at non-zero frequency occurs at the half BPF multiple which is closest to approximately 500 Hz. Furthermore, the closer this multiple is to 500 Hz, the larger the measured peak in the thrust power. This observation leads to the hypothesis that somewhere in the system an eigenfrequency is triggered, which leads to a harmonic vibration of the RSB and a corresponding peak in the frequency content of the measured thrust signal. If this is indeed the case, the thrust power frequency spectra contain peaks which do not correspond to forces generated by the propeller but instead are the result of measurement errors. Although not presented here, analysis of the data obtained at freestream velocities of 15, 26, and 30 m/s showed similar trends, with again the largest peaks in the thrust power spectra occurring around multiples of half the BPF

closest to 500 Hz. Additional tests should be performed to verify whether the hypothesis of an eigenfrequency issue is correct. It was decided to still perform frequency spectrum analyses on the installed and blown RSB signals, keeping in mind that the results might be affected by undesired phenomena. Note that the time-averaged results are not influenced by the possible eigenfrequency issue discussed above, since the additional harmonic component of the thrust signal should average out to zero when a sufficiently long measurement time is used.

5.4 Installed Configuration

The measurements performed using the powered propeller in the installed configuration served to assess the effects of installation on the pusher propeller performance. This section first discusses the time-averaged propeller performance (Subsection 5.4.1), followed by a frequency spectrum analysis of the corresponding thrust signals (Subsection 5.4.2).

5.4.1 Time-Averaged Propeller Performance

Based on the physics of the pylon - pusher propeller interaction effects it can be expected that the time-averaged thrust and torque increase in the installed configuration. When cutting through the pylon wake the propeller blades experience an increase in angle of attack resulting from the locally reduced inflow velocity. This leads to an increase in lift produced by the blade in the wake region, resulting in distinct peaks in the thrust and torque signals. This increase is partially offset by the reduction in dynamic pressure experienced in the pylon wake. However, numerical evaluations showed that the effect of the change in dynamic pressure is relatively small compared to that of the increase in angle of attack, hence the installed time-averaged thrust and torque are expected to be higher than the corresponding isolated values.

Figure 5.12 displays the time-averaged installed performance for a freestream velocity of 19 m/s. The isolated propeller performance at the corresponding velocity (see Figure 5.8) is also shown. Comparable results measured at 15 and 26 m/s are presented in Appendix C.2.3.

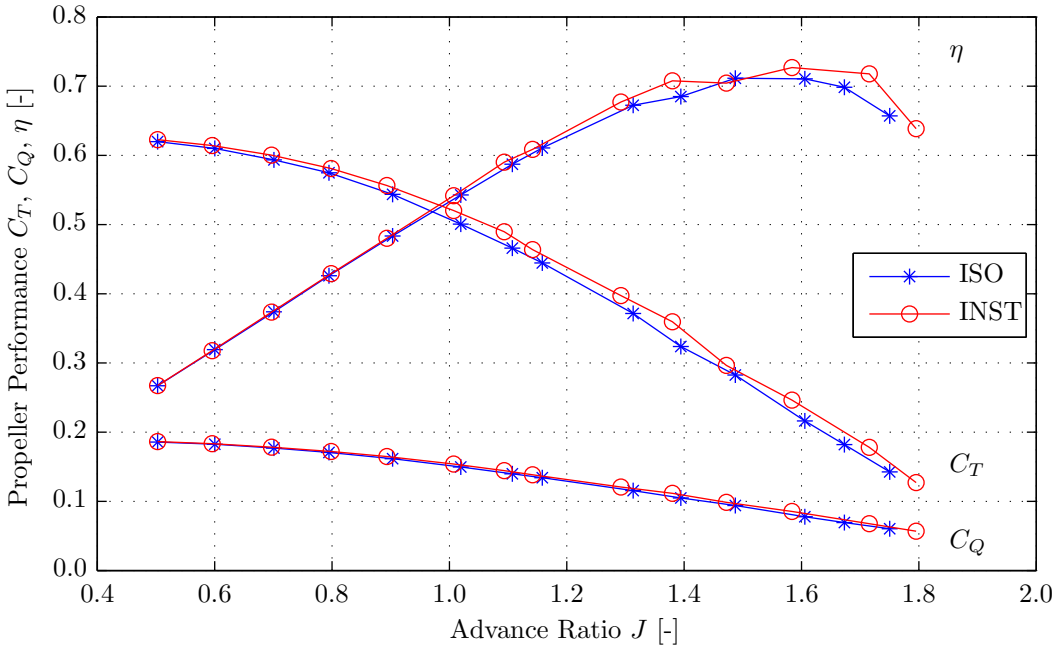

Figure 5.12: Propeller performance diagram: effects of installation.
Isolated and installed configurations, $U_\infty = 19$ m/s, $0.5 \leq J \leq 1.8$, $f_{\text{cut}} = 2,500$ Hz.

Figure 5.12 shows that for the selected data set the time-averaged thrust and torque coefficients display a small increase due to the installation effects. To analyze the installation effects in more detail the relative differences between the installed and isolated thrust and torque coefficients were computed for the data measured at freestream velocities of 15, 19, and 26 m/s. The results are presented in Figures 5.13 and 5.14, in which the approximate variability of the RSB measurements is indicated by the dashed black lines. Differences between the isolated and installed measurements which fall within the black lines should be considered as insignificant with respect to the accuracy of the RSB measurements.

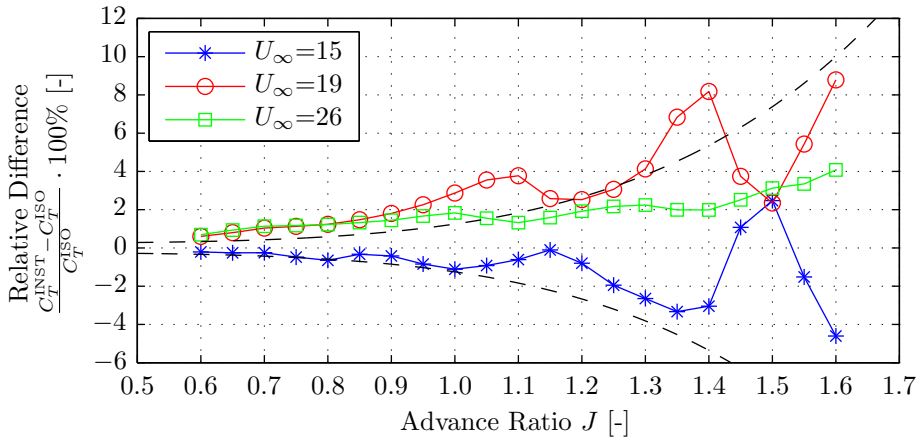

Figure 5.13: Relative effects of installation on the time-averaged thrust coefficient. Isolated and installed configurations, $U_\infty = [15, 19, 26]$ m/s, $0.6 \leq J \leq 1.6$, $f_{\text{cut}} = 2,500$ Hz.

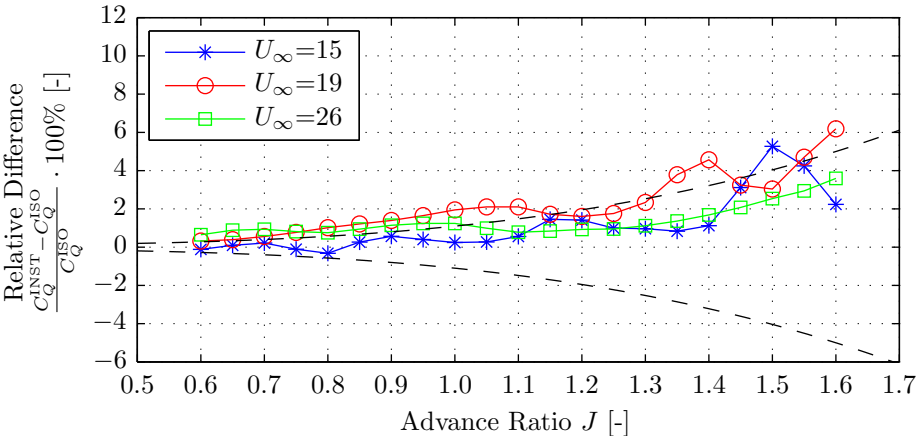

Figure 5.14: Relative effects of installation on the time-averaged torque coefficient. Isolated and installed configurations, $U_\infty = [15, 19, 26]$ m/s, $0.6 \leq J \leq 1.6$, $f_{\text{cut}} = 2,500$ Hz.

Figure 5.13 does not show a clear trend in the effects of installation on the thrust coefficient. The differences observed between the isolated and installed data are close to the expected variability of the RSB measurements. For freestream velocities of 19 and 26 m/s the thrust coefficient increases due to installation, with larger increases observed for higher advance ratios. In both cases the difference between the installed and isolated thrust is about 1% at $J = 0.6$. At the maximum advance ratio considered ($J = 1.6$) the difference has increased to about 8% for $U_\infty = 19$ m/s and 4% for $U_\infty = 26$ m/s. For $U_\infty = 15$ m/s on the other hand the thrust coefficient decreases when the pylon is placed in front of the propeller. At $J = 0.6$ the installed and isolated thrust coefficients are approximately equal, while at $J = 1.6$ a decrease in thrust coefficient of about 5% is observed in the installed configuration.

The time-averaged torque coefficient data displayed in Figure 5.14 on the other hand shows that for all three freestream velocities considered the installed torque coefficients are higher than the corresponding isolated values. Furthermore, for all data sets the increase becomes larger at higher advance ratios, which corresponds to the expected behavior. Again the measured differences are very close to the expected variability of the RSB measurements.

It is concluded that the time-averaged installed propeller performance results hint at relatively small increases in the thrust and torque coefficients due to the installation effects. However, it should be noted that especially for the thrust coefficient data the trend is not consistent, with varying results obtained at the three different freestream velocities considered. Furthermore, the observed differences between the time-averaged results in the isolated and installed configurations in general are close to the expected variability in the RSB measurements. To obtain more insight in the effects of installation the frequency spectra of the thrust and torque signals were analyzed, as discussed in the following subsection.

5.4.2 Frequency Spectrum Analysis of the Thrust and Torque Signals

It was mentioned previously that the installation effects are expected to result in clear increases in the thrust and torque power levels at frequencies equal to multiples of the BPF. Therefore, it was concluded that the installation effects could possibly be quantified by comparing the frequency spectra of the isolated and installed thrust and torque signals. Comparisons of the installed and isolated thrust power levels for half BPF multiples are presented in Figure 5.15. A similar plot for the torque signals did not provide any new insights, and is presented in Appendix C.2.3.

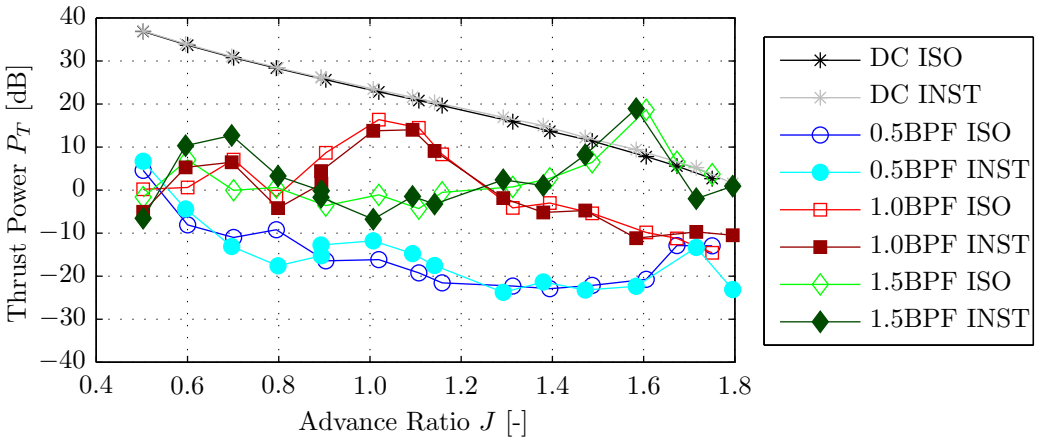

Figure 5.15: Comparison of the installed and isolated thrust power levels for half BPF multiples. Isolated and installed configurations, $U_\infty = 19$ m/s, $0.5 \leq J \leq 1.8$, $f_{\text{cut}} = 2,500$ Hz.

The isolated and installed thrust power levels presented in Figure 5.15 do not confirm the expected behavior for all advance ratios. At the lowest advance ratios the installed thrust power peak levels in general are higher than their isolated counterparts, thereby conforming to the expected trend. For the peaks corresponding to frequencies of 0.5BPF and 1.0BPF this is the case for advance ratios below around 0.7, while the installed level of the 1.5BPF peak remains above the isolated level for $J \leq 0.9$. At the higher advance ratios on the other hand the isolated and installed power peak levels are approximately equal.

Furthermore, it is observed that at all advance ratios the DC component of the installed thrust signal is higher than the corresponding isolated value. Combined with the small differences between the isolated and installed power peaks at non-zero frequency this indicates that the increase in the time-averaged thrust observed in Figure 5.12 was not the result of integrated time-dependent phenomena. Instead, it turns out to be a time-independent effect which might also have resulted from variability in the RSB measurements or other sources of measurement error. This is further confirmed by the previous finding that the measured changes in the thrust and torque coefficients due to the installation effects approximately fall within the variability of the RSB measurements. It should also be stressed again that the frequency contents of the isolated signal showed more and stronger power peaks at non-zero frequency than expected, as discussed in Subsection 5.3.2. This was attributed to a possible eigenfrequency issue, leading to harmonic vibrations of the RSB and associated measurement errors. If this hypothesis is correct, it is likely that the same phenomena have occurred during the installed measurements, thereby reducing the reliability of the thrust power spectra.

5.5 Blown Configuration

The propeller performance measurements in the blown configuration were performed to find out whether the application of pylon trailing edge blowing has an impact on the propeller performance. This section first details the time-averaged propeller performance in the blown configuration (Subsection 5.5.1). Thereafter, a frequency spectrum analysis of the measured thrust signal is presented (Subsection 5.5.2).

5.5.1 Time-Averaged Propeller Performance

The time-averaged propeller performance in the blown configuration for blowing rates of 400, 500, 600, and 680 L/min is presented in Figure 5.16. For reference, the results obtained in the isolated and installed configurations are also displayed. Similar propeller performance diagrams obtained at freestream velocities of 15 and 26 m/s are presented in Appendix C.2.4.

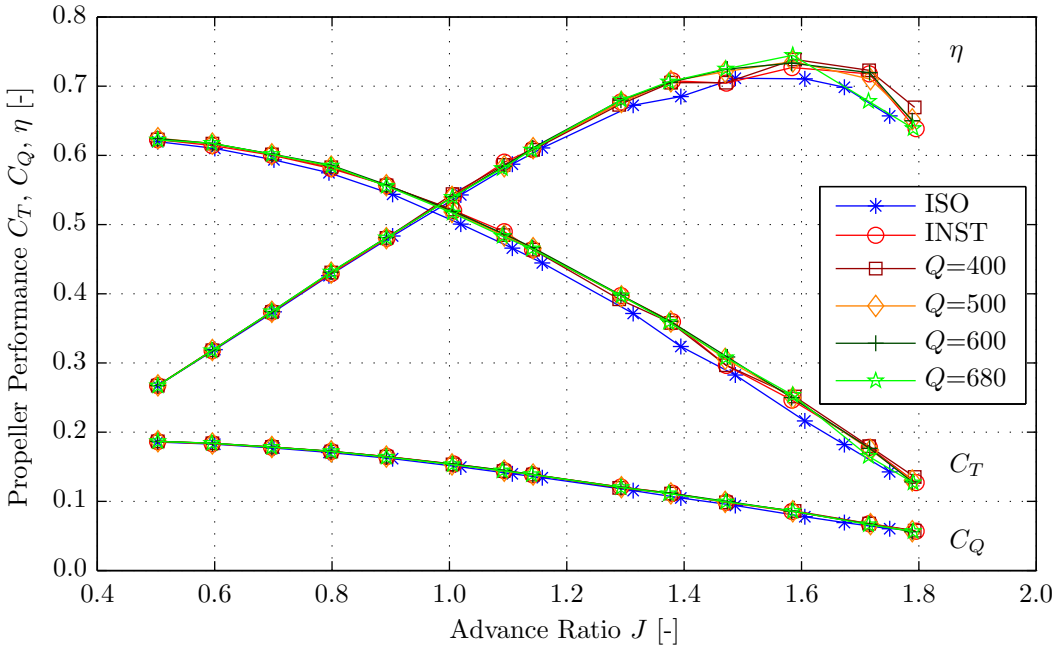

Figure 5.16: Propeller performance diagram: effects of blowing.
Isolated, installed, and blown configurations, $U_\infty = 19$ m/s, $0.5 \leq J \leq 1.8$, $f_{\text{cut}} = 2,500$ Hz.

Figure 5.16 does not show any clear effects of blowing on the time-averaged propeller performance. The blown results fall on top of the installed data, indicating that the measured effect of blowing is negligible. Only at high advance ratios minor differences start to occur in terms of the propeller efficiency. However, no consistent trend is apparent in the results, hence it is expected that these variations result from measurement errors. Also note that the isolated thrust coefficients are clearly lower than the installed and blown values, while the installed and blown results are approximately equal. Considering that the installed and blown results were obtained during a single measurement run, the explanation that the offset between the installed and isolated values is a result of measurement error is further confirmed.

A more detailed analysis of the differences between the installed and blown propeller performance was performed following the same approach as used in the discussion of the installed results. The data obtained at a freestream velocity of 19 m/s was selected, based on which the relative differences between the installed and blown interpolated estimates of the thrust and torque coefficients were computed. The results are depicted in Figures 5.17 and 5.18, in which the expected variability of the RSB measurements is indicated by the dashed black lines. Note that the same y-axis limits were selected as used in Figures 5.13 and 5.14.

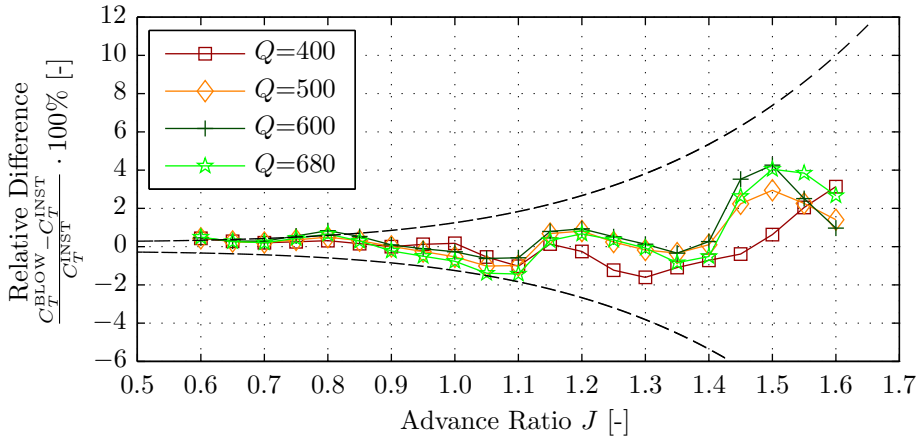

Figure 5.17: Relative differences between the installed and blown time-averaged thrust coefficients. Installed and blown configurations, $U_\infty = 19$ m/s, $0.6 \leq J \leq 1.6$, $f_{\mathrm{cut}} = 2,500$ Hz.

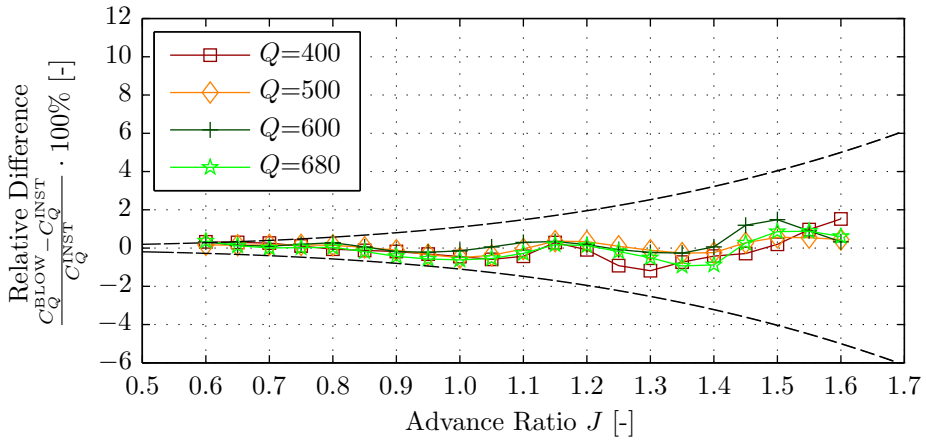

Figure 5.18: Relative differences between the installed and blown time-averaged torque coefficients. Installed and blown configurations, $U_\infty = 19$ m/s, $0.6 \leq J \leq 1.6$, $f_{\mathrm{cut}} = 2,500$ Hz.

Figures 5.17 and 5.18 confirm the conclusions drawn from Figure 5.16. The differences between the installed and blown thrust and torque coefficients fall within the expected variability of the RSB measurements for all advance ratios. Although not presented here, the differences between the installed and blown performance measured at freestream velocities of 15 m/s and 26 m/s showed similar trends as observed in the data obtained at 19 m/s. In conclusion, it can be stated that the time-averaged RSB data does not provide a clear picture of the effects of blowing on the propeller performance. It appears that the changes in performance observed with and without blowing are small. To gain additional understanding of the change in the propeller performance due to blowing the thrust and torque frequency spectra were inspected, as discussed in the following subsection.

5.5.2 Frequency Spectrum Analysis of the Thrust and Torque Signals

Frequency spectrum analysis was performed on the blown thrust and torque to complement the time-averaged performance evaluations presented in the previous subsection. In the blown configuration the velocity deficit in the pylon wake is decreased, thereby decreasing the change in the angle of attack and dynamic pressure experienced by the propeller blades when cutting through the pylon wake. Therefore, in theory the peaks in the frequency spectra of the thrust and torque signals should be lower in the blown configuration than in installed conditions.

The blown thrust and torque power levels were computed using the same approach as described in Subsections 5.3.2 and 5.4.2. For overview reasons, only the thrust power spectrum obtained at 19 m/s and a blowing rate of 680 L/min is presented below. The torque spectrum is presented in Appendix C.2.4, but did not provide any new insights.

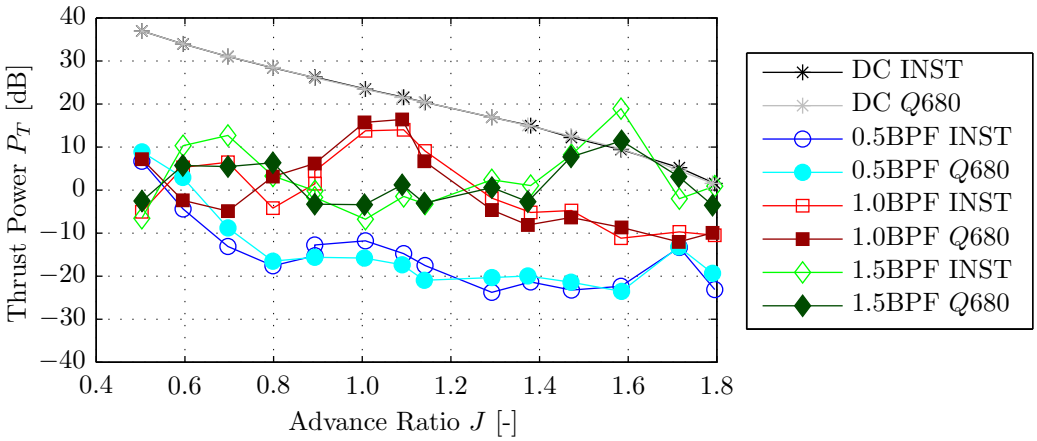

Figure 5.19: Comparison of the blown and installed thrust power levels for half BPF multiples. Installed and blown configurations, $U_\infty = 19$ m/s, $0.5 \leq J \leq 1.8$, $f_{\text{cut}} = 2,500$ Hz.

From Figure 5.19 no clear conclusions can be drawn. For the three BPF multiples considered, the blown thrust power levels are alternately lower and higher than the corresponding installed levels. Combined with the previous discussion of the frequency contents of the thrust and torque signals in the isolated and installed configurations, it is therefore concluded that the signal quality of the RSB data is insufficient to accurately measure the effects of installation and blowing on the measured propeller performance.

Chapter 6

Experimental Results: Powered Propeller Noise Emissions

The powered propeller noise measurements aimed at quantifying the possible reductions in noise emissions which could be achieved using the pylon blowing system. This chapter starts with Section 6.1 which presents an overview of the characteristics of the measurements. Before presenting the results of the actual measurements, first their signal quality and reproducibility are assessed in Section 6.2. Thereafter, Section 6.3 discusses the powered propeller noise emissions in the isolated configuration. Subsequently, the measurements performed in the installed configuration are treated in Section 6.4, followed by those executed in blown conditions in Section 6.5.

6.1 Measurement Overview

The main characteristics of the powered propeller noise measurements are given in Table 6.1.

Table 6.1: Overview of the characteristics of the powered propeller noise measurements.

Parameter	**Symbol**	**Value**	**Unit**
Freestream velocity	U_∞	19	m/s
Advance Ratio	J	$0.5 \leq J \leq 1.8$	-
Blowing rate	Q	[0,400,500,600,660][1]	L/min
Pylon-propeller spacing	ΔX	114	mm
Pylon angle of attack	α	0	deg
Microphone sideline distance	y	2.2	m
Microphone directivity angle	θ_{mic}	110[2]	deg
Sampling frequency	f_s	50	kHz
Measurement time	t_m	15	s
Average factor Welch's method	K	45	-

Except for the sound spectra all data presented in this chapter is corrected for shear layer refraction effects and scaled to a constant radius of 1.0 m.

[1]The highest blowing rate was limited to 660 L/min due to air supply pressure constraints.
[2]The isolated measurements were also performed at directivity angles of 90 and 130 degrees.

6.2 Signal Quality and Reproducibility of the Results

To assess the signal quality of the powered propeller noise measurements a similar approach was taken as applied for the unpowered propeller measurements discussed in Chapter 4. A number of measurements were performed consecutively at constant wind tunnel setting and propeller operating point. The reproducibility of the SPL of the first six BPF tones measured at a freestream velocity of 19 m/s, an advance ratio of 1.1, and a microphone angle of 110 degrees is depicted in Figure 6.1. The corresponding differences between the individual SPLs obtained from both measurements and the resulting mean values are shown in Figure 6.2.

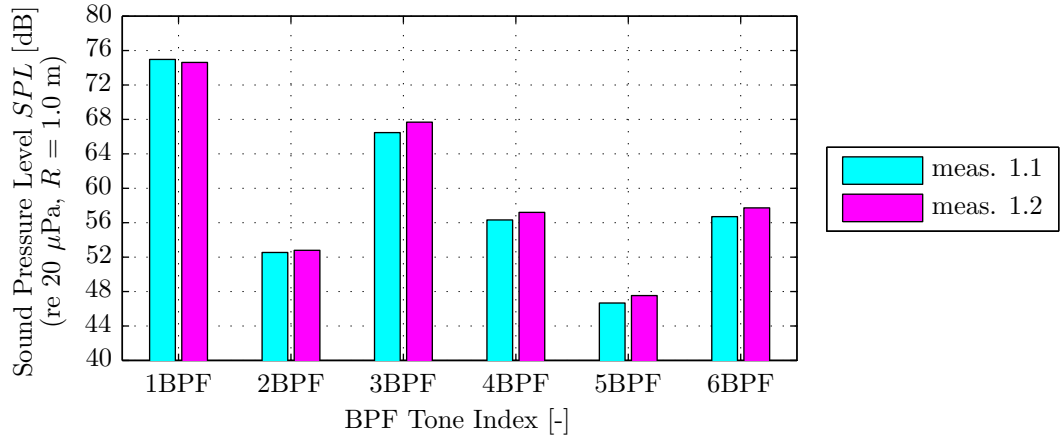

Figure 6.1: Reproducibility of consecutive powered propeller noise measurements. Isolated configuration, $U_\infty = 19$ m/s, $J = 1.1$, $\theta_{\text{mic}} = 110°$, $K = 45$.

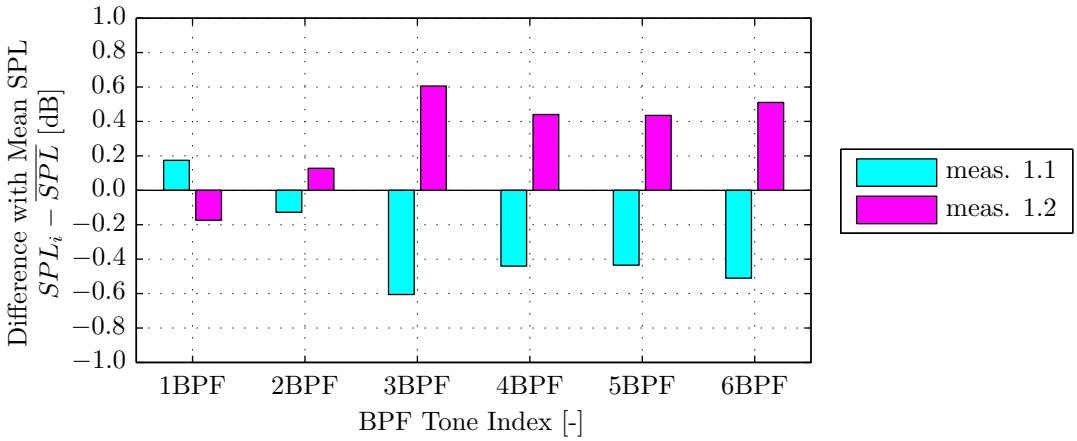

Figure 6.2: Variability of consecutive powered propeller noise measurements. Isolated configuration, $U_\infty = 19$ m/s, $J = 1.1$, $\theta_{\text{mic}} = 110°$, $K = 45$.

Figures 6.1 and 6.2 show that the variability of consecutive powered propeller noise measurements performed at constant operating conditions is within ±1 dB. Variations in this range will be considered as insignificant during the comparisons between the installed and blown noise levels discussed in Section 6.5. The same results were obtained from the measurements performed at the other advance ratios considered ($0.5 \leq J \leq 1.8$). Note that the variability of the unpowered propeller noise measurements also equaled ±1 dB.

The reproducibility of nonconsecutive measurements was evaluated by performing four additional measurements at $U_\infty = 19$ m/s and $J = 1.1$. The first two additional measurements (2.1 and 2.2) were executed during the same run as measurements 1.1 and 1.2 shown in Figures

6.1 and 6.2. Subsequently, the propeller was stopped and restarted to perform measurements 3.1 and 3.2. The measured sound pressure levels of the first six BPF tones are plotted in Figure 6.3, followed by Figure 6.4 displaying the differences with the mean values.

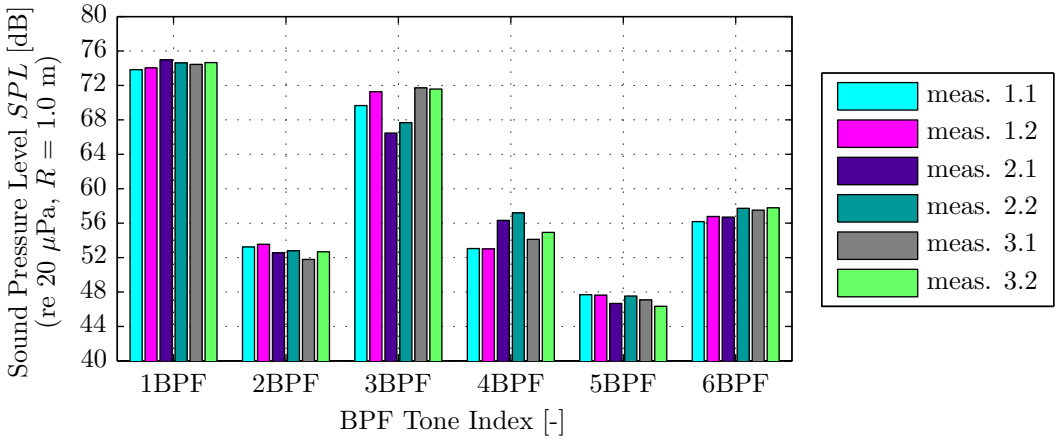

Figure 6.3: Reproducibility of nonconsecutive powered propeller noise measurements. Isolated configuration, $U_\infty = 19$ m/s, $J = 1.1$, $\theta_{\text{mic}} = 110°$, $K = 45$.

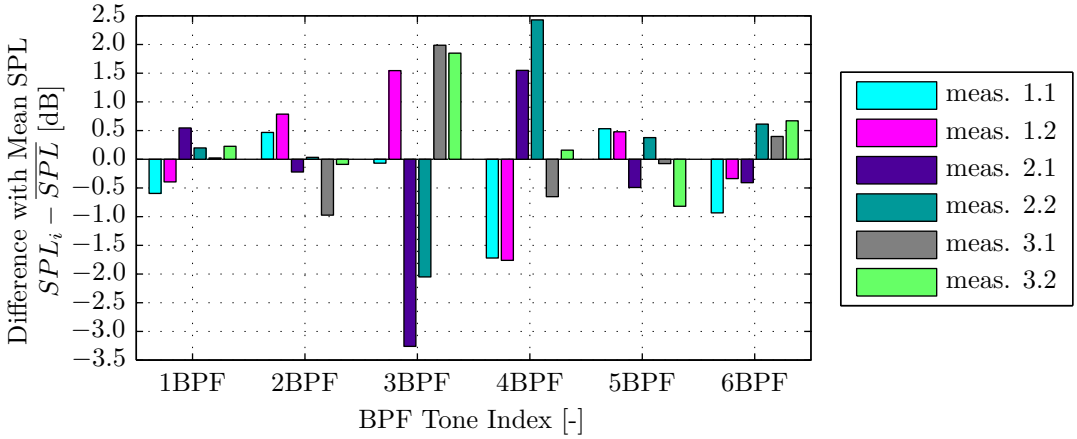

Figure 6.4: Variability of nonconsecutive powered propeller noise measurements. Isolated configuration, $U_\infty = 19$ m/s, $J = 1.1$, $\theta_{\text{mic}} = 110°$, $K = 45$.

Figures 6.3 and 6.4 show that the reproducibility of nonconsecutive measurements is worse than for measurements performed in direct succession. For the higher BPF tones differences of up to ±3 dB with the mean value are seen. This should be taken into account when comparing the isolated and installed results which were performed nonconsecutively.

6.3 Isolated Configuration

The isolated propeller noise measurements served as a baseline for comparison with the installed and blown results. The recorded microphone data was converted into sound spectra (Subsection 6.3.1) and tonal noise levels (Subsection 6.3.2).

6.3.1 Propeller Noise Spectrum

The isolated sound spectrum measured at a velocity of 19 m/s and an advance ratio of $J = 0.9$ is shown in Figure 6.5. The dashed black lines indicate integer multiples of the propeller BPF, while the dashed magenta lines correspond to the first two tones of the wind tunnel fan. The asterisks indicate the maximum tonal noise levels at integer multiples of the propeller's BPF.

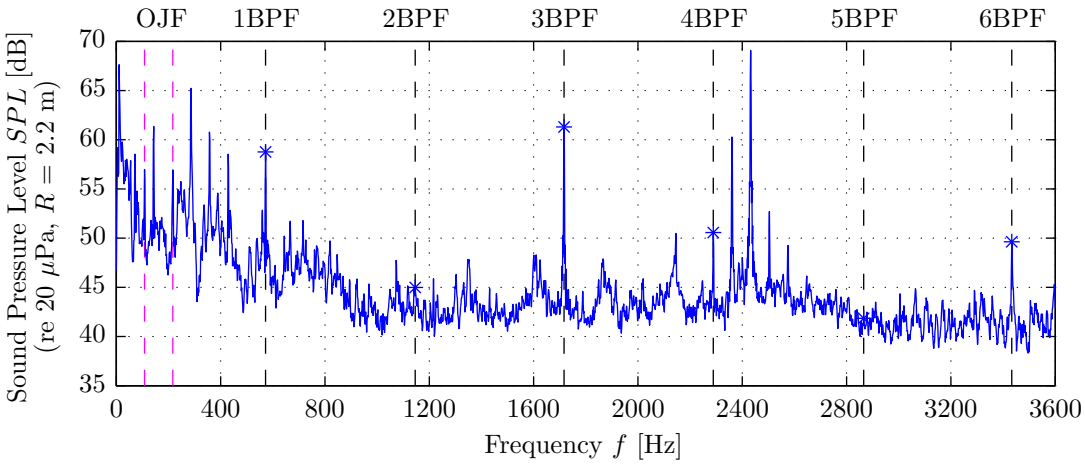

Figure 6.5: Powered propeller noise spectrum.
Isolated configuration, $U_\infty = 19$ m/s, $J = 0.9$, $\theta_{\text{mic}} = 110°$, $K = 45$.

Figure 6.5 shows that the propeller noise displays a number of dominant tonal components at multiples of the BPF. Peaks are observed at frequencies corresponding to the 1BPF, 3BPF, 4BPF, and 6BPF. For the measurement point displayed in Figure 6.5 the 3BPF tone is the loudest propeller tone. Furthermore, it is seen that tonal noise is also present at frequencies corresponding to integer multiples of individual blade passages. Two strong peaks are seen around 2,400 Hz; these correspond to the noise emitted by the motor used to power the propeller. Note that at low advance ratios (i.e. high RPM) the SPL of the motor's tonal noise is louder than that of the propeller tones. However, considering the high frequencies of the motor's noise emissions this is not expected to affect the propeller noise measurements.

The fact that the SPL of the 3BPF tone is larger than the SPL corresponding to the 1BPF tone is an unexpected result, since typically the 1BPF tone dominates the isolated propeller noise emissions (especially when the blade number is large). The relatively large amplitude of the 3BPF tone might be the result of non-uniformities in the propeller inflow, for example introduced by interactions with the downstream support strut of the propeller model.

It was already mentioned that a number of unexpected peaks are present at frequencies below the 1BPF, corresponding to tonal noise at non-integer multiples of the BPF. For overview reasons, Figure 6.6 presents a close-up of the low frequency content of the sound spectrum displayed in Figure 6.5. The black dashed lines indicate multiples of a single blade passage (BPF/8), while magenta dashed lines are again plotted at the first two BPF multiples corresponding to the wind tunnel fan. For completeness the results are presented for all three microphone directivity angles considered (90, 110, and 130 degrees).

From Figure 6.6 it is observed that tonal noise components are measured at a frequency corresponding to a single blade passage ($f = BPF/B = 0.125BPF$) and all subsequent multiples up to 1BPF, except for $\frac{7}{8}$BPF. The tones are most pronounced at microphone angles of 90 and 110 degrees, while at 130 degrees a number of the tones have disappeared. The reason for the strong tonal noise components at frequencies below the BPF should be related to an asymmetry in the propeller, for example due to variations in the pitch angles of the individual propeller blades. Note that due to the presence of the unexpected tonal noise components below the 1BPF frequency the measured SPL of the 1BPF tone shown in Figures 6.5 and 6.6 is lower than the SPL that would have been measured in the ideal case.

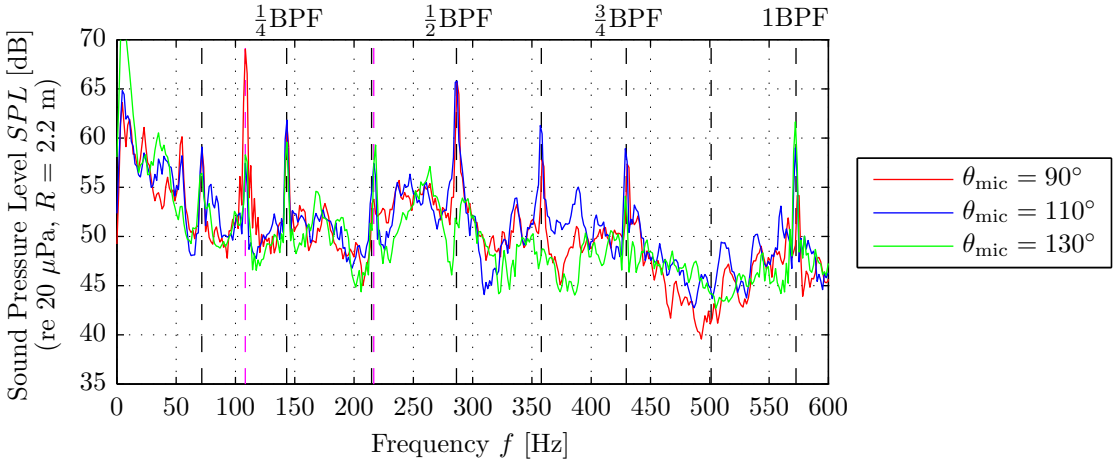

Figure 6.6: Low-frequency contents of the powered propeller noise spectrum. Isolated configuration, $U_\infty = 19$ m/s, $J = 0.9$, $\theta_{\text{mic}} = [90, 110, 130]°$, $K = 45$.

Analysis of the sound spectra obtained at all considered advance ratios showed that the relative SPL of the unexpected tones at frequencies below the fundamental BPF depends on the RPM of the propeller. As an example, a close-up of the propeller sound spectrum measured at an advance ratio of $J = 1.1$ is depicted in Figure 6.7.

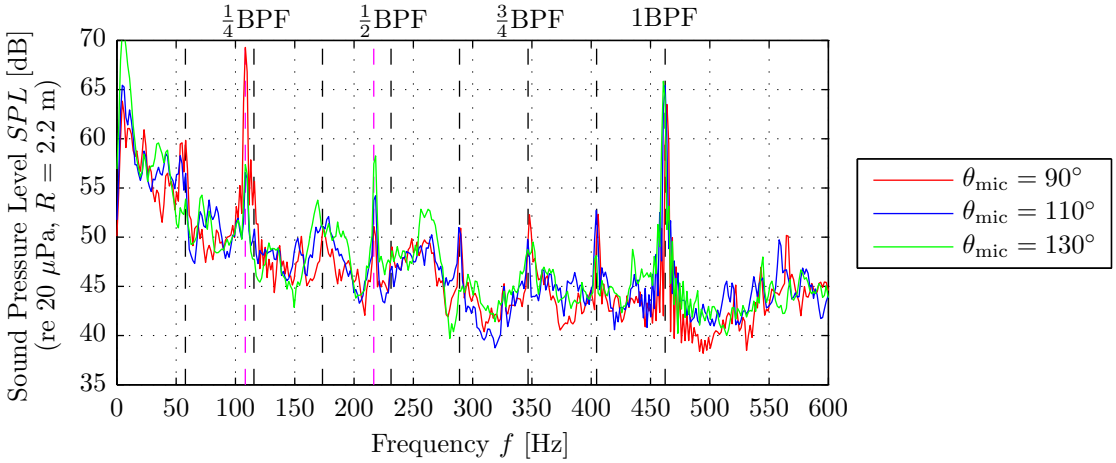

Figure 6.7: Low-frequency contents of the powered propeller noise spectrum. Isolated configuration, $U_\infty = 19$ m/s, $J = 1.1$, $\theta_{\text{mic}} = [90, 110, 130]°$, $K = 45$.

Figure 6.7 shows that at $J = 1.1$ the intensity of the low frequency tones is reduced significantly when compared to the data obtained at an advance ratio of 0.9. Although still present, now the tones below the 1BPF are characterized by an SPL which is much lower than that of the 1BPF tone itself. Similar results (i.e. the absence of strong tonal noise components at $\frac{n}{8}$BPF) were observed for all advance ratios above $J = 1.1$ and at $J = 0.6$. In the range $0.7 \leq J \leq 1.0$ on the other hand the low frequency tones are clearly present. Considering this RPM dependency, it is concluded that the tonal noise components below the fundamental BPF could also be the result of vibrations of the propeller. To be able to draw more detailed conclusions about the exact phenomena which led to the unexpected tonal components in the range of $0.7 \leq J \leq 1.0$ more detailed analyses would be required, for example using flow visualization techniques or noise source localization methods.

6.3.2 Propeller Tonal Noise Levels

From the sound spectrum displayed in Figure 6.5 it was concluded that the noise emissions of the powered propeller model are mostly of tonal nature. To analyze the tonal components of the noise emissions in more detail, the sound pressure levels of the first three BPF tones were extracted from the sound spectra. The tones at frequencies below 1BPF were not considered. The resulting tonal noise levels are plotted versus the advance ratio in Figure 6.8.

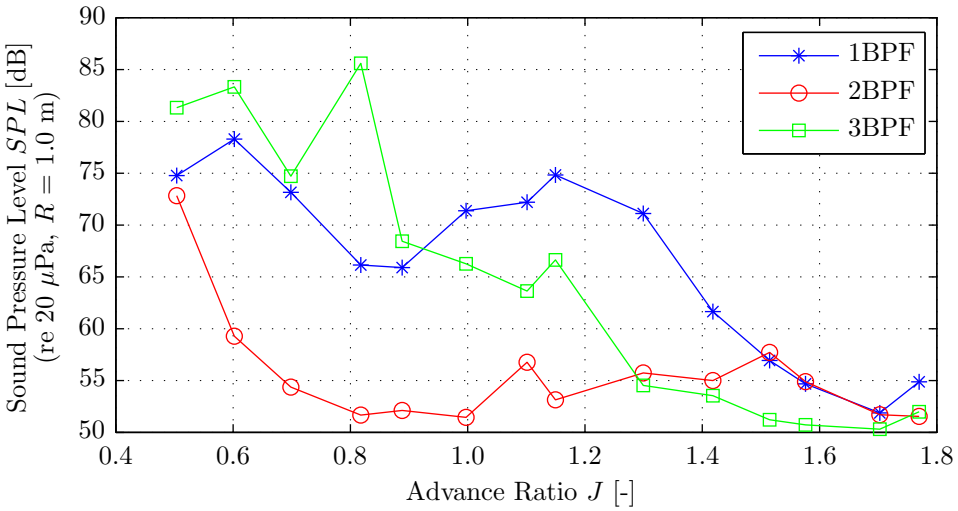

Figure 6.8: Powered propeller tonal noise levels versus the advance ratio.
Isolated configuration, $U_\infty = 19$ m/s, $0.5 \leq J \leq 1.8$, $\theta_{\text{mic}} = 110°$, $K = 45$.

From Figure 6.8 it is observed that in general the tonal SPL increases with decreasing advance ratio. This is as expected considering the larger tip Mach numbers and blade loads occurring at lower advance ratios, resulting in an increase in the thickness and loading noise. For the advance ratio range of $0.7 \leq J \leq 1.1$ the SPL of the 1BPF tone displays a local minimum. Note that this approximately corresponds to the range indicated before in which tonal noise was observed at multiples of the individual blade passages. As a result, at these advance ratios less acoustic energy is emitted at the 1BPF tone, hence its SPL is lower than expected.

Furthermore, Figure 6.8 shows that the tones corresponding to higher multiples of the BPF (2BPF, 3BPF) start to become relevant at the low advance ratios. For advance ratios between 1.0 and 1.4 in general the SPL of the 1BPF tone is at least 5 dB higher than that of the 2BPF and 3BPF tones. Below $J = 1.0$ on the other hand the SPL of the 3BPF tone increases rapidly, making it even louder than the fundamental tone emitted at 1BPF. The 2BPF tone remains insignificant for advance ratios above 0.6, while for $J = 0.5$ it is almost as loud as the 1BPF tone. For advance ratios below $J = 1.0$ the relative sound pressure level of the 3BPF tone is higher than expected compared to the SPL of the 1BPF tone. Whereas normally for an isolated propeller the 1BPF tone clearly dominates the other tones, from Figure 6.8 it is observed that for these advance ratios the SPL of the 3BPF even becomes higher than that of the 1BPF tone. Although this can partially be attributed to the reduction in the SPL of the 1BPF tone due to the tonal noise emissions at multiples of individual blade passage frequencies, the SPL of the 3BPF tone is still higher than expected. More information of the flow field is required to draw detailed conclusions on the actual mechanism behind the sound generation of the 3BPF tone. However, as mentioned before it is expected that the relatively high levels are the result of non-uniformities in the propeller inflow, for example due to interactions with the propeller's support strut.

6.4 Installed Configuration

In the installed configuration the inflow at the propeller disk becomes non-uniform due to the wake shed by the upstream pylon. As a result, the propeller blades experience a time-dependent blade loading which results in unsteady loading noise. This section first presents the installed propeller noise spectrum (Subsection 6.4.1). Subsequently, the tonal noise levels are discussed (Subsection 6.4.2). In both cases comparisons are made with the data obtained using the powered propeller model in the isolated configuration. To reduce the variability in the installed propeller noise data at all considered advance ratios at least one repeat measurement was performed. The results presented in this section consider the sound pressure levels averaged over all available measurements for each advance ratio considered.

6.4.1 Propeller Noise Spectrum

The installed propeller's noise spectrum measured at $U_\infty = 19$ m/s and $J = 0.9$ is depicted in Figure 6.9. For reference, the corresponding sound spectrum of the propeller in the isolated configuration is added as well. Note that the installed measurements were performed at an RPM about 70 lower than that used for the isolated measurements, resulting in an offset in the frequency corresponding to 1BPF of approximately 9 Hz. Again the black dashed vertical lines indicate multiples of the propeller BPF (based on the average RPM of the isolated and installed measurements), while the magenta dashed lines correspond to the frequencies of the first two BPF tones of the wind tunnel fan. The asterisks indicate the position of the maximum tonal noise emissions at integer multiples of the propeller BPF.

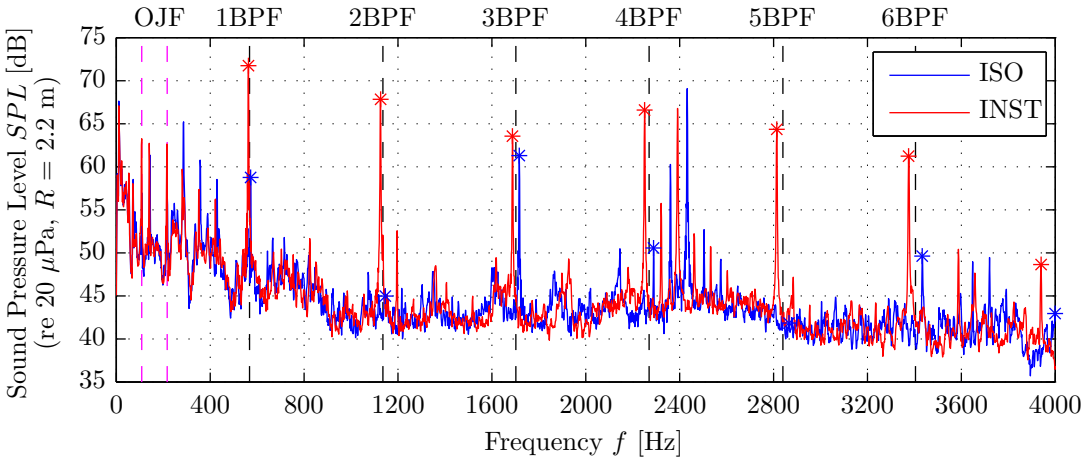

Figure 6.9: Powered propeller noise spectrum: effects of installation.
Isolated and installed configurations, $U_\infty = 19$ m/s, $J = 0.9$, $\theta_{\text{mic}} = 110°$, $K = 45$.

Figure 6.9 shows that the noise emissions of the propeller clearly increase due to the installation effects. The SPL of all BPF multiples is larger in the installed configuration than in isolated conditions, with tonal noise peaks at all of the first six BPF multiples. The broadband noise emissions are unaffected by the installation of the pylon upstream of the propeller.

The increase due to the installation effects of the SPL of the higher harmonics is as expected since for these harmonics the radiation efficiency of the noise emissions due to the unsteady loading is much higher than that of the steady loading noise emissions [49]. The installation effect is observed in all BPF multiples since the disturbance introduced by the pylon wake is asymmetric, hence the unsteady lift component is present in both the odd and even harmonics.

It is also observed that the SPL of the tonal components at frequencies below 1BPF is lower in installed conditions. It is unclear whether this can be attributed to the installation effects or that it is the result of the small RPM offset between the isolated and installed measurements. Inspection of the sound spectra measured at the other advance ratios learned that in most cases the tonal noise levels at frequencies below the 1BPF were approximately equal in the isolated and installed configurations, and occurred over the same advance ratio range.

6.4.2 Propeller Tonal Noise Levels

The sound spectra of the propeller noise emissions in the installed and isolated configurations showed that the tonal noise emissions of the powered propeller clearly increase due to the installation effects, while the broadband levels are unaffected. To gain more insight in the effects of installation, Figure 6.10 presents the sound pressure levels of the first six BPF tones measured in the isolated and installed configurations at the same operating point as considered in Figure 6.9 ($U_\infty = 19$ m/s and $J = 0.9$).

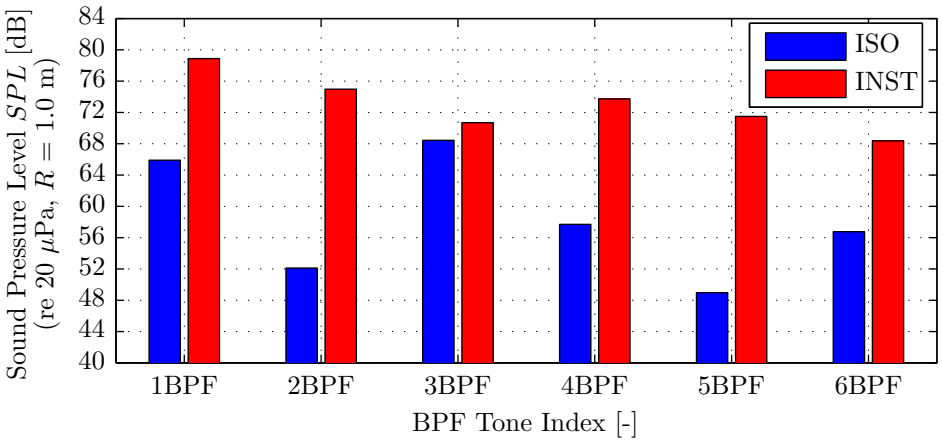

Figure 6.10: Powered propeller tonal noise levels: effects of installation. Isolated and installed configurations, $U_\infty = 19$ m/s, $J = 0.9$, $\theta_{\text{mic}} = 110°$, $K = 45$.

From Figure 6.10 it is observed that at a freestream velocity of 19 m/s and an advance ratio of $J = 0.9$ the installation effects result in a noise penalty of about 13 dB for the 1BPF tone. The 2BPF tone increases by as much as 23 dB, while the increase in the SPL of the 3BPF tone is much smaller at approximately 2 dB. For the higher BPF multiples increases of the order of 10-25 dB are observed. It should be stressed once more that the noise measurements in the isolated and installed configurations were performed nonconsecutively. As discussed in Section 6.2 this results in an increased measurement variability, hence reducing the accuracy of comparisons involving the measurements performed in isolated and installed conditions.

So far, the assessment of the noise penalty due to the installation effects focused on a single propeller operating point. To extend the analysis to other operating conditions Figure 6.11 presents the SPL of the first three BPF tones for all advance ratios considered.

Figure 6.11 shows that in the installed configuration in general the SPL of the first three BPF tones is of the same order for the entire advance ratio range. This clearly differs from the isolated case for which at high advance ratios the 1BPF tone dominated the sound spectrum. Furthermore, the expected increasing trend is recognized in the sound pressure levels of the tones with decreasing advance ratio. The variations in the sound pressure levels at successive advance ratios observed in Figure 6.11 are rather large, possibly resulting from variability in the noise measurements.

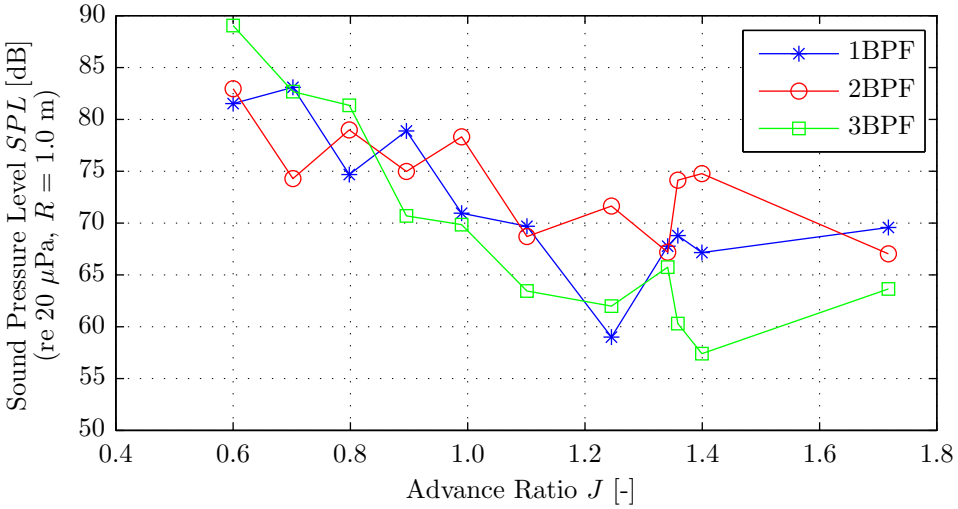

Figure 6.11: Powered propeller tonal noise levels versus the advance ratio. Installed configuration, $U_\infty = 19$ m/s, $0.6 \leq J \leq 1.7$, $\theta_{\text{mic}} = 110°$, $K = 45$.

To compare the results presented in Figure 6.11 to the isolated case treated in Figure 6.8 the measured noise penalty due to the installation effects is presented in Figure 6.12 as a function of the advance ratio. The test matrix used for the installed measurements contained less advance ratios than considered in the isolated evaluations. Figure 6.12 only displays those measurement points which were performed at the same advance ratio in both configurations.

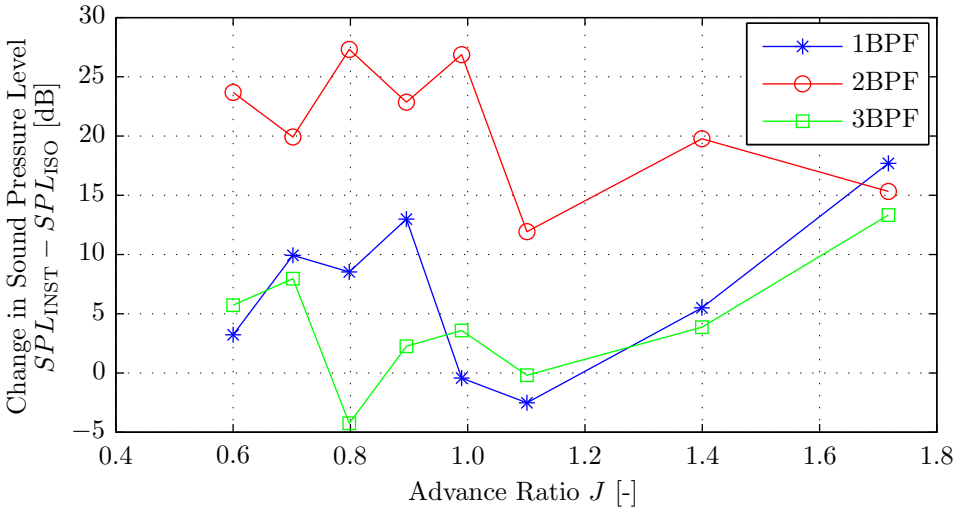

Figure 6.12: Change in the tonal noise levels due to installation versus the advance ratio. Isolated and installed configurations, $U_\infty = 19$ m/s, $0.6 \leq J \leq 1.7$, $\theta_{\text{mic}} = 110°$, $K = 45$.

Figure 6.12 shows that at the highest advance ratio considered ($J = 1.7$) the noise penalty due to the installation effects is large, with increases in the SPL of about 15 dB for the first three BPF tones. Upon decreasing the advance ratio a decreasing trend is observed in the noise penalty due to installation for the 1BPF and 3BPF tones. At an advance ratio of around $J = 1.2$ the noise penalty becomes approximately zero for these two tones, after which at an advance ratio of $J = 1.1$ for the 1BPF tone in the installed configuration even a noise reduction is seen of about 2.5 dB. It is expected that this is the result of cancellation of the sound fields associated with the steady and unsteady blade loads. This has also been observed in the literature on various occasions in both experimental and numerical studies [24, 50].

For advance ratios below $J = 1.1$ the noise penalty due to installation starts to increase again, reaching a level of about 10 dB for the 1BPF tone for advance ratios between 0.7 and 0.9. The 3BPF tone on the other hand shows an additional minimum at $J = 0.8$ with a noise reduction in the installed configuration of 5 dB, after which the change in the SPL due to installation becomes positive again for even lower advance ratios. At the lowest advance ratios considered, for the 1BPF tone the change in the SPL due to installation decreases again. It is expected that this is the result of increased noise levels due to steady loading, which then dominate the noise emissions at directivity angles close to the propeller plane.

The 2BPF tone remains much louder in the installed configuration than in isolated conditions over the entire advance ratio range. In the isolated configuration the 2BPF tone did not stand out from the background noise level for any of the advance ratios considered. In the installed configuration on the other hand it is clearly measured, hence resulting in a large noise penalty due to installation effects.

6.5 Blown Configuration

Application of the pylon blowing system should partially fill up the pylon wake, thereby reducing the noise penalty due to the installation effects. Throughout this section the blown results are compared to their unblown installed counterparts. To increase the accuracy of the comparisons the installed and blown noise measurements were performed consecutively. Following the lay-out of the previous sections, first the propeller noise spectrum is presented (Subsection 6.5.1). Thereafter, the tonal noise emissions are analyzed (Subsection 6.5.2).

6.5.1 Propeller Noise Spectrum

The sound spectrum of the noise emitted by the propeller in the isolated, installed, and blown configurations at a freestream velocity of 19 m/s and an advance ratio of 0.9 is presented in Figure 6.13. The blown measurement was performed using the maximum achievable blowing rate of 660 L/min, while the isolated and installed data correspond to those displayed before in Figures 6.5 and 6.9.

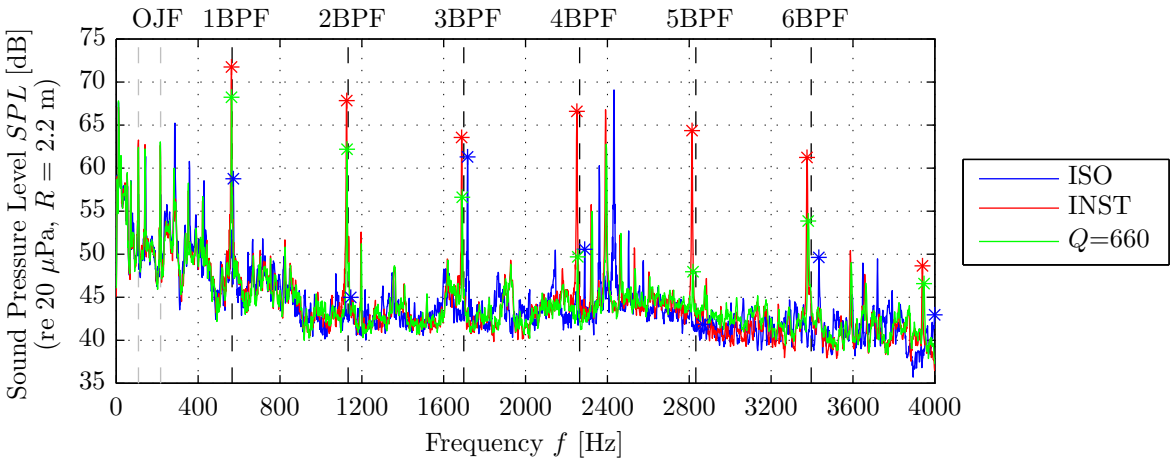

Figure 6.13: Powered propeller noise spectrum: effects of blowing.
Isolated, installed, and blown configurations, $U_\infty = 19$ m/s, $J = 0.9$, $\theta_{\text{mic}} = 110°$, $K = 45$.

From Figure 6.13 it is observed that for the considered combination of propeller operating point and blowing rate the application of pylon blowing indeed reduces the propeller noise emissions. For all tones the SPL in the blown configuration is lower than in the installed configuration, while in most cases the isolated level is even lower. Furthermore, for the operating point considered in Figure 6.13 the broadband noise levels are unaffected by the blowing system. For advance ratios above $J = 1.3$, for which the propeller broadband emissions have a lower SPL, the application of the blowing system resulted in an increase in broadband noise levels of at maximum 5 dB at frequencies of about 2,500-4,000 Hz. The absolute level of the corresponding sound was however much lower than that of the propeller tones.

6.5.2 Propeller Tonal Noise Levels

Figure 6.14 displays the SPL of the first six propeller tones for the range of blowing rates considered, together with the corresponding installed result. The data was again obtained at a freestream velocity of 19 m/s and an advance ratio of $J = 0.9$, hence corresponding to the sound spectrum displayed in Figure 6.13. The resulting differences between the blown and installed sound pressure levels are plotted in Figure 6.15. The dashed yellow lines in Figure 6.15 indicate the expected variability of the consecutively performed measurements (±1 dB).

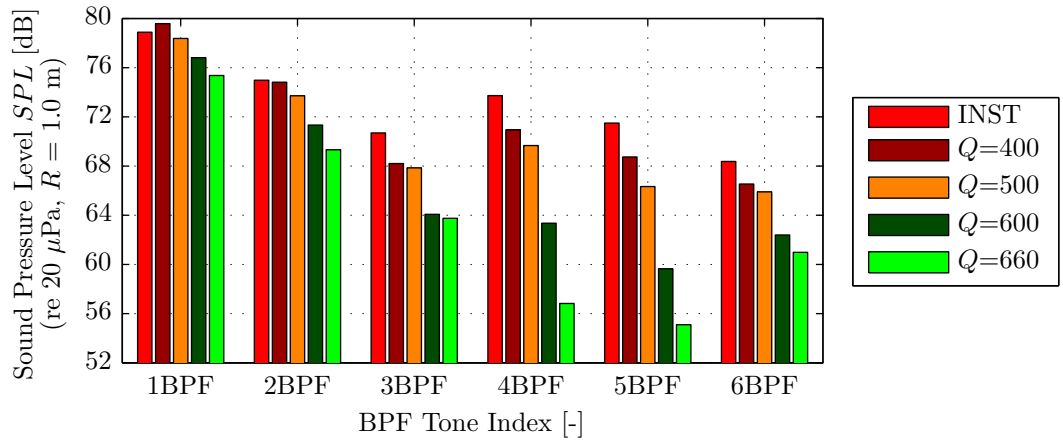

Figure 6.14: Powered propeller tonal noise levels: effects of blowing.
Installed and blown configurations, $U_\infty = 19$ m/s, $J = 0.9$, $\theta_{\text{mic}} = 110°$, $K = 45$.

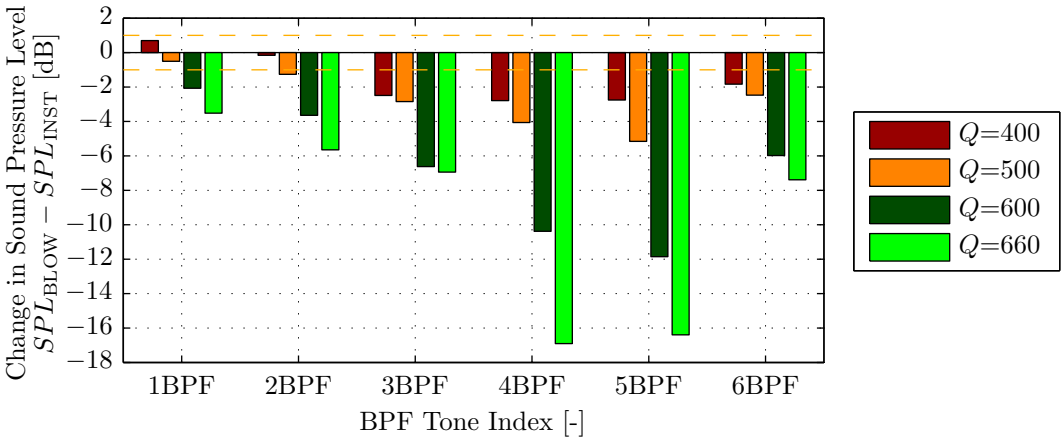

Figure 6.15: Tonal noise reduction due to blowing: effects of the blowing rate.
Blown configuration, $U_\infty = 19$ m/s, $J = 0.9$, $\theta_{\text{mic}} = 110°$, $K = 45$.

Figures 6.14 and 6.15 show that the application of blowing reduces the sound pressure levels of the BPF tones for all but one of the blowing rates considered. The SPL of the propeller tones decreases with increasing blowing rate, with the reductions becoming significant for all six tones at the blowing rates of 600 and 660 L/min. When blowing at the maximum rate of 660 L/min the 1BPF tone is reduced by almost 4 dB, while the reductions for the higher BPF multiples are even larger. The SPL of the 2BPF and 3BPF tones is reduced by 6 dB and 7 dB, respectively, while the 4BPF and 5BPF tones are essentially eliminated with reductions of around 16 dB. For the tone corresponding to 6BPF the SPL is decreased by around 7 dB.

Considering the wake profiles presented in Subsection 3.4.2 and the evolution of the integrated wake velocity deficit with the blowing rate shown in Figure 3.9 it might be surprising that the noise emissions at $Q = 660$ L/min are lower than those measured at blowing rates of 500 and 600 L/min. For the latter two blowing rates the value of the integral wake velocity deficit displayed a global minimum. At a blowing rate of $Q = 660$ L/min on the other hand the application of blowing resulted in the introduction of a jet with higher than freestream velocity in the center of the wake region. This basically reverses the installation effect compared to the situation in which a velocity deficit is present. Now the propeller blades rotate through a region of increased inflow velocity, resulting in a local decrease of the angle of attack and increase of the dynamic pressure experienced by the blades. This in turn is expected to result in temporarily decreased blade loads, hence a reduction in the loading noise emissions. Although in this case blade load fluctuations are still present, the reduced absolute blade loading might in the end reduce the overall sound pressure level of the propeller tones.

Another explanation for the observed maximum in the noise reductions due to blowing at a blowing rate of $Q = 660$ L/min can be found by noting again that the wake profile measurements discussed in Chapter 3 were performed using the isolated pylon model. It was mentioned previously that this is not expected to affect the non-dimensional wake velocity profiles to a significant extent. However, it was observed before in Chapters 3 and 4 that the effectiveness of the blowing system reduces with increasing external flow velocity. As a result, it is concluded that it might be the case that the locally increased velocities ahead of the thrusting propeller demand a higher blowing rate to fill up the pylon wake than required for the isolated case. As such, it might be possible that in powered conditions the wake profile at the propeller plane shows a minimum integral velocity deficit for a blowing rate of 660 L/min, thereby explaining the best performance at this blowing rate. To test this hypothesis wake surveys should be performed with the rotating propeller present behind the pylon.

It is expected that there exists a certain blowing rate for which the noise reductions due to blowing display a maximum, after which the noise levels increase again for higher blowing rates. Considering that the noise levels continued to decrease with increasing blowing rate for all blowing rates considered, it is concluded that the optimum blowing rate might not have been reached. Additional tests should be performed at higher blowing rates to verify this.

Until now the effects of blowing on the sound pressure levels of the propeller BPF tones focused on a single propeller operating condition ($J = 0.9$). To assess the effects at other advance ratios the sound pressure levels of the first three propeller tones were extracted from the sound spectra for all other operating points considered. The results are presented in Figures 6.16, 6.17, and 6.18, displaying the change in the SPL due to blowing versus the advance ratio for the 1BPF, 2BPF, and 3BPF tone, respectively. The dashed yellow lines again indicate the expected measurement variability (± 1 dB).

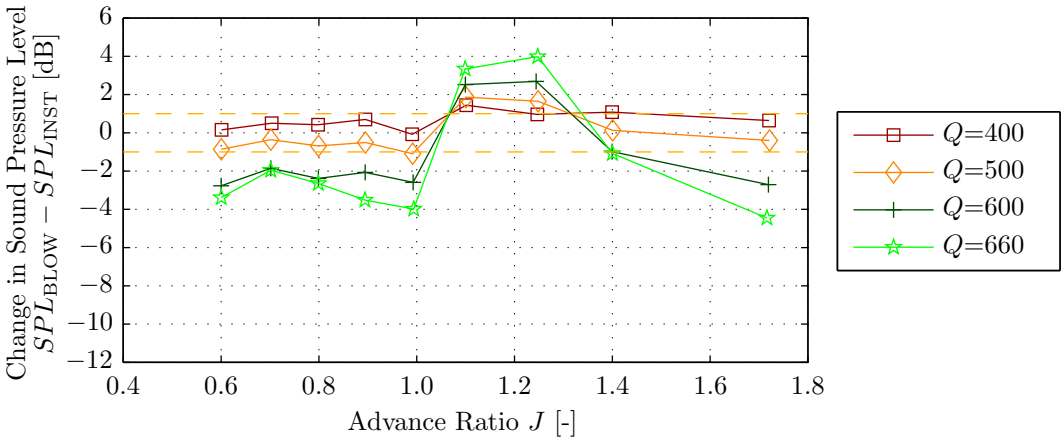

Figure 6.16: Noise reductions due to blowing for the 1BPF tone.
Blown configuration, $U_\infty = 19$ m/s, $0.6 \leq J \leq 1.7$, $\theta_{\mathrm{mic}} = 110°$, $K = 45$.

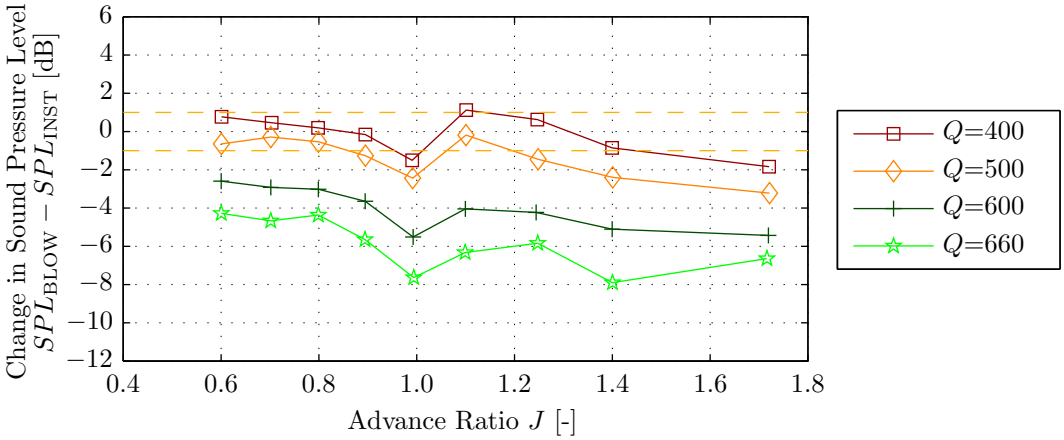

Figure 6.17: Noise reductions due to blowing for the 2BPF tone.
Blown configuration, $U_\infty = 19$ m/s, $0.6 \leq J \leq 1.7$, $\theta_{\mathrm{mic}} = 110°$, $K = 45$.

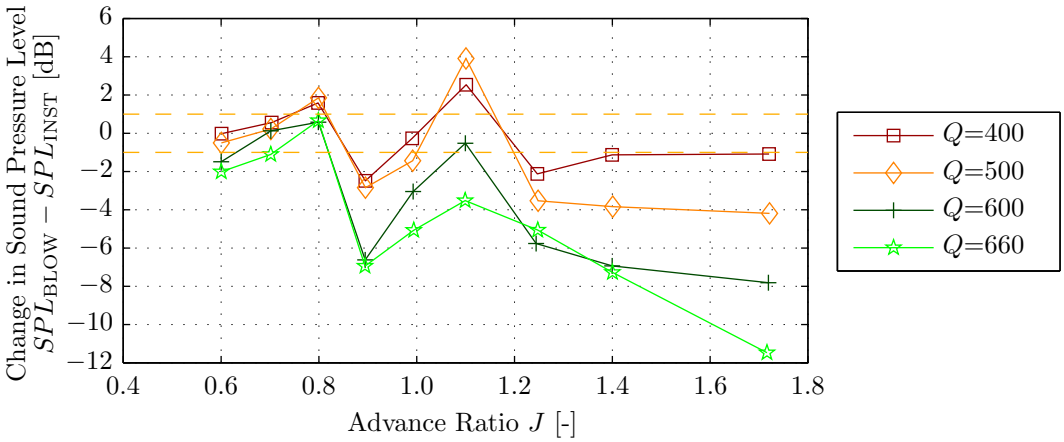

Figure 6.18: Noise reductions due to blowing for the 3BPF tone.
Blown configuration, $U_\infty = 19$ m/s, $0.6 \leq J \leq 1.7$, $\theta_{\mathrm{mic}} = 110°$, $K = 45$.

From Figure 6.16 it is observed that the application of blowing at $J = 1.7$ clearly reduces the SPL of the 1BPF tone, with increasing reductions obtained with increasing blowing rates. At a blowing rate of 660 L/min the SPL reduction equals about 4 dB. When the advance ratio is decreased to $J = 1.4$ the effects of blowing start to become smaller and the blown noise levels become approximately equal to the installed values. Further reduction of the advance ratio then displays the inverse of the behavior observed at $J = 1.7$. For advance ratios between 1.1 and 1.2 the SPL of the 1BPF tone increases due to blowing compared to the installed case, with higher sound pressure levels observed for higher blowing rates. Upon decreasing the advance ratio to around 1.0 the blowing system becomes effective again, with a noise reduction of 4 dB at $Q = 660$ L/min. Below $J = 1.0$ the maximum SPL reduction due to blowing decreases to about 2 dB at an advance ratio of 0.7. At the final advance ratio considered ($J = 0.6$) a noise reduction of approximately 4 dB is obtained. Note that for advance ratios smaller than or equal to 0.8 the reduction in tonal SPL due to blowing is approximately equal for the blowing rates of $Q = 600$ L/min and $Q = 660$ L/min.

Comparison of Figure 6.16 with Figure 6.12 shows that for the 1BPF tone the noise reduction due to blowing follows the inverse trend of the noise penalty due to installation. The increase in SPL with increasing blowing rate observed for the advance ratio range $1.0 < J < 1.3$ corresponds to the region where the change in SPL due to installation is negative in Figure 6.12. Based on this observation it was concluded before that at these operating points apparently the noise emissions due to the unsteady loading partially cancel the steady loading noise. The application of blowing reduces the noise emissions due to unsteady loading, thereby leading to an increase in noise emissions for these advance ratios.

The SPL of the 2BPF tone is decreased by blowing for all advance ratios considered, with larger noise reductions obtained at larger blowing rates. At $Q = 660$ L/min a maximum SPL reduction of 8 dB is observed at advance ratios of 1.0 and 1.4, while the minimum reduction equals 4 dB at the lowest advance ratio considered ($J = 0.5$). Note that the reductions in tonal noise levels are much larger for the 2BPF tone than for the 1BPF tone. This is as expected considering the strong installation effect on the SPL of the 2BPF tone observed before in Figure 6.12.

Finally, Figure 6.18 shows that the SPL reduction of the 3BPF tone displays an increasing trend with increasing blowing rate. At an advance ratio of $J = 1.7$ blowing at a rate of 660 L/min reduces the tonal noise level by almost 12 dB. Decreasing the advance ratio results in decreasing noise reductions, with the lowest noise reductions observed at $J = 1.1$. At this advance ratio the application of blowing increases the SPL of the 3BPF tone for blowing rates of 400 and 500 L/min, while at $Q = 660$ L/min still a reduction of 4 dB is observed. Further decreases of the advance ratio result in increased noise reductions, with a local minimum observed at $J = 0.9$. At this advance ratio a noise reduction due to blowing of about 7 dB is observed for blowing rates of 600 and 660 L/min. Below $J = 0.9$ the blown noise levels start to increase again, leading to a local maximum at $J = 0.8$. For this advance ratio the blown noise emissions are larger than those measured in the installed configuration for all blowing rates considered, with an increase of approximately 1 dB at the two highest blowing rates. Further reductions of the advance ratio then again lead to reductions in the blown noise emissions, resulting in a noise reduction of 2 dB at an advance ratio of $J = 0.6$ for the blown results obtained with blowing rates of 600 and 660 L/min.

Part II

Numerical Work

"All which is beautiful and noble is the result of reason and calculation."
Charles Baudelaire

In Part II of this report the numerical investigations of the potential of pylon trailing edge blowing to reduce the adverse pusher propeller installation effects are discussed. After a treatment of the setup of the developed numerical methods, the computed pylon wake profiles, powered propeller performance, and powered propeller noise emissions are presented in separate chapters.

Chapter 7

Numerical Setup

This chapter describes the setup of the numerical analysis performed to compute the propeller performance and noise emissions of a single-rotating pusher propeller in isolated, installed, and blown conditions. For this purpose the custom-made propeller analysis tool mROTOR was developed. A schematic flowchart of the mROTOR program is depicted in Figure 7.1.

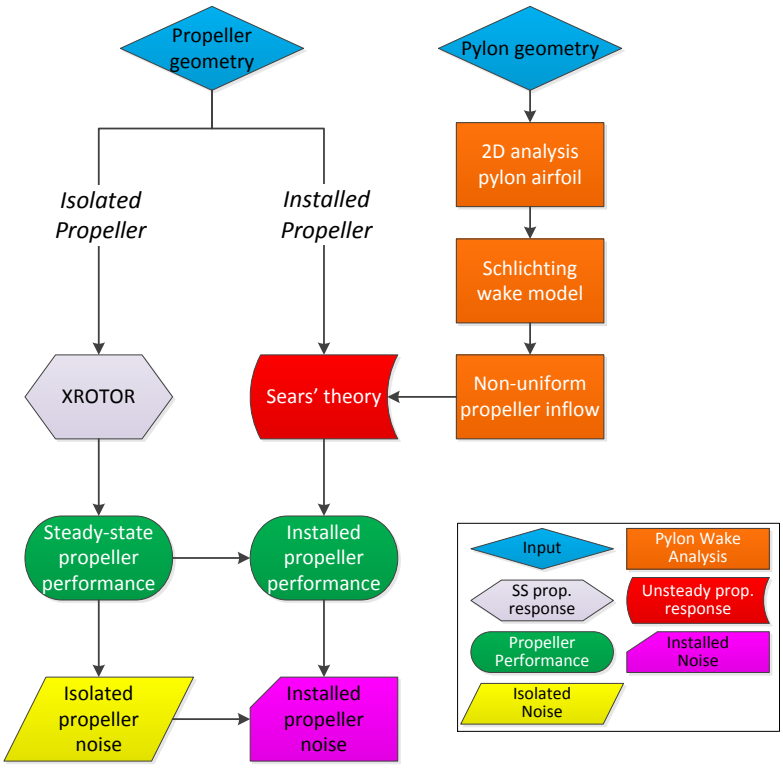

Figure 7.1: Schematic flowchart of mROTOR: single-rotating propeller analysis tool.

The numerical analyses performed within mROTOR are discussed in detail in this chapter. First, the method used to compute the pylon wake profiles is discussed in Section 7.1. Subsequently, the propeller performance computations are treated in Section 7.2, after which the noise emission prediction tools are described in Section 7.3. In both cases separate subsections are used to discuss the isolated and installed configurations, while the blown configuration is not treated separately since it can be considered as a subcase of the installed problem.

7.1 Pylon Wake Profiles

To compute the effects of installation on the propeller performance and noise emissions the pylon wake profiles need to be computed first. This section discusses the methods used for the unblown pylon (Subsection 7.1.1) and the blown pylon (Subsection 7.1.2).

7.1.1 Unblown Pylon Wake Profiles

In the installed case the propeller inflow is perturbed by the wake of the upstream pylon. To define the inflow at the propeller plane the velocity deficit in the pylon wake needs to be determined as a function of the position of the propeller with respect to the pylon. The assumption is made that the presence of the propeller does not affect the pylon wake profiles.

The velocity deficit in the pylon wake is modeled using a Schlichting wake profile, as already introduced in Subsection 2.5.1. For convenience, the two governing equations of the Schlichting wake model are repeated here:

$$\frac{\Delta u}{U_\infty}\left(X_\mathrm{w}, Y_\mathrm{w}\right) = \frac{\sqrt{10}}{18\beta}\sqrt{\frac{c_d c}{X_\mathrm{w}}}\left[1 - \left|\frac{Y_\mathrm{w}}{b_\mathrm{w}}\right|^{\frac{3}{2}}\right]^2 \tag{7.1}$$

$$b_\mathrm{w}\left(X_\mathrm{w}\right) = \beta\sqrt{10 c_d c X_\mathrm{w}} \tag{7.2}$$

with b_w the wake semi-width, c the pylon chord, c_d the pylon 2D drag coefficient, and β an empirical constant set to $\beta = 0.18$ based on experiments performed by Schlichting and Reichardt [33, 34]. The wake-based coordinate system $\mathbf{X}_\mathrm{w}$ was defined in Figure 2.2. The pylon drag coefficient is computed using XFOIL.

Since the propeller axis is located on the (extended) pylon chord line, the wake velocity deficit in the wake-based coordinate system computed using Equation (7.1) can directly be used to specify the inflow conditions at the propeller plane. The required values for X_w and Y_w correspond to the longitudinal and lateral separations between the pylon's trailing edge and the point in the propeller plane at which the pylon wake velocity deficit is to be computed.

7.1.2 Blown Pylon Wake Profiles

The concept of pylon blowing aims at reducing the velocity deficit in the pylon wake by injecting air from the pylon's trailing edge. Within mROTOR no numerical tools are available to compute the effects of pylon blowing on the resulting pylon wake velocity deficit profile. Instead, it is possible to manually input a blown pylon wake profile (velocity deficit Δu versus lateral coordinate Y_w), based on either numerical or experimental data obtained from an external source. Furthermore, it is also possible to specify a wake velocity deficit reduction factor, which is applied as a scaling factor to the pylon wake velocity deficit computed using Equation (7.1).

7.2 Propeller Performance

The numerical assessment of the propeller performance performed by mROTOR is built around the propeller analysis and design program XROTOR (see reference [51]). This section presents the computation methods for the isolated propeller performance (Subsection 7.2.1), followed by a discussion of the tools used to analyze the installed case (Subsection 7.2.2).

7.2.1 Isolated Propeller Performance

The isolated (steady-state) propeller performance is computed using XROTOR, which was released under the GNU General Public License in 2011. Based on classical propeller lifting-line theory, the XROTOR analysis follows an iterative process of which a simplified flowchart is given in Figure 7.2.

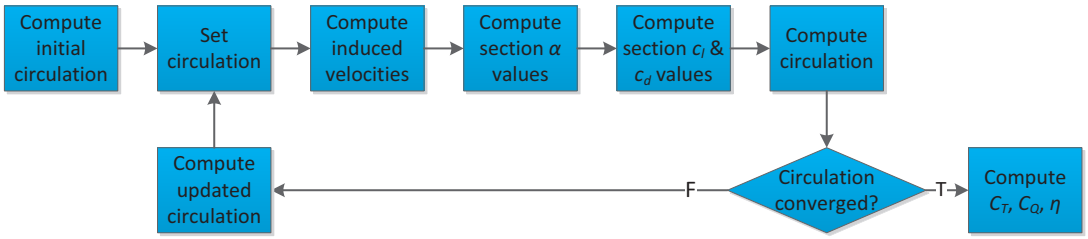

Figure 7.2: Simplified flowchart of XROTOR's iterative solution procedure.

Initially, the solution for the circulation is set without considering induced effects. With this initial solution defined, the iterative process is started in which the circulation is converged using a Newton method. After convergence, the final outputs are the steady-state thrust and torque coefficients together with the corresponding propeller efficiency.

A description of the computations performed in XROTOR is presented in Appendix D, which elaborates upon all the different steps depicted in Figure 7.2. Below, only a discussion is given of the determination of the input propeller blade section characteristics (Paragraph 7.2.1.1) and the implementation of the correction for rotational effects (Paragraph 7.2.1.2).

7.2.1.1 Determination of the Input Blade Section Characteristics

For XROTOR to be able to compute the section lift and drag coefficients, the following ten parameters need to be given as input for each blade section:

- Maximum lift coefficient $c_{l_{\max}}$
- Minimum lift coefficient $c_{l_{\min}}$
- Zero-lift angle α_0
- Lift gradient c_{l_α}
- Lift gradient after stall $c_{l_{\alpha_{\text{stall}}}}$
- Lift increment to stall $\Delta c_{l_{\text{stall}}}$
- Minimum drag coefficient c_{d_0}
- Lift coefficient at minimum drag coefficient $c_l^{c_d=c_{d_0}}$
- Gradient of drag coefficient with respect to lift coefficient squared $\partial c_d/\partial c_l^2$
- Critical Mach number M_{crit}

The ten parameters listed above are to be based on curve fits to lift and drag polars for the individual blade sections determined using a dedicated airfoil analysis program. Within *m*ROTOR both XFOIL and RFOIL are integrated and available to perform the blade section analysis. The Reynolds numbers used for this analysis are different for each section, and are computed by taking the average local Reynolds numbers observed over the advance ratio range for which the numerical results are to be computed. Having determined the original

lift and drag curves for a section, two separate multi-variable optimizations are performed to find the values of the parameters listed above that result in the best match between the original and the fitted lift and drag curves. The corresponding objective function of the minimization problem is defined as the difference squared between the original and the fitted lift and drag coefficients at all angles of attack. The optimizations are performed using the Nelder-Mead method (see reference [52]), with suitable lower and upper bounds imposed on the design variables by means of a penalty function. Examples of the raw airfoil data and the corresponding fits for the c_l-α and c_d-α curves of a given blade section are presented in Figure 7.3 and 7.4, respectively.

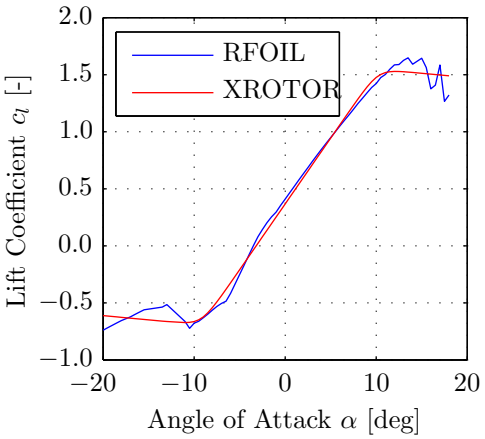

Figure 7.3: Example of raw (RFOIL) and fitted (XROTOR) c_l-α curve.

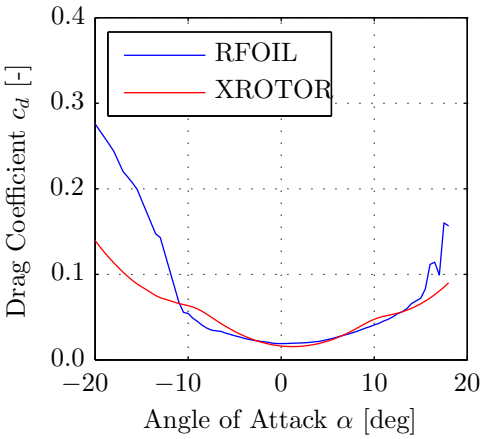

Figure 7.4: Example of raw (RFOIL) and fitted (XROTOR) c_d-α curve.

7.2.1.2 Rotational Effects

XROTOR makes use of two-dimensional aerodynamic characteristics to compute the lift and drag coefficients generated by the propeller blade sections. As a result, the flow is simplified into axial and tangential components only. However, the rotation of the propeller adds a radial velocity component to the flow field. As first concluded by Himmelskamp, at higher angles of attack the 2D approach results in an underprediction of the forces acting on the rotating blades [53]. To correct for this effect the empirical model developed by Snel et al. (see reference [54]) is implemented in *m*ROTOR. This model corrects the raw 2D airfoil data for rotational effects as a function of the local blade solidity c/r: [54]

$$c_{l_i}^{\text{rot}} = c_{l_i} + \tanh\left\{A\left(\frac{c}{r}\right)_i^B\right\}\left(c_{l_i} - c_{l_{\text{lin}_i}}\right) \tag{7.3}$$

with A and B tuning parameters, set to their default values of $A = 3$ and $B = 2$, respectively [54]. The drag coefficient is not corrected for rotational effects.

If enabled, the rotation correction defined by Equation (7.3) is applied to the fitted lift coefficient values rather than the original raw airfoil data. This approach is chosen since Equation (7.3) requires the 2D equivalent linear lift coefficient as input, which can be computed successfully only after the fitting parameters have been defined using the uncorrected lift coefficient data. Having applied the rotation correction, the fitting procedure is performed again for the corrected lift coefficient data, resulting in updated values for the parameters used in XROTOR's c_l-α model. These values are then given as input to XROTOR, thereby automatically implementing the rotation correction in the XROTOR computations.

7.2.2 Installed Propeller Performance

Following the isolated performance computations the installation effects for a single-rotating pusher propeller are considered. In the installed configuration the inflow at the propeller disk is characterized by a non-uniform velocity field due to the velocity deficit present in the pylon wake. The non-uniform inflow at the propeller plane results in a time-varying inflow velocity as seen by the rotating propeller blades. Cutting through the pylon wake, the blades experience an unsteady flow which results in an unsteady blade loading. The reduced inflow velocity in the pylon wake region results in a locally reduced dynamic pressure and increased angle of attack. The assumption is made that the final installed blade loading can be computed by following the principle of superposition. Hence, the installed blade loading is split up into three separate contributions:

1. *The steady-state propeller blade loads.*
   The steady-state blade loads are obtained using the method for the isolated propeller outlined in Subsection 7.2.1.

2. *The change in blade loads due to the change in dynamic pressure in the pylon wake region, assuming zero change in angle of attack relative to the isolated case.*
   The change in blade response due to the varying dynamic pressure in the wake region is computed by correcting the steady-state lift and drag for the change in effective velocity.

3. *The change in blade loads due to the change in angle of attack in the pylon wake region, assuming zero change in the dynamic pressure relative to the isolated case.*
   The change in blade loads due to the variation in angle of attack is computed using an unsteady aerodynamic analysis. The approach described in references [55], [56], and [57] is adopted, in which the pylon wake's velocity deficit is expressed as a periodic gust normal to the propeller blades. Then, the response is calculated using Sears' 1D unsteady theory for flat plates subject to periodic gusts (see references [58] and [59]).

A flowchart of the unsteady propeller performance analysis routine is presented in Figure 7.5. The remainder of this subsection follows the steps depicted in this flowchart.

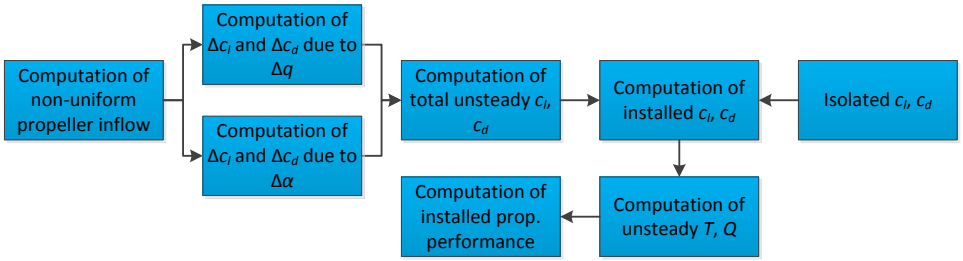

Figure 7.5: Flowchart of the installed propeller performance computation routine.

7.2.2.1 Non-Uniform Propeller Inflow Due to the Pylon Wake

The wake shed behind the pylon results in a non-uniform inflow at the propeller plane. To obtain the final velocity deficit at the propeller plane, Equations (7.1) and (7.2) are evaluated for a non-uniform 1D grid in the lateral direction covering the entire propeller disk ($-R \leq Y_w \leq R$), at a longitudinal coordinate X_w equal to the desired pylon - propeller spacing. For computational efficiency the grid is defined such that the resolution in the pylon

wake region is large, while outside of the wake region a minimum number of points is used. After computation of the deficit velocities in the wake-based coordinate system $\mathbf{X}_{\mathrm{w}}$ (see Figure 2.2) they are converted to the Cartesian propeller disk coordinate system $\mathbf{X}$ (see Figure 2.3). In this way the velocity deficit at the propeller plane is obtained as a function of the Y- and Z-coordinates: $\Delta u\,(Y, Z)$. An example of the resulting velocity deficit at the propeller plane for a right-mounted engine (as seen from the top) is depicted in Figure 7.6.

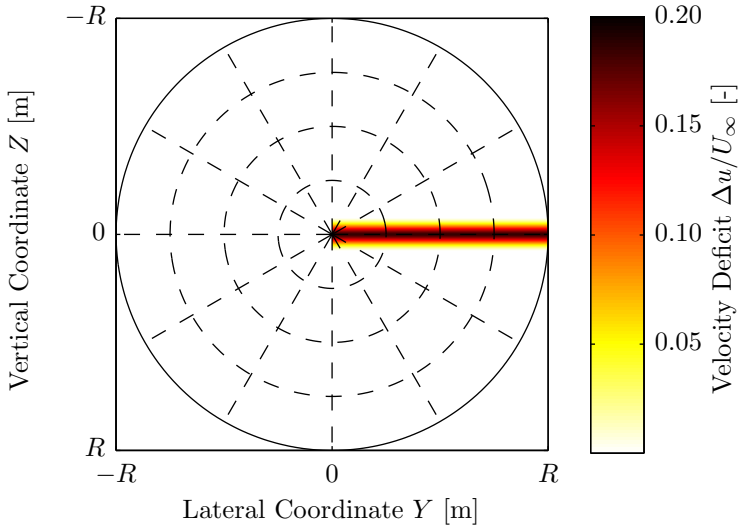

Figure 7.6: Example of a non-dimensional pylon wake velocity deficit distribution at the propeller plane (front view, right-mounted engine).

7.2.2.2 Change in Blade Loads Due to the Varying Dynamic Pressure

The change in blade loads due to the varying dynamic pressure is evaluated at the local angles of attack computed for the isolated case. The assumption is made that the isolated lift and drag coefficients per radial station are constant over the full rotation, hence Reynolds number effects are neglected. Furthermore, it is assumed that the induced velocities corresponding to the steady-state solution apply at each polar angle ϕ without modification.

The local dynamic pressure is directly related to the local effective velocity W. Defining the local change in velocity due to the pylon wake by the variable Δu and using the assumptions stated above, the local effective velocity in installed conditions W_{inst} follows from:

$$W_{\mathrm{inst}}\,(\eta, \phi) = \sqrt{\left\{U_\infty + u_{\mathrm{a}}\,(\eta) + \Delta u\,(\eta, \phi)\right\}^2 + \left\{\Omega \eta R - u_{\mathrm{t}}\,(\eta)\right\}^2} \tag{7.4}$$

with u_{a} the axial induced velocity and u_{t} the tangential induced velocity. Note that a velocity deficit in the pylon wake corresponds to negative values for the variable Δu, hence locally reducing the effective velocity W_{inst}.

With the local velocity obtained from Equation (7.4), the change in the lift and drag coefficients due to the variation in dynamic pressure at constant angle of attack is computed using:

$$\Delta c_{l_{\mathrm{inst}}}^{\Delta q}\,(\eta, \phi) = c_l^{\mathrm{SS}}\,(\eta)\left\{\frac{W_{\mathrm{inst}}^2\,(\eta, \phi)}{W_{\mathrm{iso}}^2\,(\eta)} - 1\right\} \tag{7.5}$$

$$\Delta c_{d_{\mathrm{inst}}}^{\Delta q}\,(\eta, \phi) = c_d^{\mathrm{SS}}\,(\eta)\left\{\frac{W_{\mathrm{inst}}^2\,(\eta, \phi)}{W_{\mathrm{iso}}^2\,(\eta)} - 1\right\} \tag{7.6}$$

with W_{iso} the undisturbed effective velocity obtained by setting Δu to zero in Equation (7.4).

7.2.2.3 Change in Blade Loads due to the Varying Angle of Attack

The change in blade loads due to the variation in the angle of attack in the pylon wake region is computed using Sears' method, which is described in references [58] and [59]. Only the lift coefficient is considered; the effects on the drag coefficient are neglected. The first steps of the analysis are to rewrite the velocity deficit in the pylon wake as a periodic gust normal to the propeller blades and subsequently to Fourier transform the result. Thereafter, the actual blade response is computed using the Sears function.

Computation of the Periodic Gusts Normal to the Propeller Blades

The pylon wake velocity deficit at the propeller plane Δu can be superimposed on the steady-state flow field by considering it as a gust in axial direction:

$$U_{\mathrm{a}}^{\mathrm{inst}} = U_{\mathrm{a}}^{\mathrm{iso}} + \Delta u = U_{\mathrm{a}}^{\mathrm{iso}} + V_{\mathrm{g}} \tag{7.7}$$

with the undisturbed axial velocity $U_{\mathrm{a}}^{\mathrm{iso}}$ consisting of the freestream velocity U_∞ and the axial induction velocity u_{a}. Note that this velocity component is used to compute the steady-state propeller performance following the methods outlined in Subsection 7.2.1.

The unsteady blade loads are driven by the gust component V_{g}. First a transformation is made from the Cartesian coordinate system (Y, Z) to a polar coordinate system in the propeller plane (η, ϕ). In the polar coordinate system the gust can be expressed as:

$$V_{\mathrm{g}}(\eta, \phi) = \Delta u(\eta, \phi) \tag{7.8}$$

The gust component V_{g} is periodic in terms of the polar angle with a period of 2π. This corresponds to a period T of one blade passage ($T = 2\pi/\Omega$).

The computation of the unsteady blade response requires the gust to be defined in an upward direction normal to the blade section chord. Therefore, the result from Equation (7.8) needs to be multiplied with the cosine of the blade pitch angle β, after which its sign is reversed:

$$V_{\mathrm{g_n}}(\eta, \phi) = -V_{\mathrm{g}}(\eta, \phi) \cos\beta(\eta) \tag{7.9}$$

An example of one period of the local gust profile in the normal direction is presented in Figure 7.7 for a range of radial stations.

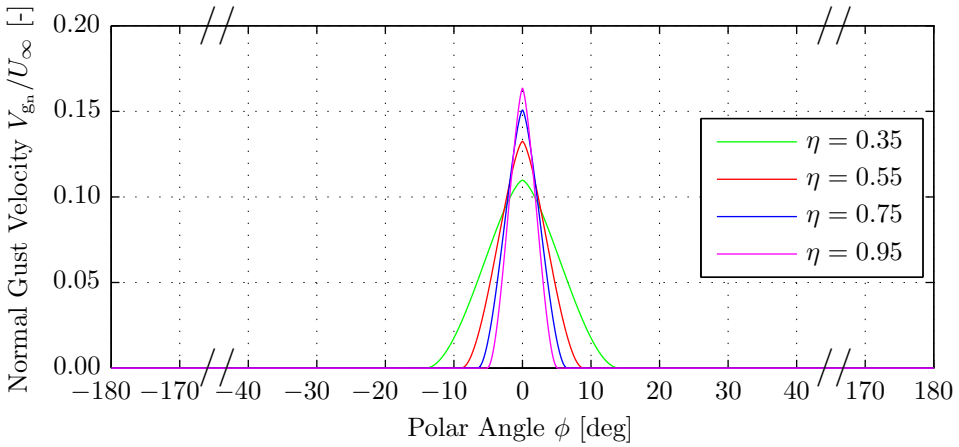

Figure 7.7: Example of one period of the local gust profile in the normal direction $V_{\mathrm{g_n}}$ for a number of non-dimensional radial stations $\eta = r/R$.

The computation of the unsteady blade response is performed in the frequency domain. Therefore, the periodic gust profile defined by Equation (7.9) is expressed as a complex Fourier series as follows:

$$V_{\mathrm{g_n}}(\eta,\phi) = \sum_{k=-\infty}^{\infty} v_{\mathrm{g_{n_k}}}(\eta)\mathrm{e}^{\mathrm{i}k\phi} \tag{7.10}$$

with k the harmonic order and $v_{\mathrm{g_{n_k}}}$ the Fourier coefficients of the normal gust velocity given by:

$$v_{\mathrm{g_{n_k}}}(\eta) = \frac{1}{2\pi}\int_0^{2\pi} V_{\mathrm{g_n}}(\eta,\phi)\mathrm{e}^{-\mathrm{i}k\phi}\mathrm{d}\phi \tag{7.11}$$

The Fourier coefficients of the gust profile $v_{\mathrm{g_{n_k}}}$ computed using Equation (7.11) are used as input for the computation of the unsteady blade lift coefficients as discussed next.

Computation of the Blade Response: Sears' Theory

Having computed the harmonics of the unsteady gust resulting from the velocity deficit in the pylon wake, the effect of the gust on the propeller blade's lift coefficient is computed for each radial segment. The harmonics of the unsteady blade lift coefficient due to the change in angle of attack in the pylon wake region are defined by: [55, 56]

$$\Delta c_{l_{\mathrm{inst}_k}}^{\Delta\alpha}(\eta) = 2\pi\frac{v_{\mathrm{g_{n_k}}}(\eta)}{W_{\mathrm{iso}}(\eta)}\overline{T} \tag{7.12}$$

with $\overline{T}$ the aerodynamic transfer function and W_{iso} the undisturbed effective velocity.

For the current problem the theory of Sears is particularly suitable [55–57]. Using Sears' theory, the aerodynamic transfer function is expressed in terms of the Sears function S:

$$\overline{T} = S \tag{7.13}$$

The original, incompressible Sears function $S_{M=0}$ is defined by: [58]

$$S_{M=0}(\sigma) = [J_0(\sigma) - \mathrm{i}J_1(\sigma)]\,C(\sigma) + \mathrm{i}J_1(\sigma) = \frac{J_0(\sigma)\,K_1(\mathrm{i}\sigma) + \mathrm{i}J_1(\sigma)\,K_0(\mathrm{i}\sigma)}{K_1(\mathrm{i}\sigma) + K_0(\mathrm{i}\sigma)} \tag{7.14}$$

with C Theodorsen's function, J_0 and J_1 the zeroth- and first-order Bessel functions of the first kind, K_0 and K_1 the modified zeroth- and first-order Bessel functions of the second kind, and σ the reduced frequency ($\sigma = \frac{k_\phi c}{2} = \frac{k\Omega c}{2W_{\mathrm{iso}}}$).

Note that due to the rotation of the propeller the local effective Mach numbers of the outboard sections typically attain values for which compressibility effects can no longer be ignored. Therefore, a compressibility correction is applied to the result obtained from Equation (7.14) as follows: [60]

$$S(\sigma, M_{\mathrm{iso}}) = \frac{S_{M=0}\left(\sigma/\beta_{\mathrm{iso}}^2\right)}{\beta_{\mathrm{iso}}}\left\{J_0\left(\frac{M_{\mathrm{iso}}^2\sigma}{\beta_{\mathrm{iso}}^2}\right) + \mathrm{i}J_1\left(\frac{M_{\mathrm{iso}}^2\sigma}{\beta_{\mathrm{iso}}^2}\right)\right\}\mathrm{e}^{\frac{-\mathrm{i}\sigma f(M_{\mathrm{iso}})}{\beta_{\mathrm{iso}}^2}} \tag{7.15}$$

with M_{iso} the effective Mach number ($M_{\mathrm{iso}} = W_{\mathrm{iso}}/a_\infty$), β_{iso} the Prandtl-Glauert compressibility factor based on the effective Mach number, and f a correction factor defined by: [60]

$$f(M_{\mathrm{iso}}) = (1-\beta_{\mathrm{iso}})\ln(M_{\mathrm{iso}}) + \beta_{\mathrm{iso}}\ln(1+\beta_{\mathrm{iso}}) - \ln(2) \tag{7.16}$$

Equation (7.15) is valid for $\sigma M_{\text{iso}}/\beta_{\text{iso}}^2 < 1$ [60]. If this condition is not satisfied, the high-frequency compressible Sears function derived by Landahl needs to be used: [61]

$$S_{\text{HF}}(\sigma, M_{\text{iso}}) = \frac{\mathrm{e}^{-\mathrm{i}\sigma}}{\pi\sigma}\sqrt{\frac{2\mathrm{i}}{M_{\text{iso}}}}F\left(\sqrt{\frac{4\sigma M_{\text{iso}}}{\pi\left(1+M_{\text{iso}}\right)}}\right) \tag{7.17}$$

with $F(x) = \int_0^x \mathrm{e}^{\frac{\mathrm{i}\pi\xi^2}{2}} d\xi$ the complex Fresnel integral.

Having computed the harmonics of the unsteady lift coefficient using Equation (7.12) in combination with Equation (7.15) or (7.17), the local unsteady lift coefficients are obtained as a function of the blade's polar angle ϕ by taking the inverse Fourier transform of the harmonics:

$$\Delta c_{l_{\text{inst}}}^{\Delta\alpha}(\eta, \phi) = \sum_{k=-\infty}^{\infty} \Delta c_{l_{\text{inst}_k}}^{\Delta\alpha}(\eta)\, \mathrm{e}^{\mathrm{i}k\phi} \tag{7.18}$$

7.2.2.4 Unsteady Propeller Blade Loads

The changes in the lift and drag coefficients due to the effects of the reduced dynamic pressure and the increased angle of attack in the pylon wake region are superimposed to obtain the final unsteady propeller blade loads c_l^{US} and c_d^{US}:

$$c_l^{\text{US}}(\eta, \phi) = \Delta c_{l_{\text{inst}}}^{\Delta q}(\eta, \phi) + \Delta c_{l_{\text{inst}}}^{\Delta\alpha}(\eta, \phi) \tag{7.19}$$

$$c_d^{\text{US}}(\eta, \phi) = \Delta c_{d_{\text{inst}}}^{\Delta q}(\eta, \phi) \tag{7.20}$$

7.2.2.5 Installed Propeller Blade Loads

With the change in blade loading due to the installation effects known from Equations (7.19) and (7.20), the total installed blade loads are straightforwardly computed using:

$$c_{l_{\text{inst}}}(\eta, \phi) = c_l^{\text{SS}}(\eta) + c_l^{\text{US}}(\eta, \phi) \tag{7.21}$$

$$c_{d_{\text{inst}}}(\eta, \phi) = c_d^{\text{SS}}(\eta) + c_d^{\text{US}}(\eta, \phi) \tag{7.22}$$

7.2.2.6 Unsteady Propeller Performance

The unsteady thrust and torque for a single-bladed propeller in the installed configuration are computed by integrating the contributions of all radial segments:

$$T_{1\text{B}}^{\text{US}}(\phi) = R\int_{\eta_{\text{hub}}}^{1} \mathrm{d}T_{1\text{B}}^{\text{US}}(\eta, \phi)\,\mathrm{d}\eta \simeq \sum_{i=1}^{N_{\text{r}}} T_{1\text{B}_i}^{\text{US}}(\phi) \tag{7.23}$$

$$Q_{1\text{B}}^{\text{US}}(\phi) = R\int_{\eta_{\text{hub}}}^{1} \mathrm{d}Q_{1\text{B}}^{\text{US}}(\eta, \phi)\,\mathrm{d}\eta \simeq \sum_{i=1}^{N_{\text{r}}} Q_{1\text{B}_i}^{\text{US}}(\phi) \tag{7.24}$$

with $T^{\mathrm{US}}_{1\mathrm{B}_i}$ and $Q^{\mathrm{US}}_{1\mathrm{B}_i}$ the contributions of the individual radial blade segments. These are computed using the unsteady lift and drag coefficients due to installation effects c_l^{US} and c_d^{US}:

$$T^{\mathrm{US}}_{1\mathrm{B_i}}(\phi) = \frac{1}{2}\rho {W_i}^2 \left(c^{\mathrm{US}}_{l_i}(\phi)\cos\varphi_i - c^{\mathrm{US}}_{d_i}(\phi)\sin\varphi_i\right) c_i \Delta\eta_i R \tag{7.25}$$

$$Q^{\mathrm{US}}_{1\mathrm{B_i}}(\phi) = \frac{1}{2}\rho {W_i}^2 \left(c^{\mathrm{US}}_{l_i}(\phi)\sin\varphi_i + c^{\mathrm{US}}_{d_i}(\phi)\cos\varphi_i\right) c_i \eta_i \Delta\eta_i R^2 \tag{7.26}$$

with φ_i the advance angle (including induced effects) of section i. Note that the assumption is made that the additional lift and drag resulting from the installation effects act perpendicular and parallel to the local effective velocity including induced effects.

Having computed the unsteady thrust and torque for a single-bladed propeller using Equations (7.23) and (7.24), the results are generalized to a B-bladed propeller by taking into account the proper phase shifts between the various blades. Note that interaction effects between the blades are neglected.

$$T^{\mathrm{US}}(\phi) = \sum_{i=1}^{B} T^{\mathrm{US}}_{1\mathrm{B}}\left(\phi - (i-1)\frac{2\pi}{B}\right) \tag{7.27}$$

$$Q^{\mathrm{US}}(\phi) = \sum_{i=1}^{B} Q^{\mathrm{US}}_{1\mathrm{B}}\left(\phi - (i-1)\frac{2\pi}{B}\right) \tag{7.28}$$

with ϕ defined relative to the blade positioned at $\phi = 0$ at the start of the rotation.

The unsteady thrust and torque coefficients corresponding to the results obtained from Equations (7.27) and (7.28) are computed in the same way as used for the steady-state results:

$$C_T^{\mathrm{US}}(\phi) = \frac{T^{\mathrm{US}}(\phi)}{\rho n^2 D^4} \tag{7.29}$$

$$C_Q^{\mathrm{US}}(\phi) = \frac{Q^{\mathrm{US}}(\phi)}{\rho n^2 D^5} \tag{7.30}$$

7.2.2.7 Installed Propeller Performance

The installed propeller performance is computed by adding the unsteady thrust and torque components obtained from Equations (7.27) and (7.28) to the steady-state values computed using the XROTOR analysis:

$$T^{\mathrm{inst}}(\phi) = T^{\mathrm{SS}} + T^{\mathrm{US}}(\phi) \tag{7.31}$$

$$Q^{\mathrm{inst}}(\phi) = Q^{\mathrm{SS}} + Q^{\mathrm{US}}(\phi) \tag{7.32}$$

Finally, the installed thrust and torque coefficients and the propeller efficiency are obtained using:

$$C_T^{\mathrm{inst}}(\phi) = \frac{T^{\mathrm{inst}}(\phi)}{\rho n^2 D^4} \tag{7.33}$$

$$C_Q^{\mathrm{inst}}(\phi) = \frac{Q^{\mathrm{inst}}(\phi)}{\rho n^2 D^5} \tag{7.34}$$

$$\eta^{\mathrm{inst}}(\phi) = \frac{J}{2\pi}\frac{C_T^{\mathrm{inst}}(\phi)}{C_Q^{\mathrm{inst}}(\phi)} \tag{7.35}$$

7.3 Propeller Noise Emissions

Propeller noise emissions can be divided into three categories: harmonic noise, broadband noise, and narrow-band noise. Typically, up to moderate frequencies the harmonic noise dominates the other two components (except for the case of severe turbulence) [49]. Therefore, in the following only harmonic noise sources are considered.

In the literature various harmonic propeller noise calculation methods are available, both in the time and frequency domains. Here, the helicoidal surface theory developed by Hanson is adopted, which models the linear harmonic propeller noise sources in the frequency domain. Originally published in references [62] and [63], reviewed in reference [49], and confirmed by Parry in references [64], [65] and [66], Hanson's theory is capable of modeling the noise emissions of both the isolated and the installed propeller.

A generic flowchart of the propeller noise analysis routine implemented in mROTOR is presented in Figure 7.8. The remainder of this section discusses the details of the methods used to analyze the isolated (Subsection 7.3.1) and the installed (Subsection 7.3.2) configurations.

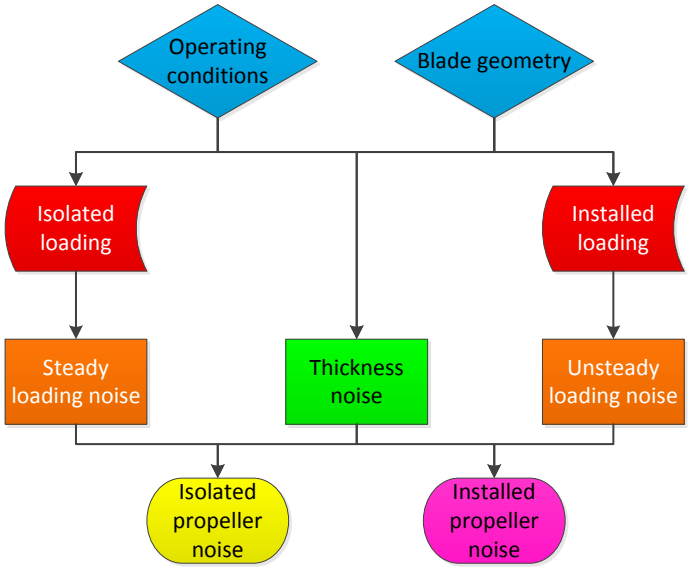

Figure 7.8: Flowchart of the propeller noise analysis routine implemented in mROTOR.

7.3.1 Isolated Propeller Noise Emissions

The isolated propeller at zero angle of incidence relative to the freestream experiences a blade loading which is steady in blade-fixed coordinates. Hence, for a fixed observer the fluid forces fluctuate at the blade passage frequency. As a result, the isolated propeller noise is emitted at frequencies equal to multiples of the blade passage frequency.

The isolated, steady noise sources are typically divided into three categories: linear thickness, linear loading, and non-linear quadrupole. Thickness noise, represented by a monopole source distribution, results from the periodic displacement of air by the volume of the passing blade element. Loading noise is a combination of lift and drag components which result from the pressure fields generated by the blades as a result of their motion. Quadrupole sources can be used to model all viscous and propagation effects not included in the linear thickness and loading terms, which can become relevant at transonic blade section speeds. [49]

The starting point of Hanson's analytic noise computation method is Goldstein's version of the acoustic analogy: [67]

$$\rho'(\mathbf{x},t) = -\frac{1}{a_\infty^2}\int_{-T}^{T}\int_{S(\tau)}\left(\rho_\infty V_\mathrm{n}\frac{\partial G}{\partial \tau} + f_i\frac{\partial G}{\partial y_i}\right)\mathrm{d}S(y)\,\mathrm{d}\tau + \frac{1}{a_\infty^2}\int_{-T}^{T}\int_{\nu(\tau)}\left(T_{ij}\frac{\partial^2 G}{\partial y_i \partial y_j}\right)\mathrm{d}y\mathrm{d}\tau \tag{7.36}$$

which is an exact result and applies to any region $\nu(\tau)$ bounded by impermeable surfaces $S(\tau)$ in arbitrary motion, provided the source distributions f_i and T_{ij} are localized enough to ensure convergence of the integrals [67]. The monopole source term V_n represents the normal surface velocity, the dipole source term f_i is the ith component of the force per unit area exerted by the fluid on the boundaries, and the quadrupole source T_{ij} is Lighthill's stress tensor. Note that quadrupole sources are neglected in the following.

For the full derivation of the harmonic propeller noise equations derived from Equation (7.36) the reader is referred to reference [62], here only the final results are presented. Assuming that the surface boundary conditions are allowed to be satisfied on the mean surface rather than at the blade upper and lower surfaces, considering far-field conditions, and Fourier transforming the resulting equations, noise waveforms for a propeller with B blades can be expressed as: [62]

$$p(t) = \sum_{m=-\infty}^{\infty} P_{mB}\mathrm{e}^{-\mathrm{i}mB\Omega_\mathrm{D}t} \tag{7.37}$$

with Ω_D the Doppler shifted angular velocity of the propeller ($\Omega_\mathrm{D} = \frac{\Omega}{1-M_\infty\cos\theta}$) and P_{mB} the mB^{th} noise harmonic. The latter is expressed as the summation of the effects due to volume displacement P_{V_m}, drag P_{D_m}, and lift P_{L_m}:

$$P_{mB} = P_{\mathrm{V}_m} + P_{\mathrm{D}_m} + P_{\mathrm{L}_m} \tag{7.38}$$

The noise harmonics P_{V_m}, P_{D_m}, and P_{L_m} are computed using: [62]

$$\begin{Bmatrix} P_{\mathrm{V}_m} \\ P_{\mathrm{D}_m} \\ P_{\mathrm{L}_m} \end{Bmatrix} = -\frac{\rho_\infty a_\infty^2 B}{16\pi\frac{R_\mathrm{obs}}{D}(1-M_\infty\cos\theta)}\mathrm{e}^{\mathrm{i}mB\left(\frac{\Omega_\mathrm{D}R_\mathrm{obs}}{a_\infty}-\frac{\pi}{2}\right)}\times \int_{\eta_\mathrm{hub}}^{1} M_\mathrm{r}^2\mathrm{e}^{\mathrm{i}(\phi_\mathrm{o}+\phi_\mathrm{s})}J_{mB}\left(\frac{mB\eta M_\mathrm{t}\sin\theta}{1-M_\infty\cos\theta}\right)\begin{Bmatrix} 2k_x^2 t_\mathrm{b}\psi_\mathrm{V}(k_x) \\ \mathrm{i}k_x c_{f_1}\psi_\mathrm{D}(k_x) \\ \mathrm{i}k_y c_{f_2}\psi_\mathrm{L}(k_x) \end{Bmatrix}\mathrm{d}\eta \tag{7.39}$$

with:

- a_∞ the speed of sound
- c_{f_1} and c_{f_2} the local blade section drag and lift coefficients defined relative to the local section advance direction *without* induced effects
- D the propeller diameter
- J_{mB} a Bessel function of the first kind of order mB
- k_x and k_y non-dimensional wave numbers
- M_r the local effective Mach number
- M_∞ the freestream Mach number

- R_{obs} the observer distance from the propeller center
- t_{b} the local blade thickness-to-chord ratio
- η the non-dimensional radial coordinate
- θ the axial directivity angle
- ρ_{∞} the air density
- ϕ_{o} the phase shift due to blade offset
- ϕ_{s} the phase shift due to sweep
- ψ_{V}, ψ_{D}, ψ_{L} the frequency domain distribution functions for volume displacement, drag, and lift

The non-dimensional wave numbers k_x and k_y are defined by: [62]

$$k_x = \frac{2M_{\text{t}}}{M_{\text{r}}}\left[\frac{mB}{1 - M_{\infty}\cos\theta}\right]\frac{c}{D} \tag{7.40}$$

$$k_y = \frac{-2}{\eta M_{\text{r}}}\left[\frac{mB\left(M_{\text{r}}^2\cos\theta - M_{\infty}\right)}{1 - M_{\infty}\cos\theta}\right]\frac{c}{D} \tag{7.41}$$

with c the local blade chord.

The phase shifts due to blade offset and sweep ϕ_{o} and ϕ_{s} are computed using: [62]

$$\phi_{\text{o}} = \frac{2}{\eta M_{\text{r}}}\left[\frac{mB\left(M_{\text{r}}^2\cos\theta - M_{\infty}\right)}{1 - M_{\infty}\cos\theta}\right]\frac{FA}{D} \tag{7.42}$$

$$\phi_{\text{s}} = \frac{2M_{\text{t}}}{M_{\text{r}}}\left[\frac{mB}{1 - M_{\infty}\cos\theta}\right]\frac{MCA}{D} \tag{7.43}$$

with FA the distance from the blade section normal to the blade planform, and MCA the distance between the local mid-chord point and the pitch change axis (PCA).

The frequency domain distribution functions for volume displacement, drag, and lift ψ_{V}, ψ_{D}, and ψ_{L} are defined by: [62]

$$\begin{Bmatrix} \psi_{\text{V}}(k_x) \\ \psi_{\text{D}}(k_x) \\ \psi_{\text{L}}(k_x) \end{Bmatrix} = \int_{-1/2}^{1/2} \begin{Bmatrix} H(X) \\ f_{\text{D}}(X) \\ f_{\text{L}}(X) \end{Bmatrix} \mathrm{e}^{\mathrm{i}k_x X}\mathrm{d}X \tag{7.44}$$

with X a chordwise coordinate ranging from -0.5 at the leading edge of the blade section to $+0.5$ at the section's trailing edge, H the chordwise thickness distribution function (normalized by the thickness-to-chord ratio of the local blade section), f_{D} the chordwise drag loading distribution function (normalized for unit area), and f_{L} the chordwise lift loading distribution function (normalized for unit area).

As mentioned, the section force coefficients c_{f_1} and c_{f_2} substituted into Equation (7.39) are defined relative to the local advance direction *without* consideration of induced effects. Therefore, the lift and drag coefficients obtained from the isolated propeller performance analysis first need to be corrected for the corresponding shift in the advance angle and the change in effective velocity before they can be used as input to the noise computation procedure.

This is illustrated in Figure 7.9, in which the original lift and drag coefficients are defined as c_l and c_d and the shifted force coefficients are denoted c_{f_1} and c_{f_2}.

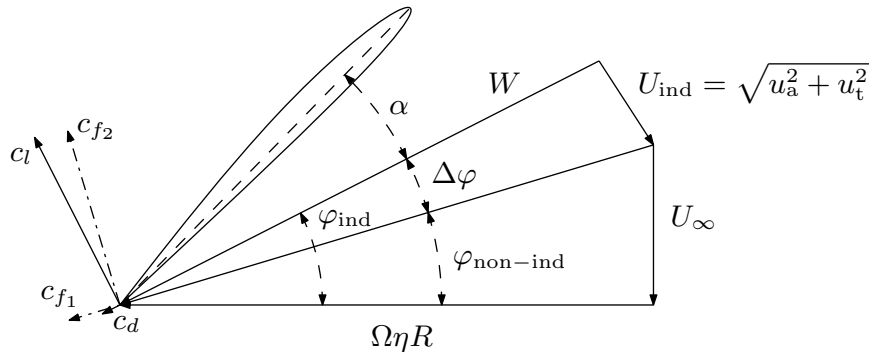

Figure 7.9: Illustration of the definition of the shifted lift and drag coefficients used in the propeller noise computation methods.

The required force coefficients c_{f_1} and c_{f_2} are computed from the original lift and drag coefficients as follows:

$$c_{f_1} = \frac{W^2}{U_\infty^2 + (\Omega\eta R)^2} \left(c_l \sin\Delta\varphi + c_d \cos\Delta\varphi\right) \tag{7.45}$$

$$c_{f_2} = \frac{W^2}{U_\infty^2 + (\Omega\eta R)^2} \left(c_l \cos\Delta\varphi - c_d \sin\Delta\varphi\right) \tag{7.46}$$

The shift in the advance angle $\Delta\varphi$ is defined as:

$$\Delta\varphi = \varphi_{\text{ind}} - \varphi_{\text{non-ind}} \tag{7.47}$$

with φ_{ind} the advance angle with induced effects taken into account and $\varphi_{\text{non-ind}}$ the advance angle with induced effects *not* taken into account.

The sound pressure levels corresponding to the harmonic noise components computed using Equation (7.39) are determined as follows:

$$SPL_{mB} = 10\log_{10}\left(\frac{2P_{mB}\overline{P_{mB}}}{p_0^2}\right) \tag{7.48}$$

with p_0 the acoustic reference pressure of 20μPa. Note that Equation (7.48) assumes that the noise harmonics are only computed for positive harmonic numbers (one-sided analysis), after which the result is multiplied by two to also include the noise harmonic at the corresponding negative harmonic order.

7.3.2 Installed Propeller Noise Emissions

The derivation of the harmonic noise equations for the installed propeller follows the same steps as for the isolated propeller. However, due to the installation effects the loading sources are unsteady and thus should be considered as harmonics as well.

To incorporate the installation effects into the harmonic propeller noise prediction routine again use is made of the work of Hanson. The equations originally derived in reference [63] are applicable to contra-rotating open rotor engines, in which interactions are present between

the front and rear rotors. For the current work, where only a fixed distortion on a single-rotating propeller is considered, this case is simplified by considering a virtual front rotor with unity blade number and zero rotational velocity. Upon substitution of these two parameters the following expressions are obtained for the installed drag and lift loading noise harmonics radiated by a single-rotating propeller operating in a flow field with a fixed distortion: [63]

$$\left\{ \begin{array}{c} P_{\mathrm{D}_m} \\ P_{\mathrm{L}_m} \end{array} \right\} = -\frac{\mathrm{i}\rho_\infty a_\infty^2 B}{16\pi \frac{R_{\mathrm{obs}}}{D}\left(1 - M_\infty \cos\theta\right)} \sum_{k=-\infty}^{\infty} \mathrm{e}^{\mathrm{i}\left[(mB-k)\left(\phi-\frac{\pi}{2}\right)+mB\Omega_{\mathrm{D}}\frac{R_{\mathrm{obs}}}{a_\infty}\right]} \times \int_{\eta_{\mathrm{hub}}}^{1} M_{\mathrm{r}}^2 \mathrm{e}^{\mathrm{i}(\phi_0+\phi_{\mathrm{s}})} J_{mB-k}\left(\frac{mB\eta M_{\mathrm{t}} \sin\theta}{1 - M_\infty \cos\theta}\right) \left\{ \begin{array}{c} k_x c_{f_{1_k}} \psi_{\mathrm{D}_k}\left(k_x\right) \\ k_y c_{f_{2_k}} \psi_{\mathrm{L}_k}\left(k_x\right) \end{array} \right\} \mathrm{d}\eta \tag{7.49}$$

with k the index used for the harmonics of the unsteady lift and drag coefficients (following the notation used in Subsection 7.2.2), and ϕ the circumferential directivity angle.

The non-dimensional wave numbers k_x and k_y are now defined by: [63]

$$k_x = \frac{2M_{\mathrm{t}}}{M_{\mathrm{r}}}\left[\frac{mB}{1 - M_\infty \cos\theta} - k\right]\frac{c}{D} \tag{7.50}$$

$$k_y = \frac{-2}{\eta M_{\mathrm{r}}}\left[\frac{mB\left(M_{\mathrm{r}}^2 \cos\theta - M_\infty\right)}{1 - M_\infty \cos\theta} + kM_\infty\right]\frac{c}{D} \tag{7.51}$$

The phase shifts due to blade offset and sweep ϕ_{o} and ϕ_{s} are computed using: [63]

$$\phi_{\mathrm{o}} = \frac{2}{\eta M_{\mathrm{r}}}\left[\frac{mB\left(M_{\mathrm{r}}^2 \cos\theta - M_\infty\right)}{1 - M_\infty \cos\theta} + kM_\infty\right]\frac{FA}{D} \tag{7.52}$$

$$\phi_{\mathrm{s}} = \frac{2M_{\mathrm{t}}}{M_{\mathrm{r}}}\left[\frac{mB}{1 - M_\infty \cos\theta} - k\right]\frac{MCA}{D} \tag{7.53}$$

The chordwise load distributions ψ_{D_k} and ψ_{L_k} can be specified per harmonic k or taken constant for all k harmonics, and are computed in the same way as for the isolated propeller as defined by Equation (7.44).

The harmonics of the installed lift and drag coefficients are obtained by Fourier transforming the results determined during the installed performance computations. However, it should be noted that again first the shift in the advance angle due to the induced effects should be corrected for using Equations (7.45) and (7.46).

Chapter 8

Numerical Results: Pylon Wake Profiles

The analytic prediction of the pylon wake profiles was performed as a first step in the numerical assessment of the effects of installation and blowing on pusher propeller performance and noise emissions. This chapter starts with a general overview of the analyses performed to compute the pylon wake profiles in Section 8.1. Subsequently, Section 8.2 presents a comparison of the computed wake profiles behind the default, extended, and sharp pylon models. Finally, the effects of the freestream velocity on the resulting wake profiles are discussed in Section 8.3.

8.1 Analysis Overview

The unblown pylon wake profiles were computed using the Schlichting wake model discussed in Section 7.1 for the default, extended, and sharp pylon models used during the experimental evaluations. Four freestream velocities were considered (15, 19, 26, and 30 m/s), while results were computed for two axial positions behind the pylon's trailing edge: $X_{\mathrm{w}} = 50$ mm and $X_{\mathrm{w}} = 114$ mm. In all cases the pylon angle of attack was set to zero degrees. Again, the effect of the presence of the rotating propeller behind the pylon was neglected in all evaluations. The wake profiles behind the blown pylon could not be predicted using the implemented numerical methods, and therefore are not further discussed here. Subsequent numerical results related to the blown configuration were obtained using the experimental blown wake profiles presented in Chapter 3. A comparison between the computed and measured unblown wake profiles is presented in Section 11.1.

8.2 Wake Profiles Behind the Default, Extended, and Sharp Pylon Models at Constant Freestream Velocity

The analytic wake profiles behind the default, extended, and sharp pylon models were computed for a freestream velocity of 19 m/s, hence directly corresponding to one of the measurement points evaluated in the experimental analyses. As discussed in Subsection 7.1.1, the computation of the wake width and wake depth using the Schlichting wake model requires the input of the pylon's profile drag coefficient. Therefore, these were obtained first using XFOIL for the three pylon models, with the analyses performed at Reynolds numbers corresponding to a freestream velocity of 19 m/s and the pylon chord lengths given in Table 2.1. The transition point was fixed to the position of the zigzag tape installed on the wind tunnel models. An overview of the resulting drag coefficients is presented in Table 8.1.

Table 8.1: Computed drag coefficients of the default, extended, and sharp pylons. $U_\infty = 19$ m/s.

Pylon Model	c_d [–]
Default	0.0122
Extended	0.0113
Sharp	0.0105

Table 8.1 shows that the drag coefficient of the default pylon model is highest at 0.0122, followed by the extended and sharp pylons, respectively. This is as expected considering the trailing edge thicknesses of the different pylons. Having determined the drag coefficients, the wake profiles behind the pylons were computed using Equations (7.1) and (7.2). The resulting non-dimensional velocity profiles at axial positions of 50 and 114 mm behind the pylon's trailing edge are presented in Figure 8.1. The values of the wake width and depth corresponding to the wake profiles shown in Figure 8.1 are presented in Table 8.2.

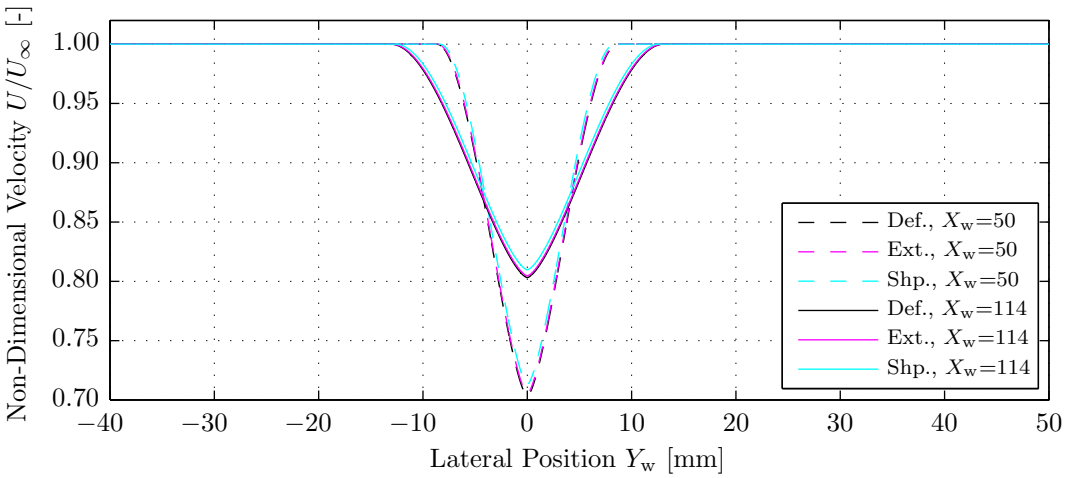

Figure 8.1: Non-dimensional velocity profiles in the wakes of the default (Def.), extended (Ext.), and sharp (Shp.) pylon models. $U_\infty = 19$ m/s, $X_w = [50, 114]$ mm.

Table 8.2: Wake width and wake depth of the wake profiles behind the default, extended, and sharp pylons. $U_\infty = 19$ m/s, $X_w = [50, 114]$ mm.

Pylon Model	$2b_w$ **[mm]**		$\Delta U_{max}/U_\infty$ **[-]**	
	$X_w = 50$ mm	$X_w = 114$ mm	$X_w = 50$ mm	$X_w = 114$ mm
Default	17.3	26.2	0.297	0.197
Extended	17.2	26.0	0.295	0.195
Sharp	16.8	25.3	0.287	0.190

The results shown in Figure 8.1 and Table 8.2 are as expected considering the governing equations of the Schlichting wake model. Both the wake width and depth are direct functions of the drag coefficient, and increase with increasing drag coefficient. Based on the drag coefficients listed in Table 8.1 it would therefore be expected that the wake profile behind the default pylon is characterized by the largest wake width and depth, while the sharp pylon should have the narrowest and shallowest wake profile. Inspection of the numerical wake data shows that this is indeed the case. However, the differences between the computed wake profiles behind the three different pylon models are small. Therefore, it was decided to

only consider a single pylon model in the remainder of the numerical analyses. Following the experimental work, for this purpose the extended pylon model was selected.

8.3 Effects of the Freestream Velocity on the Pylon Wake Profiles

In relatively low Reynolds number flow the wake profiles behind the pylon models evaluated at different freestream velocities should show small differences. For the range of Reynolds numbers considered here ($10^5 - 10^6$) the increase in Reynolds number associated with an increase in the freestream velocity should result in a reduction in the pylon drag coefficient. Following the equations of the Schlichting wake model this would then directly translate into a decrease in the wake width and the wake depth. To assess whether the pylon wake profile computations are capable of predicting the effect of changes in the freestream velocity on the resulting wake profiles, the extended pylon's drag coefficient was computed for freestream velocities of 15, 19, 26, and 30 m/s. The corresponding results are presented in Table 8.3.

Table 8.3: Computed extended pylon drag coefficients for a range of freestream velocities.

U_∞	c_d [−]	U_∞	c_d [−]
15	0.0119	26	0.0105
19	0.0113	30	0.0102

Table 8.3 shows that the computed pylon drag coefficient indeed decreases with increasing freestream velocity, hence following the expected trend. The wake profiles computed using the drag coefficient data presented in Table 8.3 are plotted in Figure 8.2, followed by an overview of the wake width and the wake depth data presented in Table 8.4.

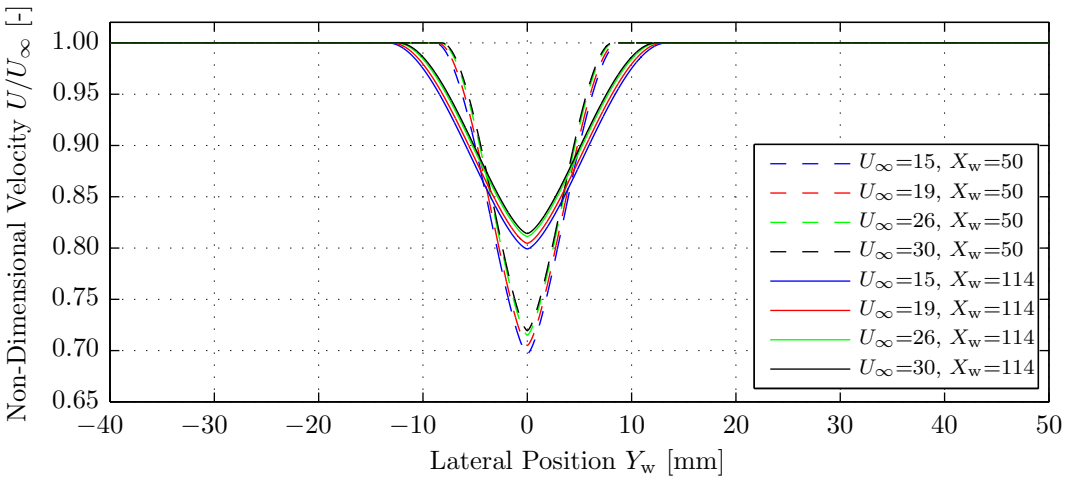

Figure 8.2: Non-dimensional velocity profiles in the wake of the extended pylon model. $U_\infty = [15, 19, 26, 30]$ m/s, $X_w = [50, 114]$ mm.

Table 8.4: Wake width and wake depth of the wake profiles behind the extended pylon. $U_\infty = [15, 19, 26, 30]$ m/s, $X_w = [50, 114]$ mm.

U_∞ [m/s]	$2b_w$ [mm]		$\Delta U_{max}/U_\infty$ [-]	
	$X_w = 50$ mm	$X_w = 114$ mm	$X_w = 50$ mm	$X_w = 114$ mm
15	17.7	26.7	0.303	0.201
19	17.2	26.0	0.295	0.195
26	16.6	25.1	0.285	0.189
30	16.4	24.7	0.280	0.186

The results presented in Figure 8.2 and Table 8.4 confirm the expectations based on the drag coefficients shown in Table 8.3. The wake width and depth indeed decrease with increasing freestream velocity. To quantify the differences between the different wake profiles, the relative change in the wake depth and the wake width relative to the values obtained at a freestream velocity of 19 m/s are presented in Table 8.5. Note again that the relative differences are independent of the axial position X_{w}.

Table 8.5: Difference in the wake width and the wake depth behind the extended pylon relative to the corresponding values at 19 m/s.

U_∞	$\frac{\left(b_{\mathrm{w}} - b_{\mathrm{w_{def}}}\right)}{b_{\mathrm{w_{def}}}} \cdot 100\%$ [-]	$\frac{\left(\Delta U_{\max}/U_\infty - \Delta U_{\max_{U19}}/19\right)}{\Delta U_{\max_{U19}}/19} \cdot 100\%$ [-]
15	2.8	2.8
19	0	0
26	-3.4	-3.4
30	-4.9	-4.9

Table 8.5 shows that the relative differences between the wake characteristics in the velocity range considered can become significant if the change in the velocity is large. For example, when comparing the wake width and depth at velocities of 19 and 30 m/s a difference of about five percent is observed. Although not further investigated here, the same sensitivity is found to the definition of the location of the transition point on the pylon airfoil used in the XFOIL computations. This variable has a distinct effect on the computed drag coefficient, which would directly translate into clear differences in the wake characteristics obtained using the Schlichting wake model.

Chapter 9

Numerical Results: Powered Propeller Performance

The propeller performance computations were performed to gain insight in the effects of installation and blowing on the propeller performance. Furthermore, the computed blade load distributions served as the inputs for the analytic propeller noise computations of which the results are presented in Chapter 10. The current chapter starts with an overview of the numerical propeller performance analyses in Section 9.1. Subsequently, Section 9.2 discusses the computed isolated propeller performance. Thereafter, the results obtained for the installed configuration are treated in Section 9.3, including an overview of the propeller inflow. Finally, the performance of the propeller in the blown configuration is considered in Section 9.4.

9.1 Analysis Overview

The performance of the powered propeller model in the isolated, installed, and blown configurations was computed using the methodology discussed in Section 7.2. The exact same propeller geometry was used for the numerical analyses as for the wind tunnel tests, while also similar operating conditions were simulated. The propeller performance was computed for freestream velocities of 15, 19, 26, and 30 m/s, at an advance ratio range of $0.5 \leq J \leq 1.9$. In all analyses the propeller was discretized using thirty radial stations.

For the isolated case the induced velocities were computed using the potential method based on the extended version of Goldstein's method as discussed in Appendix D.1. The propeller blade section characteristics were determined using RFOIL, after which suitable fits were generated to determine the inputs required by XROTOR using the process described in Paragraph 7.2.1.1. Computations were performed with the empirical rotation enabled and disabled, while the Reynolds number scaling exponent used to correct the drag coefficient for Reynolds number effects was set to zero. The selection of an exact value for this coefficient would have been based on an educated guess only, and it was found that using a value of zero led to the best predictions of the torque coefficient when compared to the experimental data.

The propeller performance in the installed and blown configurations was computed for a pylon – propeller spacing of $\Delta X = 114$ mm, with the pylon angle of attack set to zero degrees. In all cases the change in the section lift coefficient due to the change in the angle of attack was computed using the low-frequency compressible Sears function defined by Equation

(7.15). A right-mounted propeller was considered (when looking from the top), with the chord line of the pylon positioned at $\phi = 0°$. The rotation direction of the propeller was taken counter-clockwise when looking from the front. The extended pylon model was used in all computations, with the blown pylon wake profile extracted from the experimental measurements and equal to the result shown in Figure 3.7 for a blowing rate of $Q = 600$ L/min.

9.2 Isolated Configuration

The isolated propeller performance was computed as a baseline to which the installed and blown results could be compared. Figure 9.1 presents the results computed for a freestream velocity of 19 m/s as obtained with and without the empirical rotation correction defined by Equation (7.3). The thrust coefficient C_T, torque coefficient C_Q, and propeller efficiency η displayed in Figure 9.1 are defined by Equations (D.15) through (D.17).

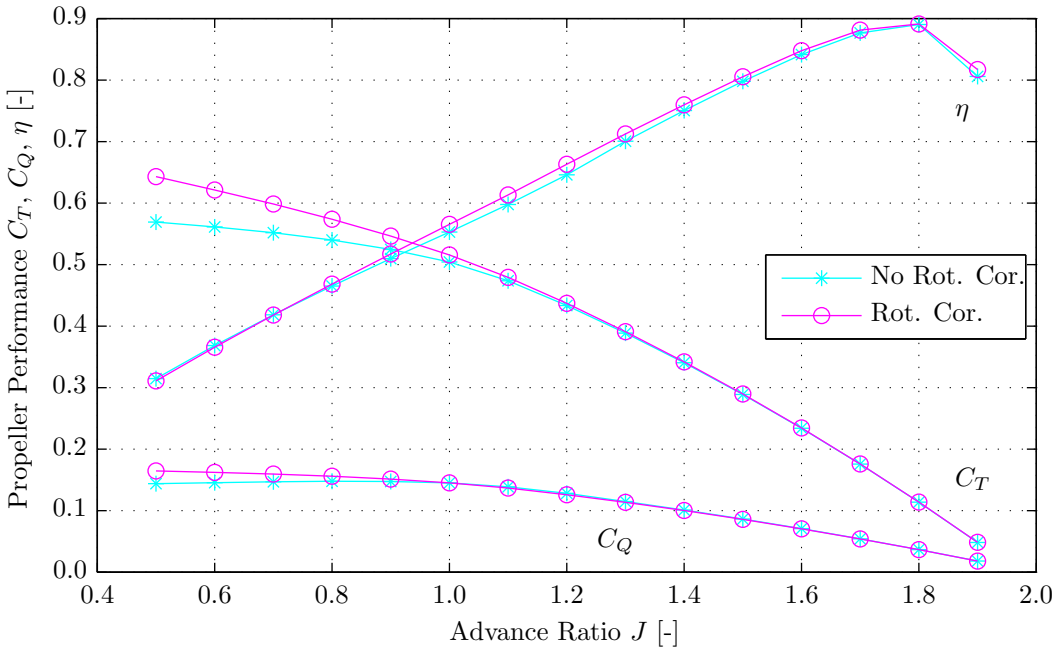

Figure 9.1: Propeller performance diagram: effects of application of the rotation correction. Isolated configuration, $U_\infty = 19$ m/s, $0.5 \leq J \leq 1.9$, with/without rotation correction.

With respect to the thrust coefficient it is observed from Figure 9.1 that for advance ratios above approximately 1.1 a quasi-linear response is obtained, corresponding to moderate to low blade angles of attack. Correspondingly, in this advance ratio range the application of the rotation correction does not lead to any differences in the computed thrust coefficient. At the lower advance ratios the angles of attack experienced by the blade sections become larger, resulting in a non-linear behavior of the thrust coefficient. Without application of the rotation correction the thrust coefficient clearly starts to flatten for advance ratios below approximately $J = 1.2$, indicating the onset of non-linearities in the lift response of the propeller blades. The application of the rotation correction increases the stall angle of the blade sections, hence the lift coefficients at higher angles of attack. This is directly recognized in the thrust coefficient response, which at the lowest advance ratios considered shows a much larger gradient when the rotation correction is applied than when it is not used. At $J = 0.5$ the difference between the thrust coefficients computed with and without the rotation correction equals approximately 10% ($C_T = 0.64$ versus $C_T = 0.57$).

For the torque coefficient similar trends are observed as for the thrust coefficient. However, without application of the rotation correction the torque coefficient decreases with decreasing advance ratio for $J < 0.8$. This results from the definition of the torque coefficient; the dimensional torque did increase with decreasing advance ratio over the entire measurement range. However, because of induced effects the gradient of the effective velocity at low advance ratios is decreased relative to the gradient of the propeller's rotational rate. Therefore, if the dimensional torque does not increase sufficiently fast the torque coefficient will decrease. With the rotation correction applied on the other hand the torque coefficient keeps increasing with decreasing advance ratio.

Based on the discussion above it is concluded that from a qualitative point of view the numerical propeller performance results obtained for the isolated propeller are acceptable. To quantitatively assess the quality of the numerical results a comparison with the experimental data is required, which is the topic of discussion of Section 11.2. This comparison will also make it possible to draw conclusions on the applicability of the rotation correction. However, considering the more realistic behavior of the torque coefficient at low advance ratios obtained with the rotation correction enabled, it was decided to apply the rotation correction during all computations of which the results are discussed in the remainder of this chapter.

9.3 Installed Configuration

Following the isolated propeller performance computations, the installed configuration was considered. To be able to compute the installed propeller performance, first the non-uniform propeller inflow resulting from the wake shed by the upstream pylon needs to be determined (Subsection 9.3.1). Subsequently, both the time-accurate and time-averaged propeller performance can be obtained (Subsections 9.3.2 and 9.3.3). All results discussed in this section were computed for a freestream velocity of 19 m/s, while the propeller was positioned at the same position behind the pylon trailing edge as in the experimental evaluations: $\Delta X = 114$ mm.

9.3.1 Propeller Inflow

The propeller inflow was determined using the computed pylon wake profiles discussed in Chapter 8, which resulted in the propeller inflow depicted in Figure 9.2.

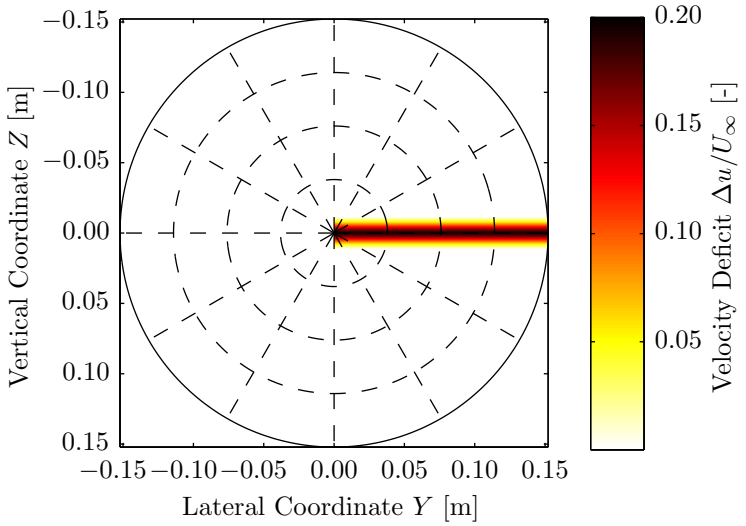

Figure 9.2: Propeller inflow: overview of the velocity deficit at the position of the propeller disk. Installed configuration, $U_\infty = 19$ m/s, extended pylon.

Figure 9.2 shows that the effects of installation on the propeller inflow velocity field are confined to a limited polar region centered around the position of the pylon. This is as expected considering the relatively thin wake profile shed behind the pylon. The unsteady lift resulting from the presence of the velocity deficit at the propeller plane requires the input of the gust velocity normal to the airfoil, defined positive in the direction of the outward normal of the blade section's upper surface. The normal gust velocities corresponding to the velocity deficit data shown in Figure 9.2 are presented in Figure 9.3.

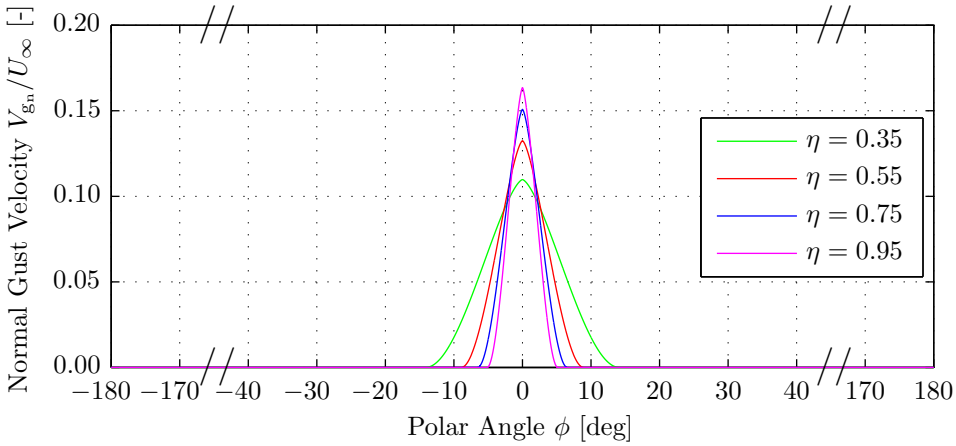

Figure 9.3: Propeller inflow: gust profile in the normal direction at various radial stations $\eta = r/R$. Installed configuration, $U_\infty = 19$ m/s, extended pylon.

From Figure 9.3 it is observed that at the inboard radial stations the constant-width wake region is experienced over a larger range of polar angles than at the outboard stations. Furthermore, the effect of the conversion of the gust from the axial to the normal direction is to change the amplitude of the gust velocities. Because of the increase of the blade pitch angle with increasing radial coordinate the amplitude of the local normal gust velocity should increase from root to tip. This is confirmed by Figure 9.3.

The computation of the unsteady lift coefficient due to the change in the angle of attack in the pylon wake requires the input of the Fourier coefficients of the normal gust profiles which were presented in Figure 9.3. The absolute values of the Fourier coefficients computed for the gust profiles displayed in Figure 9.3 are depicted in Figure 9.4.

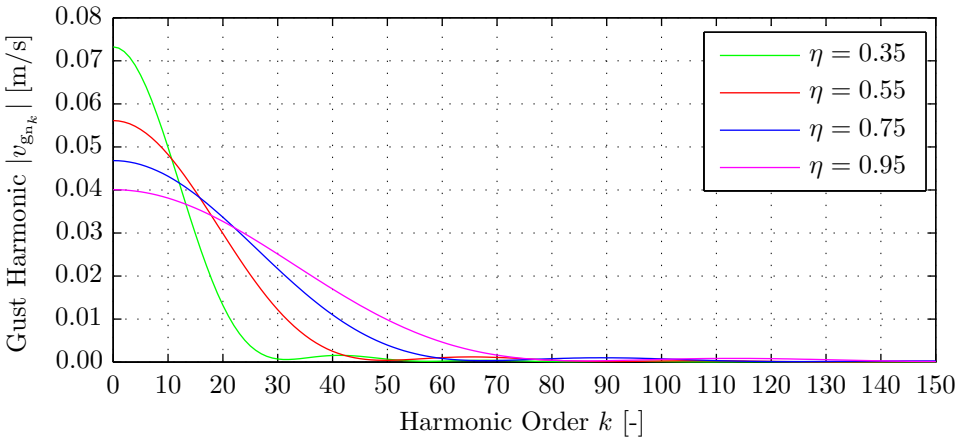

Figure 9.4: Propeller inflow: Fourier coefficients of the gust in the normal direction at various radial stations $\eta = r/R$. Installed configuration, $U_\infty = 19$ m/s, extended pylon.

The Fourier coefficients displayed in Figure 9.4 show that the gust harmonics are present at both the odd and the even harmonic orders. This agrees with the absence of symmetry features in the gust profiles. Furthermore, it is observed that the number of harmonic orders for which the Fourier coefficients have a significant value increases with increasing radial coordinate. This is explained by the previous observation that the gust velocity profile becomes increasingly steep with increasing radial coordinate. Finally, although not visible in Figure 9.4, it should be noted that because the gust profiles are even functions the imaginary parts of the Fourier coefficients are equal to zero for all harmonics.

9.3.2 Time-Accurate Propeller Performance

With the propeller inflow in the installed configuration computed, the time-accurate response of the blade sections was determined following the methods outlined in Subsection 7.2.2. The analysis first considered a single blade, for which the change in the lift and drag coefficients due to the installation effects were computed as a function of the polar angle ϕ (Paragraph 9.3.2.1). Both the change in the dynamic pressure and the angle of attack experienced in the pylon wake region were taken into account. With the response of a single blade computed for all polar angles, the results were converted to thrust and torque time histories and generalized to the entire propeller (Paragraph 9.3.2.2).

9.3.2.1 Lift and Drag of a Single Blade

The normal gust profiles experienced by the propeller blades as depicted in Figure 9.3 result in time-dependent changes to the steady-state lift and drag forces. Because of the velocity deficit, in the pylon wake region both the dynamic pressure and the angle of attack experienced by the blade sections change when compared to the undisturbed conditions. The resulting effects on the blade lift and drag response are discussed below. All results presented in this paragraph were computed for a freestream velocity of 19 m/s and an advance ratio of $J = 0.9$.

Steady-State Lift and Drag Response

The effects of installation on the propeller blade loads are assessed by taking the isolated, steady-state solution as baseline. Therefore, first the computed radial distributions of the lift and drag coefficients in the isolated configuration are presented in Figures 9.5 and 9.6, respectively. For reference, the computed blade angles of attack are added to Figure 9.5.

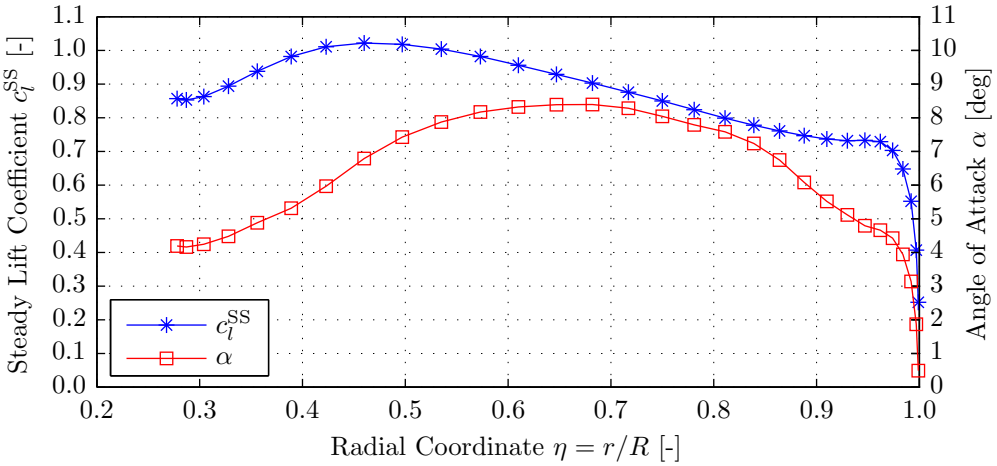

Figure 9.5: Radial distributions of the steady-state lift coefficient and section angle of attack. Isolated configuration, $U_\infty = 19$ m/s, $J = 0.9$.

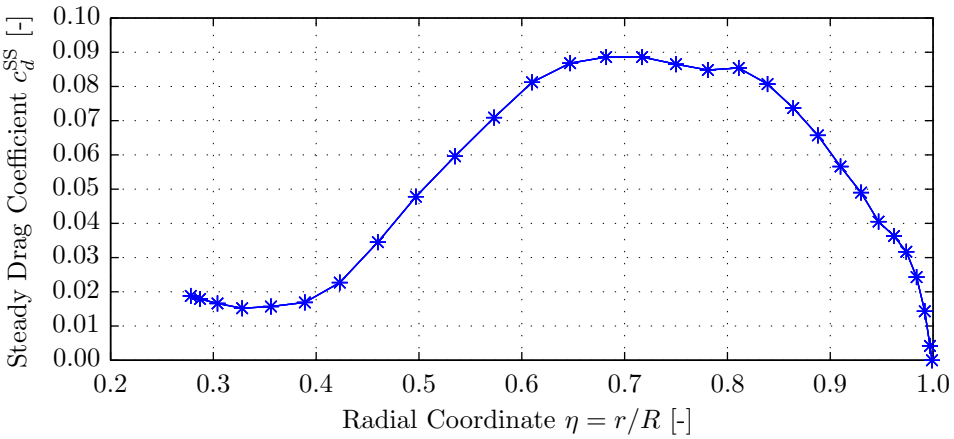

Figure 9.6: Radial distribution of the steady-state drag coefficient. Isolated configuration, $U_\infty = 19$ m/s, $J = 0.9$.

The lift distribution depicted in Figure 9.5 shows that the highest lift coefficients are obtained at the inboard sections. Analysis of the angle of attack distribution shows that the maximum angle of attack on the other hand is reached around radial stations between 0.5 and 0.8 times the propeller radius. However, considering the small thickness-to-chord ratio of the outboard blade sections in the outboard region of the blade at these angles of attack the blades will already start to stall, thereby limiting the local lift coefficients. The drag coefficient shown in Figure 9.6 is relatively high at the radial stations between 0.5 and 0.9 times the propeller radius, hence confirming the hypothesis of the onset of stall on the outboard sections.

Unsteady Lift and Drag Response

The unsteady lift and drag response is obtained by adding the effects due to the change in the dynamic pressure and the change in the angle of attack in the wake region. These two contributions are elaborated upon in more detail in Appendix E.1.2 and E.1.3; below only the total unsteady response is discussed. Figures 9.7 and 9.8 present the unsteady lift and drag coefficients as a function of the polar angle for the same radial stations as considered in previous figures shown in the current subsection. Note that the final installed lift and drag coefficients are computed at each radial station by adding the unsteady lift and drag coefficients to the steady-state values presented in Figures 9.5 and 9.6.

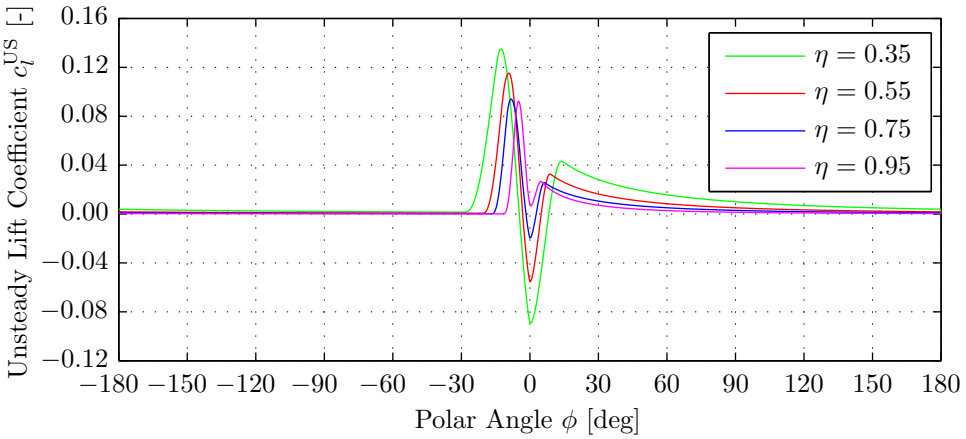

Figure 9.7: Unsteady lift coefficient due to the installation effects at various radial stations $\eta = r/R$. Installed configuration, $U_\infty = 19$ m/s, $J = 0.9$, extended pylon.

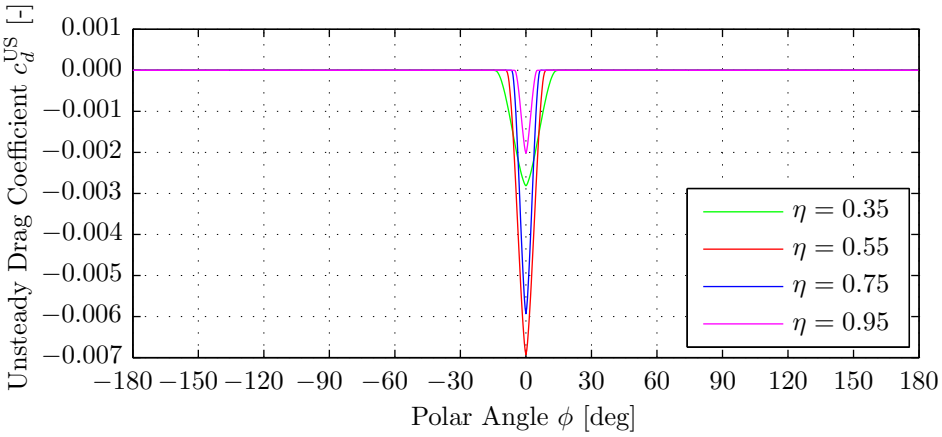

Figure 9.8: Unsteady drag coefficient due to the installation effects at various radial stations $\eta = r/R$. Installed configuration, $U_\infty = 19$ m/s, $J = 0.9$, extended pylon.

The unsteady lift response plotted in Figure 9.7 shows a pattern with one local maximum at a positive lift coefficient and one local minimum at a negative value for the inboard stations. This results from the fact that at the inboard radial stations the response due to the change in the angle of attack leads the gust vector by a larger phase angle than at the outboard stations. As a result, the contributions to the unsteady lift of the change in the dynamic pressure and the change in the angle of attack are separated, which is recognized directly in the total unsteady lift response. In the outboard part of the blade the lift response due to the change in the angle of attack displays a smaller phase shift from the gust velocity vector. Now the reduction in the lift coefficient due to the reduced dynamic pressure is mostly offset by the increase in lift due to the increase in the angle of attack, thereby increasing the value of the local minimum towards zero.

The unsteady drag coefficient depicted in Figure 9.8 follows the change in the dynamic pressure in the wake region, since the effect of the change in the angle of attack is neglected. The absolute levels for the different radial stations depend on the steady-state drag coefficient and the relative magnitude of the velocity deficit compared to the undisturbed effective velocity.

For future reference, the Fourier coefficients corresponding to the unsteady lift response depicted in Figure 9.7 are presented in Figure 9.9.

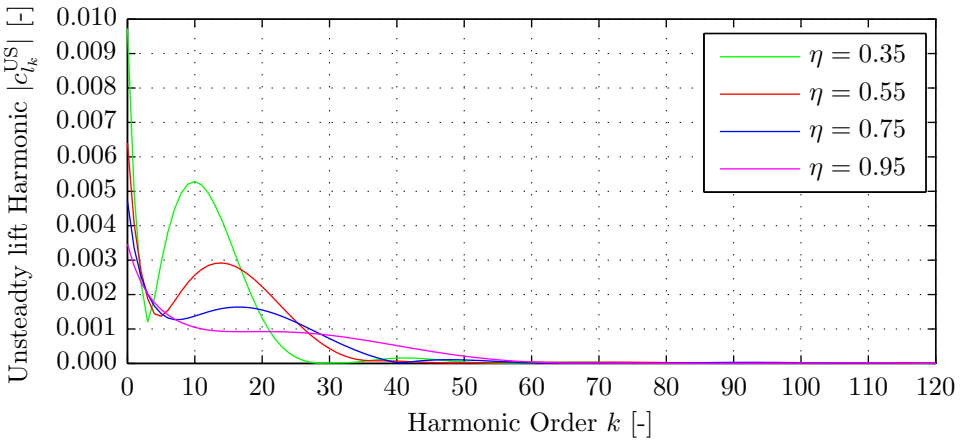

Figure 9.9: Fourier coefficients of the unsteady lift coefficient at various radial stations $\eta = r/R$. Installed configuration, $U_\infty = 19$ m/s, $J = 0.9$, extended pylon.

Figure 9.9 shows that the importance of the high frequency content in the unsteady lift coefficient increases with increasing radial coordinate. This is as expected considering the unsteady lift profiles shown in Figure 9.7. To properly reconstruct the unsteady lift response at all radial stations approximately sixty Fourier coefficients are required.

9.3.2.2 Thrust and Torque of the Entire Propeller

With the lift and drag response computed for a single blade, the unsteady thrust and torque due to the installation effects are computed for the entire propeller. The results are plotted versus the polar angle ϕ of the first blade section (located at $\phi = 0°$ at the beginning of the rotation) in Figures 9.10 and 9.11, respectively. Apart from the total unsteady thrust and torque coefficients, also the separate contributions due to the change in the angle of attack and the change in the dynamic pressure in the pylon wake region are indicated. Furthermore, the corresponding time-averaged result is also added.

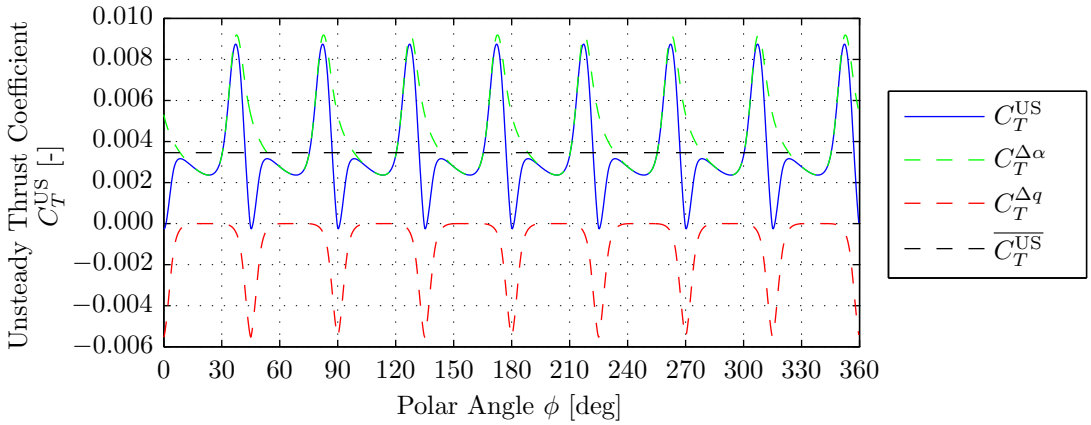

Figure 9.10: Unsteady thrust coefficient versus the polar angle ϕ.
Installed configuration, $U_\infty = 19$ m/s, $J = 0.9$, extended pylon.

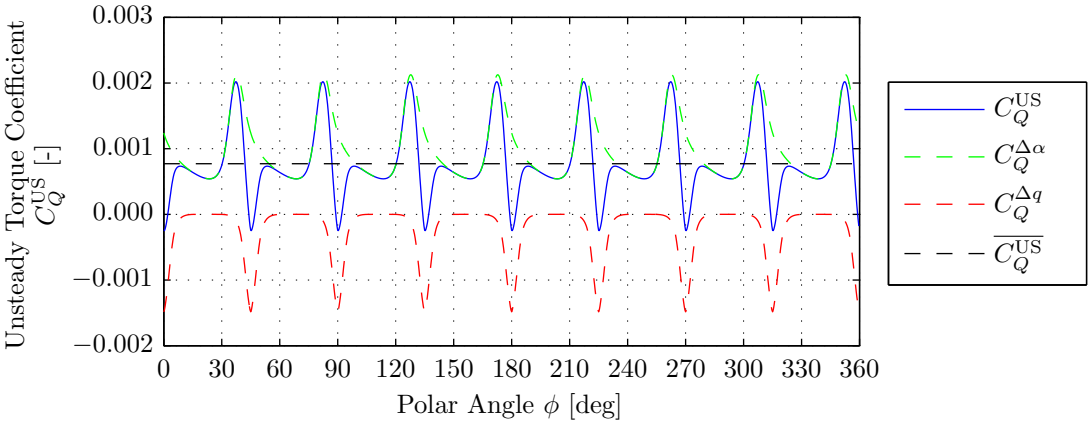

Figure 9.11: Unsteady torque coefficient versus the polar angle ϕ.
Installed configuration, $U_\infty = 19$ m/s, $J = 0.9$, extended pylon.

Figures 9.10 and 9.11 show that the change in the propeller thrust and torque due to the installation effects behaves as a superposition of the radial blade responses presented in Figures 9.7 and 9.8 (showing the unsteady additional lift and drag coefficients, respectively). The additional thrust and torque due to installation peak around ten degrees before a blade passes through the center of the pylon wake ($\phi = (i-1)\cdot 45°$, with i the index of the blade). In total eight positive peaks are present, corresponding to the number of blades of the propeller.

The unsteady thrust and torque coefficients shown in Figures 9.10 and 9.11 are added to the isolated values to compute the total installed thrust and torque coefficients. A comparison of the resulting data for the isolated and installed configurations is presented in Figure 9.12.

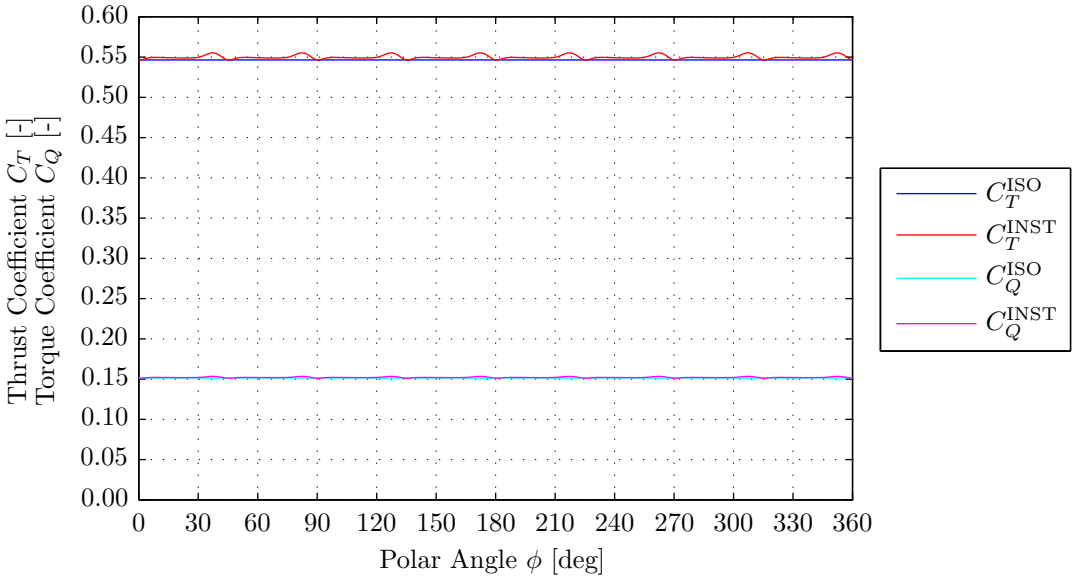

Figure 9.12: Effects of installation on the thrust and torque coefficient versus the polar angle ϕ. Isolated and installed configurations, $U_\infty = 19$ m/s, $J = 0.9$, extended pylon.

Figure 9.12 shows that at the selected operating point the effects of installation on the thrust and torque coefficients are small. For comparison reasons, Table 9.1 presents the numerical data corresponding to the most important results depicted in Figure 9.12.

Table 9.1: Comparison of the isolated and installed propeller thrust and torque coefficients. $U_\infty = 19$ m/s, $J = 0.9$, extended pylon.

Parameter	Value [-]	Parameter	Value [-]
C_T^{ISO}	0.547	C_Q^{ISO}	0.151
$\overline{C_T^{\mathrm{INST}}}$	0.550	$\overline{C_Q^{\mathrm{INST}}}$	0.152
$\frac{\left(\overline{C_T^{\mathrm{INST}}} - C_T^{\mathrm{ISO}}\right)}{C_T^{\mathrm{ISO}}}$	0.6%	$\frac{\left(\overline{C_Q^{\mathrm{INST}}} - C_Q^{\mathrm{ISO}}\right)}{C_Q^{\mathrm{ISO}}}$	0.5%
$\max\left(C_T^{\mathrm{INST}}\right)$	0.555	$\max\left(C_Q^{\mathrm{INST}}\right)$	0.153
$\min\left(C_T^{\mathrm{INST}}\right)$	0.546	$\min\left(C_Q^{\mathrm{INST}}\right)$	0.151
$\frac{\max\left(C_T^{\mathrm{INST}}\right) - \min\left(C_T^{\mathrm{INST}}\right)}{\overline{C_T^{\mathrm{INST}}}}$	1.6%	$\frac{\max\left(C_Q^{\mathrm{INST}}\right) - \min\left(C_Q^{\mathrm{INST}}\right)}{\overline{C_Q^{\mathrm{INST}}}}$	1.5%

The data presented in Table 9.1 confirms the observation that the effects of installation on the time-accurate thrust and torque coefficients are small. At the selected operating point the peak-to-peak variation in the installed thrust coefficient data equals approximately 2% of the average value. Note that the results presented in Table 9.1 are only valid for a single propeller operating point. For completeness, Figure 9.13 depicts the peak-to-peak variations in the installed thrust and torque signals for all considered advance ratios.

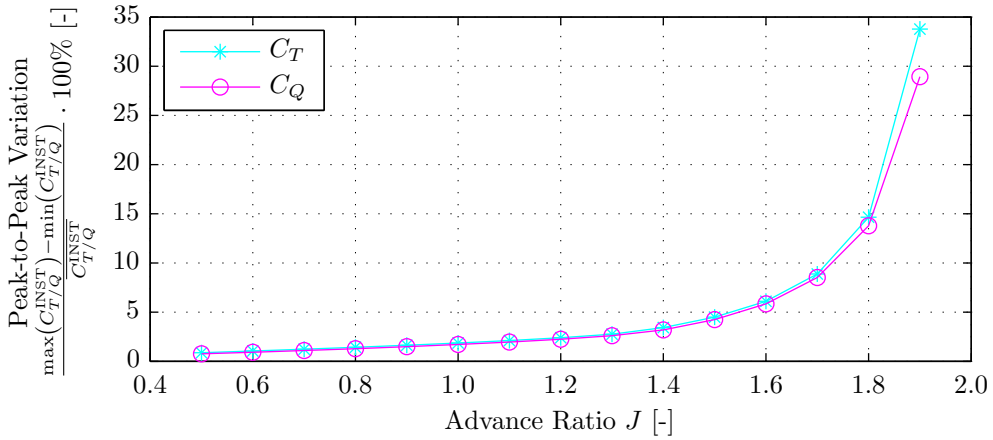

Figure 9.13: Peak-to-peak variations in the time-accurate thrust and torque coefficients. Installed configuration, $U_\infty = 19$ m/s, $0.5 \leq J \leq 1.9$, extended pylon.

Figure 9.13 shows that for advance ratios below $J = 1.4$ the maximum peak-to-peak variations in the installed thrust and torque signals are smaller than 4%. For higher advance ratios the peak-to-peak variations increase rapidly as a result of the increased impact of the installation effects. Also, the steady-state loading is much smaller at these high advance ratios, hence increasing the relative effect of the additional thrust and torque due to the installation effects.

9.3.3 Time-Averaged Propeller Performance

Time-accurate data was computed for all advance ratios in the range $0.5 \leq J \leq 1.9$, and subsequently averaged to obtain the installed propeller performance diagram. This diagram is presented in Figure 9.14, in which the propeller performance for the isolated configuration is also plotted.

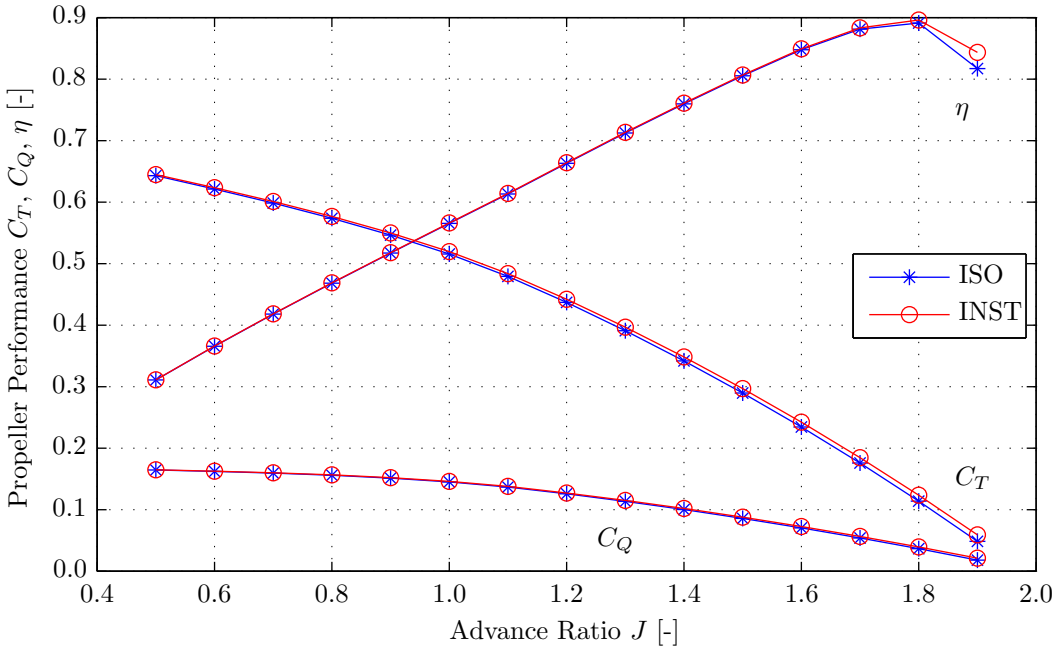

Figure 9.14: Propeller performance diagram: effects of installation. Isolated and installed configurations, $U_\infty = 19$ m/s, $0.5 \leq J \leq 1.9$, with rotation correction.

Figure 9.14 confirms that the effects of installation on the propeller performance are small. To further assess the difference between the time-averaged performance in the installed and isolated configurations, the relative differences between the installed and isolated thrust and torque coefficients were computed for all advance ratios considered and plotted in Figure 9.15.

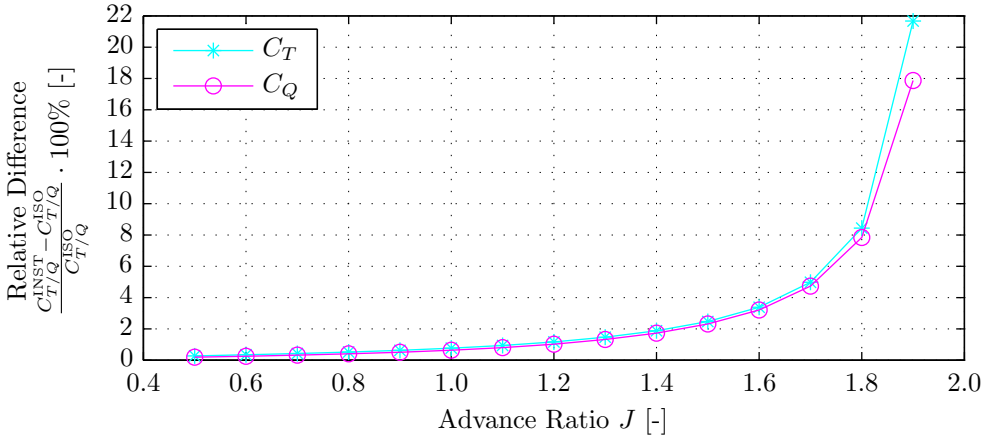

Figure 9.15: Relative effects of installation on the time-averaged thrust and torque coefficients. Isolated and installed configurations, $U_\infty = 19$ m/s, $0.5 \leq J \leq 1.9$, extended pylon.

The results presented in Figure 9.15 conform to the expectations. For advance ratios up to $J = 1.0$ the change in the time-averaged thrust and torque coefficients is smaller than one percent. At these low advance ratios the rotational velocity of the propeller is high hence the effect of a change in the inflow velocity is relatively small. When increasing the advance ratio the effects of installation gradually become more pronounced. At $J = 1.4$ the installation effects result in an increase in the thrust and torque coefficients of about 2% relative to the isolated values, while at the highest advance ratio considered ($J = 1.8$) the difference is around 20%. It should be noted that at this advance ratio the propeller is barely producing thrust so small differences in thrust and torque due to the installation effects will lead to large relative differences.

9.4 Blown Configuration

To quantify the effects of pylon trailing edge blowing on the propeller performance computations were also performed for the propeller in the blown configuration. The same operating conditions were considered as before, with a freestream velocity of 19 m/s and an advance ratio range equal to $0.5 \leq J \leq 1.9$. The blown pylon wake profile was extracted from the experimental data, after which the remainder of the computations followed the approach taken for the unblown, installed case. Again, first the propeller inflow was computed (Subsection 9.4.1). With the non-uniform inflow determined, the time-accurate and time-averaged propeller performance were obtained (Subsections 9.4.2 and 9.4.3, respectively).

9.4.1 Propeller Inflow

The blown pylon wake profile used in the numerical evaluations was obtained from the experimental measurements. The selected profile was obtained at a blowing rate of $Q = 600$ L/min, hence corresponding to the result shown in Figure 3.7. The entire wake velocity profile was scaled such that the velocity deficit outside of the pylon wake region was equal to zero. The resulting inflow on the propeller plane is depicted in Figure 9.16.

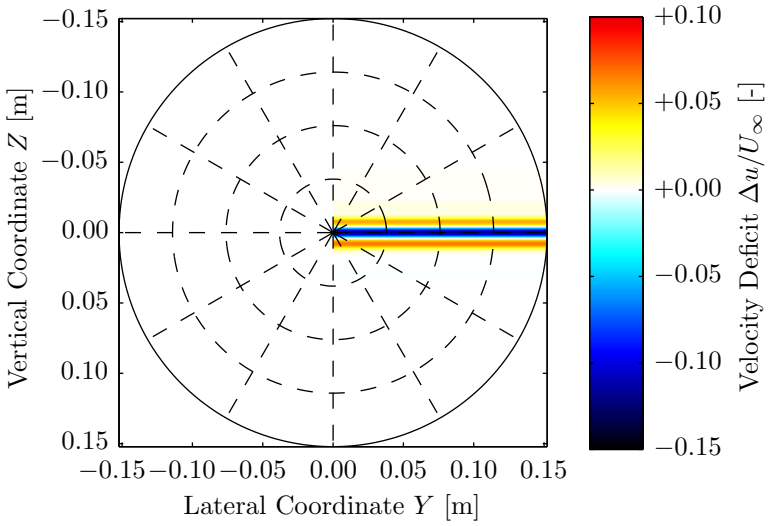

Figure 9.16: Propeller inflow: overview of the velocity deficit at the position of the propeller disk. Blown configuration, $U_\infty = 19$ m/s, $Q = 600$ L/min, extended pylon.

The results presented in Figure 9.16 show that the application of blowing in this case did not fully eliminate the velocity deficit in the pylon wake. In the center of the wake the velocity deficit is negative, corresponding to a velocity larger than that of the freestream. Overall, the magnitude of the variations in inflow velocity on the propeller disk are smaller than for the installed case shown in Figure 9.2.

The presence of the velocity deficit (be it positive or negative) results in unsteady lift production by the propeller blades. The resulting change in the blade section's angle of attack is obtained by considering the velocity deficit as a gust normal to the airfoil, as plotted in Figure 9.17 for the same range of radial coordinates as used before.

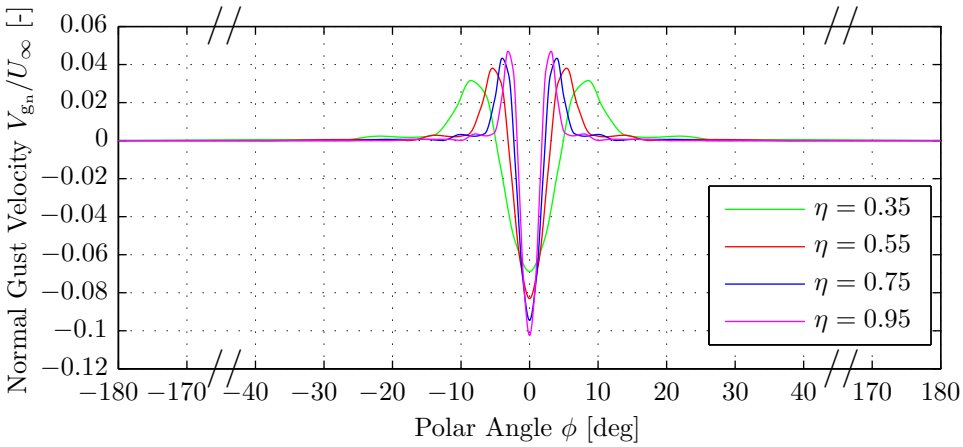

Figure 9.17: Propeller inflow: gust profile in the normal direction at various radial stations $\eta = r/R$. Blown configuration, $U_\infty = 19$ m/s, $Q = 600$ L/min, extended pylon.

Figure 9.17 shows that the amplitude of the gusts at the different radial stations are different because the conversion from velocity deficit to normal gust includes the radially decreasing blade pitch angle. The method used to compute the unsteady lift coefficients resulting from the change in the angle of attack in the wake region is performed in the frequency domain. Therefore, the Fourier coefficients of the normal gust profiles are required. The corresponding results are depicted in Figure 9.18.

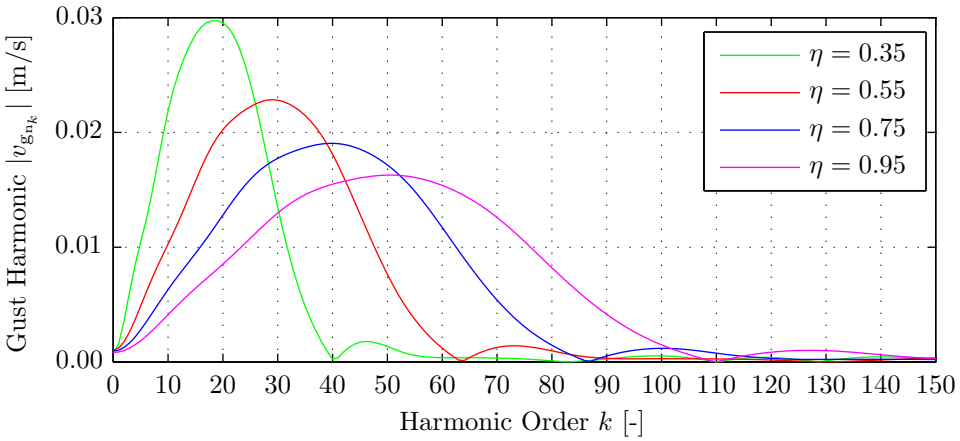

Figure 9.18: Propeller inflow: Fourier coefficients of the gust in the normal direction at various radial stations $\eta = r/R$. Blown configuration, $U_\infty = 19$ m/s, $Q = 600$ L/min, extended pylon.

Comparison with the Fourier coefficients computed for the installed case shown in Figure 9.4 learns that in the blown configuration the higher harmonics have become more important. Whereas in the installed configuration the absolute value of the gust harmonics continuously decreased with increasing harmonic order, in blown conditions the maximum value is obtained at non-zero harmonic order for all radial stations. The position of this maximum shifts towards the higher harmonics when increasing the value of the radial coordinate, which is as expected considering the smaller radial extent of the pylon wake region at the outboard stations.

9.4.2 Time-Accurate Propeller Performance

Having determined the propeller inflow in the blown configuration, the analysis proceeded to find the time-accurate propeller performance. For this purpose again the methods discussed in Subsection 7.2.2 were used. First, a single blade was considered for which the time-dependent lift and drag coefficients were computed as a function of the polar angle ϕ (Paragraph 9.4.2.1). Knowing the time-dependent lift and drag coefficients produced by a single blade, the thrust and torque response of the entire propeller could be computed (Paragraph 9.4.2.2).

9.4.2.1 Lift and Drag of a Single Blade

The unsteady lift and drag coefficients computed from the propeller inflow discussed in Section 9.4.1 are presented in Figures 9.19 and 9.20, respectively.

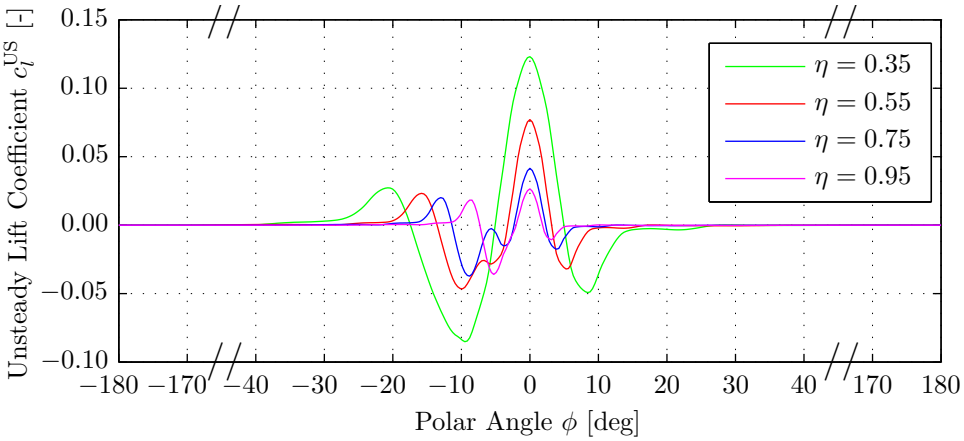

Figure 9.19: Unsteady lift coefficient due to the installation effects at various radial stations $\eta = r/R$. Blown configuration, $U_\infty = 19$ m/s, $J = 0.9$, $Q = 600$ L/min, extended pylon.

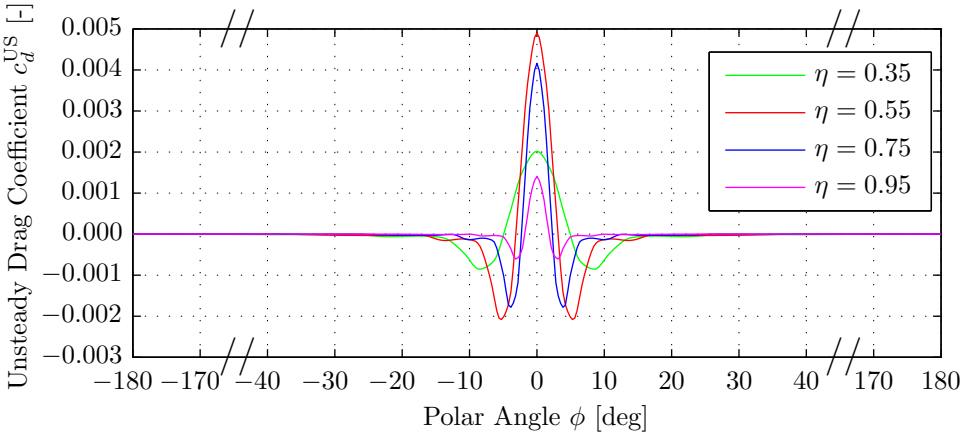

Figure 9.20: Unsteady drag coefficient due to the installation effects at various radial stations $\eta = r/R$. Blown configuration, $U_\infty = 19$ m/s, $J = 0.9$, $Q = 600$ L/min, extended pylon.

The unsteady lift coefficient plotted in Figure 9.19 shows that when a blade section rotates towards the wake region the lift first starts to increase. When continuing towards the center of the pylon wake the blades experience a strong negative peak in the velocity deficit, indicating that the inflow velocity is increased relative to the undisturbed value. Correspondingly, the angle of attack is reduced and the lift coefficient starts to decrease. Subsequently, around the center of the pylon wake the local increase in the dynamic pressure starts to become relevant, resulting in a clear increase in the lift coefficient. Thereafter, for larger polar angles a second local minimum is observed due to the reduced dynamic pressure in the final part of the wake region. The amplitude of the lift fluctuations decreases when going outboard. This is as expected considering the relatively smaller effect at the outboard stations of a change in the inflow velocity on the total effective velocity, and the higher frequencies of the gusts experienced by the outboard sections.

The unsteady drag coefficient plotted in Figure 9.20 only contains a contribution from the change in the dynamic pressure in the pylon wake region. As a result, the shape of the response is equal to the negative of the velocity deficit profile presented before in Figure 9.17.

The Fourier coefficients corresponding to the unsteady lift response depicted in Figure 9.19 are presented in Figure 9.21.

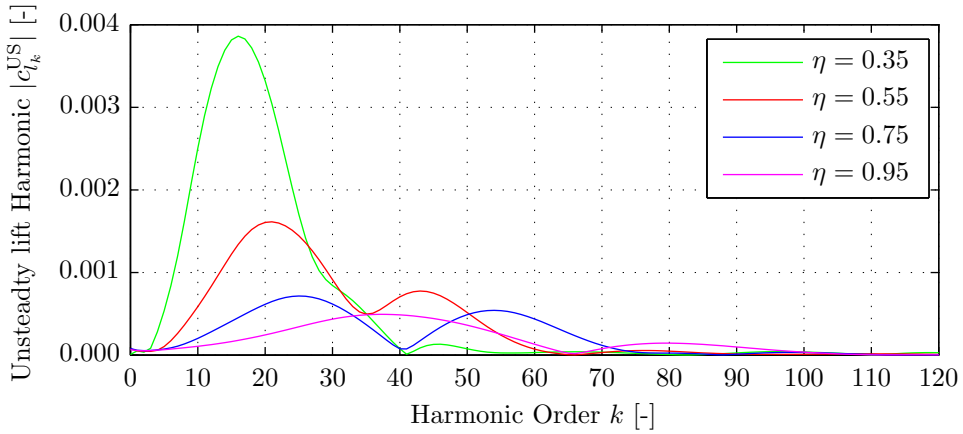

Figure 9.21: Fourier coefficients of the unsteady lift coefficient at various radial stations $\eta = r/R$. Blown configuration, $U_\infty = 19$ m/s, $J = 0.9$, $Q = 600$ L/min, extended pylon.

The harmonic content of the unsteady lift coefficient in the blown configuration shown in Figure 9.21 is as expected considering the behavior of the Fourier coefficients of the blown gust profile depicted in Figure 9.18. Comparison with the installed results presented in Figure 9.9 shows that in general the magnitude of the coefficients is smaller in the blown configuration, while the application of blowing results in a clear shift towards the higher harmonics.

9.4.2.2 Thrust and Torque of the Entire Propeller

The unsteady change in the thrust and torque coefficients due to the pylon wake effects in the blown configuration are shown in Figures 9.22 and 9.23. Again the signals are referenced to the polar angle ϕ of the blade that was positioned at $\phi = 0°$ at the start of the rotation.

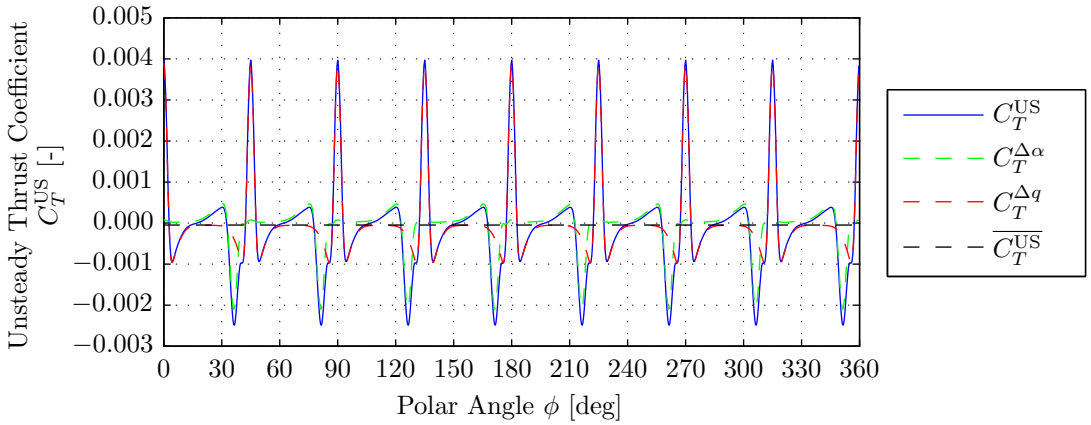

Figure 9.22: Unsteady thrust coefficient versus the polar angle ϕ.
Blown configuration, $U_\infty = 19$ m/s, $J = 0.9$, $Q = 600$ L/min, extended pylon.

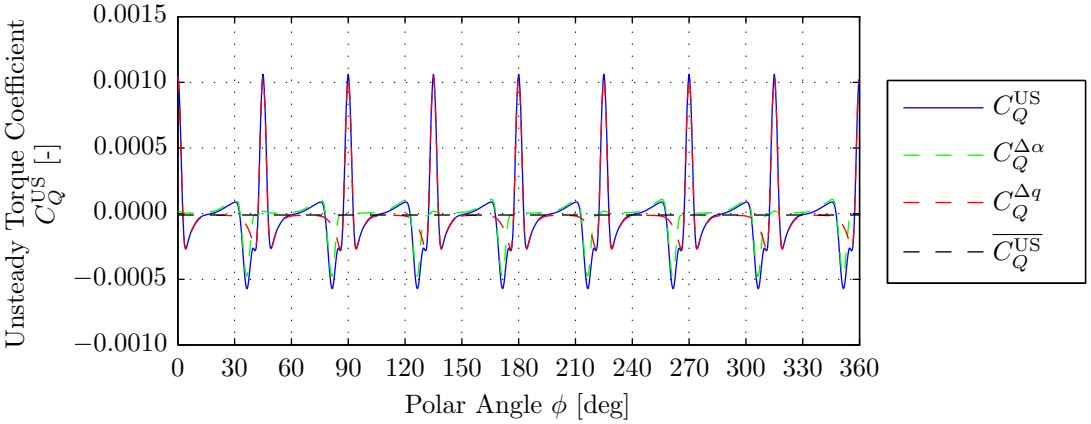

Figure 9.23: Unsteady torque coefficient versus the polar angle ϕ.
Blown configuration, $U_\infty = 19$ m/s, $J = 0.9$, $Q = 600$ L/min, extended pylon.

Figures 9.22 and 9.23 show similar patterns. The change in the dynamic pressure in the wake region results in a clear positive peak in the change in the thrust and torque coefficient following the passage of a blade through the pylon wake region. The change in the angle of attack is mainly recognized as a moderate negative peak in the thrust and torque response, occurring slightly before the blades reach the center of the pylon wake.

The unsteady thrust and torque coefficients resulting from the installation effects were added to the steady-state results to obtain the final thrust and torque coefficients in the blown configuration. The corresponding results are plotted in Figure 9.24, in which the isolated (steady-state) results are also added for comparison reasons.

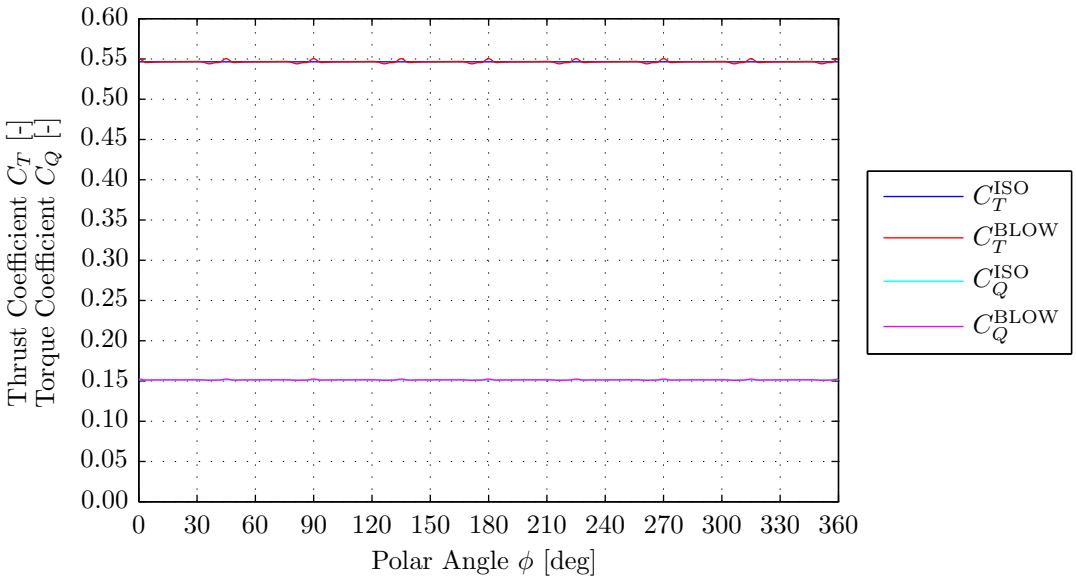

Figure 9.24: Blown thrust and torque coefficient versus the polar angle ϕ.
Blown configuration, $U_\infty = 19$ m/s, $J = 0.9$, $Q = 600$ L/min, extended pylon.

From Figure 9.24 it is observed that also in the blown configuration the effects of installation on the propeller thrust and torque are very small. To allow for an accurate quantitative comparison between the time-accurate isolated and blown propeller performance, the most important results from Figure 9.24 are summarized in Table 9.2.

Table 9.2: Comparison of the isolated and blown propeller thrust and torque coefficients.
$U_\infty = 19$ m/s, $J = 0.9$, $Q = 600$ L/min, extended pylon.

Parameter	Value [-]	Parameter	Value [-]
C_T^{ISO}	0.547	C_Q^{ISO}	0.151
$\overline{C_T^{\mathrm{BLOW}}}$	0.546	$\overline{C_Q^{\mathrm{BLOW}}}$	0.151
$\frac{\left(\overline{C_T^{\mathrm{BLOW}}} - C_T^{\mathrm{ISO}}\right)}{C_T^{\mathrm{ISO}}}$	-0.01%	$\frac{\left(\overline{C_Q^{\mathrm{BLOW}}} - C_Q^{\mathrm{ISO}}\right)}{C_Q^{\mathrm{ISO}}}$	-0.01%
$\max\left(C_T^{\mathrm{BLOW}}\right)$	0.550	$\max\left(C_Q^{\mathrm{BLOW}}\right)$	0.152
$\min\left(C_T^{\mathrm{BLOW}}\right)$	0.544	$\min\left(C_Q^{\mathrm{BLOW}}\right)$	0.151
$\frac{\max\left(C_T^{\mathrm{BLOW}}\right) - \min\left(C_T^{\mathrm{BLOW}}\right)}{\overline{C_T^{\mathrm{BLOW}}}}$	1.2%	$\frac{\max\left(C_Q^{\mathrm{BLOW}}\right) - \min\left(C_Q^{\mathrm{BLOW}}\right)}{\overline{C_Q^{\mathrm{BLOW}}}}$	1.1%

Table 9.2 shows that the isolated and blown propeller performance are virtually equal. At the considered operating point the remaining fluctuations in the thrust and torque coefficients in the blown configuration amount to a peak-to-peak variation of about 1% of the time-averaged value. Note again that the values presented in Table 9.2 are only valid for a single operating point ($U_\infty = 19$ m/s and $J = 0.9$). Figure 9.25 is presented to quantify the peak-to-peak variations in the time-accurate thrust and torque coefficients in the blown configuration for all considered advance ratios.

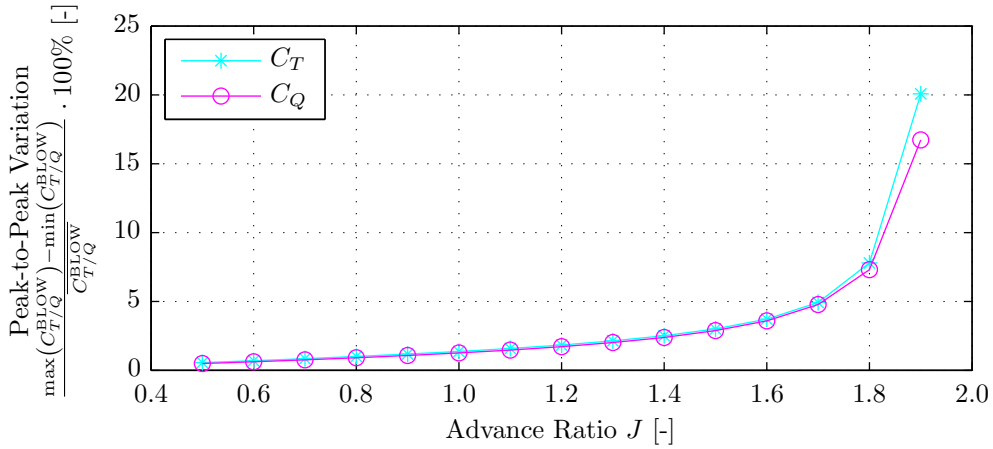

Figure 9.25: Peak-to-peak variations in the time-accurate thrust and torque coefficients. Blown configuration, $U_\infty = 19$ m/s, $0.5 \leq J \leq 1.9$, $Q = 600$ L/min, extended pylon.

Figure 9.25 shows that the evolution of the peak-to-peak variations in the thrust and torque signals in the blown configuration is similar to that shown in Figure 9.13 for the installed configuration. However, the application of blowing reduces the amplitude of the fluctuations. For advance ratios below $J = 1.4$ the maximum peak-to-peak variations in the thrust and torque signals equal around 2%. At higher advance ratios the magnitude of the fluctuations starts to increase rapidly as a result of the larger relative effects of installation.

9.4.3 Time-Averaged Propeller Performance

The time-accurate blown propeller performance was computed for the entire advance ratio range $0.5 \leq J \leq 1.9$. The resulting time-averaged propeller performance is displayed in Figure 9.26, in which the results computed for the isolated configuration are added as reference.

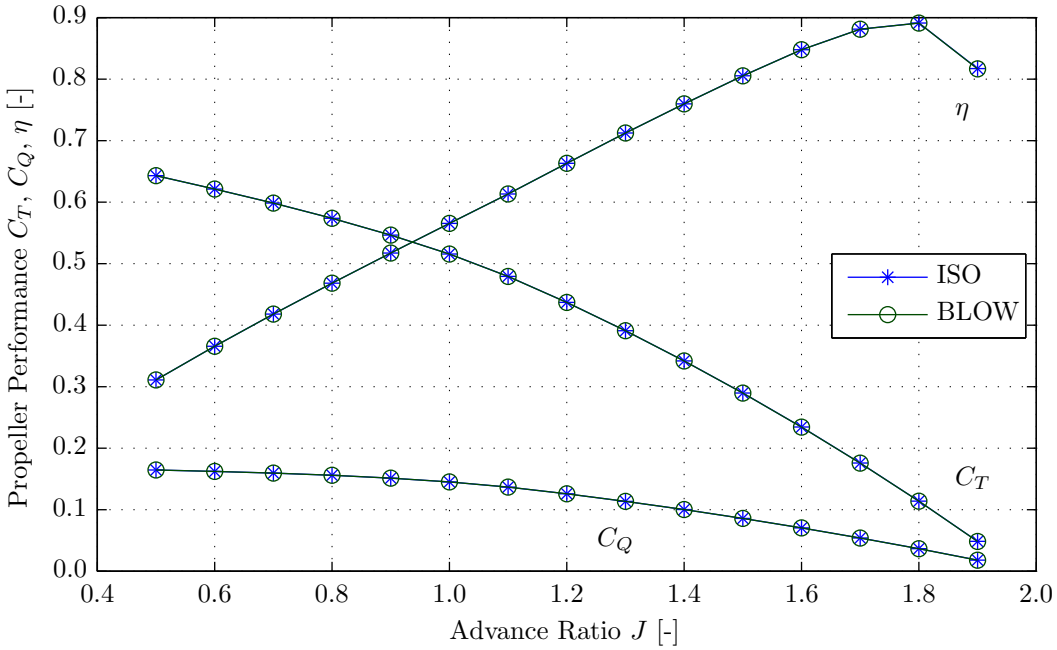

Figure 9.26: Propeller performance diagram: effects of blowing.
Blown configuration, $U_\infty = 19$ m/s, $0.5 \leq J \leq 1.9$, $Q = 600$ L/min, with rotation correction.

From Figure 9.26 it appears that the differences between the time-averaged propeller performance in the isolated and blown configurations are very small. Over the entire advance ratio range considered the thrust and torque coefficients computed for both configurations are directly on top of each other. To gain additional insight in the effects of installation on the time-averaged propeller performance the relative differences between the blown and isolated thrust and torque coefficients were computed. The corresponding results are depicted in Figure 9.27.

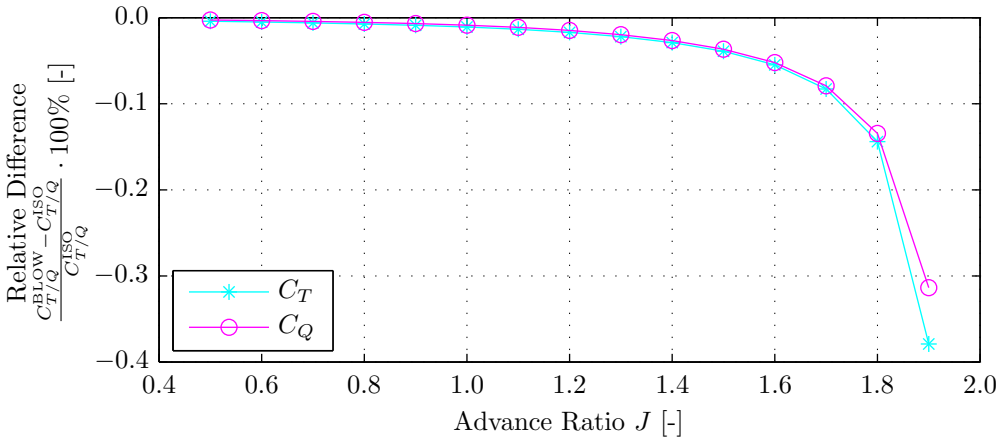

Figure 9.27: Relative differences between the isolated and blown time-averaged thrust and torque coefficients. Isolated and blown configurations, $U_\infty = 19$ m/s, $0.5 \leq J \leq 1.9$, $Q = 600$ L/min, extended pylon.

Figure 9.27 confirms the previous conclusion that the time-averaged isolated and blown propeller performance are virtually equal. The relative differences between the thrust and torque coefficients computed for both configurations are within -0.5% over the entire advance ratio range. A comparison with the results for the installed configuration depicted in Figure 9.15 shows that the application of blowing decreases the effects of installation on the time-averaged propeller performance. It should however be noted that for the installed configuration the effects were already small.

Chapter 10

Numerical Results: Powered Propeller Noise Emissions

The final chapter describing the results obtained from the numerical analysis focuses on the analytic computation of the propeller noise emissions. Similarly as for the propeller performance evaluations again the isolated, installed, and blown configurations are considered. This chapter is started with Section 10.1 which presents an overview of the main analysis settings used for the analytic noise computations. Subsequently, the results for the isolated propeller are presented in Section 10.2, followed by a discussion of the computed noise emissions in the installed configuration in Section 10.3. Finally, Section 10.4 presents the noise emissions computed for the blown configuration.

10.1 Analysis Overview

The analytic noise computations were performed using the frequency domain methods developed by Hanson, as outlined in Section 7.3. The same freestream velocities were considered as used in the propeller performance computations and the experimental measurements: 15, 19, 26, and 30 m/s. Additionally, two higher, more realistic velocities were used: 50 and 80 m/s. The computations were performed for the advance ratio range $0.5 \leq J \leq 1.9$, except for the computations at the freestream velocities of 50 and 80 m/s for which the minimum advance ratios were selected such that the maximum tip Mach number remained below 0.85.

Two different noise sources were considered: thickness noise and loading noise. Regarding the thickness noise the blade section thickness distributions corresponding to the actual profiles were extracted from three-dimensional CAD drawings. The loading noise computations required the input of the blade loads obtained from the performance computations. For simplicity, the chordwise distributions of the lift and drag were assumed to be uniform. Although not very accurate, this assumption in general is acceptable at low harmonic order and reasonably low tip speeds for which non-compactness effects are negligible [49]. The effects of the assumption of uniform chordwise loading are discussed in more detail in Appendix E.2.1.2.

All results presented in this chapter are referenced to an observer distance of 1.0 m, while computations were performed for different axial and circumferential directivity angles θ and ϕ (as defined in Section 2.2). Note that the position of the pylon was fixed at $\phi = 0°$, corresponding to the position used for the computations of the propeller performance as

discussed in Chapter 9. While fully implemented in the noise computation method, for all results discussed in this chapter the effects of blade offset and sweep were neglected by setting the parameters ϕ_o and ϕ_s to zero. Considering the straight planform of the propeller blades analyzed in this report this is however not expected to have a significant effect on the final results. Furthermore, all Doppler factors were set to unity to simulate wind tunnel conditions.

10.2 Isolated Configuration

The isolated propeller noise emissions are a result of the periodic displacement of air by the volume of the blades (thickness noise), and the periodic passing of the pressure fields that result from the steady-state blade loads (loading noise). As a result, the propeller noise emissions directly depend on the operating condition of the propeller. This section first discusses the typical directivity patterns of the isolated noise emissions (Subsection 10.2.1), followed by an investigation of the effects of the propeller operating point on the computed noise emissions (Subsection 10.2.2). Finally, the tonal noise components are considered (Subsection 10.2.3).

10.2.1 Directivity Analysis

This subsection discusses the typical axial directivity properties of the computed propeller noise emissions in the isolated configuration. The total sound pressure levels were computed considering the first ten harmonic components due to thickness and loading noise. With the individual harmonics determined, the total sound pressure was obtained by summation. Furthermore, the sound pressures corresponding to the separate harmonic contributions were also determined. An example noise directivity plot is depicted in Figure 10.1, which presents data computed for a freestream velocity of $U_\infty = 50$ m/s and an advance ratio of $J = 0.9$.

It should be noted that in Figure 10.1 the loading noise due to F_1 is in general of the same magnitude as that due to F_2. As discussed in Appendix E.2.1.1 this is the result of the definition of the lift and drag components used in the noise computations. Whereas the actual lift and drag coefficients are defined relative to the advance direction with induced effects taken into account, the force coefficients used in the noise computations are defined relative to the advance direction without induced effects. This was illustrated before in Figure 7.9. Since the addition of the induced effects rotates the lift vector backwards, the change of the coordinate system towards the advance direction without induced effects increases the effective value of the F_1 component. Hence, the loading noise due to F_1 shown in Figure 10.1 mainly results from a contribution of the original lift vector which tends to strongly increase the effective axial force used in the noise computations.

Figure 10.1 shows that for the considered operating point the propeller noise emissions peak around $\theta = 95°$, corresponding to a position slightly aft of the propeller plane. The noise contributions due to thickness and loading due to the F_1 force show a simple directivity pattern without any lobes. The loading noise due to F_2 on the other hand displays a two-lobe directivity pattern with a local minimum at $\theta = 50°$. Analysis of Equations (7.39) and (7.41) learns that for a blade element the node between the two lobes should occur at the axial directivity angle for which $M_\infty - M_r^2 \cos\theta = 0$ holds. Since the pressures in the two separate lobes are 180 degrees out of phase, at directivity angles below the node angle the F_2 loading noise reduces the total loading noise by interfering with the constant-phase loading noise due to F_1. At directivity angles above the node angle on the other hand the two loading noise components have equal phase and hence add up to result in a larger value of the loading noise.

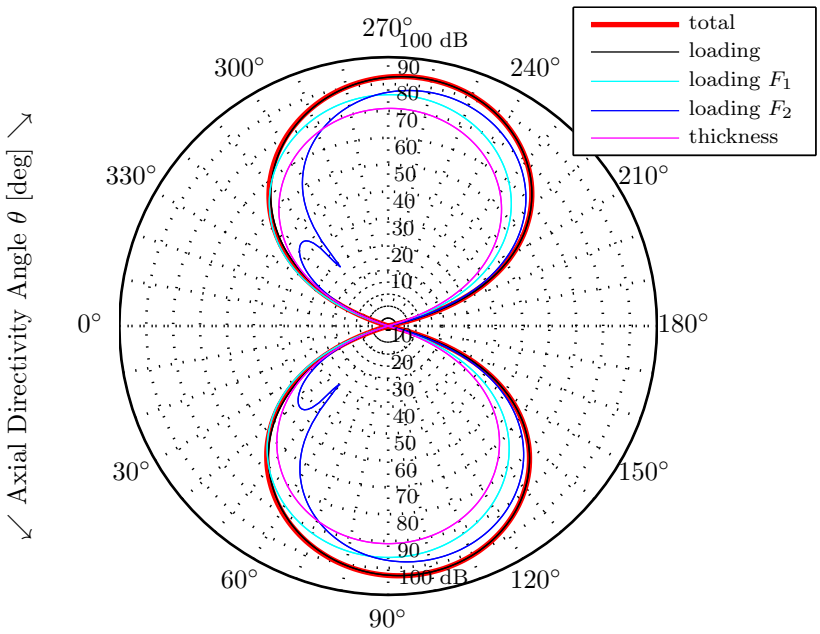

Figure 10.1: Sound pressure level (re 20 μPa, $R = 1.0$ m) versus the axial directivity angle θ. Isolated configuration, $U_\infty = 50$ m/s, $J = 0.9$, $M_t = 0.53$.

10.2.2 Effects of the Propeller Operating Point on the Total SPL

The isolated propeller noise directivity pattern presented in the previous subsection was obtained at a single operating point. Now, the influence of the operating conditions on the isolated propeller's noise emissions is assessed. Both the freestream velocity and the advance ratio were varied, while a constant axial directivity angle of $\theta = 90°$ was selected (corresponding to noise emissions in the propeller plane). First, the propeller noise emissions are analyzed as a function of the advance ratio for a range of different freestream velocities (Paragraph 10.2.2.1). Thereafter, the influence of the tip Mach number is discussed (Paragraph 10.2.2.2).

10.2.2.1 Noise Emissions Versus Advance Ratio and Freestream Velocity

The total sound pressure levels in the propeller plane ($\theta = 90°$) are plotted in Figure 10.2 as a function of the freestream velocity and the advance ratio.

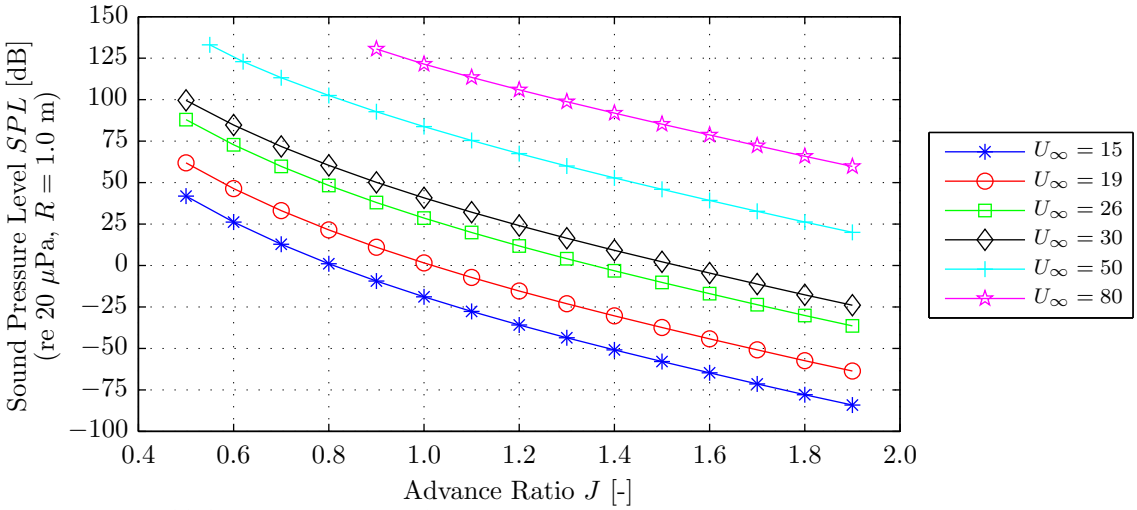

Figure 10.2: Computed total SPL versus the freestream velocity and the advance ratio. Isolated configuration, $U_\infty = [15, 19, 26, 30, 50, 80]$ m/s, $0.5 \leq J \leq 1.9$, $\theta = 90°$.

Figure 10.2 shows that the noise emissions increase with increasing freestream velocity. However, for the lower freestream velocities ($U_\infty \leq 30$ m/s) the SPL decreases more rapidly with the advance ratio than expected. For $U_\infty = 15$ m/s it is observed that even at $J = 0.5$ the SPL is not higher than about 45 dB, while for $J > 0.8$ the SPL becomes smaller than 0 dB corresponding to a sound pressure level inaudible to human ears. Similar trends are observed for freestream velocities in between 19 and 30 m/s, while only for the velocities of 50 and 80 m/s more realistic sound pressure levels are observed at the higher advance ratios.

Based on this observation it is concluded that the behavior of the computed isolated propeller noise is not as expected: for low freestream velocities the SPL decreases more rapidly with the advance ratio than foreseen. This was however independently confirmed by Dr. H.H. Brouwer from the NLR[1], who applied the propeller noise prediction programs developed at the NLR for low freestream velocities and obtained comparable results (for a different propeller geometry). Considering the similarities between the propeller noise prediction methods applied here and used at the NLR it is concluded that the unexpected behavior is not the result of an error in the implementation of the method, but instead should be considered as a limitation of the isolated propeller noise prediction routine. For the combination of a large blade number and a low tip Mach number the radiation efficiency of the noise emissions is underpredicted, which is the result of the behavior of the Bessel function in the equation used to compute the noise harmonics as discussed in detail in Appendix E.2.1.3.

10.2.2.2 Noise Emissions Versus Tip Mach Number and Freestream Velocity

To further investigate the apparent underprediction of the noise levels at low freestream velocities the effect of the tip Mach number on the SPL was analyzed. Figure 10.3 shows the tip Mach number as a function of the advance ratio, followed by Figure 10.4 which presents the computed sound pressure levels versus the tip Mach number. In the interpretation of Figure 10.4 it should be noted that equal tip Mach numbers at different freestream velocities correspond to different advance ratios, hence different blade loading conditions.

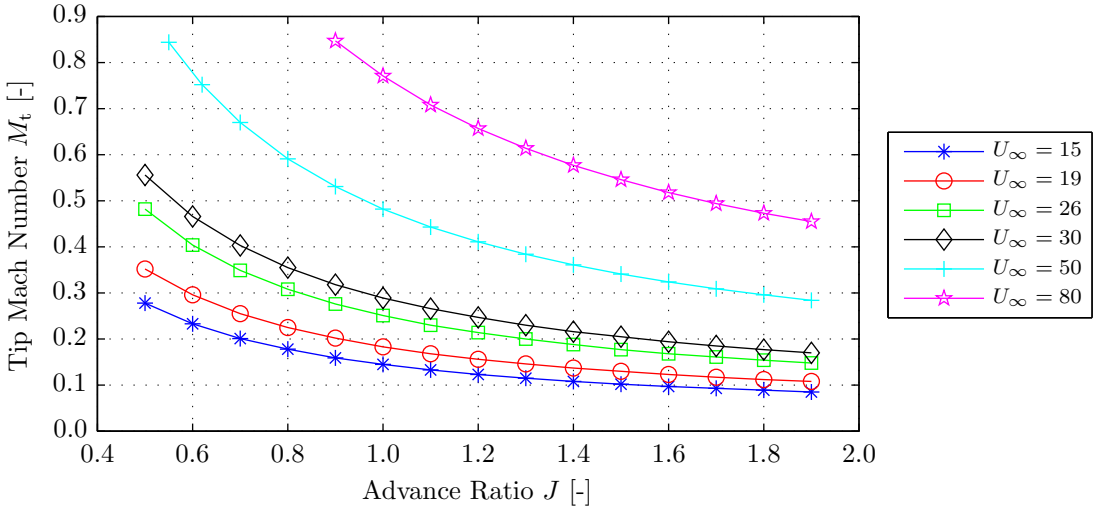

Figure 10.3: Tip Mach number versus the freestream velocity and the advance ratio. Isolated configuration, $U_\infty = [15, 19, 26, 30, 50, 80]$ m/s, $0.5 \leq J \leq 1.9$.

[1]National Aerospace Laboratory of the Netherlands.

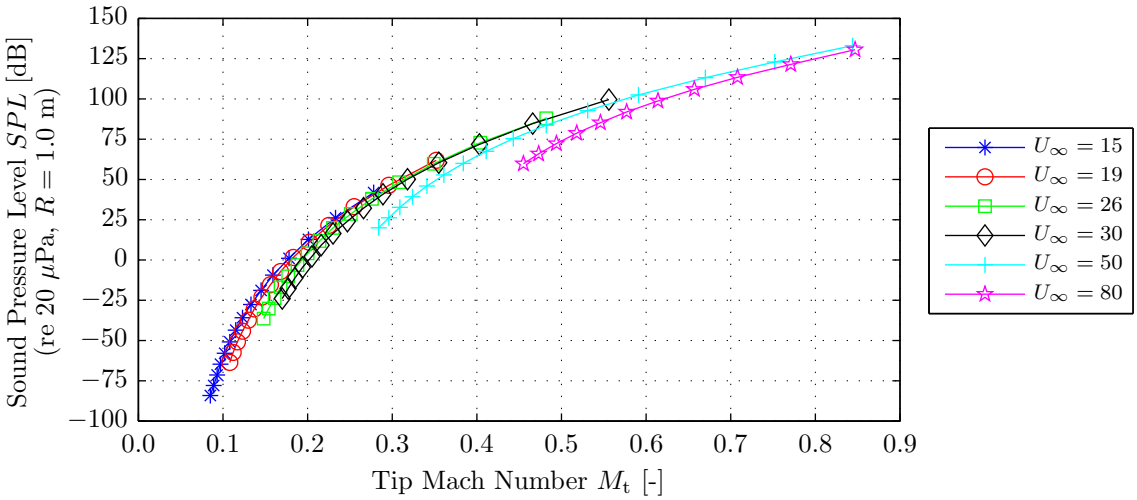

Figure 10.4: Computed total SPL versus the tip Mach number.
Isolated configuration, $U_\infty = [15, 19, 26, 30, 50, 80]$ m/s, $0.5 \leq J \leq 1.9$, $\theta = 90°$.

From Figure 10.3 it is concluded, as expected, that at constant freestream velocity the tip Mach number increases with decreasing advance ratio, while at constant advance ratio the tip Mach number increases with increasing freestream velocity.

Figure 10.4 shows that the tip Mach number has a distinct effect on the computed total SPL. The SPL increases with increasing tip Mach number, with the increase especially rapid for tip Mach numbers below approximately $M_t = 0.3$. At this tip Mach number the SPL is around 50 dB at velocities of 15 up to and including 30 m/s, while for tip Mach numbers below 0.2 the SPL becomes smaller than zero. Furthermore, it is observed that at constant tip Mach number the SPL increases with decreasing freestream velocity. This is explained from the fact that at constant tip Mach number the advance ratio is lower for the lower velocity, with lower advance ratios corresponding to higher blade loads. For two subsequent velocities the difference between the sound pressure levels at the same tip Mach number decreases with increasing tip Mach number. This is as expected considering that at some point the solution computed for the lower freestream velocity reaches the lower advance ratios, at which the blade response starts to flatten because of the onset of stall. As a result the relative differences between the blade loads occurring at the two different freestream velocities become smaller, thereby reducing the difference in the noise levels observed between both solutions.

10.2.3 Tonal Noise Levels

The sound pressure levels presented so far in this section were based on complete sound spectra, i.e. the combination of all harmonic noise components. To quantitatively assess the distribution of the different harmonics in the sound spectrum, this subsection considers the separate tonal components in the computed isolated propeller noise emissions. Only the effects of the operating point on the tonal noise levels are presented here, for a discussion of the directivity characteristics of the tonal noise emissions the reader is referred to Appendix E.2.1.4. Figure 10.5 presents the sound pressure levels of the 1BPF, 2BPF, 3BPF, and 4BPF tones as a function of the advance ratio for a freestream velocity of 50 m/s. For reference, the total sound pressure levels at the considered operating points are also indicated.

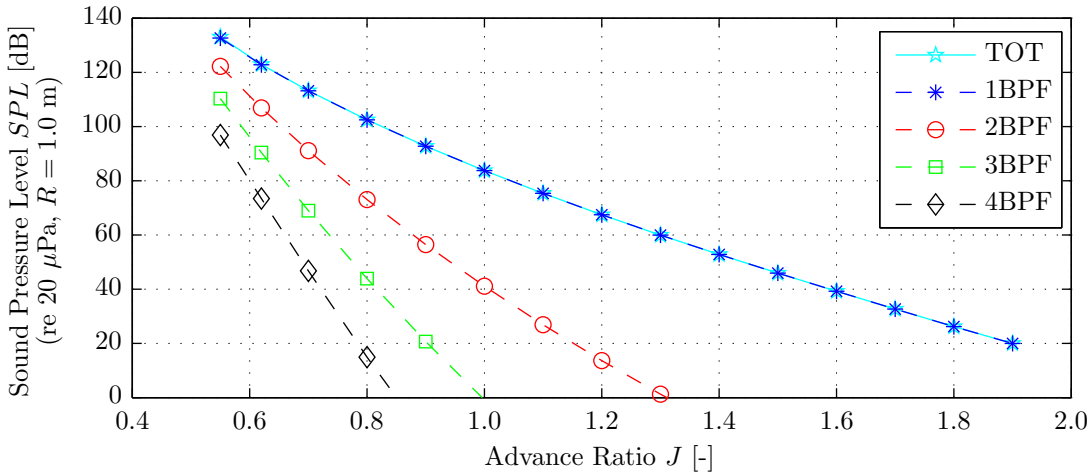

Figure 10.5: Total SPL of the tonal noise components versus the advance ratio. Isolated configuration, $U_\infty = 50$ m/s, $0.5 \leq J \leq 1.9$, $\theta = 90°$.

The results depicted in Figure 10.5 confirm that the 1BPF tone clearly dominates the computed isolated propeller sound spectra. At all advance ratios considered the total SPL is practically equal to that of the 1BPF tone. With increasing advance ratio an increasingly strong reduction in the tonal SPL is observed with increasing harmonic number. Therefore, the relative contribution of the tones corresponding to the higher harmonics becomes larger at the lowest advance ratios. However, even at $J = 0.5$ the 1BPF tone is about 10 dB louder than the 2BPF tone. In short, it can be concluded that for a freestream velocity of 50 m/s the predicted noise emissions of the isolated propeller are completely dominated by the 1BPF tone. Although not presented here, similar results were obtained for all other freestream velocities considered in the analytic propeller noise computations.

10.3 Installed Configuration

In the installed configuration additional noise is generated compared to the isolated case because of the unsteady blade loading resulting from the presence of the pylon wake. This section first considers the effects of installation on the directivity of the propeller noise emissions (Subsection 10.3.1). Subsequently, the effect of the propeller operating point on the resulting total sound pressure levels is evaluated (Subsection 10.3.2). Finally, the distribution of the tonal noise components in the complete sound spectrum is considered (Subsection 10.3.3). Note that in all cases the centerline of the pylon wake is positioned at $\phi = 0°$.

10.3.1 Directivity Analysis

The unsteady loading noise interacts with the steady loading noise, thereby changing the directivity pattern of the propeller noise emissions. Whereas for the isolated case the noise is constant with the circumferential angle ϕ, the effects of installation result in distinct lobes in the circumferential direction. At the same time the directivity pattern in the axial direction is also modified by the installation effects. This subsection compares the directivity patterns of the total SPL in the installed and isolated configurations; for a detailed discussion of the directivity of the separate noise components (thickness and loading noise) the reader is referred to Appendix E.2.2.1. The same operating point was selected as used before, corresponding to $U_\infty = 50$ m/s and $J = 0.9$. First, Figure 10.6 presents a comparison for the axial directivity angle θ. Following previous results, the isolated data is shown in blue while the installed results are depicted in red.

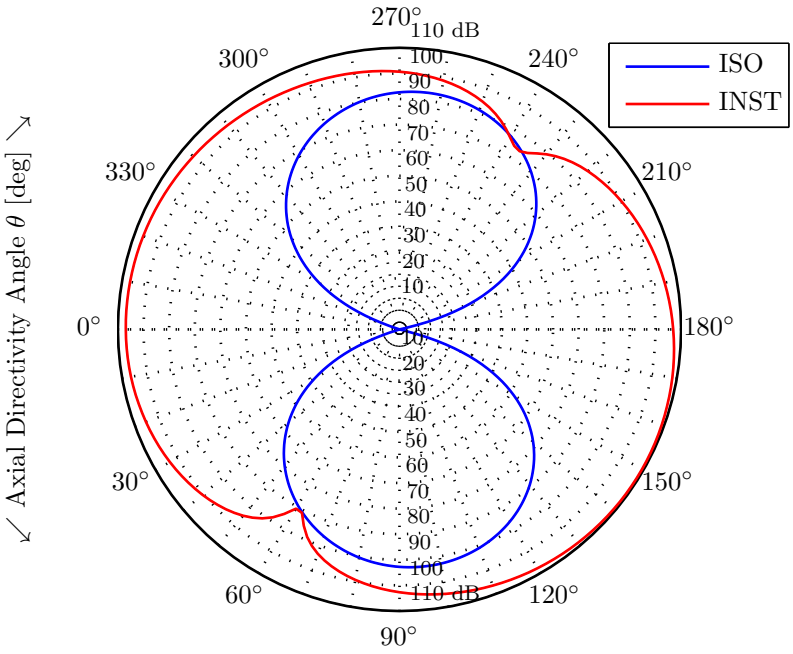

Figure 10.6: Sound pressure level (re 20 μPa, $R = 1.0$ m) versus the axial directivity angle θ. Isolated and installed configurations, $U_\infty = 50$ m/s, $J = 0.9$, $M_t = 0.53$, $\phi = 90°$.

Figure 10.6 shows that the computed sound pressure levels in the installed configuration are higher than the isolated values for all axial directivity angles θ, except for the location of the node in the installed directivity pattern around $\theta = 240°$. The largest differences are observed near the propeller axis ($\theta = 0°$ and $\theta = 180°$), where the isolated SPL rapidly decays to zero but the installed results are close to the maximum SPL observed for all axial directivity angles. This is explained by examination of Equations (7.39) and (7.49) which are used to compute the harmonics of the noise emissions in the isolated and installed configurations, respectively. The radiation efficiency of the noise harmonics is governed by the Bessel function which appears within the integral term in both Equations (7.39) and (7.49). When going towards the propeller axis the argument of this Bessel function will rapidly drop towards zero considering the dependency on the term $\sin\theta$. Since Bessel functions of the first kind are always zero for zero argument except when the order also equals zero, the only harmonics that contribute to the noise emissions on the propeller axis are those for which the order of the Bessel function equals zero. For the isolated propeller, governed by Equation (7.39), this corresponds to a harmonic order (m) of zero. However, for zero harmonic order the isolated propeller noise harmonic will always equal zero since both k_x and k_y will equal zero. As a result, the computed acoustic pressure on the propeller axis will always equal zero for the isolated propeller. For the installed configuration on the other hand Equation (7.49) shows that for the order of the Bessel function term to be zero the quantity $mB - k$ needs to equal zero. At these combinations the wave number k_y will never equal zero, hence the resulting noise harmonic will never become zero either on the propeller axis. Considering that the propeller has eight blades ($B = 8$), at each BPF harmonic $mB - k$ will equal zero for the unsteady loading harmonic $k = 8m$. Inspection of Figure 9.9 shows that the harmonic components of the unsteady lift coefficient are still characterized by significant values at these harmonic numbers. Because of the high radiation efficiency the resulting harmonic noise components computed around the propeller axis then dominate the entire axial directivity spectrum.

Figure 10.7 presents the circumferential directivity of the noise emissions in the isolated and installed configurations. All results were obtained at a constant axial directivity angle of $\theta = 90°$.

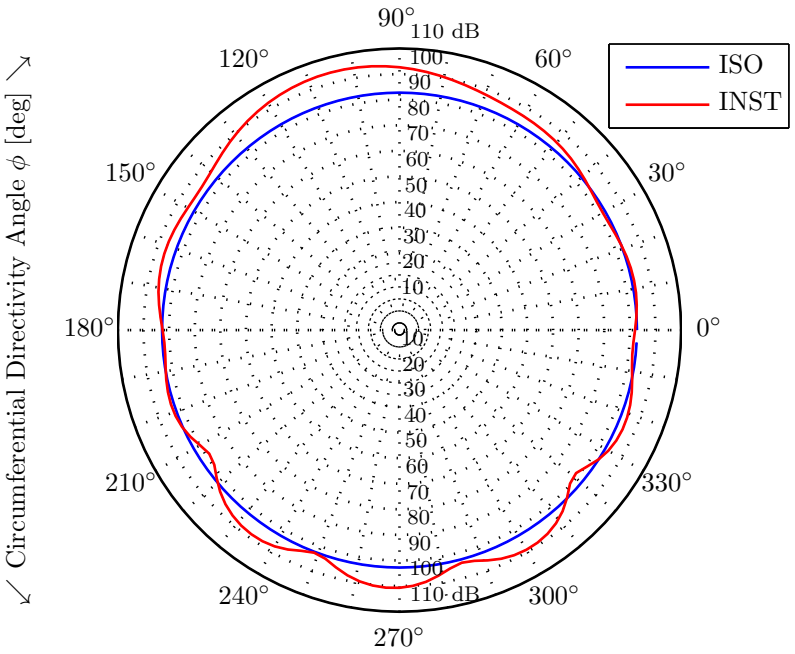

Figure 10.7: Sound pressure level (re 20 μPa, $R = 1.0$ m) versus the circumferential directivity angle ϕ. Isolated and installed configurations, $U_\infty = 50$ m/s, $J = 0.9$, $M_t = 0.53$, $\theta = 90°$.

Figure 10.7 shows that the largest noise increases due to the installation effects are observed perpendicular to the pylon plane (i.e. around $\phi = 90°$ and $\phi = 270°$). This corresponds to experimental results presented in the literature [20, 24]. At circumferential angles close to the pylon plane (around $\phi = 0°$ and $\phi = 180°$) on the other hand the circumferential directivity of the installed noise emissions approximately equals that of the isolated propeller.

10.3.2 Effects of the Propeller Operating Point on the Total SPL

The propeller noise emissions in the installed configuration presented so far were all computed for a single operating point ($U_\infty = 50$ m/s and $J = 0.9$). To quantify the effects of changes in the freestream velocity and the advance ratio on the installed propeller noise, computations were also performed for a range of different freestream velocities and advance ratios. This subsection first presents the total sound pressure levels as a function of the advance ratio for all freestream velocities and advance ratios considered (Paragraph 10.3.2.1). Subsequently, the effects of the tip Mach number are quantified (Paragraph 10.3.2.2). Finally, the differences between the installed and isolated noise emissions are discussed (Paragraph 10.3.2.3).

10.3.2.1 Noise Emissions Versus Advance Ratio and Freestream Velocity

The total sound pressure levels computed at an axial directivity angle of $\theta = 90°$ and a circumferential directivity angle of $\phi = 90°$ are plotted in Figure 10.8 for freestream velocities of 15, 19, 26, 30, 50, and 80 m/s and an advance ratio range equal to $0.5 \leq J \leq 1.9$. For reference, for the freestream velocity of 80 m/s the results obtained for the isolated propeller are also added.

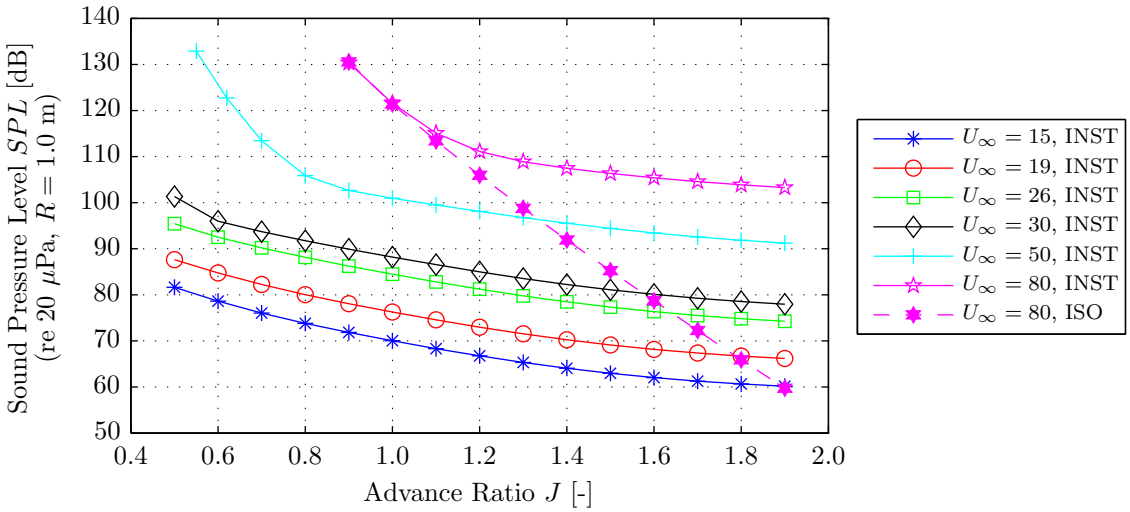

Figure 10.8: Computed total SPL versus the freestream velocity and the advance ratio. Installed configuration, $U_\infty = [15, 19, 26, 30, 50, 80]$ m/s, $0.5 \leq J \leq 1.9$, $\theta = \phi = 90°$.

Figure 10.8 shows that, similarly as for the isolated results, at constant advance ratio the total SPL increases with increasing freestream velocity. Furthermore, for all freestream velocities considered the SPL increases with decreasing advance ratio, resulting from the associated increase in blade loads and effective Mach numbers. In the curves computed for freestream velocities of 30, 50, and 80 m/s kinks are visible, after which the gradient of the SPL with respect to the advance ratio clearly changes. This is the result of a shift of the dominant noise generating mechanism. At the higher advance ratios, at which the steady-state blade loads are relatively small, the propeller noise in the installed configuration is dominated by the fluctuating unsteady loads. When decreasing the advance ratio on the other hand the steady-state blade loads increase until at some point they start to dominate the noise spectrum. In this process the gradient of the SPL versus the advance ratio shows a distinct change.

10.3.2.2 Noise Emissions Versus Tip Mach Number and Freestream Velocity

To gain additional insight in the propeller noise generating mechanisms for different freestream velocities, Figure 10.9 presents the total sound pressure levels for all considered freestream velocities and advance ratios as a function of the tip Mach number. Again, when analyzing Figure 10.9 it should be noted that equal tip Mach numbers at different freestream velocities correspond to different advance ratios, hence different blade loading conditions.

Figure 10.9 shows that at constant tip Mach number the SPL increases with increasing freestream velocity. This is explained by considering that at a constant tip Mach number the advance ratio increases along the direction of increasing freestream velocity, and higher advance ratios correspond to more dominant interaction effects. Again clear kinks are observed in the sound pressure levels computed for freestream velocities of 30, 50, and 80 m/s. As discussed before, these kinks result from a shift in the dominant noise generating mechanism from unsteady to steady blade loading. After the position of the kink the situation observed before in Figure 10.4 should be restored, where the SPL at equal tip Mach number increased with decreasing freestream velocity. This is indeed confirmed by Figure 10.9, which shows that above a tip Mach number of $M_t = 0.63$ the noise levels computed for $U_\infty = 50$ m/s become higher than for $U_\infty = 80$ m/s at a constant tip Mach number.

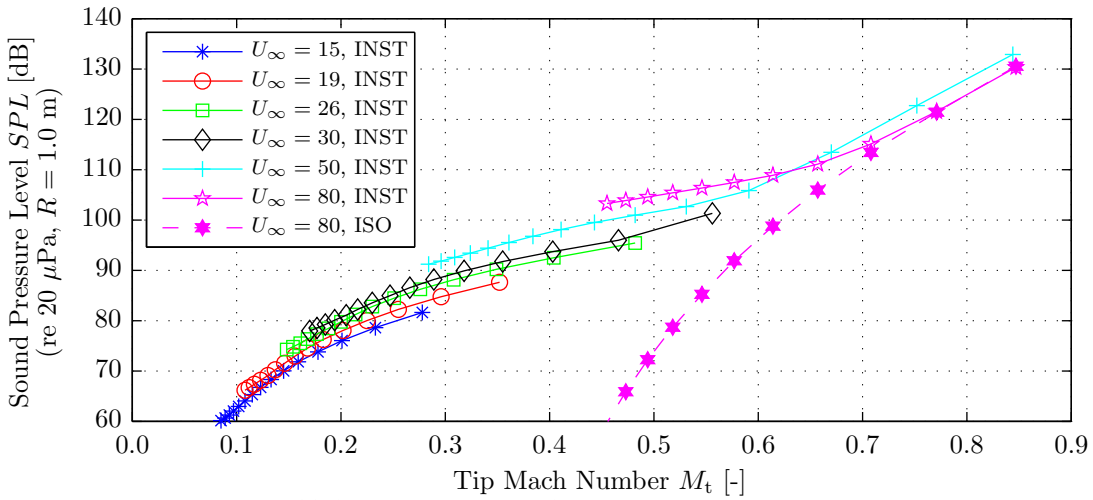

Figure 10.9: Computed total SPL versus the tip Mach number.
Installed configuration, $U_\infty = [15, 19, 26, 30, 50, 80]$ m/s, $0.5 \leq J \leq 1.9$, $\theta = \phi = 90°$.

10.3.2.3 Comparison between the Isolated and Installed Configurations

The increase in the SPL due to installation is depicted in Figure 10.10 as a function of the advance ratio. The same range of freestream velocities and advance ratios is considered as used before ($15 \leq U_\infty \leq 80$ m/s, $0.5 \leq J \leq 1.9$). Note that results are only presented for directivity angles equal to $\theta = 90°$ and $\phi = 90°$. At directivity angles closer to the propeller axis the differences between the sound pressure levels in the isolated and installed configurations increase, as shown for a single operating point in Figure 10.6.

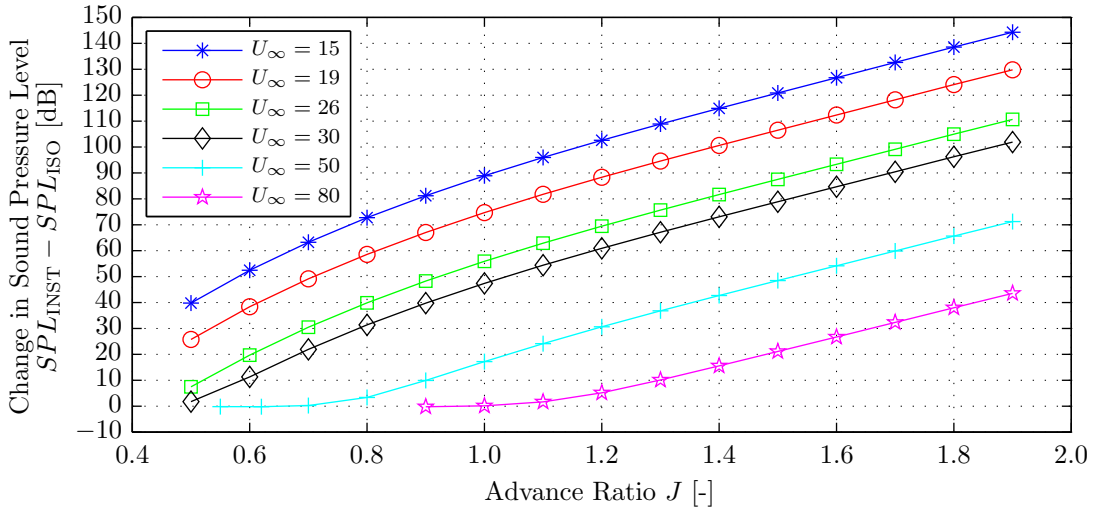

Figure 10.10: Change in the total SPL due to installation versus the advance ratio. Isolated and installed configurations, $U_\infty = [15, 19, 26, 30, 50, 80]$ m/s, $0.5 \leq J \leq 1.9$, $\theta = \phi = 90°$.

Figure 10.10 shows that at constant freestream velocity the noise penalty due to installation increases with increasing advance ratio, since the relative impact of the installation effects increases with increasing advance ratio. At constant advance ratio the noise penalty due to installation decreases with increasing freestream velocity. This is explained from the fact that the radiation efficiency of the isolated noise emissions increases more rapidly with the tip Mach number than for the installed noise emissions. Also, the frequencies of the gusts experienced by the propeller blades in the pylon wake increase with increasing freestream velocity, resulting in smaller unsteady loads for higher freestream velocities. Finally, for freestream velocities

of 30, 50, and 80 m/s it is observed that the noise penalty due to installation becomes zero below a given advance ratio. This is the result of the shift in the noise generating mechanism from dominated by unsteady blade loading to steady blade loading, as discussed before. Note that the noise penalty due to installation computed for low freestream velocities is larger than expected due to the unrealistically low noise levels computed for the isolated propeller at low tip Mach numbers, as discussed in Subsection 10.2.2.

10.3.3 Tonal Noise Levels

This subsection discusses the sound pressure levels of the propeller tones as a function of the advance ratio. For an analysis of the directivity characteristics of the tonal noise emissions the reader is referred to Appendix E.2.2.2. Figure 10.11 presents the sound pressure levels of the first four BPF tones for the isolated and installed configurations. The results were computed for $U_\infty = 50$ m/s and $0.5 \leq J \leq 1.9$, and directivity angles of $\theta = 90°$ and $\phi = 90°$.

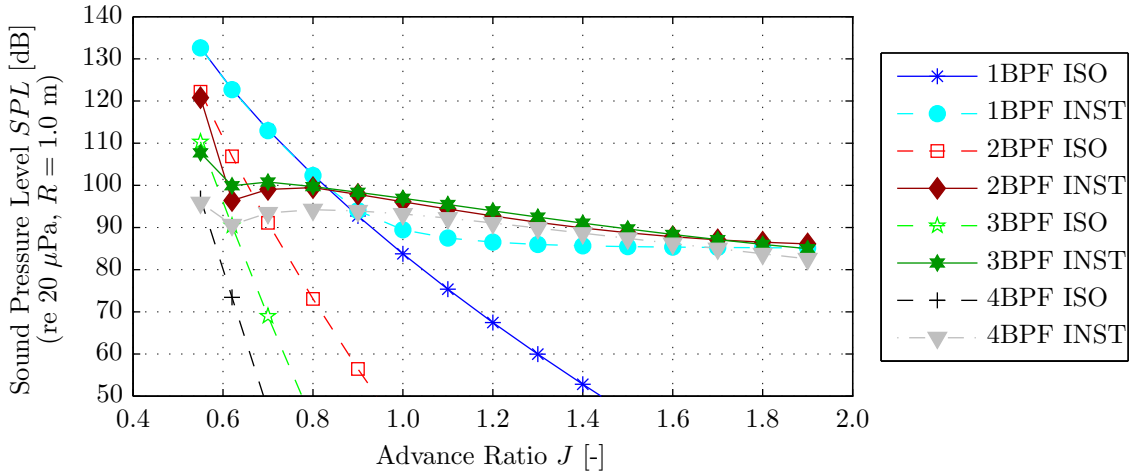

Figure 10.11: Effects of installation on the tonal noise levels.
Isolated and installed configurations, $U_\infty = 50$ m/s, $0.5 \leq J \leq 1.9$, $\theta = \phi = 90°$.

Figure 10.11 shows that at advance ratios above $J = 0.9$ the propeller noise emissions are dominated by installation effects. Correspondingly, for these advance ratios the sound pressure levels of the higher BPF multiples are significantly higher in the installed configuration than in isolated conditions. For the isolated propeller on the other hand the only significant tonal noise component is the 1BPF tone. The pronounced differences between the sound pressure levels of especially the higher BPF harmonics at the higher advance ratios are the result of radiation efficiency effects related to the Bessel term in Equation (7.49). It can be shown that with increasing harmonic number m an increasing number of unsteady loading harmonics k radiates efficiently, hence leading to strong increases in the sound pressure levels of the tonal noise components of higher harmonic orders compared to the isolated configuration.

10.4 Blown Configuration

This section discusses the computed propeller noise emissions in the blown configuration. Following the previous section, first a directivity analysis of the blown noise emissions is performed (Subsection 10.4.1). Subsequently, the effects of the propeller operating conditions on the noise emissions are evaluated (Subsection 10.4.2). Thereafter, the tonal noise levels

present in the propeller sound spectra are discussed (Subsection 10.4.3). In these three subsections the blown pylon wake profile was used as measured behind the extended pylon at a freestream velocity of 19 m/s and a blowing rate of $Q = 600$ L/min (see Figure 3.7). Having analyzed the noise emissions in the blown configuration corresponding to the wake profile obtained from the experimental data, the sensitivity of the noise emissions to the amount of reduction in the velocity deficit in the pylon wake is considered for numerically determined wake profiles (Subsection 10.4.4).

10.4.1 Directivity Analysis

This subsection presents a comparison between the directivity of the total sound pressure levels of the propeller noise emissions in the isolated, installed, and blown configurations. The operating point was defined by $U_\infty = 50$ m/s and $J = 0.9$. For a discussion of the directivity characteristics of the different noise components the reader is referred to Appendix E.2.3.1.

The axial directivity angle θ is considered first. Figure 10.12 presents the isolated, installed, and blown total sound pressures computed for $\phi = 90°$ as a function of θ.

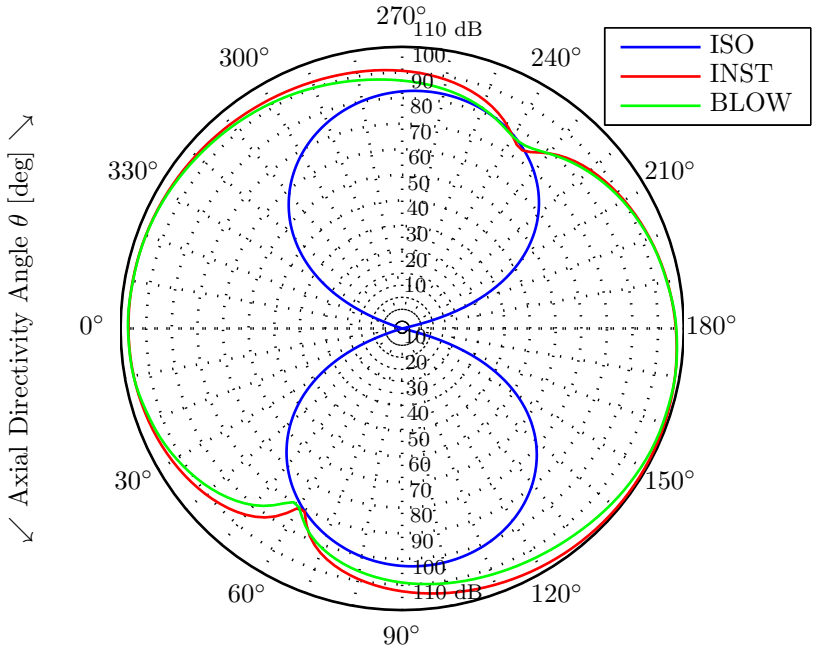

Figure 10.12: Sound pressure level (re 20 μPa, $R = 1.0$ m) versus the axial directivity angle θ. Isolated, installed, and blown configurations, $U_\infty = 50$ m/s, $J = 0.9$, $M_t = 0.53$, $\phi = 90°$.

From Figure 10.12 it is concluded that the axial directivity patterns computed for the installed and the blown configurations have similar shapes. The isolated propeller noise emissions on the other hand show a distinctively different axial directivity pattern with much lower sound pressure levels for directivity angles near the propeller axis. Considering that the differences between the isolated and installed axial directivity patterns were discussed before in Subsection 10.3.1, these are not further elaborated upon here. Comparison of the installed and blown directivity patterns shows that at the current circumferential directivity angle the application of blowing results in noise reductions of at maximum 5 dB for the axial directivity ranges $30° < \theta < 150°$ and $240° < \theta < 300°$. This is the result of the reduction in the magnitude of the unsteady blade loading coefficients resulting from the application of blowing, which was observed in Chapter 9.

Figure 10.13 compares the circumferential directivity of the isolated, installed, and blown noise emissions for an axial directivity angle equal to $\theta = 90°$.

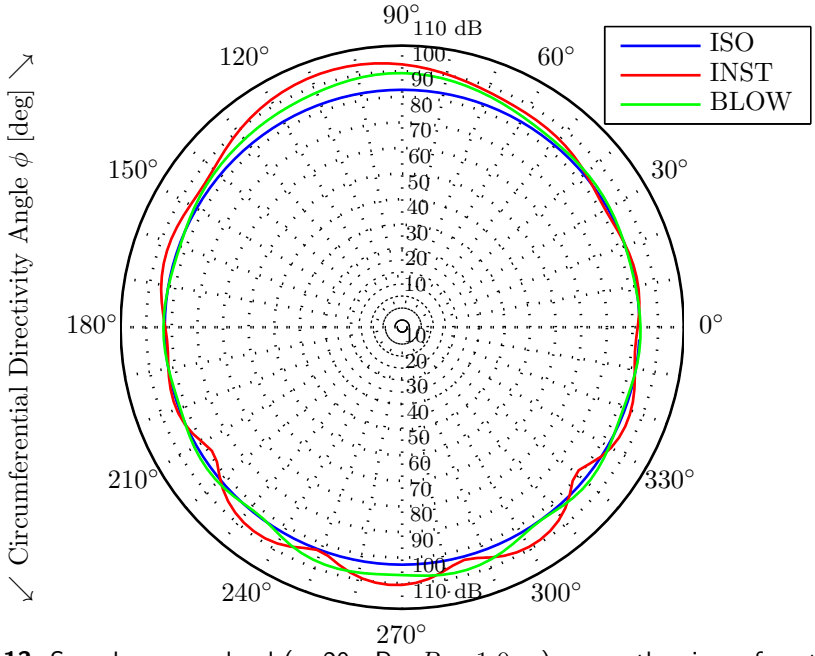

Figure 10.13: Sound pressure level (re 20 μPa, $R = 1.0$ m) versus the circumferential angle ϕ. Isolated, installed, and blown configurations, $U_\infty = 50$ m/s, $J = 0.9$, $M_t = 0.53$, $\theta = 90°$.

Figure 10.13 shows that the circumferential directivity of the blown propeller noise falls in between the results for the isolated and installed configurations. The application of blowing reduces the number and amplitude of the lobes, while the response is not yet constant in ϕ as for the isolated propeller. Again, the differences between the installed and blown results are explained by the reduction in the magnitude of the unsteady loading coefficients.

10.4.2 Effects of the Propeller Operating Point on the Total SPL

Having discussed the directivity characteristics of the noise emissions in the blown configuration, the effects of the propeller operating conditions on the noise emissions are evaluated. First, the total sound pressure levels are presented as a function of the freestream velocity and the advance ratio (Paragraph 10.4.2.1). Thereafter, the differences between the behavior of the propeller noise in the installed and blown configurations are quantified (Paragraph 10.4.2.2). The influence of the tip Mach number on the propeller noise emissions is not discussed in this subsection since the results were comparable to those obtained for the isolated and installed configurations. The corresponding results are presented in Appendix E.2.3.2.

10.4.2.1 Noise Emissions Versus Advance Ratio and Freestream Velocity

The results obtained for the installed and isolated configurations showed that the behavior of the total SPL as a function of the operating conditions was significantly different for both cases. Now, the effects of changes in the freestream velocity and the advance ratio on the blown propeller noise emissions are assessed. Figure 10.14 presents the total sound pressure levels computed for freestream velocities of 15, 19, 26, 30, 50, and 80 m/s and an advance ratio range of $0.5 \leq J \leq 1.9$. The axial and circumferential directivity angles were fixed to $\theta = 90°$ and $\phi = 90°$ in all computations. For reference, for the freestream velocity of 80 m/s the results obtained for the isolated and installed configurations are also added.

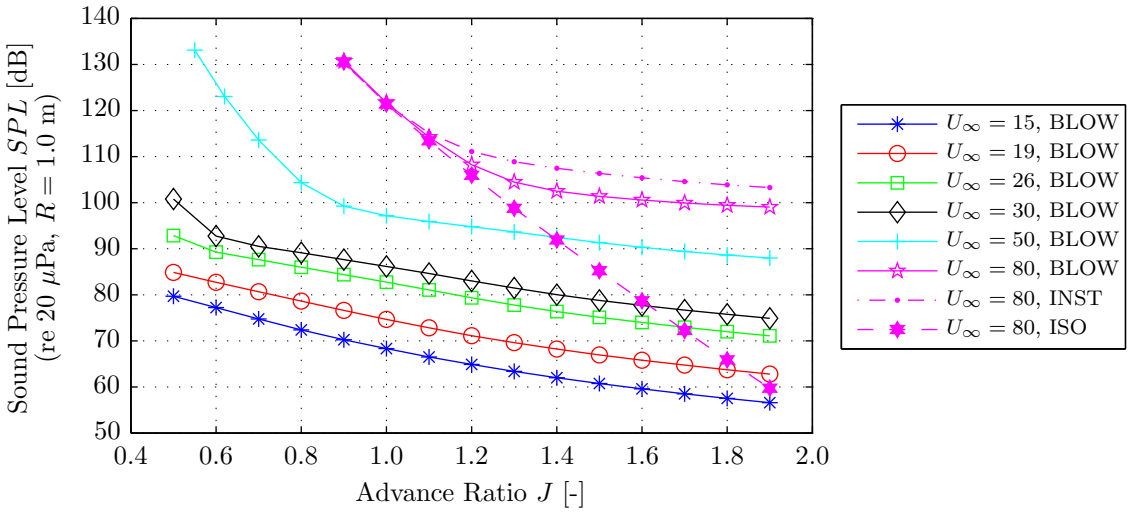

Figure 10.14: Computed total SPL versus the freestream velocity. Blown configuration, $U_\infty = [15, 19, 26, 30, 50, 80]$ m/s, $0.5 \leq J \leq 1.9$, $\theta = \phi = 90°$.

Figure 10.14 shows that at constant advance ratio the SPL of the blown propeller noise increases with increasing freestream velocity, while at constant freestream velocity the SPL increases with decreasing advance ratio. These results are the same as for the noise emissions of the propeller in the isolated and installed configurations. Similarly as for the installed results, for freestream velocities of 30, 50, and 80 m/s clear kinks are visible, corresponding to a shift in the dominant noise generating mechanism from unsteady blade loading dominated to steady-state blade loading dominated. Note that at the higher advance ratios the noise levels in the blown configuration are consistently lower than in installed conditions. This is discussed in more detail in the next Paragraph.

10.4.2.2 Comparison between the Installed and Blown Configurations

The differences between the installed and blown noise levels were computed to assess the possible noise reductions due to blowing. Figure 10.15 presents the noise reductions as a function of the advance ratio for the same operating conditions as considered before. The SPL reductions are depicted versus the tip Mach number in Figure 10.16.

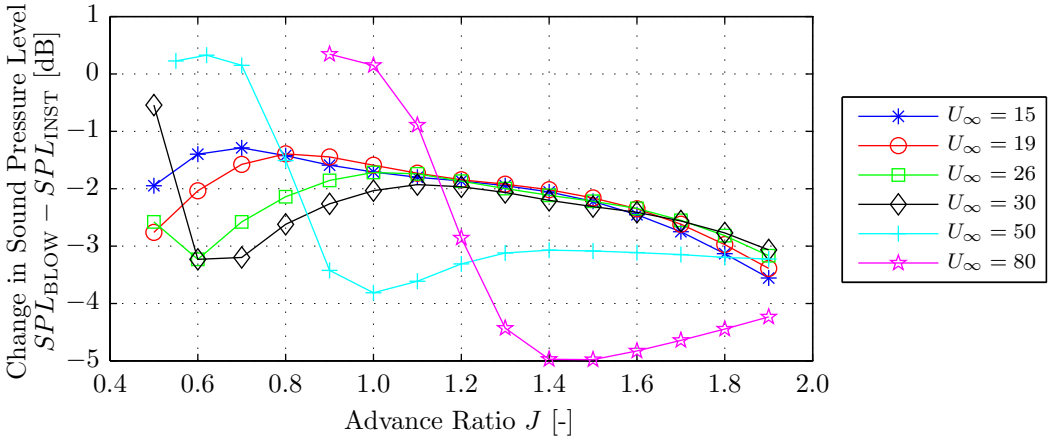

Figure 10.15: Change in the total SPL due to installation versus the advance ratio. Installed and blown configurations, $U_\infty = [15, 19, 26, 30, 50, 80]$ m/s, $0.5 \leq J \leq 1.9$, $\theta = \phi = 90°$.

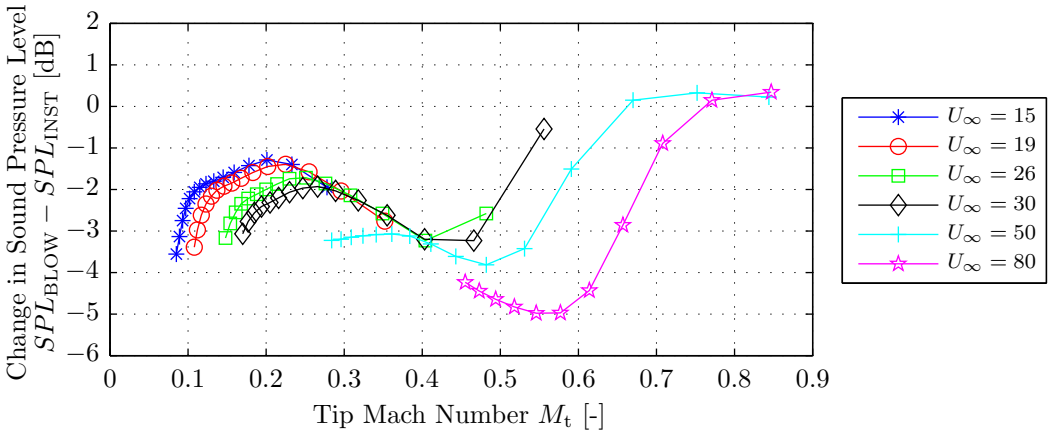

Figure 10.16: Change in the total SPL due to installation versus the tip Mach number. Installed and blown configurations, $U_\infty = [15, 19, 26, 30, 50, 80]$ m/s, $0.5 \leq J \leq 1.9$, $\theta = \phi = 90°$.

Figures 10.15 and 10.16 confirm that the application of blowing reduces the noise emissions over the entire advance ratio range for which the installation effects are dominant.

For freestream velocities of 15, 19, 26, and 30 m/s the noise reductions due to blowing are approximately equal for $J > 1.1$, with the increasing SPL reduction with increasing advance ratio explained from the fact that the installation effects become more dominant with increasing advance ratio. For advance ratios below $J = 1.1$ different responses are obtained, with increasing noise reductions obtained for decreasing advance ratios. This is explained by considering that the magnitude of the unsteady lift response decreases with increasing gust frequency. Since the application of blowing increases the frequencies of the gusts experienced by the propeller blades in the pylon wake region, from a given advance ratio onward the noise emissions in the blown configuration display a smaller increase with decreasing advance ratio than in installed conditions. This explanation is confirmed by Figure 10.16 which shows that in the tip Mach number range between approximately 0.25 and 0.40 the noise reductions due to blowing are equal for the computations performed at 15, 19, 26, and 30 m/s. Apparently, for these combinations of freestream velocity and advance ratio the tip Mach number dominates the installation effects, and not the advance ratio. For velocities of 26 and 30 m/s finally at the lowest advance ratio ($J = 0.5$) a steep decrease is observed in the noise reduction due to blowing, which is explained by the fact that at these points the propeller noise starts to become dominated by the steady-state blade loads.

The behavior of the noise reductions due to blowing for 50 and 80 m/s is similar to that observed for the other freestream velocities. However, the trend is shifted towards higher advance ratios with increasing freestream velocity. This is explained by the increase in tip Mach number accompanied with an increase in freestream velocity at constant advance ratio.

It is concluded that the SPL reductions due to blowing are dominated by a combination of the advance ratio and the tip Mach number. At low tip Mach numbers the noise reductions increase with increasing advance ratio, since the installation effects become more pronounced at the higher advance ratios. When increasing the tip Mach number on the other hand the response becomes dominated by the effects of the frequencies of the gust profiles in the blown pylon wake. Now, a decrease in the advance ratio results in an increase in the noise reduction, since the increase in the tip Mach number results in a decrease in magnitude of the unsteady lift coefficient which is larger in the blown configuration than in installed conditions.

10.4.3 Tonal Noise Levels

This subsection presents the differences between the tonal noise emissions in the blown and installed configurations. A discussion of the absolute levels computed for the blown configuration is given in Appendix E.2.3.3, while a directivity analysis is presented in Appendix E.2.3.4. Figure 10.17 plots the SPL reduction due to blowing versus the advance ratio for the first three BPF tones. The same operating point is considered as selected before.

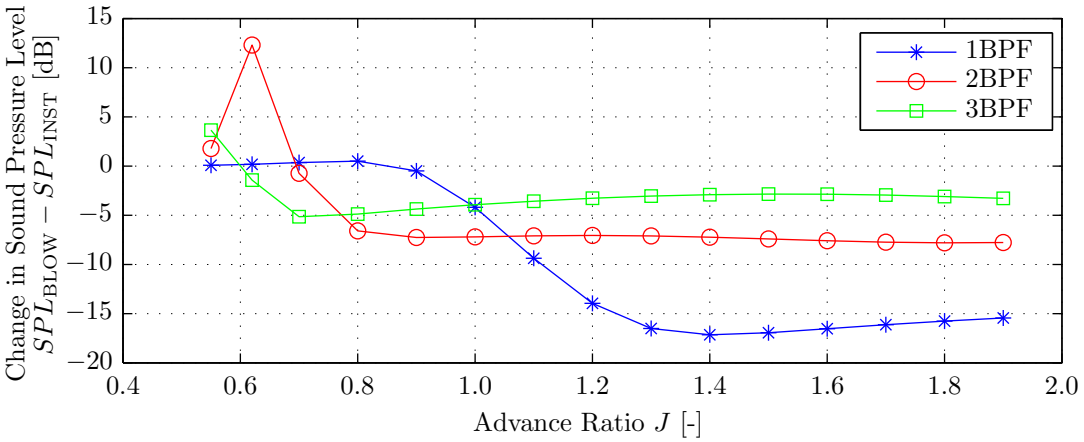

Figure 10.17: SPL reduction due to blowing for the first 3 BPF tones.
Installed and blown configurations, $U_\infty = 50$ m/s, $0.5 \leq J \leq 1.9$, $\theta = \phi = 90°$.

Figure 10.17 shows that at high advance ratios the largest SPL reductions due to blowing are obtained for the 1BPF tone. This is explained by the fact that the decrease of the magnitude of the unsteady lift harmonics due to blowing is largest for lower harmonic orders. Since the order of the unsteady lift harmonics resulting in efficient noise radiation increases with increasing BPF harmonic, for the current blown wake profile at moderate to high advance ratios the largest noise reductions are observed for the 1BPF tone. For $J < 0.9$ the steady-state blade loads start to dominate the propeller noise emissions. As a result the installed noise levels converge towards the isolated values, hence reducing the noise reductions obtained by blowing. This is clearly illustrated in Figure 10.17 in which the SPL reduction due to blowing goes towards (or even above) zero for all BPF tones at the lowest advance ratios.

10.4.4 Noise Emissions Versus the Amount of Pylon Wake Fill-Up

Whereas the previous subsections presented the noise emissions computed using a measured wake profile at a constant blowing rate, now the sensitivity of the propeller noise to the amount of wake fill-up is analyzed. The unblown, installed data discussed in Section 10.3 was used as baseline, after which the noise emissions were computed for wake profiles with a decreasing velocity deficit. The velocity deficit reduction was defined as the ratio between the new and original velocity deficits at the center of the pylon wake. Seven different cases were considered: 0%, 25%, 50%, 75%, 85%, 95%, and 100% reduction in the velocity deficit (referred to as 'fill-up' in the following). Note that 0% fill-up corresponds to the unblown situation, while 100% fill-up corresponds to isolated conditions. All computations were performed for a freestream velocity of $U_\infty = 50$ m/s and an advance ratio range of $0.5 \leq J \leq 1.9$. This subsection first presents the pylon wake profiles corresponding to the various amounts of wake fill-up (Paragraph 10.4.4.1). Subsequently, the axial and circumferential directivity patterns are given (Paragraph 10.4.4.2). Finally, the sensitivity of the propeller noise emissions to the operating conditions is assessed for the various amounts of wake fill-up (Paragraph 10.4.4.3).

10.4.4.1 Computed Pylon Wake Profiles

The computed pylon wake velocity profiles for all amounts of wake fill-up are plotted in Figure 10.18. An axial distance from the pylon's trailing edge of $X_w = 114$ mm was considered.

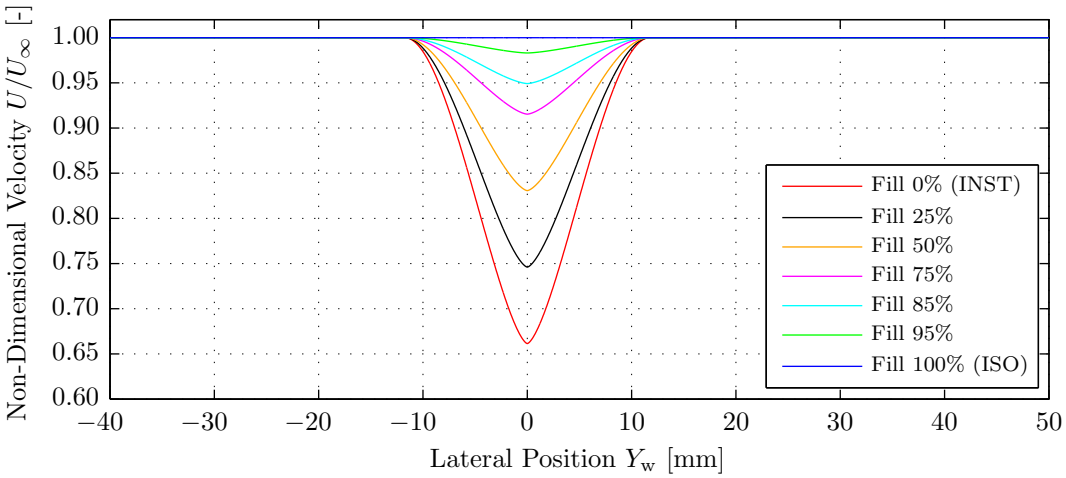

Figure 10.18: Non-dimensional velocity profiles in the wake of the extended pylon for various amounts of wake fill-up. $U_\infty = 50$ m/s, $X_w = 114$ mm.

The pylon wake profiles shown in Figure 10.18 are as expected. The application of the multiplication factor shifts the entire wake profile upwards hence reducing the velocity deficit in the wake region. The wake width on the other hand remains unaffected.

10.4.4.2 Directivity Patterns of the Total Sound Pressure

The propeller noise emissions were computed using the pylon wake profiles depicted in Figure 10.18. Figure 10.19 presents the resulting total sound pressure levels as a function of the axial directivity angle θ for the operating point defined by $U_\infty = 50$ m/s and $J = 0.9$.

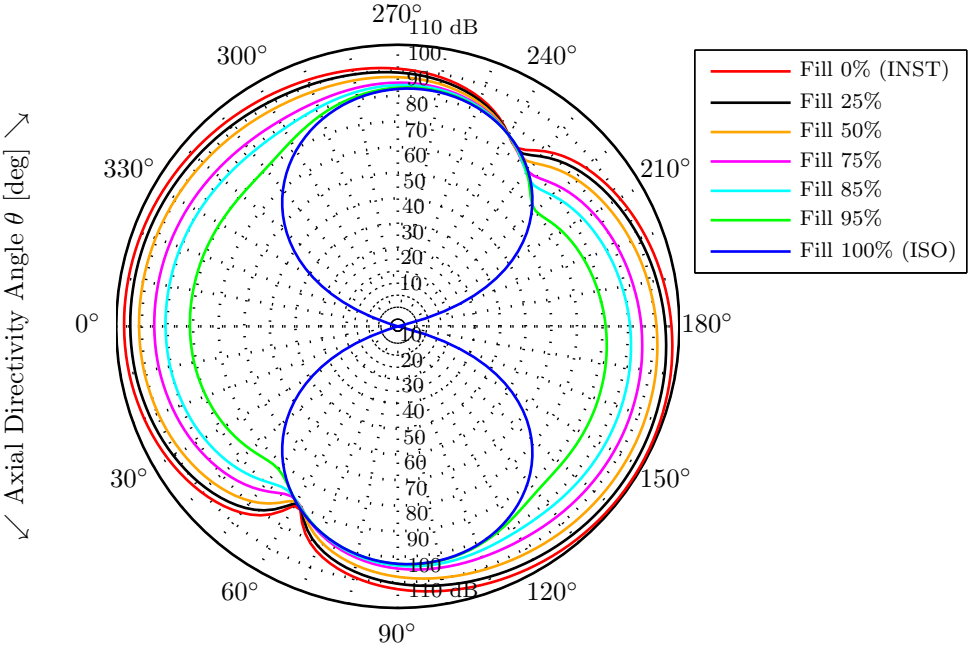

Figure 10.19: Sound pressure level (re 20 μPa, $R = 1.0$ m) versus the axial directivity angle θ for different amounts of wake fill-up. Installed and blown configurations, $U_\infty = 50$ m/s, $J = 0.9$, $M_t = 0.53$, $\phi = 90°$.

Figure 10.19 shows that the application of an increasing amount of wake fill-up brings the installed noise levels increasingly close to the isolated case (corresponding to 100% fill-up). Around the position of the propeller plane ($\theta = 90°$) the effects of installation are practically eliminated for a wake fill-up of 75% and higher. In the forward and rearward arcs the absolute reductions in noise levels are larger. Compared to the isolated case however still a large SPL increase remains even for a wake fill-up of 95 %, with sound pressure levels around the propeller axis equal to around 80 dB. Clearly, a very small amount of unsteady blade loading still results in large increases in noise emissions near the propeller axis.

Figure 10.20 presents the computed noise emissions for the same amounts of wake fill-up as considered before as a function of the circumferential directivity angle ϕ.

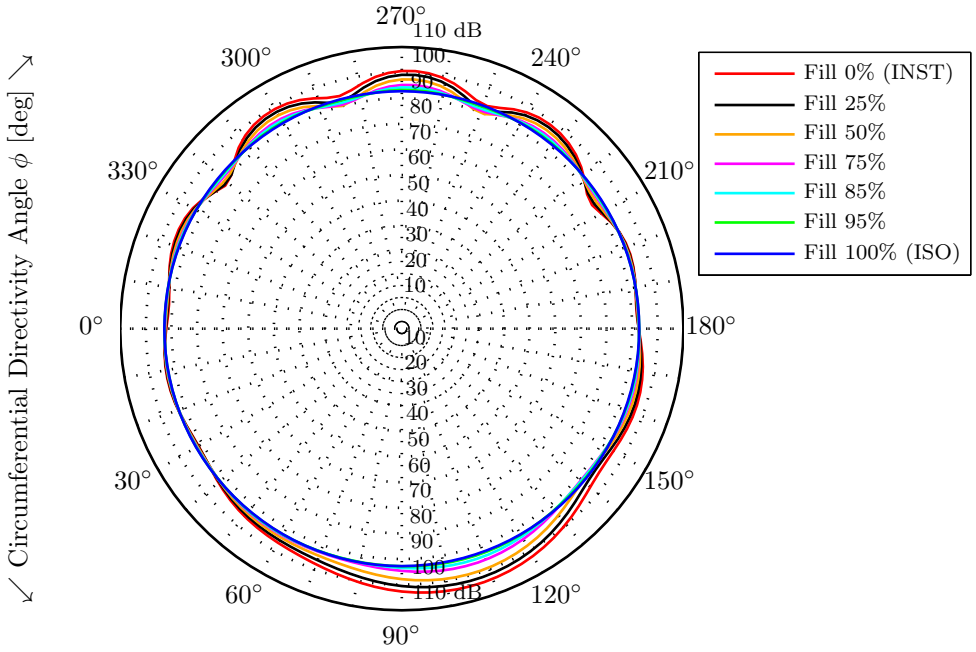

Figure 10.20: Sound pressure level (re 20 μPa, $R = 1.0$ m) versus the circumferential directivity angle ϕ for different amounts of wake fill-up. Installed and blown configurations, $U_\infty = 50$ m/s, $J = 0.9$, $M_t = 0.53$, $\theta = 90°$.

From the results shown in Figure 10.20 it is concluded that the application of an increasing amount of wake fill-up leads to a circumferential directivity pattern which becomes increasingly close to that corresponding to the isolated configuration. For a wake fill-up of 85% or more the change in the sound pressure level in the lobes in circumferential direction becomes smaller than 2 dB for all circumferential directivity angles.

10.4.4.3 Effects of the Propeller Operating Point on the Total SPL

The previous paragraph considered the effects of wake fill-up on the directivity patterns in the axial and circumferential directions for a single operating point. Now, the noise emissions at constant directivity angles ($\theta = \phi = 90°$) are computed for a range of operating conditions. The freestream velocity was set constant at $U_\infty = 50$ m/s, while the advance ratio was varied from $J = 0.5$ up to and including $J = 1.9$. Figure 10.21 displays the resulting computed sound pressure levels for the same amounts of wake fill-up as considered before, while Figure 10.22 presents the corresponding noise reductions compared to the unblown case (0% wake fill-up).

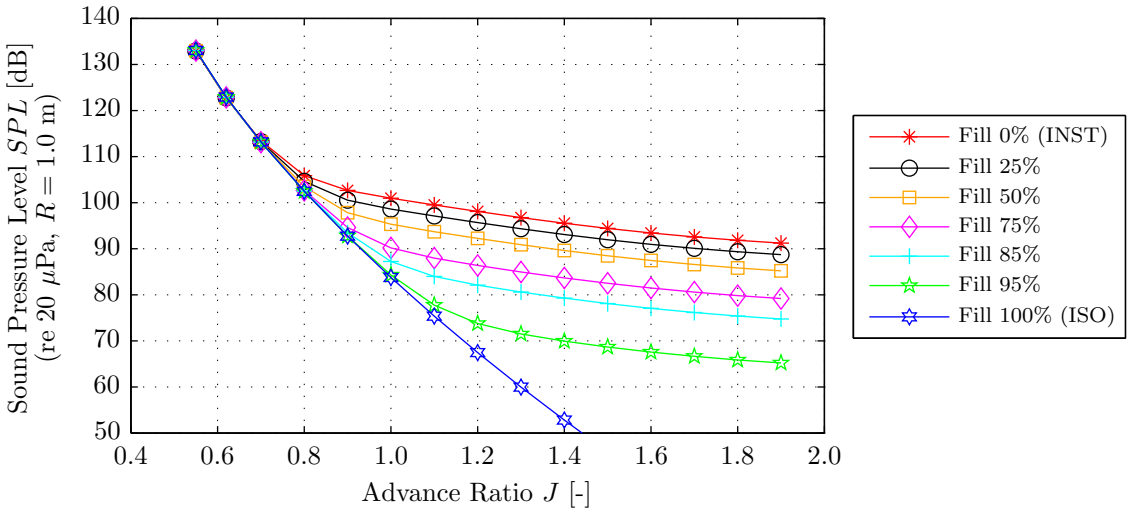

Figure 10.21: Computed total SPL versus the advance ratio for different amounts of wake fill-up. Installed and blown configurations, $U_\infty = 50$ m/s, $0.5 \leq J \leq 1.9$, $\theta = \phi = 90°$.

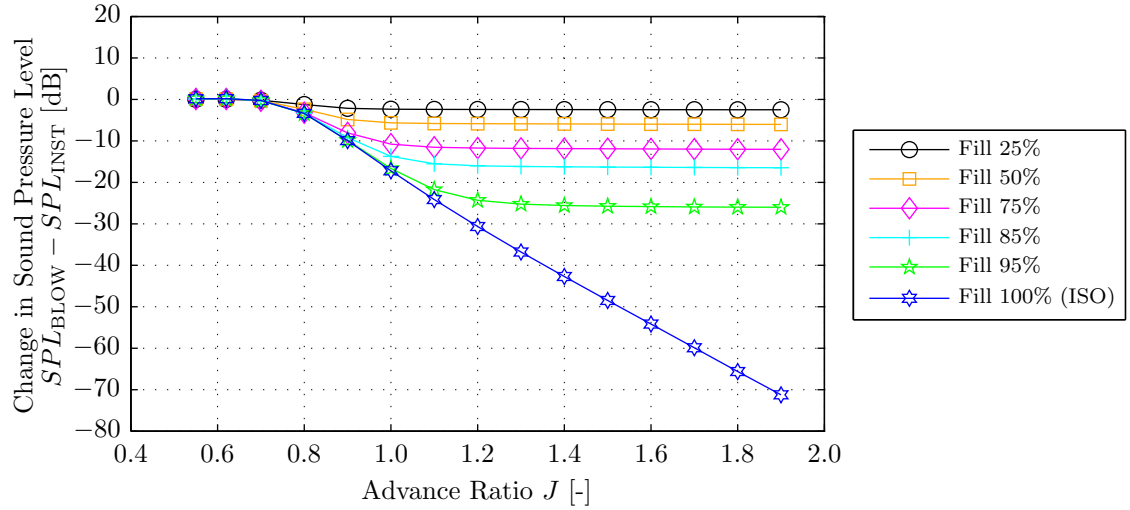

Figure 10.22: Computed SPL reduction due to blowing versus the advance ratio for different amounts of wake fill-up. Blown configuration, $U_\infty = 50$ m/s, $0.5 \leq J \leq 1.9$, $\theta = \phi = 90°$.

Figures 10.21 and 10.22 show that for advance ratios above around $J = 0.8$ the total sound pressure level decreases rapidly with an increasing amount of wake fill-up. At 75% wake fill-up noise reductions of about 10 dB are observed compared to the unblown case. Increasing the amount of wake fill-up results in increasing noise reductions. However, at 95% fill-up still a large noise penalty exists compared to the isolated case (represented by the case of 100% fill-up in Figures 10.21 and 10.22). This once more confirms that even a very small amount of unsteady blade loading can still result in large increases in the propeller noise emissions.

Part III

Synthesis

"A hard beginning maketh a good ending."
John Heywood

Following the separate discussion of the experimental and numerical results in the previous parts of this report, Part III presents a synthesis of all data. First, where possible the experimental and numerical results are compared to obtain additional insight in their accuracy and validity. Finally, conclusions and recommendations for future work are presented.

Chapter 11

Comparison of Experimental and Numerical Results

The previous two parts of this report presented the experimental and numerical evaluations of the effects of installation on pusher propeller performance and noise emissions, including an analysis of the potential benefits obtainable by application of pylon trailing edge blowing. Now, it is time to compare the experimental and numerical results.

Following the structure of the previous parts, first Section 11.1 discusses the pylon wake profiles. Note that only the unblown results are considered, since the numerical methods did not allow for the computation of wake profiles in the blown configuration. Subsequently, the measured and computed propeller performance are compared in Section 11.2. Finally, the similarities and differences between the experimental and numerical propeller noise emissions are discussed in Section 11.3.

11.1 Pylon Wake Profiles

This section compares the wake profiles obtained from the experiments to the computed velocity deficit profiles determined by applying the Schlichting wake model. Considering that the propeller performance and noise emission results presented in the previous two parts of this report mainly focused on the extended pylon, only this pylon model is considered here. The comparisons for the default and sharp pylon models are presented in Appendix F.1.

All results presented in this section are valid for a freestream velocity of 26 m/s, and are defined at the longitudinal positions $X_w = 50$ mm and $X_w = 114$ mm. In Chapter 3 it was observed that the measured wake profiles displayed a non-zero velocity deficit outside of the wake region, which was explained by considering that the measurements were influenced by the presence of the pylon. To allow for a fair comparison between the experimental and numerical data it was decided to shift the experimental wake profiles such that the average velocity deficit outside of the wake region became equal to zero. Note that in the quantitative comparison of the measured and computed wake profiles the wake width is defined as the lateral distance between the first points left and right of the centerline of the wake at which the velocity becomes equal to 99% of the freestream value.

Figure 11.1 presents the measured and computed wake profiles for the extended pylon, while an overview of the corresponding wake widths and wake depths is given in Table 11.1.

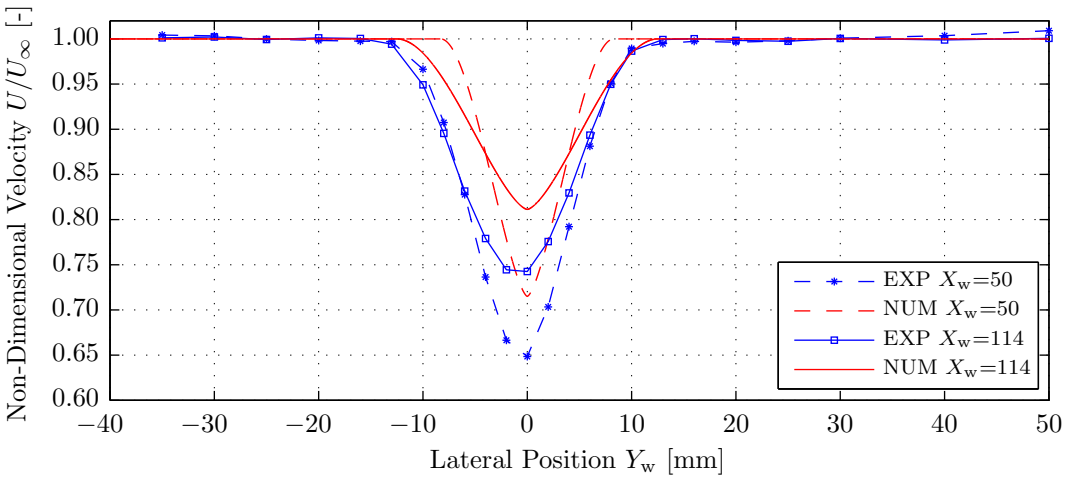

Figure 11.1: Measured and computed wake profiles behind the extended pylon model. $U_\infty = 26$ m/s, $X_w = [50, 114]$ mm.

Table 11.1: Comparison of computed and measured wake width and depth for the extended pylon. $U_\infty = 26$ m/s, $X_w = [50, 114]$ mm.

Data Set	$2b_w$ **[mm]**		$\Delta U_{max}/U_\infty$ **[-]**	
	$X_w = 50$ mm	$X_w = 114$ mm	$X_w = 50$ mm	$X_w = 114$ mm
Experimental	22	23	0.35	0.26
Numerical	15	21	0.29	0.19

Figure 11.1 and Table 11.1 show that the computed and measured wake profiles are significantly different. In the numerical results the increase in the wake width with increasing axial spacing is much larger than in the measured data. At $X_w = 50$ mm the computed wake width is around 30% smaller than the experimental value, while at $X_w = 114$ mm the difference is reduced to 8%. Regarding the wake depth it is observed that at both values of X_w the computed maximum velocity deficit in the pylon wake is smaller than the value obtained from the measurements. At $X_w = 50$ mm the computed wake depth is around 20% smaller than the measured value. The results at $X_w = 114$ mm show an even bigger difference, with the numerical result approximately 25% smaller than the experimentally determined value.

The differences observed between the experimental and numerical results can be attributed to a number of different factors. The offset in both the wake width and the wake depth at a given position X_w could be the result of an inaccurate computation of the drag coefficient used as input for the Schlichting wake model. If the input drag coefficient is inaccurate the resulting wake profiles will also be inaccurate. Furthermore, it is clear that the model used to compute the evolution of the wake width with axial distance behind the pylon trailing edge does not match the experimentally determined results.

11.2 Propeller Performance

The propeller performance was analyzed to assess the effects of installation and pylon blowing on pusher propeller performance. This section presents a comparison of the computed and measured performance of the propeller model in the isolated and installed configurations (Subsections 11.2.1 and 11.2.2, respectively). Considering the very small differences between the results computed and measured for the installed and blown configurations, the latter is not discussed here. Instead, it is the topic of discussion of Appendix F.2.

All results discussed in this section were obtained for the advance ratio range $0.5 \leq J \leq 1.9$, while again a freestream velocity of 26 m/s was selected. Note that all analyses were also performed at freestream velocities of 15, 19, and 30 m/s. However, the results obtained at these velocities were similar to those observed for the case with $U_\infty = 26$ m/s and therefore are not further discussed here. The installed results were computed and measured for a pylon position corresponding to a pylon - propeller spacing of $\Delta X = 114$ mm.

11.2.1 Isolated Configuration

The computed and measured isolated propeller performance diagrams are depicted in Figure 11.2. The experimental data was filtered using a cut-off frequency of 2,500 Hz.

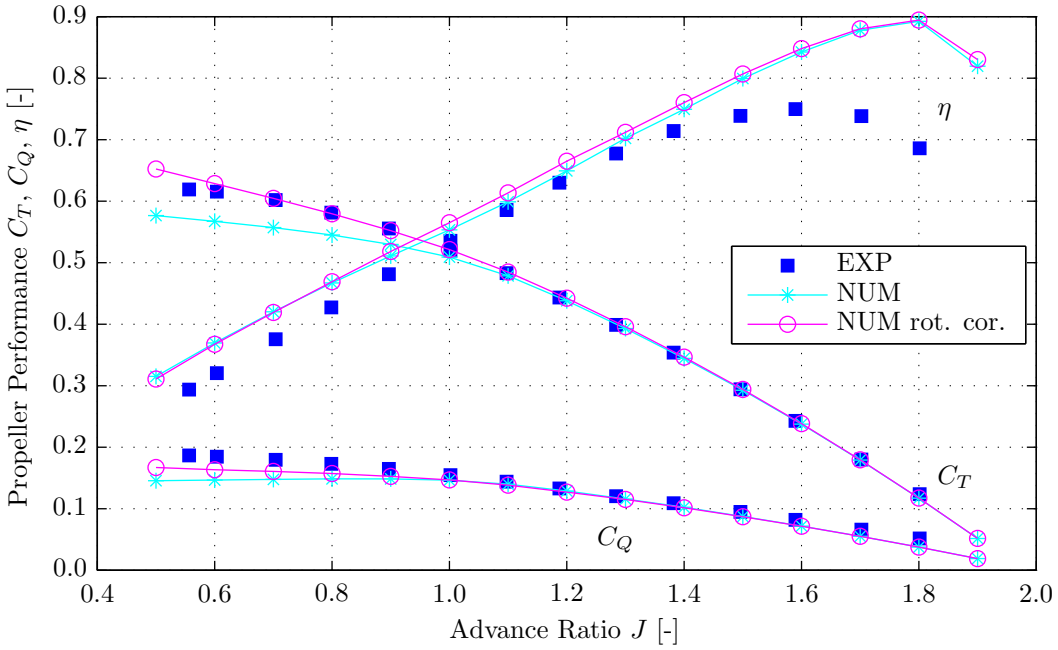

Figure 11.2: Measured and computed propeller performance diagrams. Isolated configuration, $U_\infty = 26$ m/s, $0.5 \leq J \leq 1.9$, $f_{\text{cut}} = 2,500$ Hz.

Figure 11.2 shows that when the rotation correction is applied a good match is obtained between the computed and measured propeller performance in the isolated configuration. Regarding the thrust coefficient it is observed that for advance ratios above $J = 0.7$ the computed and measured values are practically equal with the computed results within ± 0.005 of the measured data, corresponding to a relative difference of approximately 1%. At the lowest advance ratios larger differences are observed, with the maximum difference equal to approximately 0.02 at an advance ratio of $J = 0.55$, corresponding to a relative difference of 3%. This is as expected considering the reduced accuracy of the numerical analysis of the blade section response at the high angles of attack experienced at low advance ratios. It is concluded that the rotation correction overpredicts the increase in the maximum lift coefficient of the blade sections. It is expected that even better agreement between the experimental and numerical data can be obtained at the lowest advance ratios by modifying the values of the tuning parameters present in the model (see Equation (7.3)).

The correspondence between the computed and measured torque coefficients is not as good as for the thrust coefficient. For the advance ratio range of $1.0 \leq J \leq 1.5$ the match between

the experimental and numerical results is very good, with differences in the torque coefficient of at maximum 2% to 5%. However, at lower and higher advance ratios the differences between the computed and measured torque coefficients are larger. The discrepancy between the experimental and numerical results at high advance ratios ($J > 1.5$) is likely the result of inaccuracies in the drag coefficient data used in the XROTOR computations. These inaccuracies are the result of the fitting process performed to convert the drag coefficient response obtained from the numerical analysis of the blade section response to the inputs required by XROTOR, as discussed in Paragraph 7.2.1.1. At low advance ratios on the other hand the differences between the numerical and experimental results are again expected to result from inaccuracies in the blade section response obtained from the airfoil analysis program.

Regarding the propeller efficiency it is seen that the experimental and numerical results show relatively large differences, especially at the extremes of the advance ratio range. These differences are a direct result of the offsets between the experimental and numerical thrust and torque coefficients. The computed efficiency is higher than the measured efficiency for all advance ratios. At the lowest advance ratios ($J < 0.7$) the difference equals about five percentage points, while at high advance ratios the difference becomes even larger since the measured efficiency reaches its maximum at a lower advance ratio than for the computed results. For the advance ratio range $0.9 \leq J \leq 1.4$ the offset between the computed and measured efficiency equals around three percentage points.

11.2.2 Installed Configuration

Having discussed the isolated propeller performance, now the installed propeller performance results are considered. Figure 11.3 presents the computed and measured propeller performance diagrams for the installed configuration. For the numerical results again a distinction is made between the data computed with and without the empirical rotation correction.

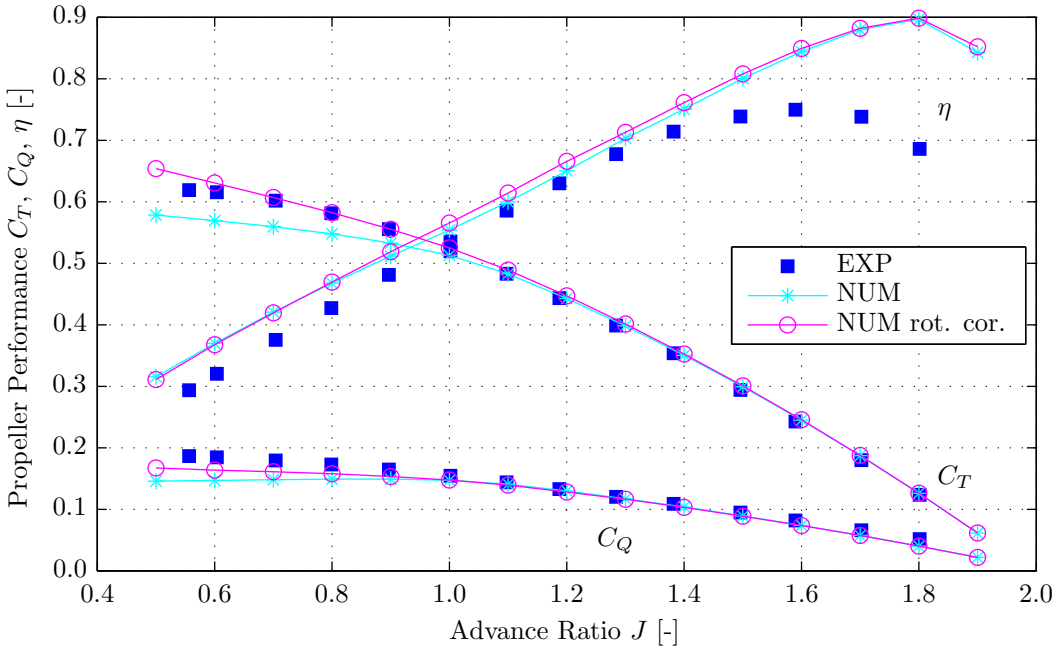

Figure 11.3: Measured and computed propeller performance diagrams.
Installed configuration, $U_\infty = 26$ m/s, $0.5 \leq J \leq 1.9$, $f_{\text{cut}} = 2,500$ Hz, extended pylon.

From Figure 11.3 it is observed that the computed and measured installed propeller performance show a slightly worse correspondence than for the isolated propeller. Over the entire advance ratio range the computed thrust coefficients are higher than the experimental results, with a difference of around 2% for the advance ratio range $0.7 \leq J \leq 1.5$. Considering the differences between the computed and measured propeller performance for the isolated propeller (see Figure 11.2), it is concluded that the numerical methods predict an increase in the time-averaged thrust coefficient due to installation which is larger than that measured during the experiments. At the lowest advance ratios the differences between the experimental and numerical results increase, similarly as for the isolated propeller results. With respect to the torque coefficient comparable trends are observed as seen before in Figure 11.2 for the isolated propeller. At this point it should be noted again that the installed propeller performance measurements were influenced by the low signal quality of the RSB data. The differences between the isolated and installed time-averaged thrust and torque coefficients were too small to exclude the possibility of measurement variability influencing the results.

11.3 Propeller Noise Emissions

The propeller noise emissions were computed and measured for the isolated, installed, and blown configurations. This section compares the experimental and numerical results, with the focus on the sound pressure levels of the first three BPF tones. The isolated propeller noise emissions are considered first (Subsection 11.3.1). Subsequently, the differences between the computed and measured sound pressure levels obtained for the installed configuration are discussed (Subsection 11.3.2). Finally the blown configuration is treated (Subsection 11.3.3). All results presented in this section correspond to a freestream velocity of 19 m/s, while the advance ratio range $0.5 \leq J \leq 1.9$ was considered. Furthermore, constant axial and circumferential directivity angles were selected: $\theta = 110°$ and $\phi = 90°$.

11.3.1 Isolated Configuration

The computed and measured sound pressure levels of the first three BPF tones in the isolated configuration are presented as a function of the advance ratio in Figure 11.4.

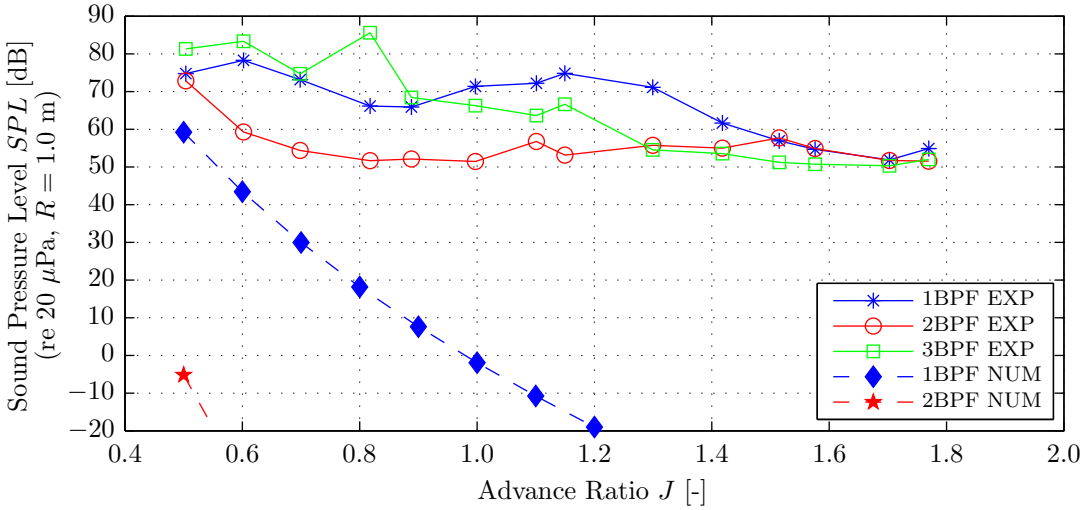

Figure 11.4: Comparison of computed and measured tonal noise levels versus the advance ratio. Isolated configuration, $U_\infty = 19$ m/s, $0.5 \leq J \leq 1.8$, $\theta = 110°$.

From Figure 11.4 it is observed that the computed and measured sound pressure levels show large differences. This is as expected considering the previous discussions of the experimental and numerical data for the isolated propeller. The experimental results returned unexpected results with the 3BPF tone dominating the sound spectrum at the lower advance ratios, while the SPL of the 1BPF tone was lower than expected over part of the advance ratio range as a result of additional tonal noise emissions at frequencies corresponding to individual blade passages. The numerical data on the other hand was characterized by a very rapid drop in the SPL with increasing advance ratio. This was the result of the low tip Mach numbers combined with the large number of blades and was considered as a limitation of the noise prediction method (see Subsection 10.2.2). In the end, it can be concluded that the accuracy of both the experimental and numerical noise emission data for the isolated propeller is low.

11.3.2 Installed Configuration

Following the comparison for the isolated propeller the noise emissions in the installed configuration are considered. A comparison between the experimental and numerical data for the sound pressure levels of the first three BPF tones as a function of the advance ratio is presented in Figure 11.5.

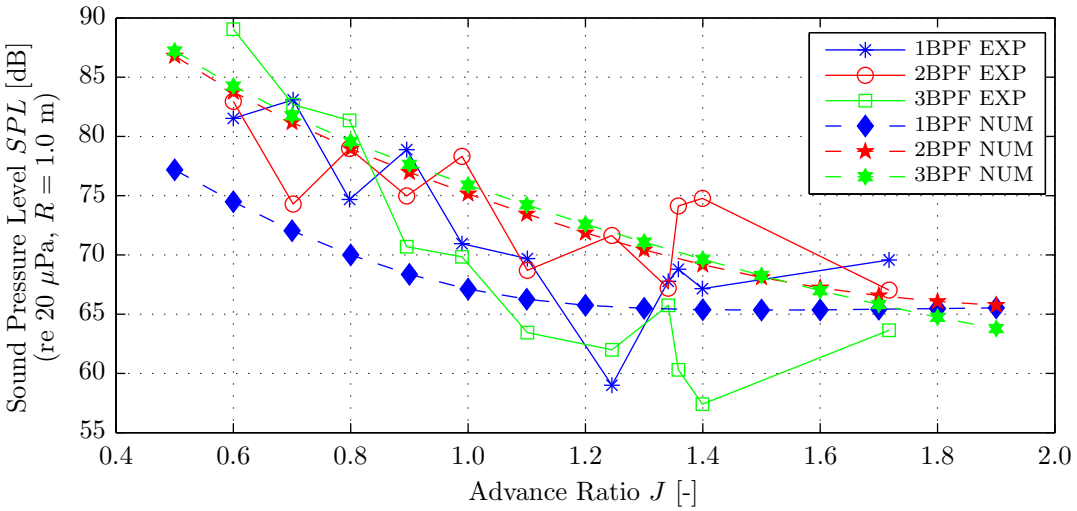

Figure 11.5: Comparison of computed and measured tonal noise levels versus the advance ratio. Installed configuration, $U_\infty = 19$ m/s, $0.5 \leq J \leq 1.9$, $\theta = 110°$, $\phi = 90°$.

The results presented in Figure 11.5 show that the agreement between the computed and measured results is better for the installed configuration than for the isolated case. The strong underprediction of the noise levels observed for the isolated configuration is no longer seen in the installed configuration, since the radiation efficiency issues experienced for the isolated configuration do not affect the computed installed propeller noise emissions. Although the experimental data shows larger than expected variations between the SPL measured at successive advance ratios and the absolute values are not equal, the general trends in the computed and measured results are comparable.

For the 1BPF tone the computed sound pressure levels are about 5-10 dB lower at most advance ratios when compared to a curve fit through the experimental data. Not taking into account the large fluctuations present in the experimental data, the trends observed in the experimental and numerical data for the SPL of the 2BPF tone are also similar, while

the absolute levels are within approximately ±5 dB. Finally, the behavior observed for the 3BPF tone shows the largest differences between the experimental and numerical results. The measured data shows a steeper increase in SPL with decreasing advance ratio than the computed results. Considering that at low advance ratios the isolated noise emissions are dominant, this might be the result of the unexpected strong increase in the SPL of the 3BPF tone with decreasing advance ratio measured for the isolated configuration.

11.3.3 Blown Configuration

Having discussed the agreement between the experimental and numerical noise emissions for the propeller in the isolated and installed configurations, finally the blown configuration is considered. Figure 11.6 presents the computed and measured sound pressure levels of the first three BPF tones as a function of the advance ratio.

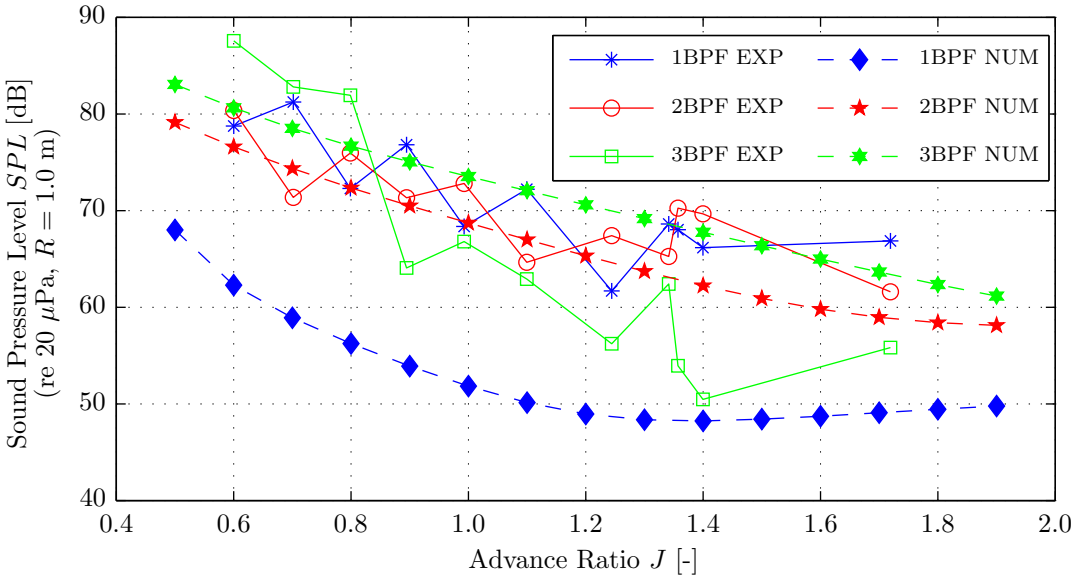

Figure 11.6: Comparison of computed and measured tonal noise levels versus the advance ratio. Blown configuration, $U_\infty = 19$ m/s, $0.5 \leq J \leq 1.9$, $Q = 600$ L/min, $\theta = 110°$, $\phi = 90°$.

From Figure 11.6 it is observed that, similarly as for the installed results, the experimental data is again characterized by a large variability between the measurements performed at successive advance ratios.

With respect to the trends observed in the data for the 1BPF tone it is concluded that the numerical method returns a comparable trend as that obtained from the experiments, albeit at a sound pressure level which is approximately 10 dB lower. In the blown configuration the noise generating mechanisms come closer to those dominating the isolated propeller noise. Considering that at the low freestream velocity of $U_\infty = 19$ m/s the numerical method strongly underpredicts the isolated propeller noise emissions, the large offset between the computed and measured results is as expected. The correspondence between the computed and measured SPL for the 2BPF tone is better, with both the trend and the absolute values relatively close to each other. Finally, for the 3BPF tone the same conclusion is drawn as in the previous subsection. Again, the experimental data shows a stronger increase in the SPL with decreasing advance ratio than the computed data.

In addition to the comparison of the absolute sound pressure levels in the blown configuration, also the SPL reductions due to blowing compared to the unblown, installed case are considered. Figure 11.7 depicts the reduction in tonal noise levels due to blowing for the first three BPF tones, as obtained from both the experimental and numerical evaluations.

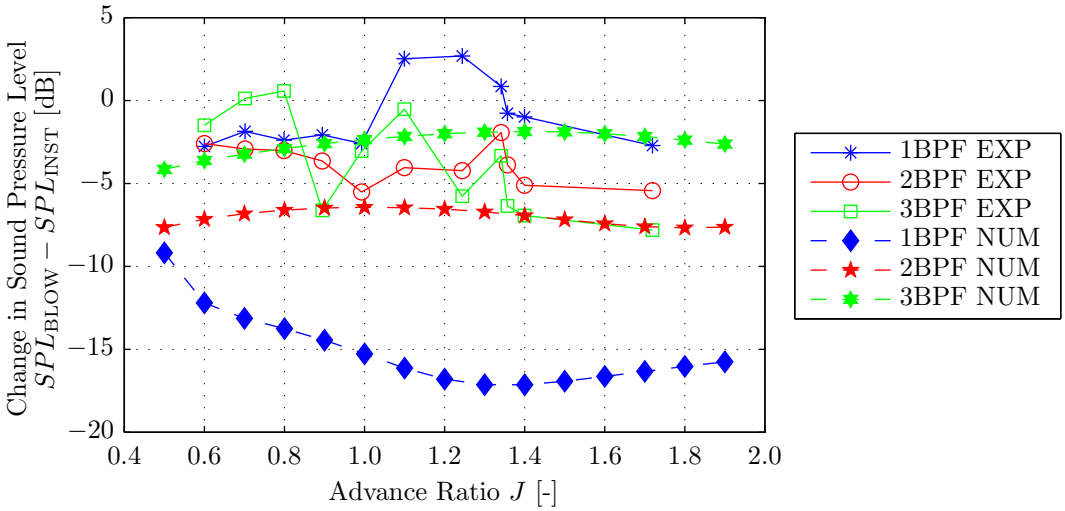

Figure 11.7: Change in the tonal noise levels due to blowing versus the advance ratio. Installed and blown configurations, $U_\infty = 19$ m/s, $0.5 \leq J \leq 1.9$, $Q = 600$ L/min, $\theta = 110°$, $\phi = 90°$.

Figure 11.7 shows that for the 1BPF tone the computed SPL reductions are much larger than the measured values. This is again explained by considering the differences observed between the isolated computations and measurements, since the noise generating mechanism in the blown configuration closely resembles that of the isolated noise emissions. The computed SPL reductions due to blowing for the 2BPF and 3BPF tones show a better agreement with the experimental data than obtained for the 1BPF tone, although still relatively large differences are observed. For the 2BPF tone the results are best, with approximately comparable trends in the experimental and numerical data at an offset of about 2-4 dB. The experimental results for the 3BPF tone display strong variations between the different advance ratios which are not present in the numerical results. Furthermore, while the computed results show an increasing noise reduction due to blowing with decreasing advance ratio, the experimental data displays the inverse trend.

Chapter 12

Conclusions and Recommendations

This chapter presents the conclusions and recommendations for future work derived from all results presented in this report. The conclusions are discussed first in Section 12.1, followed by the recommendations which are given in Section 12.2.

12.1 Conclusions

This report dealt with an experimental and numerical study focusing on the potential of pylon trailing edge blowing to reduce the adverse installation effects experienced by rear-fuselage mounted propellers in a pusher configuration. The aim of the research project was to experimentally and numerically analyze the performance and noise emissions of a pylon - pusher propeller combination, with and without pylon trailing edge blowing.

From experimental wake measurements performed using a typical pylon model with a custom designed Uniform Blowing Rod (UBR) integrated in its trailing edge it was concluded that the current design of the UBR does not result in a completely uniform outflow profile in the spanwise direction. This was attributed to non-uniform inflow resulting from separation in the divergent part of the air inlet channel, which can possibly be solved by optimizing the design whereby the entire geometry of the blowing system should be reconsidered. To achieve a uniform inflow at the propeller, the flow blown into the pylon wake by the pylon blowing system needs to mix with the external flow before it reaches the propeller disk. This mixing process turned out to be a strong function of the relative velocity of the external and blown flows. It was found that the velocity of the flow blown into the wake needs to be larger than that of the external flow for the blowing system to be effective. Using the proper flow rates it was measured that application of the current pylon blowing system does not completely eliminate the pylon wake. Instead, the introduction of the blown flow resulted in a velocity overshoot on the wake centerline with two local minima left and right of it. However, it was concluded that compared to the unblown case the magnitude of the velocity fluctuations experienced by the propeller blades was reduced by blowing, with reductions in the integral wake velocity deficit of up to 60%.

The developed numerical method used to analyze the pusher propeller installation effects does not allow for the computation of the blown pylon wake profiles. Instead, it can only be used to predict the wake profiles corresponding to the unblown pylon models. Comparison with the experimental data showed that the numerical method in general underpredicts the wake

width and depth at a given axial position, with differences observed of up to 25%. It was concluded that these differences could be the result of inaccuracies in the computed pylon drag coefficient, while it was also found that the equation used to compute the wake width does not match the trends observed in the experimental data.

The propeller performance was evaluated for the isolated, installed, and blown configurations using both experimental and numerical methods. The experimental data suffered from a low signal quality of the available Rotating Shaft Balance (RSB). At low advance ratios the peak-to-peak noise levels were found to be of the same order as the actual average thrust value, while at high advance ratios the signal-to-noise ratio became even worse. As a result, it was concluded that the RSB signals were unusable for time-accurate evaluations. Furthermore, a frequency spectrum analysis of the measured thrust data showed a number of unexpected peaks in the isolated measurements. Considering the close coupling between the level of the main power peaks and their frequency of occurrence it was concluded that the most likely explanation for this unexpected behavior is an eigenfrequency issue. Based on a comparison of the time-averaged results for different cut-off frequencies it was concluded that the RSB signals could still be used to assess time-averaged effects. An acceptable measurement repeatability was obtained and in the isolated configuration the expected Reynolds number effects were successfully measured. The differences between the isolated and installed time-averaged thrust and torque coefficients however were found to be too small to be quantified using the RSB, with inconsistent results obtained for the different freestream velocities considered. Accordingly, it was not possible to accurately quantify the effects of blowing on the propeller performance.

From the numerical assessment of the propeller performance it was concluded that when an empirical rotation correction is used to correct the blade section response at high angles of attack, excellent agreement is reached between the experimental and numerical results for advance ratios above $J = 0.7$. The maximum difference between the computed and measured thrust coefficients equaled around 1% for this advance ratio range. At the lower advance ratios the differences between the computed and measured propeller performance increased due to the reduced accuracy of the computations of the blade section characteristics at high angles of attack. However, still good agreement was obtained with a maximum difference between the experimental and numerical thrust coefficients of about 3%. Application of the numerical tool to the installed configuration showed that the effects of installation on the propeller performance are small. For advance ratios below $J = 1.4$ the differences between the computed time-averaged thrust and torque coefficients in the isolated and installed configurations were found smaller than 2%, with peak-to-peak variations in the time-accurate installed signals of at maximum 4%. Computations of the blown propeller performance using an experimentally determined pylon wake profile showed that the application of blowing further reduces the effects of installation on the propeller performance.

Experimental and numerical methods were used to quantify the effects of pylon trailing edge blowing on the propeller noise emissions. From the experimental measurements using two out-of-flow microphones it was concluded that the variability of the noise measurements was only acceptable for consecutive measurements performed at constant operating conditions, with variations in the measured sound pressure levels in the range of ± 1 dB. Based on preliminary studies using an unpowered propeller model it was concluded that the effects of installation on the propeller noise emissions are significant, and application of the pylon blowing system proved successful in reducing the noise penalty due to installation. The measurements performed using the isolated powered propeller model displayed a tonal character, with the

1BPF tone dominant for advance ratios above $J = 1.0$ and the 3BPF tone dominant for lower advance ratios. The high sound pressure level (SPL) of the 3BPF tone was explained by the presence of non-uniform inflow on the propeller, possibly resulting from interactions between the propeller model's support strut and the propeller itself. Additionally, unexpected tonal noise sources were identified at frequencies equal to integer multiples of the BPF divided by the number of blades, which was expected to be the result of an asymmetry in the propeller model. As a result, the measured SPL of the 1BPF tone will have been lower than that corresponding to the ideal case for which the unexpected low frequency tones would not occur. The measurements in the installed configuration showed clear noise penalties due to installation for the first six BPF tones with differences of up to 10 to 25 dB when compared to the isolated noise levels, depending on the propeller tone and the advance ratio. Broadband levels on the other hand were unaffected by the presence of the upstream pylon. It should be noted that the isolated and installed noise measurements could not be performed consecutively, thereby reducing the accuracy of the comparisons. Noise measurements of the powered propeller model with the blowing system enabled led to the conclusion that the blowing system is successful in reducing the tonal propeller noise. Depending on the advance ratio, at the maximum blowing rate of $Q = 680$ L/min SPL reductions for the 1BPF tone were achieved of up to 4 dB. For the 2BPF and 3BPF tones the maximum noise reductions were found even larger at 8 and 12 dB, respectively. Finally, the higher BPF tones (4BPF and higher) were practically eliminated by the application of blowing. Considering that the noise reductions due to blowing were largest for the highest blowing rate, it was concluded that the optimum blowing rate might not have been reached. Higher blowing rates could however not be achieved with the used air supply system.

The results obtained from the computations of the propeller noise emissions using the analytic frequency domain methods developed by Hanson led to the conclusion that for the isolated propeller the noise emissions are strongly underpredicted for low freestream velocities. It was found that this is the result of a combination of low tip Mach number and high blade number, leading to a very small radiation efficiency of the isolated propeller noise emissions at low velocities. Analysis of the tonal components of the sound spectra showed that the 1BPF tone clearly dominated the computed isolated propeller noise emissions. The computation of the installed noise levels showed that the presence of the upstream pylon dramatically changes the axial and circumferential directivity patterns of the propeller noise emissions. The unsteady loads result in a strong sound radiation towards the propeller axis, while in the circumferential direction clear lobes are introduced in the directivity pattern. In the propeller plane the total sound pressure levels computed for the installed configuration were significantly higher than for the isolated case, except at the lowest advance ratios for which the steady blade loads dominate the sound spectrum. The computations for the blown configuration were performed using an experimentally determined wake profile and showed that noise reductions could indeed be achieved by blowing when compared to the unblown installed configuration. It was concluded that the noise reductions obtainable by blowing are a function of both the advance ratio and the tip Mach number. At the lowest advance ratios the steady-state blade loads become dominant, hence the application of blowing no longer reduces the propeller noise emissions. Additional computations using simulated amounts of pylon wake fill-up showed that very small amounts of unsteady blade loading still lead to a strong increase in the sound pressure levels emitted at axial directivity angles close to the propeller axis. The additional noise emissions near the propeller plane on the other hand can be eliminated more easily,

with the computed SPL in the blown configuration about equal to the isolated case for 75% wake fill-up and more.

From the experimental and numerical evaluations of the potential of pylon trailing edge blowing to reduce the adverse installation effects experienced by pusher propellers it is concluded that the application of blowing can result in clear noise reductions, while the effects of installation on the propeller performance are small. Taking into account the significant fuel savings promised by future engine concepts employing propeller(s) in a pusher configuration this is an important result which can be used to develop potential solutions for the relatively high sound pressure levels emitted by such propulsion systems. The work presented in this report should not be considered as a final outcome, but instead as the starting point of more involved investigations of the effects of blowing on pusher propeller performance and noise emissions. To increase understanding of the working principles of the blowing system and its effects on the propeller performance and noise emissions additional research is required, for which a number of recommendations are presented in the following section.

12.2 Recommendations for Future Work

The experimental and numerical work presented in this report led to a number of clear conclusions as formulated in the previous section. However, in the course of the research project it was realized at several moments that opportunities for improvement of the results were still present. These are summarized below as recommendations for future work aimed at analyzing the effects of pylon blowing on pusher propeller performance and noise emissions.

Throughout the work discussed in this report it was assumed that the pylon wake profiles are unaffected by the presence of the downstream thrusting propeller. To improve the knowledge of the exact characteristics of the flow impinging on the propeller blades in the installed configuration it is recommended to also perform wake evaluations with the propeller model present behind the pylon. Regarding the experimental data, for this purpose a non-intrusive technique such as Particle Image Velocimetry (PIV) would be particularly useful. To implement the effects of the presence of the propeller in the numerical analyses more sophisticated approaches using CFD would have to be applied than the analytic models used currently.

At the same time the application of PIV and/or CFD could be used to increase the understanding of the interactions between the external flow and the flow blown into the pylon wake by the blowing system. The knowledge obtained in this way could be used to improve the design of the blowing system. Furthermore, with respect to the blowing system it is also recommended to investigate the potential of different outflow configurations. Whereas in this report only a design with an outlet in the trailing edge of the pylon was considered, outlets along the upper and lower surface upstream of the trailing edge could also be used. Such a configuration could possibly result in improved mixing of the external and blown flows, thereby leading to a more uniform inflow velocity profile at the propeller plane.

Regarding the assessment of the effectiveness of the blowing system it was found from the experimental noise measurements that it is likely that during the tests discussed in this report the optimum blowing rate was not reached. This was the result of a limitation imposed by the used air supply system which could not deliver sufficiently high air supply pressures. To increase the understanding of the effects of varying blowing rates on the propeller noise emissions, it is therefore recommended to modify the air supply system such that higher blowing rates can be achieved.

In terms of the geometry used for the experimental and numerical analyses of the effects of installation on the pusher propeller performance and noise emissions it is recommended to investigate the effect of the pylon - propeller spacing and the pylon geometry on the impact of the installation effects. In the experiments and the numerical evaluations discussed in this report the pylon - propeller spacing and the pylon were relatively large compared to typical geometries. An improved understanding of the sensitivity of the installation effects to these two parameters could be used to advantage in the design of propellers in a pusher configuration.

Although it was concluded that the effects of installation on the propeller performance are small, it is still recommended to perform force and moment measurements using an RSB with a signal quality sufficient to allow for time-accurate evaluations. The resulting data could be used to validate computations of the time-accurate blade response. Furthermore, in addition to the force and moment measurements for the total propeller using the RSB it would also be very useful to gain insight in the pressure distributions on the propeller blades. Again, a non-intrusive technique such as PIV could be suitable for this purpose. Knowledge of the time-accurate propeller response and the blade loading conditions is expected to be beneficial for the understanding of the noise generating mechanisms in the isolated, installed, and blown configurations.

Finally, with respect to the propeller noise emissions it is first of all recommended to investigate and improve the reproducibility of the microphone measurements. Furthermore, it is recommended to perform measurements on a larger and denser grid of axial directivity angles, with the measurements at the various directivity angles preferably performed simultaneously. In addition, it would be preferable to also perform measurements for varying circumferential directivity angles. Regarding the numerical evaluations of the propeller noise emissions it is recommended to put additional effort in understanding the limitations of the current models at low freestream velocities.

Bibliography

[1] C. Rohrback and F.B. Metzger. The Prop-Fan - A new Look in Propulsors. *11th AIAA/SAE Propulsion Conference*, Anaheim, CA, USA, 1975.

[2] R.D. Hager and D. Vrabel. Advanced Turboprop Project (NASA-SP-495). 1988.

[3] M.D. Bowles and V.P. Dawson. *The Advanced Turboprop Project: Radical Innovation in a Conservative Environment.* Engineering Science to Big Science: The NACA and NASA Collier Trophy Research Project Winners. Washington, D.C.: National Aeronautics and Space Administration, 1998.

[4] P. Busquin, P. Argüelles, M. Bischoff, B.A.C. Droste, Sir R. Evans, W. Kröll, J.-L. Lagardère, A. Lina, J. Lurnsden, D. Ranque, S. Rasmussen, P.I. Reutlinger, Sir R. Robins, H. Terho, and A. Wittlöv. *European Aeronautics: A Vision for 2020. Report of the Group of Personalities.* ACARE, 2001.

[5] E. Envia. NASA Open Rotor Research. *14th CEAS-ASC Workshop*, Warsaw, Poland, 2010.

[6] R.A.V. Robison. *Turbulence Ingestion Noise of Open Rotors.* PhD thesis, University of Cambridge, 2011.

[7] E.S. Hendricks and M.T. Tong. Performance and Weight Estimates for an Advanced Open Rotor Engine. *48th AIAA/ASME/SAE/ASEE Joint Propulsion Conference & Exhibit*, Atlanta, GA, USA, 2012.

[8] FAA. Continuous Lower Emissions, Energy, and Noise (CLEEN) Program, 2012. [Online] Available at: http://www.faa.gov/about/office_org/headquarters_offices/apl/research/aircraft_technology/cleen/ [Accessed 29 September 2012].

[9] Rolls-Royce plc. Sustainable and Green Engine (SAGE), 2012. [Online] Available at: http://www.rolls-royce.com/about/technology/research_programmes/gas_turbine_programmes/sage.jsp [Accessed 21 September 2012].

[10] M.D. Guynn, J.J. Berton, E.S. Hendricks, M.T. Tong, W.J. Haller, and D.R. Thurman. Initial Assessment of Open Rotor Propulsion Applied to an Advanced Single-Aisle Aircraft. *11th AIAA Aviation Technology, Integration, and Operations (ATIO) Conference*, Virginia Beach, VA, USA, 2011.

[11] P.M. Niskode, R. Stickles, B. Allmon, and R. DeJong. CLEEN Consortium Open Session, October 2010. [Online] Available at: http://www.faa.gov/about/office_org/headquarters_offices/apl/research/aircraft_technology/cleen/2010_consortium/media/GE%20-%20FAA%20CLEEN%20Consortium%202010%20-%20Unlimited%20Rights.pdf [Accessed 29 September 2012].

[12] A. Stürmer and J. Yin. DLR-AS CROR & Propeller Noise Prediction. *14th CEAS-ASC Workshop*, Warsaw, Poland, 2010.

[13] A.B. Parry, M. Kingan, and B.J. Tester. Relative importance of open rotor tone and broadband noise sources. *17th AIAA/CEAS Aeroacoustics Conference (32nd AIAA Aeroacoustics Conference)*, Portland, OR, USA, 2011.

[14] IHS Jane's. Jane's All the World's Aircraft, 2012. [Online] Available at: http://jawa.janes.com/public/jawa/index.shtml (subscription required) [Accessed 30 September 2012].

[15] C. Lambert. *SBAC Aviation and Environment Briefing Papers. 3: Open Rotor Engines.* London, UK: Society of British Aerospace Companies, 2008.

[16] P.J.W. Block. Experimental Study of the Effects of Installation on Single- and Counter-Rotation Propeller Noise (NASA-TP-2541). 1986.

[17] P.J.W. Block. Pusher Propeller Noise Directivity and Trends. *10th AIAA Aeroacoustics Conference*, Seattle, WA, USA, 1986.

[18] D.M. Elliott. Initial Investigations of the Acoustics of a Counter-Rotating Open Rotor Model With Historical Baseline Blades in a Low-Speed Wind Tunnel (NASA-TM-2012-217258). 2012.

[19] S. Funke, L. Kim, and H.A. Siller. Microphone-Array Measurements of a Model Scale Contra-Rotating Open Rotor in a Reverberant Open Wind-Tunnel. *17th AIAA/CEAS Aeroacoustics Conference (32nd AIAA Aeroacoustics Conference)*, Portland, OR, USA, 2011.

[20] J. Ricouard, E. Julliard, M. Omaïs, V. Regnier, S. Baralon, and A.B. Parry. Installation effects on contra-rotating open rotor noise. *16th AIAA/CEAS Aeroacoustics Conference*, Stockholm, Sweden, 2010.

[21] B. Shivashankara, D. Johnson, and R. Cuthbertson. Installation Effects on Counter Rotating Propeller Noise. *13th AIAA Aeroacoustics Conference*, Tallahassee, FL, USA, 1990.

[22] N. Peake and A.B. Parry. Modern Challenges Facing Turbomachinery Aeroacoustics. *Annual Review of Fluid Mechanics*, 44: pp. 227–248, 2012.

[23] A. Stürmer and J. Yin. Aerodynamic and Aeroacoustic Installation Effects for Pusher-Configuration CROR Propulsion Systems. *28th AIAA Applied Aerodynamics Conference*, Chicago, IL, USA, 2010.

[24] P.J.W. Block and G.L. Gentry, Jr. Directivity and Trends of Noise Generated by a Propeller in a Wake (NASA-TP-2609). 1986.

[25] V. Blandeau. *Aerodynamic Broadband Noise from Contra-Rotating Open Rotors*. PhD thesis, University of Southampton, 2011.

[26] N. Ben Nasr, B. Rodriguez, A. Chelius, and S. Canard-Caruana. Blowing Strategies of Pylon-Propeller Configuration for Noise Reduction using Numerical Approach. *6th AIAA Flow Control Conference*, New Orleans, LA, USA, 2012.

[27] G.L. Gentry, Jr., E.R. Booth, Jr., and M.A. Takkallu. Effect of Pylon Wake With and Without Pylon Blowing on Propeller Thrust (NASA-TM-4162). 1990.

[28] A. Stürmer and J. Yin. Active control of unsteady blade loads for installed CROR propulsion systems. *17. DGLR/STAB-Symposium*, Berlin, Germany, 2010.

[29] Delft University of Technology. Open Jet Facility, 2008. [Online] Available at: http://www.lr.tudelft.nl/en/organisation/departments-and-chairs/aerodynamics-and-wind-energy/wind-energy/facilities/open-jet-facility/ [Accessed 15 November 2012].

[30] R.P. Woodward and C.E. Hughes. Noise of a Model Counterrotation Propeller With Simulated Fuselage and Support Pylon at Takeoff/Approach Conditions. *12th AIAA Aeroacoustics Conference*, San Antonio, TX, USA, 1989.

[31] T. Sinnige. *Propeller Test Rig Setup and Operating Manual*. Delft, the Netherlands: Delft University of Technology, 2013.

[32] E.C.R. van Berkel. Technical Drawings ESPOSA Propeller Test Rig Setup, October 2012. [Accessed 01 February 2013].

[33] H. Schlichting. Über das ebene Windschattenproblem. *Archive of Applied Mechanics*, 1 (5): pp. 533–571, 1930.

[34] H. Reichardt. *Gesetzmäßigkeiten der freien Turbulenz*. V.D.I. - Forschungsheft 414, 1942.

[35] VP Instruments. VP Instruments Product Catalog 2012/2013, 2013. [Online] Available at: http://www.vpinstruments.com/download/Brochures/CAT-VP-1202-WO-Full.pdf [Accessed 5 September 2013].

[36] VP Instruments. VPFlowMate in-line, 2013. [Online] Available at: http://www.vpinstruments.com/shop/measure/flowmeters/vpflowmate/ [Accessed 5 September 2013].

[37] Mensor. Mensor Digital Pressure Gauge Series 2100 Operation Manual, 2006. [Online] Available at: http://www.mensor.com/upload/DPG2100_31281.pdf [Accessed 5 September 2013].

[38] L.G.M. Custers, A.H.W. Hoeijmakers, and A.E. Harris. Rotating shaft balance for measurement of total propeller force and moment. *15th International Congres on Instrumentation in Aerospace Simulation Facilities*, Saint-Louis, France, 1993.

[39] LinearX Systems Inc. M51 Measurement Microphone Product Brochure, 2000. [Online] Available at: http://www.linearx.com/files/pdf/M51_Mic_Brochure.pdf [Accessed 8 September 2013].

[40] P.D. Welch. The Use of Fast Fourier Transform for the Estimation of Power Spectra: A Method Based on Time Averaging Over Short, Modified Periodograms. *IEEE Transactions on Audio and Electroacoustics*, AU-15(2): pp. 70–73, 1967.

[41] J. Simonich, D. McCormick, and P. Lavrich. Interaction Noise Mechanisms for Advanced Propeller Experimental Results. *12th AIAA Aeroacoustics Conference*, San Antonio, TX, USA, 1989.

[42] W.C. Horne and P.T. Soderman. Flow-Field Survey of an Empennage Wake Interacting with a Pusher Propeller (NASA-TM-101003). 1988.

[43] J.F. Nash. *An Analysis of the Subsonic Flow past Symmetrical Blunt-Trailing-Edge Aerofoil Sections at Zero Incidence, in the Absence of a Vortex Street.* London, UK: Ministry of Aviation (Reports and Memoranda No. 3436), 1964.

[44] M. Tanner. A Method for Reducing the Base Drag of Wings with Blunt Trailing Edge. *Aeronautical Quarterly*, 23: pp. 15–23, 1972.

[45] D. Krentel and W. Nitsche. Investigation of the Near and Far Wake of a Bluff Airfoil Model with Rear End Variations using Time-resolved Particle Image Velocimetry. *16th International Symposium on Applications of Laser Techniques to Fluid Mechanics*, Lisbon, Portugal, 2012.

[46] J.F. Nash, V.G. Quincey, and J. Callinan. *Experiments on Two-Dimensional Base Flow in Subsonic and Transonic Speeds.* London, UK: Ministry of Aviation (Reports and Memoranda No. 3427), 1963.

[47] P.W. Bearman. The effect of base bleed on the flow behind a two-dimensional model with a blunt trailing edge. *Aeronautical Quarterly*, 18, 1967.

[48] C.F. Wood. Visualization of an incompressible wake with base bleed. *Journal of Fluid Mechanics*, 29(2): pp. 259–272, 1967.

[49] B. Magliozzi, D.B. Hanson, and R.K. Amiet. *Aeroacoustics of Flight Vehicles: Theory and Practice*, chapter Propeller and Propfan Noise, pages 1–61. NASA Reference Publication 1258, Vol. 1 WRDC Technical Report 90-3052. NASA, 1992.

[50] H.H. Brouwer. Analytical method for the computation of the noise from a pusher propeller. *16th AIAA/CEAS Aeroacoustics Conference*, Stockholm, Sweden, 2010.

[51] M. Drela and H. Youngren. XROTOR: an interactive program for the design and analysis of ducted and free-tip propellers and windmills, 2011. [Software] Available at: http://web.mit.edu/drela/Public/web/xrotor/ [Accessed 15 November 2012].

[52] J.A. Nelder and R. Mead. A simplex method for function minimization. *The Computer Journal*, 7(4): pp. 308–313, 1965.

[53] H. Himmelskamp. *Profile investigations on a rotating airscrew.* PhD thesis, Aerodynamische Versuchsanstalt Göttingen, 1945.

[54] H. Snel, R. Houwink, and J. Bosschers. Sectional Prediction of Lift Coefficients on Rotating Wind Turbine Blades in Stall (ECN-C–93-052). *Netherlands Energy Research Foundation (ECN) Internal Report*, 1994.

[55] Y. Colin, A. Carazo, B. Caruelle, T. Nodé-Langlois, and A.B. Parry. Computational strategy for predicting CROR noise at low-speed - Part I: review of the numerical methods. *18th AIAA/CEAS Aeroacoustics Conference (33rd AIAA Aeroacoustics Conference)*, Colorado Springs, CO, USA, 2012.

[56] M.H. Dunn and A.F. Tinetti. Advanced Time Domain Noise Prediction Methods for Open Rotors and Installation Effects. *18th AIAA/CEAS Aeroacoustics Conference (33rd AIAA Aeroacoustic Conference)*, Colorado Springs, CO, USA, 2012.

[57] A. Gérard, A. Berry, P. Masson, and Y. Gervais. Evaluation of Tonal Aeroacoustic Sources in Subsonic Fans Using Inverse Models. *AIAA Journal*, 45(1): pp. 98–109, 2007.

[58] W.R. Sears. Some Aspects of Non-Stationary Airfoil Theory and Its Practical Application. *Journal of the Aeronautical Sciences*, 8(3): pp. 104–108, 1941.

[59] W.R. Sears. *A Systematic Presentation of the Theory of Thin Airfoils in Non-Uniform Motion*. PhD thesis, California Institute of Technology, 1938.

[60] R.K. Amiet. Compressibility Effects in Unsteady Thin-Airfoil Theory. *AIAA Journal*, 12(2): pp. 252–255, 1974.

[61] M.J. Landahl. *Unsteady Transonic Flow*. New York, NY, USA: Pergamon Press, 1961.

[62] D.B. Hanson. Helicoidal Surface Theory for Harmonic Noise of Propellers in the Far Field. *AIAA Journal*, 18(10): pp. 1213–1220, 1980.

[63] D.B. Hanson. Noise of Counter-rotation Propellers. *Journal of Aircraft*, 22(7): pp. 609–617, 1985.

[64] A.B. Parry. *Theoretical Prediction of Counter-Rotating Propeller Noise*. PhD thesis, University of Leeds, 1988.

[65] A.B. Parry and D.G. Crighton. Theoretical Prediction of Single Rotation Propeller Noise. *10th AIAA Aeroacoustics Conference*, Seattle, WA, USA, 1986.

[66] A.B. Parry and D.G. Crighton. Prediction of Counter-Rotation Propeller Noise. *12th AIAA Aeroacoustics Conference*, San Antonio, TX, USA, 1989.

[67] M.E. Goldstein. *Aeroacoustics*. New York, NY, USA: McGraw-Hill, 1976.

[68] T.J. Mueller (ed.). *Aeroacoustic Measurements*. Berlin, Germany: Springer-Verlag Berlin Heidelberg New York, 2002.

[69] M. Drela and H. Youngren. XROTOR User Guide, 2013. [Online] Available at: http://web.mit.edu/drela/Public/web/xrotor/xrotor_doc.txt [Accessed 24 February 2013].

[70] S. Goldstein. On the Vortex Theory of Screw Propellers. *Proceedings of the Royal Society of London. Series A*, 123: pp. 440–465, 1929.

[71] A. Betz. Schraubenpropeller mit geringstem Energieverlust. Mit einem Zusatz von L. Prandtl. *Nachrichten von der Gesellschaft der Wissenschaften zu Göttingen*, 2: pp. 193–217, 1919.

Appendix A

Experimental Data Post-Processing

This appendix provides a detailed description of the post-processing applied to the experimental data. First, the applied measurement corrections are presented in Section A.1. Thereafter, the post-processing routines are discussed in Section A.2.

A.1 Measurement Corrections

The raw experimental data required corrections for a number of effects which adversely affect the data quality. This section describes the corrections applied to the propeller performance measurements (Subsection A.1.1) and the propeller noise measurements (Subsection A.1.2).

A.1.1 Propeller Performance Measurement Corrections

In the analysis of the RSB data corrections were applied to take into account the effects on the measurements of the propeller RPM (Paragraph A.1.1.1) and the pressure acting on the back of the propeller hub (Paragraph A.1.1.2). Note that spinner drag and RSB temperature effects were neglected, hence no corrections were performed for these two aspects.

A.1.1.1 RPM Correction

While rotating with the propeller, centrifugal loads act on the RSB, thereby affecting the measurement data. According to calculations performed by NLR, the centrifugal load only has a significant effect on the on-axis force (i.e. thrust) [38]. To take into account this effect a correction factor was applied to one of the terms of the (linear) calibration matrix used to convert the RSB measurements into actual forces. The correction factor is defined as an inverse quadratic function of the RSB's angular velocity n (expressed in revolutions per second):

$$K_{\mathrm{RPM}} = \frac{1}{A + Bn + Cn^2} \tag{A.1}$$

with A, B, and C calibration factors of which the values were provided by NLR:

$$\begin{bmatrix} A \\ B \\ C \end{bmatrix} = \begin{bmatrix} 1 \\ -6.01752 \cdot 10^{-6} \\ -6.69033 \cdot 10^{-8} \end{bmatrix} \tag{A.2}$$

The correction factor for RPM effects K_{RPM} was evaluated for each measurement point using Equations (A.1) and (A.2). Subsequently, it was multiplied with the entry of the linear RSB calibration matrix which corresponds to the contribution to the thrust of the measured voltage of the on-axis moment channel (i.e. $AR(2,3)$, see Appendix B).

A.1.1.2 Propeller Hub Back Pressure Correction

The pressure acting on the backside of the propeller hub results in an effective drag term, thereby affecting the axial force measured by the RSB:

$$F_{\mathrm{RSB}_X} = -T + D_{\mathrm{bp}} \tag{A.3}$$

with F_{RSB_X} the axial force measurement obtained from the RSB, T the actual thrust produced by the propeller, and D_{bp} the back pressure drag. Note that the longitudinal axis of the reference frame in which the RSB components are defined points in the downstream direction, hence opposite to the direction of positive thrust.

To account for the back pressure effect a pressure plate is installed at the front of the pneumatic motor, right behind the spinner gap. The pressure at this plate was measured at twenty pressure orifices, distributed over two perpendicular lines crossing through the center of the plate. The back pressure was then obtained by:

$$D_{\mathrm{bp}} = -\frac{(p_i - p_\infty)}{20} A_{\mathrm{bp}} \tag{A.4}$$

with p_i the pressure measured at back plate pressure orifice i, p_∞ the freestream static pressure, and A_{bp} the area of the pressure plate.

During all propeller performance measurements the back pressures at the twenty back plate pressure orifices were measured together with the RSB data. The drag term computed using Equation (A.4) was inserted into Equation (A.3) to obtain the corrected propeller thrust.

A.1.2 Propeller Noise Measurement Corrections

In the analysis of the microphone data corrections were applied to take into account the effects of uneven microphone frequency response (Paragraph A.1.2.1) and wind tunnel shear layer refraction (Paragraph A.1.2.2).

A.1.2.1 Microphone Frequency Response Correction

The microphone's frequency response is not completely flat over the entire frequency spectrum. To correct for this effect, frequency dependent sound pressure level correction factors are provided by the microphone's manufacturer LinearX. Figure A.1 displays the correction factors for the microphones used during the wind tunnel test campaign.

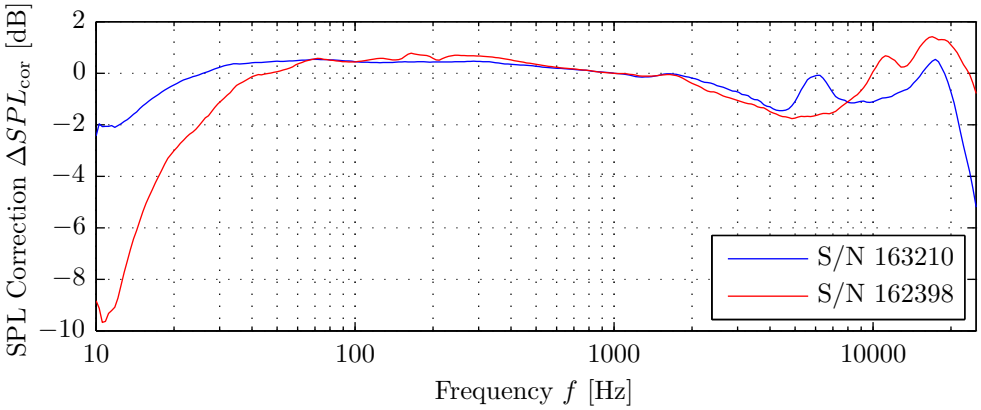

Figure A.1: Microphone frequency response correction factors as a function of the frequency for the LinearX M51 microphones with serial numbers 163210 and 162398.

The sound pressure level correction factor ΔSPL_{cor} was used to correct the microphone frequency response as follows:

$$SPL_{\text{flat}}(f) = SPL(f) - \Delta SPL_{\text{cor}}(f) \tag{A.5}$$

Note that the frequency response correction factor ΔSPL_{cor} is defined on a discrete frequency grid. Piecewise cubic interpolation was performed to obtain the microphone correction factors at the actual frequencies of interest.

A.1.2.2 Open Jet Shear Layer Refraction Correction

The propeller noise measurements were performed using out-of-flow microphones in an open jet wind tunnel. As a result, the acoustic waves had to travel through the open jet's shear layer before reaching the microphones. This results in refraction effects which change both the propagation angle as well as the sound pressure level of the acoustic waves.

To account for the effects of shear layer refraction, the method described by Mueller in reference [68] was adopted. The shear layer was modeled as an infinitely thin cylindrical vortex sheet and the jet and ambient air were assumed to be homogeneous in their own domains. Furthermore, the noise source was assumed to be located on the open jet's centerline, which is indeed approximately the case for the propeller measurements discussed in this report.

Following the assumptions mentioned above, the shear layer refraction process can be illustrated as depicted in Figure A.2. The solid line 'acoustic ray actual path' represents the refracted acoustic ray measured at the microphone position. The dashed line labeled 'path in large stream without shear layer' corresponds to the path the acoustic ray would follow in an equivalent velocity field without shear layer. The dashed line 'path in still air' represents the propagation path which the acoustic ray would follow with the jet at zero velocity and corresponds to the actual emission angle of the noise source.

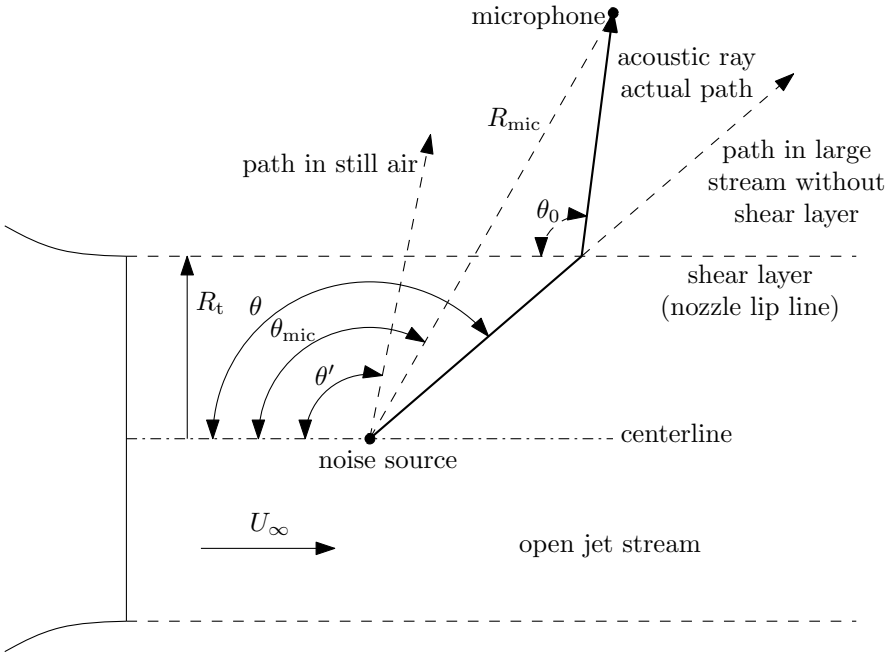

Figure A.2: Sketch of the open jet shear layer refraction process. Reproduced from [68].

To find the value of the actual emission angle of the measured sound θ', the following three equations need to be solved by iteration: [68]

$$\theta = \tan^{-1}\left\{\frac{\sin(\theta')}{\cos(\theta') - M_\infty}\right\} \tag{A.6}$$

$$R_{\text{mic}}\cos(\theta_{\text{mic}}) = R_{\text{t}}\cot(\theta) + \{R_{\text{mic}}\sin(\theta_{\text{mic}}) - R_{\text{t}}\}\cot(\theta_0) \tag{A.7}$$

$$M_\infty = \frac{1}{\cos(\theta')} - \frac{a_0/a_{\text{t}}}{\cos(\theta_0)} \tag{A.8}$$

with a_0/a_{t} the ratio between the speeds of sound outside and inside the jet, M_∞ the freestream Mach number, R_{mic} the distance between the source and the microphone, R_{t} the distance between the source and the shear layer, θ the propagation angle in an infinitely wide jet, θ_{mic} the microphone directivity angle, and θ_0 the angle to the shear layer - microphone vector.

With the relevant propagation angles obtained from the solution of Equations (A.6) through (A.8), the predicted sound pressure level at position (R,θ') (with R the distance along the emission angle from the sound source to the point at which the sound pressure level is to be estimated) is computed from the original microphone measurement at position (R_{mic},θ_{mic}) using:

$$SPL(R,\theta') = SPL(R_{\text{mic}},\theta_{\text{mic}}) + 20\log_{10}\left(\frac{p^{\text{rms}}}{p^{\text{rms}}_{\text{mic}}}\right) \tag{A.9}$$

with $SPL(R_{\text{mic}},\theta_{\text{mic}})$ the original microphone measurement and $p^{\text{rms}}/p^{\text{rms}}_{\text{mic}}$ the ratio between the RMS values of the acoustic pressures at positions (R,θ') and (R_{mic},θ_{mic}) defined by: [68]

$$\frac{p^{\text{rms}}}{p^{\text{rms}}_{\text{mic}}} = \sqrt{\frac{\rho_{\text{t}}}{\rho_0}D_{\text{t}}^{-4}\frac{R_0 R_{\text{a}}}{R^2}} \tag{A.10}$$

with ρ_{t}/ρ_0 the ratio between the air density inside and outside the jet and D_{t} the Doppler factor. Furthermore, R_0 equals the distance from the open jet stream's centerline to the microphone, measured along the path connecting the apparent source location and the microphone position. R_{a} is defined as the distance from the apparent source location to the microphone.

The Doppler factor D_{t} follows from: [68]

$$D_{\text{t}} = 1 - M_\infty\cos(\theta') \tag{A.11}$$

The distances R_0 and R_{a} are discussed in more detail in reference [68]. Here, only their definition is given: [68]

$$R_0 = R_{\text{mic}}\frac{\sin(\theta_{\text{mic}})}{\sin(\theta_0)} \tag{A.12}$$

$$R_{\text{a}} = R_0 + \frac{R_{\text{t}}}{\sin(\theta_0)}\left[\left\{\frac{\cot(\theta')}{\cot(\theta_0)}\right\}^3\left(\frac{a_0}{a_{\text{t}}}\right)^2 - 1\right] \tag{A.13}$$

Note that it was assumed that the atmospheric properties of the air inside and outside of the jet were equal, hence $a_0/a_{\text{t}} = \rho_0/\rho_{\text{t}} = 1$. Furthermore, it was decided to use a reference radius of 1 m for all acoustic measurements, hence $R = 1$ m.

A.2 Measurement Data Post-Processing Routines

The data obtained during the experimental test campaign was post-processed to obtain the final experimental results. The pressure measurements in the pylon wake region were converted into velocities following Bernoulli's principle (Subsection A.2.1). The raw propeller performance measurements were corrected for rotational effects and spinner back pressure and converted into actual forces and moments using dedicated calibration matrices (Subsection A.2.2). Finally, the raw microphone data was calibrated and converted into sound pressure levels using measured calibration data, and converted to the frequency domain for spectral analysis of the signals (Subsection A.2.3). Note that the data obtained from the flow meter did not require any post-processing, and thus is not discussed in this section.

A.2.1 Pylon Wake Profile Measurements

The raw pylon wake profile measurement data consisted of measured total and static pressure values referenced to a static tube located in the test section close to the pylon (but outside of the flow). With the total and static pressures known, the resulting local velocity U was computed following Bernoulli's principle:

$$U\left(X,Y,Z\right) = \sqrt{2\frac{\left\{p_{\mathrm{t}}\left(X,Y,Z\right) - p_{\mathrm{s}}\left(X,Y,Z\right)\right\}}{\rho_{\infty}}} \tag{A.14}$$

with ρ_{∞} the freestream air density which was obtained from the wind tunnel's diagnostics data acquisition system every time a pressure measurement was performed. Since the static and total pressure measurements were not performed at the exact same time, small differences in air density occurred between the total and static pressure measurements corresponding to the same position in the pylon wake. This was accounted for by averaging the two available values of the air densities at each measurement position in the wake domain.

Since the total and static pressure measurements were performed using the same reference pressure, the measurement data was substituted directly into Equation (A.14) to compute the local velocities in the wake for all measurement points.

A.2.2 Propeller Performance Measurements

The RSB returns analog output voltages from the four channels corresponding to the four force/moment components, together with the voltage of the 1P trigger pulse signal. To convert the measured voltages into actual forces and moments, a number of calibration steps were performed:

1. *Determining the zero loading offset of the RSB*

   The four channels of the RSB show an offset from zero in unloaded conditions. To obtain the actual response due to the propeller forces this offset needs to be subtracted from the measurements performed with the rotating propeller. The zero loading offset was determined by performing two 'zero measurements': one at the beginning (index 1) and one at the end of each measurement run (index N_{meas}). The results obtained from both zero measurements were averaged to obtain the RSB's final zero loading offsets:

$$\left(f_i\right)_0 = \frac{1}{2}\left(\frac{1}{N}\sum_{j=1}^{N}\left(f_i\right)_j^{n_{\mathrm{meas}}=1} + \frac{1}{N}\sum_{j=1}^{N}\left(f_i\right)_j^{n_{\mathrm{meas}}=N_{\mathrm{meas}}}\right) \tag{A.15}$$

with i the index of the force/moment coefficient (1 to 4), N the number of sampling points for each measurement, j the index of the sampling point, and n_{meas} the index of the measurement point in the test matrix of the measurement run.

2. *Subtracting the zero loading offsets from the recorded raw data*

   The RSB's zero loading offsets computed using Equation (A.15) were subtracted from the raw data to obtain the actual RSB response due to the propeller forces and moments:

   $$\Delta f_i = f_i - (f_i)_0 \tag{A.16}$$

   with f_i the raw measurement data and $(f_i)_0$ the zero loading offset of force/moment component i determined using Equation (A.15).

3. *Applying the RSB calibration matrices to the data obtained in step 2 to obtain the calibrated forces and moments*

   With the RSB response due to the propeller forces and moments known from Equation (A.16), the actual forces and moments were computed using calibration matrices provided by NLR:

   $$F_i = AR\,(i,j)\,\Delta f_j + AR_i\,(j,k)\,\Delta f_j \Delta f_k \tag{A.17}$$

   where Einstein's summation convention is used and $i = (1,2,3,4)$, $j = (1,2,3,4)$, and $k = (j, j+1, \ldots, 4)$. The linear calibration matrix is defined by the variable AR, while the non-linear calibration matrices corresponding to component i are denoted AR_i. The values of the entries of the RSB calibration matrices are presented in Appendix B. Note that an RPM correction was applied to the linear calibration matrix as discussed in Paragraph A.1.1.1.

4. *(optional) Filtering the RSB results to remove high-frequency noise*

   The calibrated forces and moments obtained from the previous step can be filtered using a zero-phase digital filter to remove high-frequency noise from the signals. This filter operates in both the forward and reverse directions, thereby resulting in zero phase distortion. A fourth order Butterworth filter was used, with the value of the cut-off frequency selected depending on the desired frequency content of the filtered signals.

5. *Correcting the computed thrust for the effects of propeller hub back pressure*

   With the propeller forces and moments computed, the correction for the effects of propeller hub back pressure was applied as discussed in Paragraph A.1.1.2.

6. *Computing the dimensionless propeller performance indicators*

   Lastly, the propeller forces and moments were used to compute the propeller thrust coefficient C_T, torque coefficient C_Q, and propeller efficiency η:

   $$C_T = \frac{T}{\rho n^2 D^4} \tag{A.18}$$

   $$C_Q = \frac{Q}{\rho n^2 D^5} \tag{A.19}$$

   $$\eta = \frac{J}{2\pi}\frac{C_T}{C_Q} \tag{A.20}$$

A.2.3 Propeller Noise Measurements

The raw microphone data consists of analog output voltages corresponding to the measured acoustic pressures. To convert the measured voltages into sound pressure levels a number of post-processing steps were performed:

1. *Determining the microphone calibration factors*

   To be able to convert the raw microphone data into calibrated sound pressure levels, the microphones first had to be calibrated. For this purpose, the microphones were mounted inside a pistonphone which emits a harmonic sound at a known amplitude ($SPL_{\text{cal}} = 114\,\text{dB}$). After enabling the pistonphone, the microphone signal was recorded and subsequently used to compute the microphone calibration factor K_{mic} as follows:

   $$K_{\text{mic}} = \frac{p_{\text{cal}}^{\text{rms}}}{\text{RMS}\left\{f - \bar{f}\right\}} = \frac{p_0 \cdot 10^{\frac{SPL_{\text{cal}}}{20}}}{\text{RMS}\left\{f - \bar{f}\right\}} \tag{A.21}$$

   with f the raw microphone signal obtained during the calibration procedure, $\bar{f}$ the average microphone signal obtained during the calibration procedure, p_0 the acoustic reference pressure of 20 μPa, SPL_{cal} the known reference sound pressure level emitted by the pistonphone, and $\text{RMS}\{x\}$ the RMS operator defined by:

   $$\text{RMS}\{x\} = \sqrt{\frac{1}{N}\left(x_1^2 + x_2^2 + \cdots + x_N^2\right)} \tag{A.22}$$

   with N the number of sampling points.

   Note that the calibration was performed separately for both microphones, resulting in two calibration factors (one corresponding to each of the microphones).

2. *Calibrating the raw microphone outputs*

   Having computed the calibration factor for each microphone using Equation (A.21), the raw microphone data was calibrated by multiplication with the calibration factor:

   $$f_{\text{cal}} = f K_{\text{mic}} \tag{A.23}$$

3. *Computing the Power Spectral Density using Welch's method*

   With the calibrated microphone signals computed using Equation (A.23), Welch's method (see reference [40]) was applied to compute a power spectral density (PSD) estimate of the calibrated microphone signal. Welch's method consists of dividing an input time history into a number of (possibly overlapping) segments, Fourier transforming the segments' time series, computing the modified periodogram for each segment, and finally averaging over all segments to obtain a final PSD estimate for the entire time history.

   The advantage of dividing the time history into a number of segments and subsequently averaging over all segments is that it reduces the variance of the PSD estimate compared to a single estimate based on the entire time history. On the other hand, the approach also results in shorter data records, hence a reduced resolution of the PSD estimates. Therefore, a suitable trade-off between variance reduction and resolution needs to be found.

Below the most important steps followed in Welch's method are discussed briefly. For a more detailed overview the reader is referred to the original publication by Welch, see reference [40].

Dividing the time history into segments

The input time history $X(j), j = (0, 1, \ldots, N-1)$ is first divided into K (possibly overlapping) segments of length L, with the starting points a distance D apart:

$$\begin{array}{lll} X_1(j) & = X(j) & j = 0, \ldots, L-1 \\ X_2(j) & = X(j+D) & j = 0, \ldots, L-1 \\ X_K(j) & = X(j+(K-1)D) & j = 0, \ldots, L-1 \end{array} \tag{A.24}$$

In the post-processing of the microphone data it was decided not to use any overlap, hence $D = L$. The window length was subsequently selected such that a frequency resolution Δf of about 1 to 2 Hz is obtained.

Fourier transforming the segment time series

The segment time series are all transformed to the frequency domain by taking the discrete Fourier transform:

$$A_k(n) = \frac{1}{L} \sum_{j=0}^{L-1} X_k(j) W(j) \, \mathrm{e}^{-2\mathrm{i}\frac{jkn}{L}} \qquad k = 1, 2, \ldots, K \tag{A.25}$$

with i the imaginary number and W the window function applied to the segment time series. For the current study in all cases a rectangular window was used.

Computing the modified periodograms

The Fourier transformed data obtained from Equation (A.25) is used to compute the modified periodograms I for each segment k according to:

$$I_k(f_n) = \frac{L}{U} |A_k(n)|^2 \qquad k = 1, 2, \ldots, K \tag{A.26}$$

with f_n and U defined by:

$$f_n = \frac{n}{L} \qquad n = 0, 1, \ldots, \frac{L}{2} \tag{A.27}$$

$$U = \frac{1}{L} \sum_{j=0}^{L-1} W^2(j) \tag{A.28}$$

Averaging to obtain the spectral density estimate

With the modified periodograms known from Equation (A.26), the spectral estimate of the time history $X(j)$ is determined by averaging over all segments:

$$\hat{P}(f_n) = \frac{1}{K} \sum_{k=1}^{K} I_k(f_n) \tag{A.29}$$

4. *Computing the Sound Pressure Levels*

The power spectral density estimate obtained from Equation (A.29) is converted into a sound pressure level using:

$$SPL(f_n) = 10 \log_{10} \left(\frac{\hat{P}(f_n) \Delta f \frac{NG}{CG^2}}{p_0^2} \right) \tag{A.30}$$

with Δf the frequency bin width, CG and NG the coherent gain and noise gain of the selected window function, respectively, and p_0 the acoustic reference pressure of 20μPa. The coherent gain and noise gain of the window function are defined as follows:

$$CG = \frac{1}{N} \sum_{j=0}^{N-1} W(j) \tag{A.31}$$

$$NG = \frac{1}{N} \sum_{j=0}^{N-1} W^2(j) \tag{A.32}$$

For the selected rectangular window both CG and NG are equal to 1.

5. *Correcting for microphone frequency response and shear layer refraction effects*

   The final step in the post-processing of the microphone data was to correct for the microphones' uneven frequency response and refraction effects due to the wind tunnel shear layer. For this purpose, first Equation (A.5) was applied to the sound pressure levels computed from the raw microphone data using Equation (A.30). Subsequently, the actual emission angle of the measured sound source was computed by solving Equations (A.6) through (A.8). Finally, Equation (A.9) was applied to the frequency response corrected sound pressure levels. Note that in this process the sound pressure levels were scaled to the selected reference distance of $R = 1.0$ m from the center of the propeller.

Appendix B

RSB Calibration Matrices

The raw RSB data is converted into forces and moments using a number of calibration matrices. The computations requiring the calibration matrices are presented in Appendix A.2.2; this appendix presents the values of the entries of the calibration matrices as provided by the NLR.

B.1 Linear Calibration Matrix

The linear calibration matrix AR is defined by:

$$AR = \begin{bmatrix} +5.014236 \cdot 10^{+2} & -1.601216 \cdot 10^{-1} & -3.011311 \cdot 10^{+0} & +3.941340 \cdot 10^{-1} \\ -1.351726 \cdot 10^{+0} & +4.413832 \cdot 10^{+1} & +2.913067 \cdot 10^{-2} & -2.530606 \cdot 10^{-1} \\ +3.456808 \cdot 10^{-1} & +2.495079 \cdot 10^{-1} & +5.485524 \cdot 10^{+0} & +4.463572 \cdot 10^{-3} \\ +1.034220 \cdot 10^{-2} & -2.541289 \cdot 10^{-3} & -7.089545 \cdot 10^{-3} & +1.664620 \cdot 10^{+0} \end{bmatrix}$$

B.2 Non Linear Calibration Matrices

The non-linear calibration matrices AR_1 through AR_4 are defined by:

$$AR_1 = \begin{bmatrix} -2.230120 \cdot 10^{+0} & +4.635985 \cdot 10^{+0} & +2.638223 \cdot 10^{-1} & -1.052012 \cdot 10^{-2} \\ +1.839862 \cdot 10^{-3} & -2.984765 \cdot 10^{-3} & +1.672107 \cdot 10^{-4} & +7.363899 \cdot 10^{-6} \\ +3.231852 \cdot 10^{-2} & -5.554385 \cdot 10^{-2} & +3.285285 \cdot 10^{-3} & +1.392738 \cdot 10^{-4} \\ -3.512215 \cdot 10^{-3} & +7.266614 \cdot 10^{-3} & -4.126378 \cdot 10^{-4} & -1.627950 \cdot 10^{-5} \end{bmatrix}$$

$$AR_2 = \begin{bmatrix} 0 & 0 & 0 & 0 \\ -2.585224 \cdot 10^{-3} & +4.969751 \cdot 10^{-4} & +1.093347 \cdot 10^{-4} & -7.335045 \cdot 10^{-7} \\ +3.979555 \cdot 10^{-3} & +1.187692 \cdot 10^{-4} & +8.319955 \cdot 10^{-5} & +9.278539 \cdot 10^{-6} \\ +3.741459 \cdot 10^{-5} & -2.577793 \cdot 10^{-6} & -1.517783 \cdot 10^{-6} & -3.754493 \cdot 10^{-8} \end{bmatrix}$$

$$AR_3 = \begin{bmatrix} 0 & 0 & 0 & 0 \\ 0 & 0 & 0 & 0 \\ +4.379852 \cdot 10^{-2} & +1.270376 \cdot 10^{-3} & +9.146160 \cdot 10^{-4} & +1.020714 \cdot 10^{-4} \\ +9.908191 \cdot 10^{-5} & -2.709362 \cdot 10^{-5} & +2.636578 \cdot 10^{-6} & +9.521730 \cdot 10^{-8} \end{bmatrix}$$

$$AR_4 = \begin{bmatrix} 0 & 0 & 0 & 0 \\ 0 & 0 & 0 & 0 \\ 0 & 0 & 0 & 0 \\ -7.758898 \cdot 10^{-4} & -1.744406 \cdot 10^{-3} & +1.591910 \cdot 10^{-4} & +2.005039 \cdot 10^{-5} \end{bmatrix}$$

Appendix C

Additional Experimental Results

This appendix provides additional experimental results which serve as background material to the results presented in Part I of this report. The results obtained for the pylon wake profiles are presented in Section C.1, followed by Section C.2 which discusses the additional data for the powered propeller performance. For the propeller noise emissions all results were already presented in the main text of this report, no additional results are presented here.

C.1 Pylon Wake Profiles

This section presents the non-dimensional velocity and pressure profiles measured behind the default, extended, and sharp pylon models in the unblown and blown configurations. The data serves as background to the discussion given in Chapter 3.

C.1.1 Default Pylon Model: Unblown

The non-dimensional velocity profiles in the wake of the default pylon model for wind tunnel velocities of 10, 19, and 26 m/s and axial spacings of 50 and 114 mm are presented in Figure C.1. The corresponding total and static pressure profiles are depicted in Figure C.2.

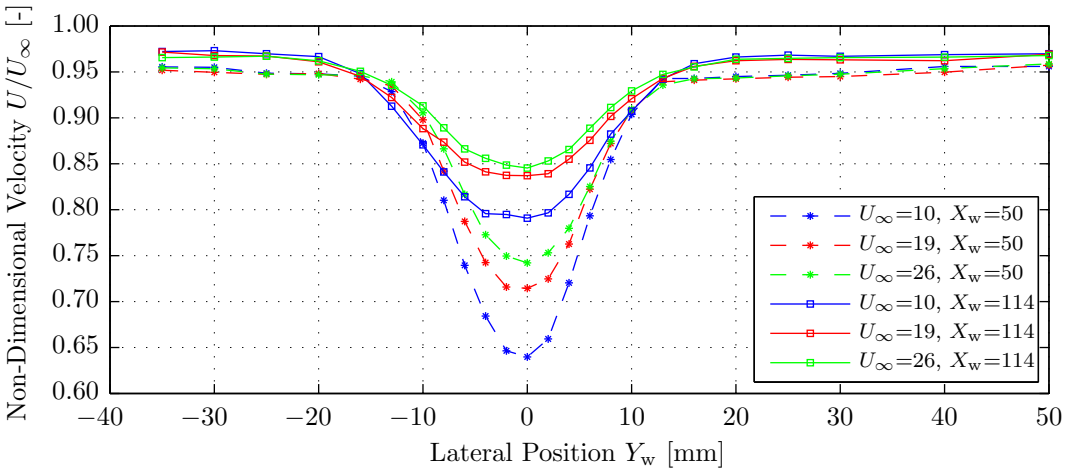

Figure C.1: Non-dimensional velocity profiles in the wake of the default pylon model. $U_\infty = [10, 19, 26]$ m/s, $X_w = [50, 114]$ mm.

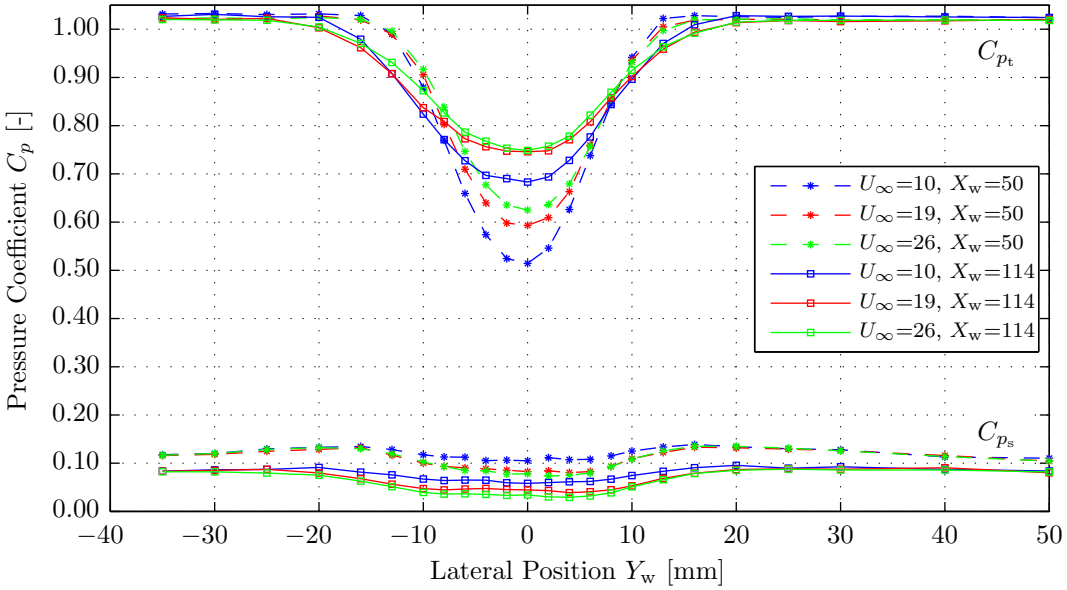

Figure C.2: Total and static pressure profiles in the wake of the default pylon model. $U_\infty = [10, 19, 26]$ m/s, $X_w = [50, 114]$ mm.

Apart from the conclusions drawn in Section 3.2, from Figure C.1 it is observed that no similarity is present in the results, i.e. the non-dimensional wake profiles obtained at the three different freestream velocities are not the same. This indicates that for the default pylon model the wake characteristics are a strong function of the Reynolds number. The wake profile becomes increasingly deep with decreasing freestream velocity, while the wake width remains approximately constant.

C.1.2 Extended Pylon Model: Unblown

Figure C.3 depicts the non-dimensional velocity profiles in the wake of the extended pylon for velocities of 19 and 26 m/s and axial spacings of 50 and 114 mm. The corresponding total and static pressure profiles are presented in Figure C.4. Note that at the freestream velocity of 19 m/s the measurements were only performed at an axial spacing of 114 mm.

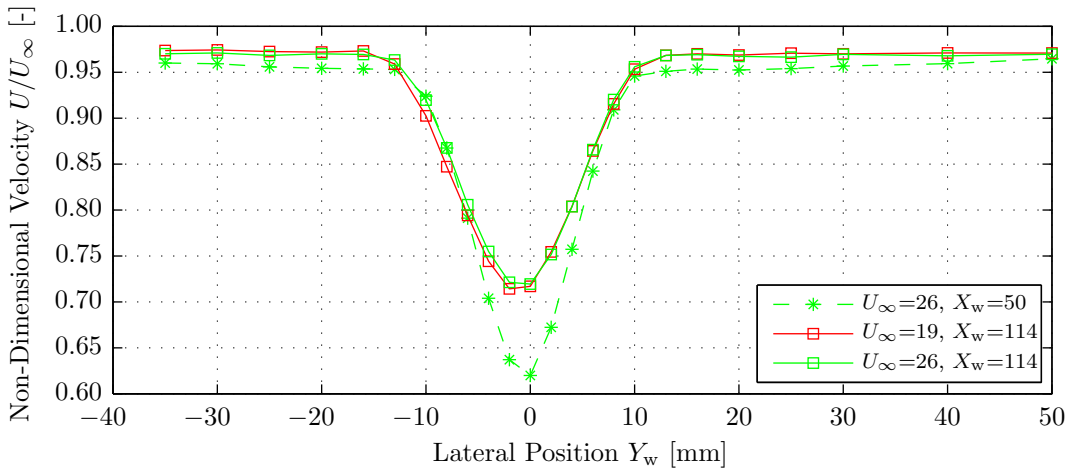

Figure C.3: Non-dimensional velocity profiles in the wake of the extended pylon model. $U_\infty = [19, 26]$ m/s, $X_w = [50, 114]$ mm.

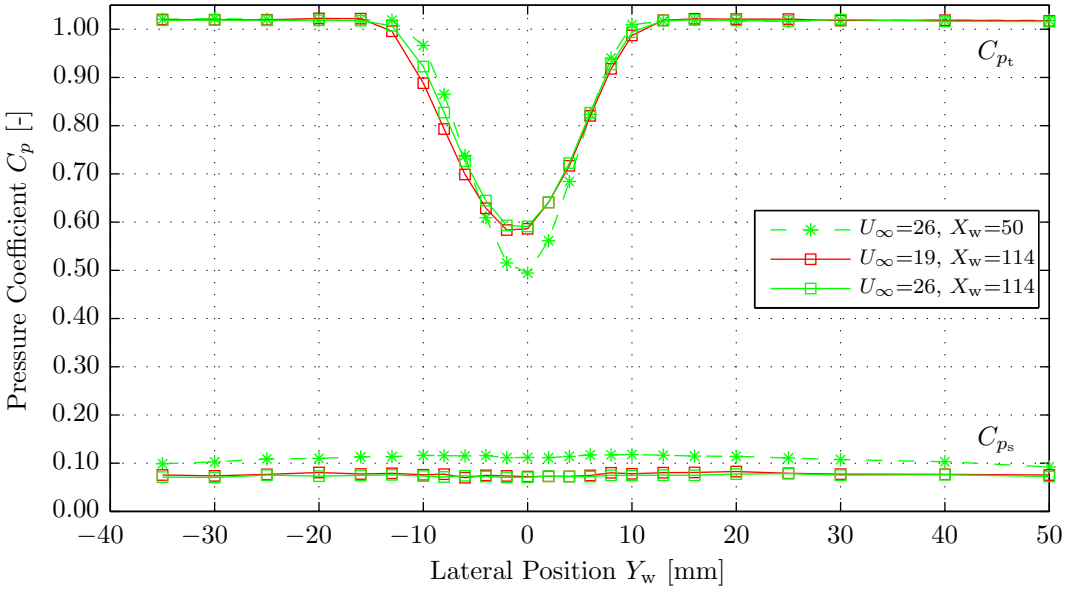

Figure C.4: Total and static pressure profiles in the wake of the extended pylon model. $U_\infty = [19, 26]$ m/s, $X_w = [50, 114]$ mm.

Figure C.3 shows that at 114 mm behind the pylon the maximum velocity deficit is about 30% of the freestream value. The results obtained at 19 and 26 m/s show only small differences, with the wake width slightly larger at the lower velocity. The static pressure profile measured at $X_w = 50$ mm shown in Figure C.4 displays a decreasing trend when moving away from the pylon's trailing edge (in lateral direction), with a small downward bump in the wake region. At an axial distance of $X_w = 114$ mm the static pressure profile is almost flat. Note that the drop in static pressure in the wake region of the extended pylon model is much smaller than that shown in Figure C.2 for the default pylon. It is expected that this is the result of the reduction in trailing edge thickness of the extended pylon compared to the default pylon.

C.1.3 Sharp Pylon Model: Unblown

The non-dimensional wake velocity profiles behind the sharp pylon model for freestream velocities of 19 and 26 m/s and axial spacings of 50 and 114 mm are shown in Figure C.5. Figure C.6 presents the corresponding total and static pressure profiles.

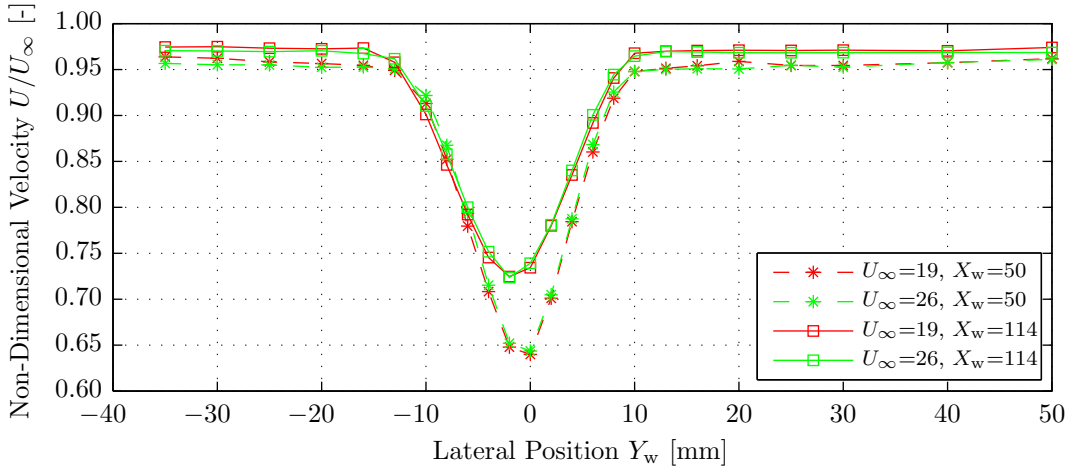

Figure C.5: Non-dimensional velocity profiles in the wake of the sharp pylon model. $U_\infty = [19, 26]$ m/s, $X_w = [50, 114]$ mm.

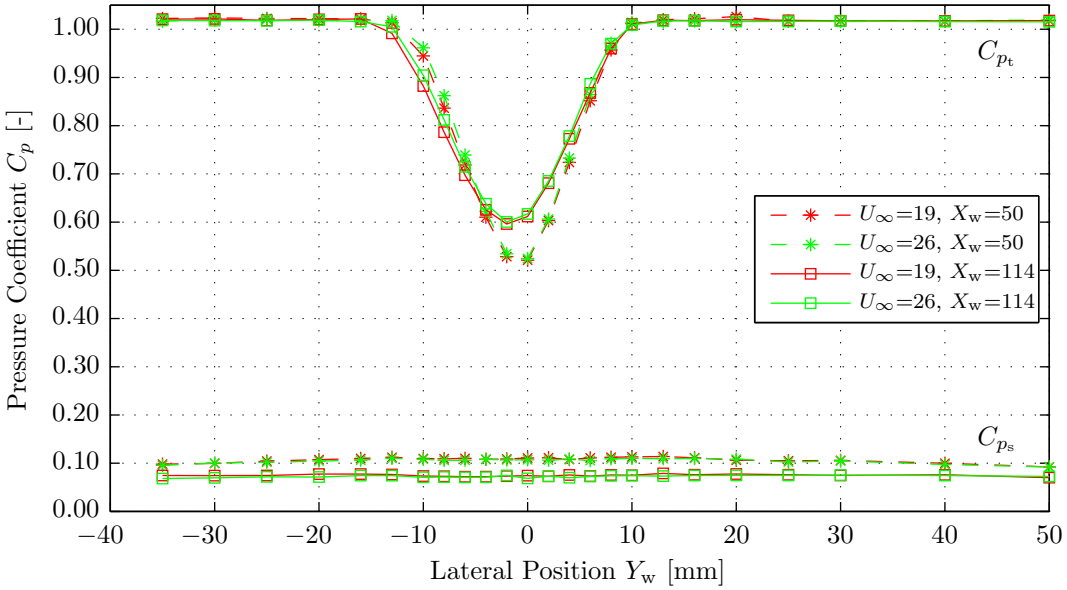

Figure C.6: Total and static pressure profiles in the wake of the sharp pylon model. $U_\infty = [19, 26]$ m/s, $X_w = [50, 114]$ mm.

The data presented in Figure C.5 shows that the results obtained at the two different freestream velocities are virtually equal, hence displaying a strong degree of similarity. The pressure coefficient data plotted in Figure C.6 also confirms the previous findings. The total pressure measured outside of the wake region has the same value as observed before in Figures C.2 and C.4. The static pressure coefficient is approximately flat over the entire lateral domain considered in the wake measurements, and again the influence of the presence of the pylon is noticed in the static pressure measurements performed outside of the wake region.

C.1.4 Default Pylon Model: Blown

The non-dimensional velocity profiles in the wake of the default pylon for a freestream velocity of 10 m/s and blowing rates of 0 and 600 L/min are presented in Figure C.7. The corresponding total and static pressure profiles are depicted in Figure C.8. Again, axial distances behind the pylon's trailing edge of 50 and 114 mm are considered.

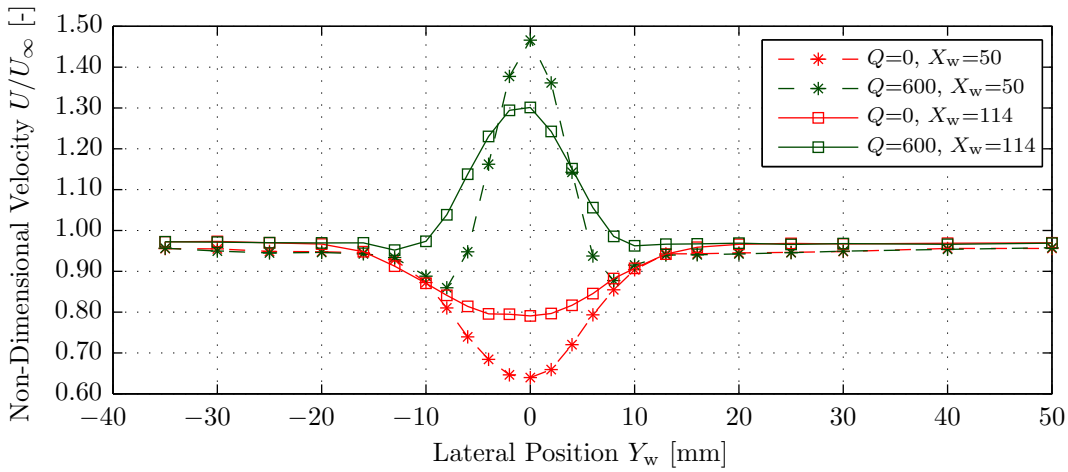

Figure C.7: Non-dimensional velocity profiles in the wake of the default pylon model. $U_\infty = 10$ m/s, $X_w = [50, 114]$ mm, $Q = [0, 600]$ L/min.

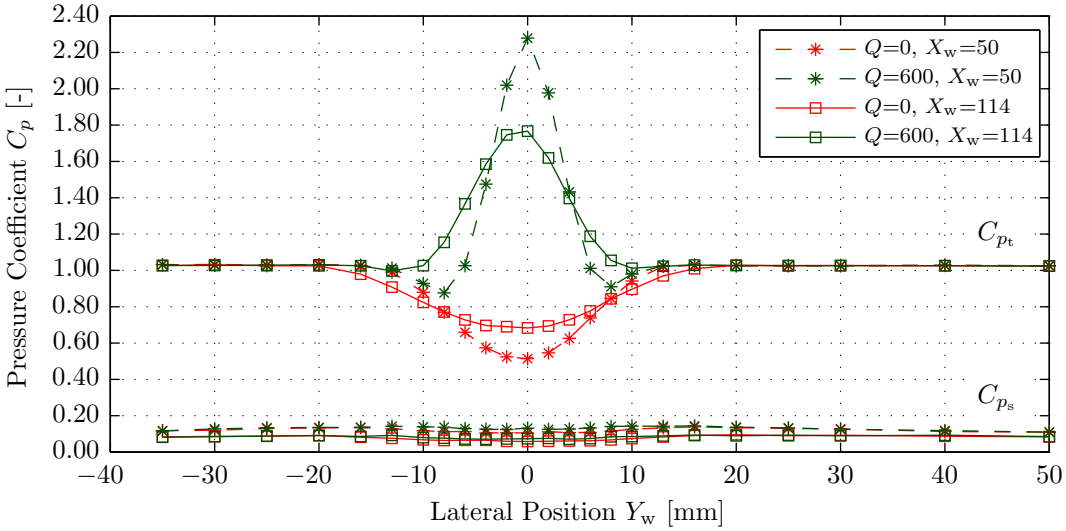

Figure C.8: Total and static pressure profiles in the wake of the default pylon model. $U_\infty = 10$ m/s, $X_w = [50, 114]$ mm, $Q = [0, 600]$ L/min.

Figure C.7 shows that at $U_\infty = 10$ m/s application of the UBR clearly increases the velocity in the pylon wake region. For $Q = 600$ L/min the velocity in the center of the wake becomes higher than that of the freestream, indicating that the blowing rate was too high for optimal wake elimination. At an axial spacing of 114 mm a reduction in the wake width of about 40% is observed, which is the result of additional mixing of the external and blown flow. However, again the selected blowing rate results in a strong 'overshoot' in the velocity profile.

The trends in the pressure profiles depicted in Figure C.8 are similar to those measured at $U_\infty = 26$ m/s as discussed in Subsection 3.4.1, and therefore are not further elaborated upon here.

The non-dimensional velocity profiles measured at a freestream velocity of 19 m/s are shown in Figure C.9, followed by the total and static pressure profiles depicted in Figure C.10. Again blowing rates of 0 and 600 L/min are considered.

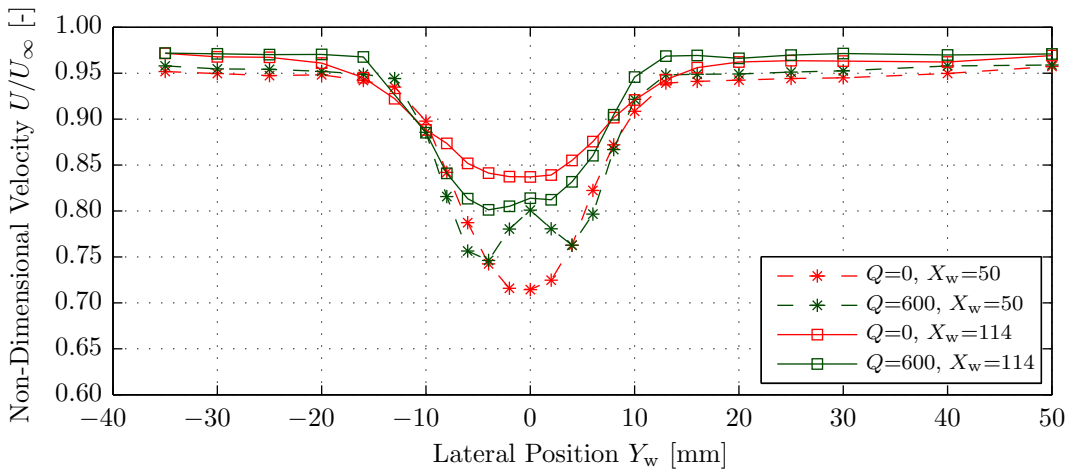

Figure C.9: Non-dimensional velocity profiles in the wake of the default pylon model. $U_\infty = 19$ m/s, $X_w = [50, 114]$ mm, $Q = [0, 600]$ L/min.

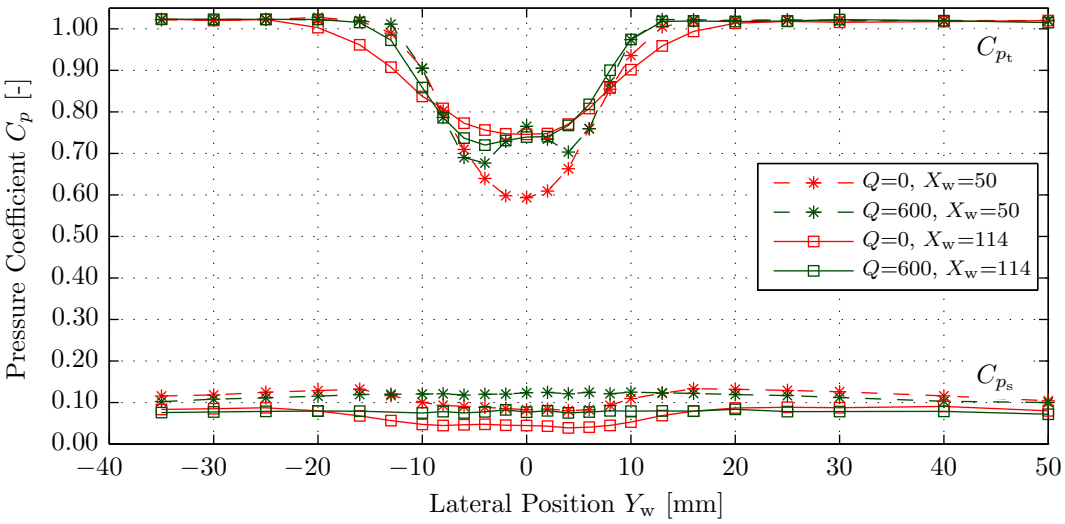

Figure C.10: Total and static pressure profiles in the wake of the default pylon model. $U_\infty = 19$ m/s, $X_w = [50, 114]$ mm, $Q = [0, 600]$ L/min.

Figure C.9 shows that at $U_\infty = 19$ m/s application of the UBR with a blowing rate of 600 L/min no longer results in a clear increase in the velocities in the pylon wake. At an axial distance of 50 mm only a small part of the wake velocity deficit is filled by blowing, while the velocity deficit around the edges of the wake region is even increased. For an axial distance of 114 mm from the trailing edge on the other hand the wake depth increases by blowing by about 5%, whereas the wake width is reduced by 40%, hence indicating a reduction in the wake decay rate for the blown case. The pressure coefficients displayed in Figure C.10 are again similar to the results obtained at $U_\infty = 26$ m/s as discussed in Subsection 3.4.1.

C.1.5 Extended Pylon Model: Blown

The non-dimensional velocity profiles measured in the extended pylon wake were discussed in Subsection 3.4.2. The corresponding pressure profiles for freestream velocities of 19 and 26 m/s are presented in Figures C.11 and C.12, respectively.

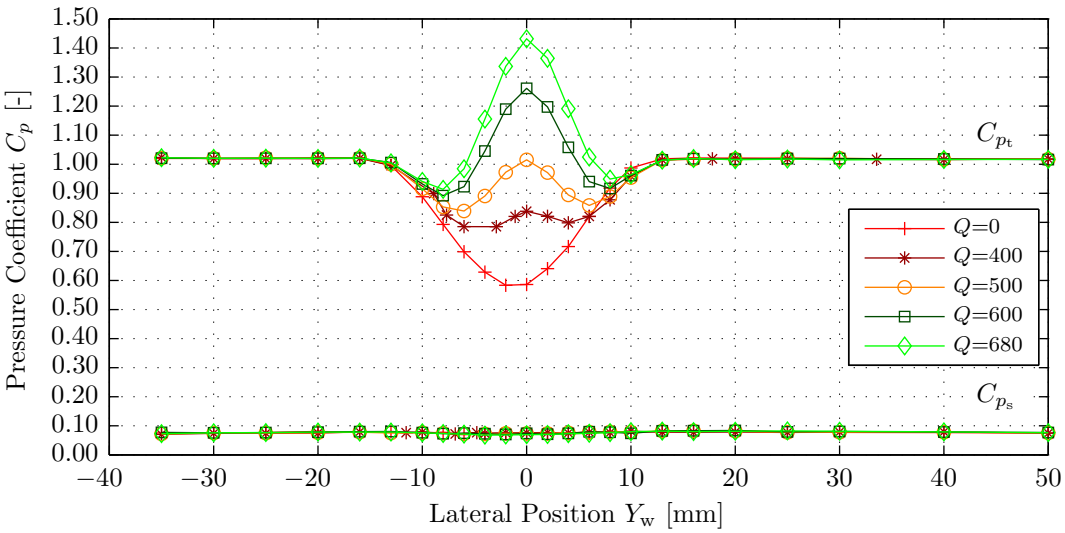

Figure C.11: Total and static pressure profiles in the wake of the extended pylon model. $U_\infty = 19$ m/s, $X_w = 114$ mm, $Q = [0, 400, 500, 600, 680]$ L/min.

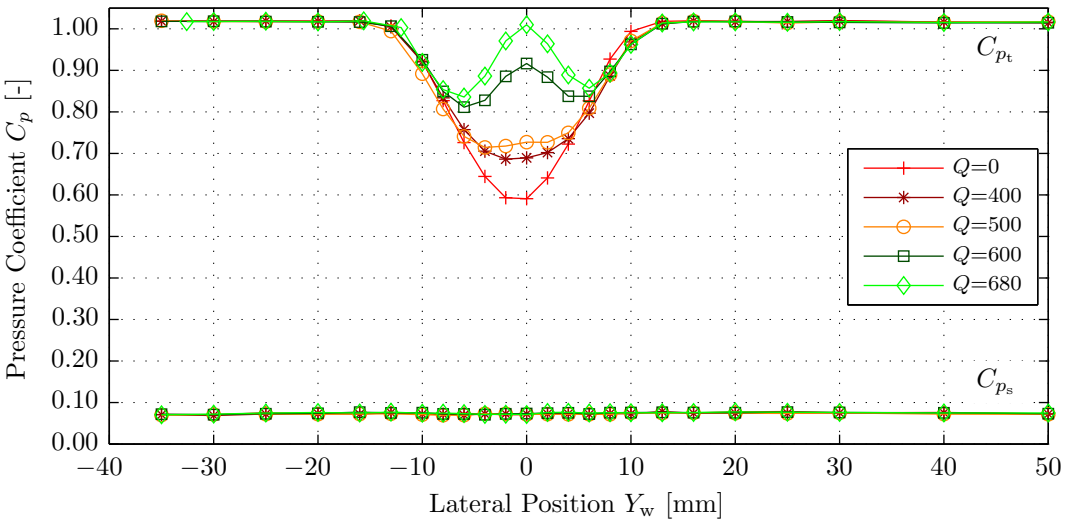

Figure C.12: Total and static pressure profiles in the wake of the extended pylon model. $U_\infty = 26$ m/s, $X_w = 114$ mm, $Q = [0, 400, 500, 600, 680]$ L/min.

Figures C.11 and C.12 again show that the total pressure coefficient profile closely follows the shape of the wake velocity profile. Furthermore, for the extended pylon model the static pressure coefficient in the wake region is not influenced by the application of blowing, and is constant over the considered measurement domain.

C.2 Powered Propeller Performance

This section presents additional results related to the powered propeller performance measurements discussed in Chapter 5. First, the signal quality and reproducibility of the measurements is considered (Subsection C.2.1). Thereafter, results related to the measurements in the isolated, installed, and blown configurations are presented (Subsections C.2.2, C.2.3, and C.2.4).

C.2.1 Signal Quality and Reproducibility of the Results

Section 5.2 assessed the signal quality and reproducibility of the measurements performed using the RSB. Below, the effects of filtering on the time-averaged thrust coefficient data are discussed first (Paragraph C.2.1.1), after which an additional plot concerning the repeatability of the measurements is presented (Paragraph C.2.1.2).

C.2.1.1 Effects of Filtering

To assess whether the time-*averaged* RSB data might be useful for comparisons between data obtained in the isolated, installed, and blown configurations, it was verified whether the noise present in the data sets is random and hence averages out to zero. For this purpose the thrust signal time histories recorded during an isolated measurement performed at 19 m/s were filtered using 28 different cut-off frequencies ranging from 10 Hz up to and including 25 kHz (corresponding to the unfiltered case). Subsequently, for each advance ratio the resulting average thrust coefficients were computed as a function of the cut-off frequency. The results are plotted in Figure C.13, which displays the computed time-averaged thrust coefficients as a function of cut-off frequency for a number of advance ratios.

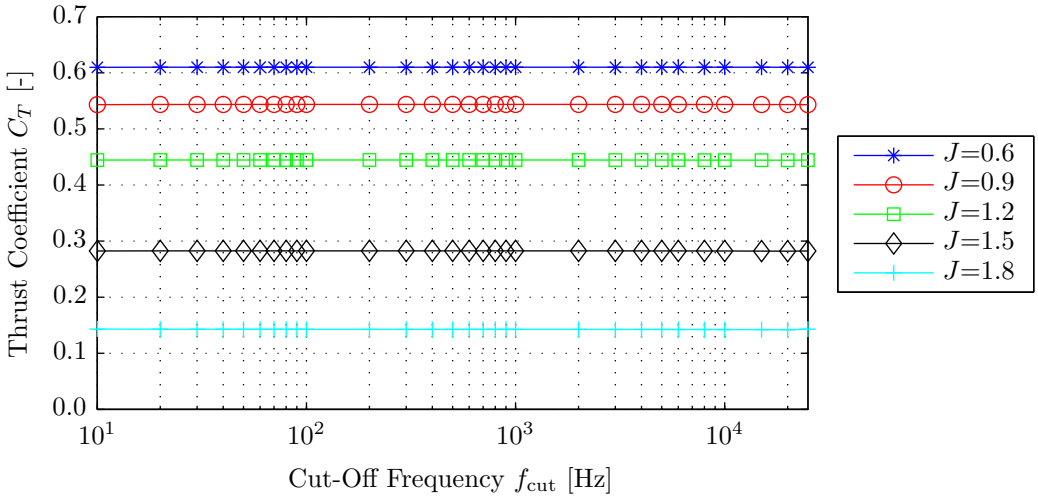

Figure C.13: Effect of the cut-off frequency on the time-averaged value of the thrust coefficient. Isolated configuration, $U_\infty = 19$ m/s, $J = [0.6, 0.9, 1.2, 1.5, 1.8]$.

If the noise present in the RSB signals would average out to zero, the time-averaged thrust should not be a function of the cut-off frequency. Based on the data shown in Figure C.13 it is concluded that this is indeed the case: the strong noise present in the RSB signals averages out to zero and thus does not affect the time-averaged data. The maximum difference observed between the filtered and unfiltered data is smaller than 1%, occurring at $J = 1.8$. At lower advance ratios the difference becomes even smaller, decreasing to about 0.05% at $J = 0.5$.

C.2.1.2 Repeatability of the RSB Measurements

Section 5.2 described the repeatability of the time-averaged RSB measurements. For overview reasons only the propeller performance diagram obtained at a freestream velocity of 19 m/s was presented. Figure C.14 displays the data measured at a freestream velocity of 26 m/s.

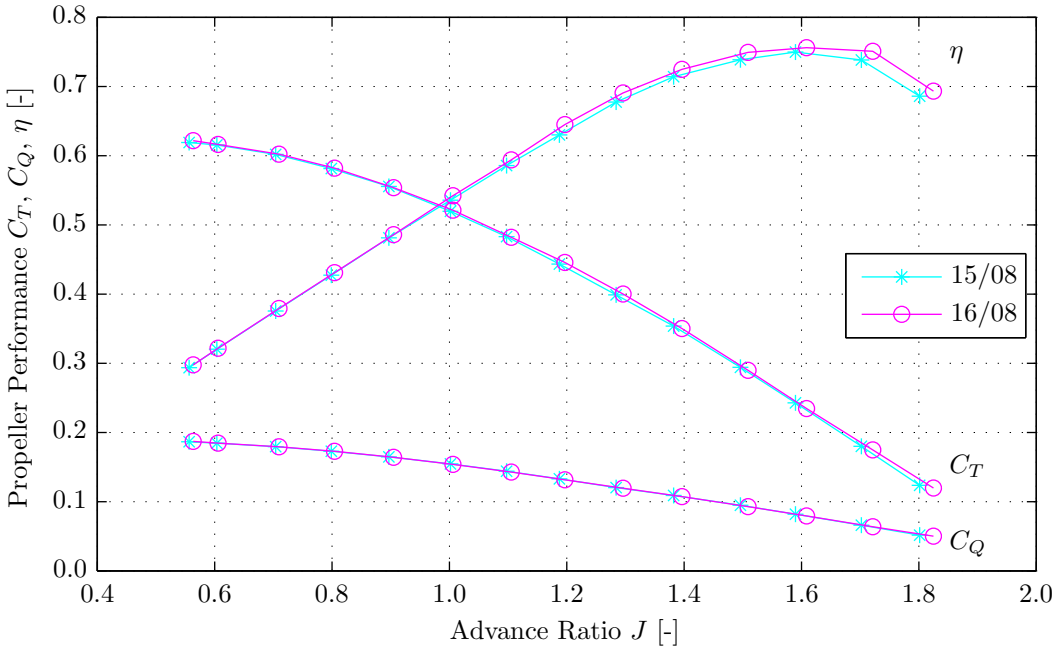

Figure C.14: Reproducibility of time-averaged propeller performance measurements. Isolated configuration, $U_\infty = 26$ m/s, $0.55 \leq J \leq 1.8$, $f_{\text{cut}} = 2,500$ Hz.

C.2.2 Isolated Configuration

The isolated propeller performance was presented in Section 5.3. Below, an additional discussion of the propeller hub back pressure is provided (Paragraph C.2.2.1). Thereafter, the results of a frequency spectrum analysis of the torque signal are presented (Paragraph C.2.2.2).

C.2.2.1 Propeller Hub Back Pressure Correction

The discussion of the isolated propeller performance presented in Section 5.3 briefly discussed the effects of the propeller hub back pressure correction on the resulting thrust measurements. In this part of the appendix an example of typical back pressure data is provided. Figure C.15 displays the average back pressure coefficient $C_p^{\mathrm{bp}} = \frac{p_{\mathrm{bp}} - p_\infty}{q_\infty}$ measured at the pressure plate as a function of the advance ratio.

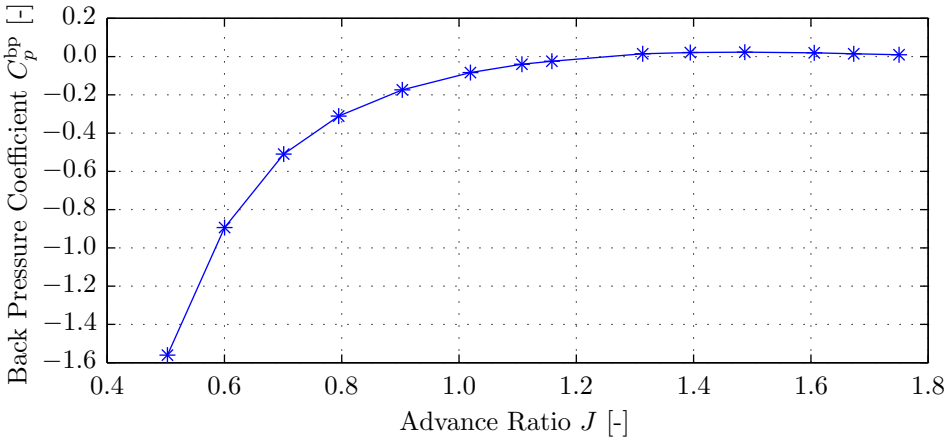

Figure C.15: Average values of the back pressure coefficient $C_p^{\mathrm{bp}} = \frac{p_{\mathrm{bp}} - p_\infty}{q_\infty}$ versus the advance ratio. Isolated configuration, $U_\infty = 19$ m/s, $0.5 \leq J \leq 1.8$.

From Figure C.15 it is observed that the back pressure coefficient decreases with decreasing advance ratio. For advance ratios above around 1.3 the pressure measured at the back of the propeller hub remains approximately equal to the freestream value ($C_p^{\mathrm{bp}} \approx 0$). Upon further decreasing the advance ratio, the back pressure coefficient decreases below zero, indicating that the pressures measured at the back of the propeller hub are lower than the freestream value. Based on actuator disk theory it would be expected that the static pressure measured directly behind the propeller disk is larger than the freestream value. However, apparently the reduction in the local pressure due to the increase in velocity experienced in the propeller slip stream region and the convex shape of the spinner ahead of the pressure plate is large enough to offset the increase in pressure generated at the propeller disk. With decreasing advance ratio the velocities in the slip stream become increasingly large, in the end resulting in a reduction in pressure measured at the pressure plate installed directly behind the propeller hub. CFD computations performed on the propeller geometry used during the wind tunnel experiments confirmed this hypothesis.

Following Equation (A.4), the measured back pressure data was converted into an equivalent drag force experienced by the RSB. The back pressure drag values corresponding to the measurement points displayed in Figure C.15 are depicted in Figure C.16, in which the results are made dimensionless using the thrust values at each measurement point. Note that positive values of the back pressure drag term indicate that the axial force measured by the RSB is lower than the actual thrust generated by the propeller.

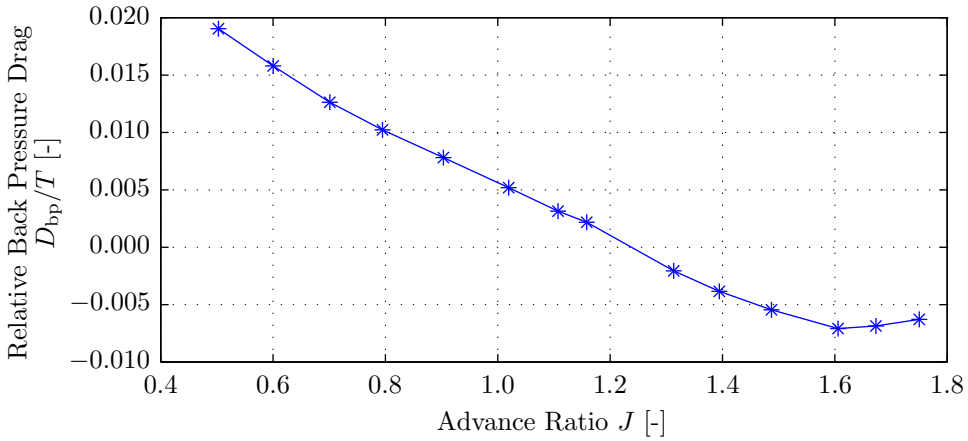

Figure C.16: Average values of the back pressure drag versus the advance ratio. Isolated configuration, $U_\infty = 19$ m/s, $0.5 \leq J \leq 1.8$.

Inspection of Figure C.16 shows that the back pressure drag remains small for all advance ratios. At $J = 0.5$ a force of 2 N is generated, corresponding to about 2% of the propeller thrust. For higher advance ratios the effect of the hub back pressure rapidly decreases towards zero.

C.2.2.2 Torque Signal Frequency Spectrum Analysis

Section 5.3.2 discussed a frequency spectrum analysis of the isolated thrust and torque signals. For overview reasons only the evolution of the peaks in the thrust power spectra as a function of the advance ratio was discussed there. Figure C.17 presents the corresponding results for the torque signal.

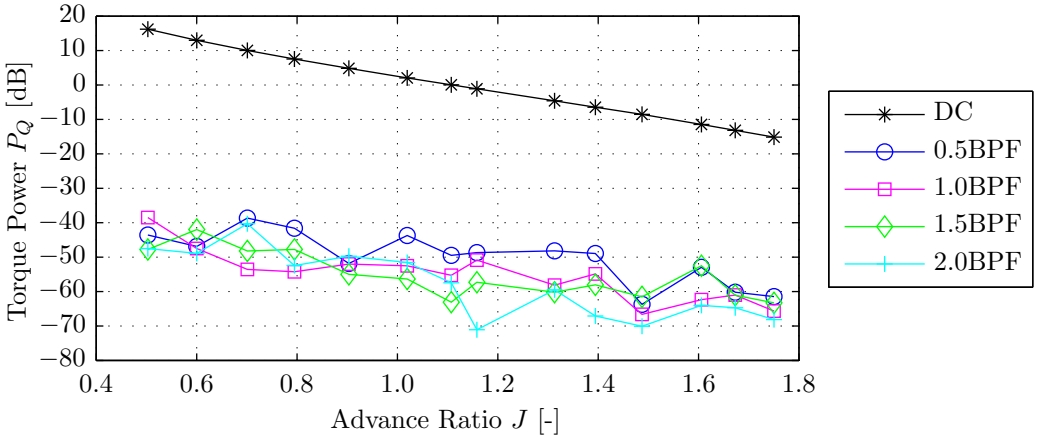

Figure C.17: Torque signal power levels for multiples of half the BPF. Isolated configuration, $U_\infty = 19$ m/s, $0.5 \leq J \leq 1.8$, $f_{cut} = 2,500$ Hz.

The torque power levels displayed in Figure C.17 confirm the conclusion that the DC component completely dominates the power spectrum of the torque signal. No distinct peaks are present at integer multiples of half the BPF.

C.2.3 Installed Configuration

The propeller performance in the installed configuration was discussed in Section 5.4. The installed propeller performance diagrams measured at freestream velocities of 15 and 26 m/s

were not presented in the main text, but instead are presented here in Figures C.18 and C.19. Thereafter, the results obtained from the frequency spectrum analysis of the torque coefficient are depicted in Figure C.20.

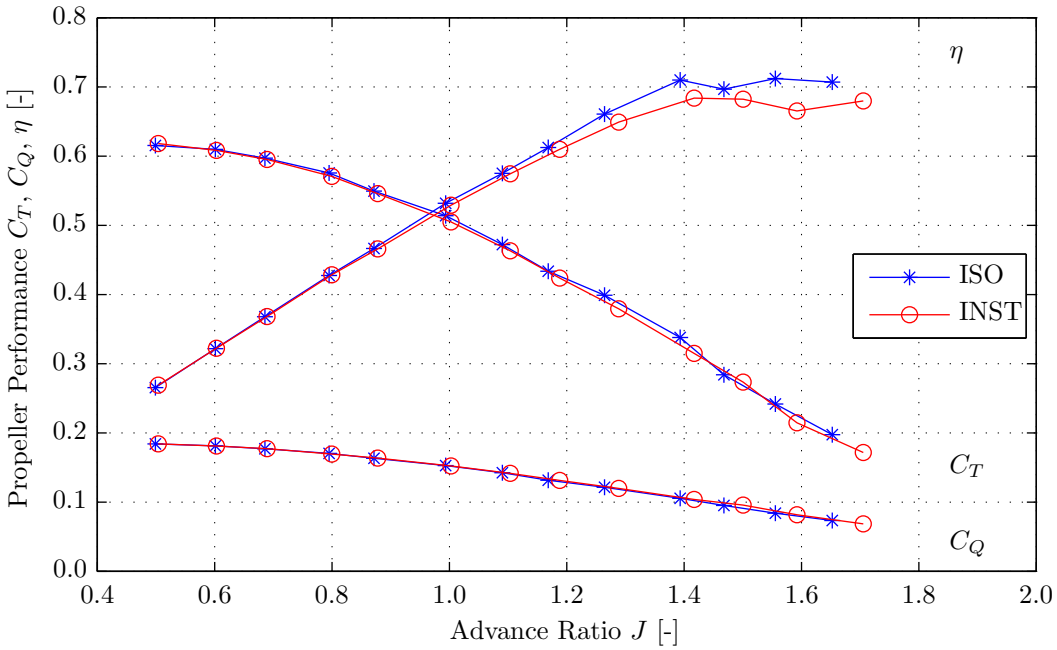

Figure C.18: Propeller performance diagram: effects of installation.
Isolated and installed configurations, $U_\infty = 15$ m/s, $0.5 \leq J \leq 1.7$, $f_{\text{cut}} = 2,500$ Hz.

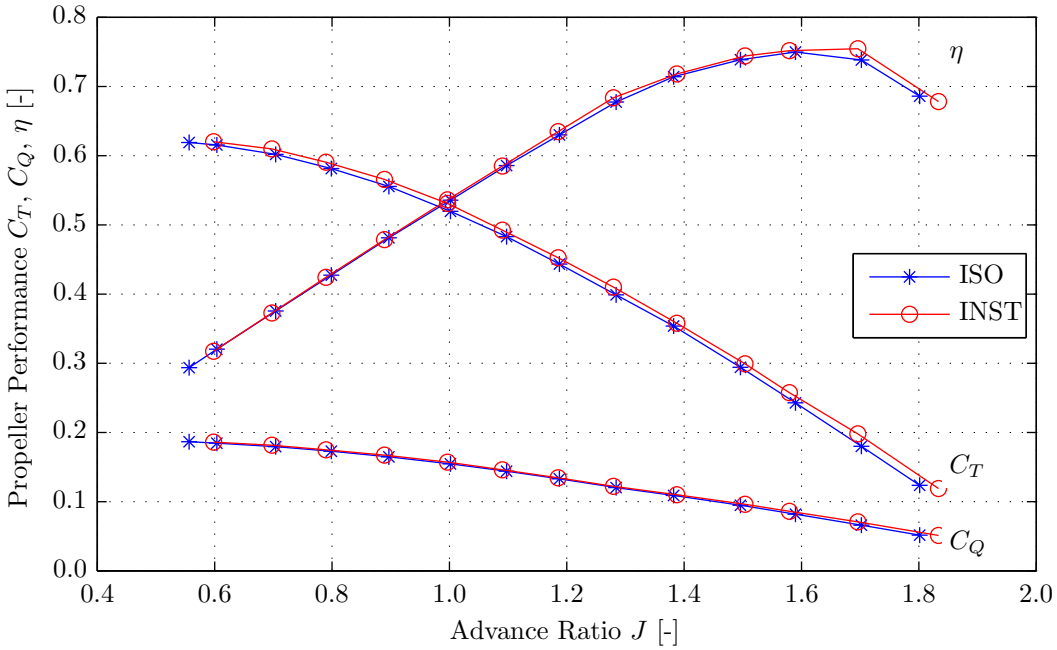

Figure C.19: Propeller performance diagram: effects of installation.
Isolated and installed configurations, $U_\infty = 26$ m/s, $0.55 \leq J \leq 1.8$, $f_{\text{cut}} = 2,500$ Hz.

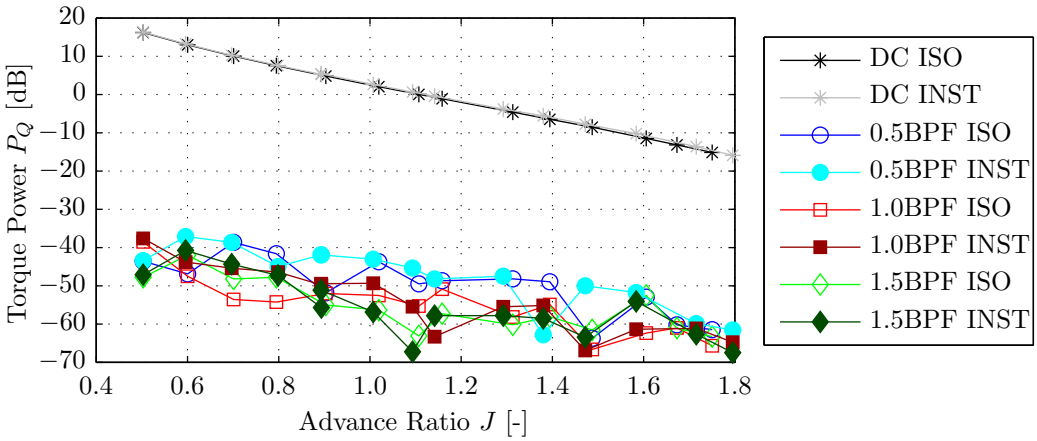

Figure C.20: Comparison of the installed and isolated torque power levels for half BPF multiples. Isolated and installed configurations, $U_\infty = 19$ m/s, $0.5 \leq J \leq 1.8$, $f_{\text{cut}} = 2,500$ Hz.

Figure C.20 shows that the installed measurements did not return a clearly different power spectrum than that obtained in isolated conditions. The values of the torque power peaks are about 50 to 60 dB smaller than the DC component. The increase in the torque coefficient in the installed configuration is explained by the small increase in the DC component in installed conditions. Therefore, the observed increase in the time-averaged torque coefficient corresponds to a time-independent effect, hence again supporting the conclusion that the measured change in the torque coefficient can be attributed to measurement variability.

C.2.4 Blown Configuration

Section 5.5 discussed the blown propeller performance measurements. The main text did not present the blown propeller performance diagrams measured at velocities of 15 and 26 m/s. Instead, these are depicted below in Figures C.21 and C.22.

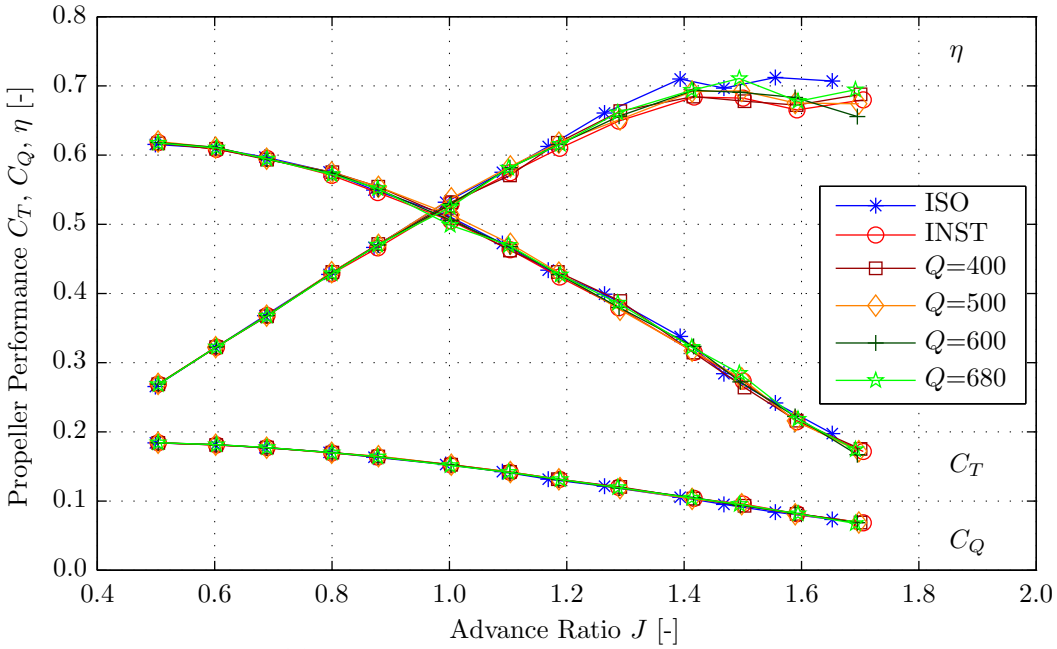

Figure C.21: Propeller performance diagram: effects of blowing. Isolated, installed, and blown configurations, $U_\infty = 15$ m/s, $0.5 \leq J \leq 1.8$, $f_{\text{cut}} = 2,500$ Hz.

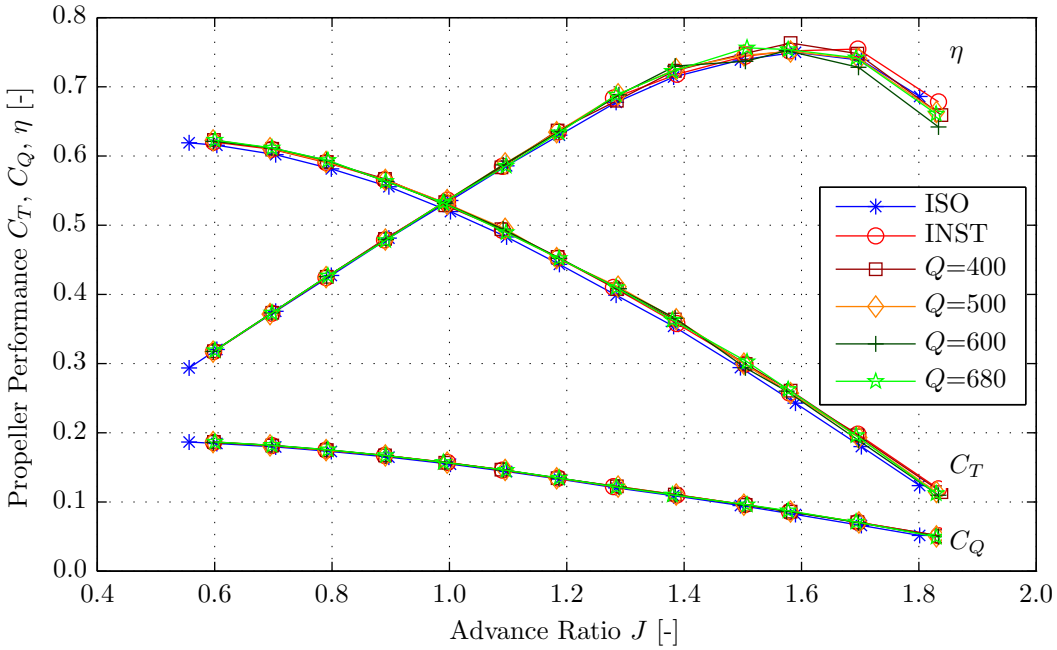

Figure C.22: Propeller performance diagram: effects of blowing.
Isolated, installed, and blown configurations, $U_\infty = 26$ m/s, $0.5 \leq J \leq 1.8$, $f_{\text{cut}} = 2,500$ Hz.

Figures C.21 and C.22 display the same trends as observed in the results obtained for a freestream velocity of 19 m/s. The propeller performance results measured in the installed and blown configurations are approximately equal, with very small differences between the results obtained at the different blowing rates.

The results obtained from a frequency spectrum analysis of the torque coefficient are depicted in Figure C.23.

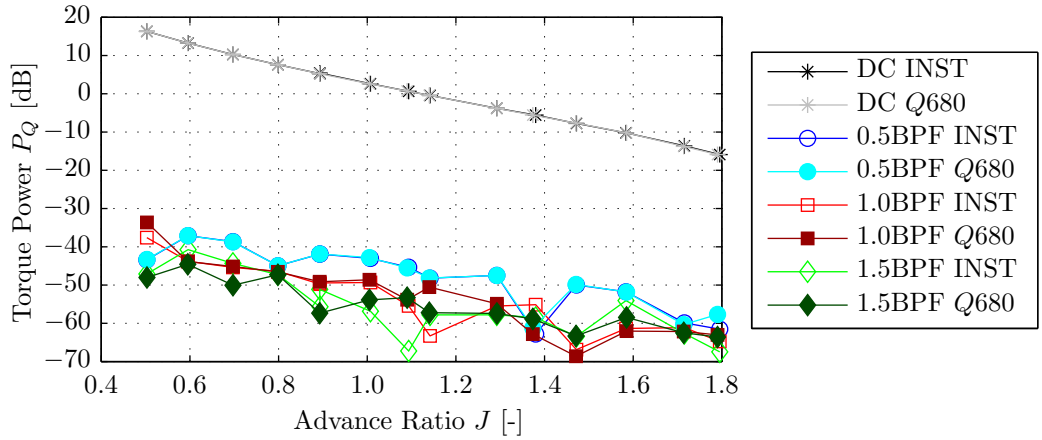

Figure C.23: Comparison of the blown and installed torque power levels for half BPF multiples.
Installed and blown configurations, $U_\infty = 19$ m/s, $0.5 \leq J \leq 1.8$, $f_{\text{cut}} = 2,500$ Hz.

Figure C.23 shows that the torque frequency spectrum cannot be used to identify differences between the installed and blown propeller response. The results measured for the installed and blown configurations are practically equal over the entire advance ratio range.

Appendix D

Description of the XROTOR Computations

As discussed in Subsection 7.2.1, the isolated propeller performance computations are performed using XROTOR (see reference [51]). This appendix describes the main computational steps performed in the XROTOR analysis, following the flowchart depicted in Figure 7.2. For a detailed user guide of the XROTOR program the reader is referred to reference [69].

D.1 Computation of the Induced Velocities

XROTOR offers three methods for the computation of the flow field induced by the propeller. By default, the axial and tangential induced velocities u_a and u_t are computed by means of a numerical analysis of the exact potential flow field about the helical vortex field. This method is an extension of Goldstein's solution for lightly-loaded two and four bladed propellers (see reference [70]), and is valid for all propeller blade numbers and advance ratios. Alternatively, both a graded-momentum formulation and a discrete vortex wake formulation are also available. The former implements the classical propeller lifting line theory developed by Betz with the tip loss correction parameter derived by Prandtl, as discussed in reference [71]. Application of this method reduces the computational cost of the analysis (which however is already low for the default potential method), while reducing the generality of the solution by restricting the validity to low advance ratios (smaller than about $J = 0.5\pi$) and many blades. The discrete vortex formulation finally is especially useful for propellers with raked or swept blades, resulting in non-radial lifting lines. Application of this method however significantly increases the computational cost of the performance analysis [69].

D.2 Computation of the Section Angles of Attack

Having determined the latest values of the induced velocities, these are first used to compute the local flow angles φ_i at all blade sections i:

$$\varphi_i = \arctan\left(\frac{W_{\mathrm{a}_i}}{W_{\mathrm{t}_i}}\right) = \arctan\left(\frac{U_\infty + u_{\mathrm{a}_i}}{\Omega\eta_i R - u_{\mathrm{t}_i}}\right) \tag{D.1}$$

with R the propeller radius, u_a the induced axial velocity, u_t the induced tangential velocity, U_∞ the freestream velocity, W_a the effective axial velocity, W_t the effective tangential velocity, η the non-dimensional radial coordinate of the blade section, and Ω the rotational velocity of the propeller. The freestream velocity U_∞ and the propeller rotational velocity Ω are known from the operating conditions at which the analysis is performed.

After the computation of the local flow angles φ_i using Equation (D.1), the blade section angles of attack α_i can be obtained directly using the local blade pitch angles β_i which need to be given as input to the method:

$$\alpha_i = \beta_i - \varphi_i \tag{D.2}$$

The relation between the local angle of attack α, blade pitch angle β, and flow angle φ is illustrated in Figure D.1.

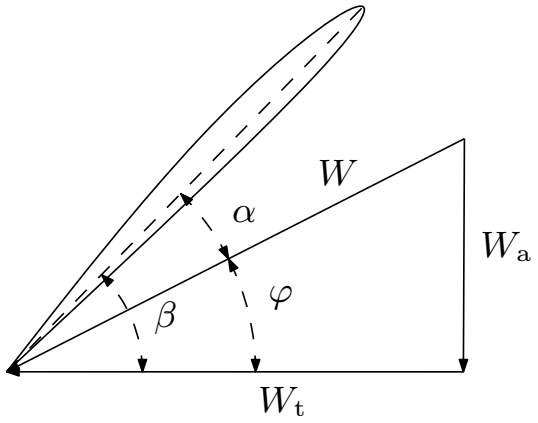

Figure D.1: Definition of the blade section angles and velocity triangle components.

D.3 Computation of the Section Lift and Drag Coefficients

The local section lift and drag coefficients c_{l_i} and c_{d_i} are computed as a function of the local angle of attack, Mach number, and Reynolds number. Note that all computations discussed in this paragraph are performed per blade section i. However, for convenience the subscript i is omitted in the remainder of this section.

D.3.1 Lift Coefficient

The blade section lift coefficient is computed in XROTOR as a function of the local angle of attack and the effective Mach number using the following equation:

$$c_l = c_{l_{\text{lin}}} - \left(1 - \frac{c_{l_{\alpha_{\text{stall}}}}}{c_{l_\alpha}}\right) \Delta c_{l_{\text{non-lin}}} \tag{D.3}$$

with $c_{l_{\text{lin}}}$ the equivalent linear lift coefficient, c_{l_α} the lift gradient in the linear part of the c_l-α curve, $c_{l_{\alpha_{\text{stall}}}}$ the lift gradient in the stalled part of the c_l-α curve, and $\Delta c_{l_{\text{non-lin}}}$ the correction applied to take into account non-linear effects due to stall.

The equivalent linear lift coefficient $c_{l_{\text{lin}}}$ is defined as:

$$c_{l_{\text{lin}}} = (\alpha - \alpha_0) \frac{c_{l_\alpha}}{\sqrt{1 - M^2}} \tag{D.4}$$

with α the angle of attack, α_0 the zero-lift angle, and M the Mach number corresponding to the effective velocity W.

The correction applied to the equivalent lift coefficient to account for non-linear effects due to stall $\Delta c_{l_{\text{non-lin}}}$ is given by:

$$\Delta c_{l_{\text{non-lin}}} = \Delta c_{l_{\text{stall}}} \ln\left(\frac{1+\exp\left\{(c_{l_{\text{lin}}} - c_{l_{\text{max}}})/\Delta c_{l_{\text{stall}}}\right\}}{1+\exp\left\{(c_{l_{\text{min}}} - c_{l_{\text{lin}}})/\Delta c_{l_{\text{stall}}}\right\}}\right) \tag{D.5}$$

with $c_{l_{\text{max}}}$ the maximum lift coefficient, $c_{l_{\text{min}}}$ the minimum lift coefficient, and $\Delta c_{l_{\text{stall}}}$ the lift increment to stall. Additionally, a simple empirical model is implemented in which the maximum and minimum lift coefficients are limited for Mach effects.

D.3.2 Drag Coefficient

The blade section drag coefficient is computed in XROTOR for all sections i as a function of the local angle of attack, effective Mach number, and Reynolds number using the following equation:

$$c_d = c_{d_{\text{lin}}} + \Delta c_{d_{\text{non-lin}}} + \Delta c_{d_{\text{M}}} \tag{D.6}$$

The equivalent linear drag coefficient $c_{d_{\text{lin}}}$ is computed using:

$$c_{d_{\text{lin}}} = \left\{c_{d_0} + \frac{\partial c_d}{\partial c_l^2}\left(c_l - c_l^{c_d=c_{d_0}}\right)^2\right\}\left(\frac{Re}{Re_{\text{ref}}}\right)^f \tag{D.7}$$

with c_{d_0} the minimum drag coefficient, $\partial c_d/\partial c_l^2$ the derivative of the drag coefficient with respect to the lift coefficient squared, $c_l^{c_d=c_{d_0}}$ the lift coefficient at which the drag coefficient attains its minimum value, Re the Reynolds number based on the local chord and inflow velocity, Re_{ref} the reference Reynolds number at which the input blade section characteristics were computed, and f the Reynolds number scaling exponent. The latter value should be selected based on the approximate Reynolds number: [69]

- $-0.2 < f < -0.1$ for high-Re turbulent flow ($Re > 2 \cdot 10^6$)
- $-1.5 < f < -0.5$ for the low-Re regime ($2 \cdot 10^5 < Re < 8 \cdot 10^5$)
- $-0.5 < f < -0.3$ for mostly-laminar airfoils at $Re < 1 \cdot 10^5$.

The additional drag coefficient in case of stalled conditions $\Delta c_{d_{\text{non-lin}}}$ follows from:

$$\Delta c_{d_{\text{non-lin}}} = 2\left\{\left(1 - \frac{c_{l_{\alpha_{\text{stall}}}}}{c_{l_\alpha}}\right)\frac{\Delta c_{l_{\text{non-lin}}}}{c_{l_\alpha}\sqrt{1-M^2}}\right\}^2 \tag{D.8}$$

The additional drag coefficient due to compressibility effects $\Delta c_{d_{\text{M}}}$ is computed using:

$$\Delta c_{d_{\text{M}}} = \begin{cases} 0 & \text{if } M < M_{\text{crit}} \\ 10(M - M_{\text{crit}})^3 & \text{if } M \geq M_{\text{crit}} \end{cases} \tag{D.9}$$

with M_{crit} the critical Mach number of the blade section.

D.4 Computation of the Circulation

Having determined the section lift coefficients c_{l_i}, the local circulation Γ_i is computed using:

$$\Gamma_i = \frac{1}{2} W_i c_i c_{l_i} \tag{D.10}$$

with c_i the chord and W_i the magnitude of the effective velocity.

D.5 Computation of the Propeller Performance

After convergence of the circulation, the isolated propeller performance (in terms of the steady-state thrust T^{SS} and torque Q^{SS}) is computed by summing the responses of the individual blade segments:

$$T^{\mathrm{SS}} = R \int_{\eta_{\mathrm{hub}}}^{1} \mathrm{d}T^{\mathrm{SS}}(\eta)\,\mathrm{d}\eta \simeq \sum_{i=1}^{N_{\mathrm{r}}} T_i^{\mathrm{SS}} \tag{D.11}$$

$$Q^{\mathrm{SS}} = R \int_{\eta_{\mathrm{hub}}}^{1} \mathrm{d}Q^{\mathrm{SS}}(\eta)\,\mathrm{d}\eta \simeq \sum_{i=1}^{N_{\mathrm{r}}} Q_i^{\mathrm{SS}} \tag{D.12}$$

with N_{r} the number of radial stations used in the XROTOR computations, and T_i^{SS} and Q_i^{SS} the local steady-state thrust and torque values produced by the radial blade segment i. T_i^{SS} and Q_i^{SS} are computed using:

$$T_i^{\mathrm{SS}} = B\frac{1}{2}\rho W_i^2 \left(c_{l_i}\cos\varphi_i - c_{d_i}\sin\varphi_i\right) c_i \Delta\eta_i R \tag{D.13}$$

$$Q_i^{\mathrm{SS}} = B\frac{1}{2}\rho W_i^2 \left(c_{l_i}\sin\varphi_i + c_{d_i}\cos\varphi_i\right) c_i \eta_i \Delta\eta_i R^2 \tag{D.14}$$

with B the number of propeller blades, $\Delta\eta_i$ the non-dimensional spanwise extent of section i, and ρ the air density. $\Delta\eta_i$ is taken as the distance between the midpoint of the previous segment $i-1$ and the next segment $i+1$. At the first segment the starting point is taken at the radial station of the hub, while at the last segment the end point is defined at the tip of the propeller blade ($\eta = 1$).

With the steady-state thrust and torque known from Equations (D.11) and (D.12), the corresponding thrust and torque coefficients C_T^{SS} and C_Q^{SS} are computed using:

$$C_T^{\mathrm{SS}} = \frac{T^{\mathrm{SS}}}{\rho n^2 D^4} \tag{D.15}$$

$$C_Q^{\mathrm{SS}} = \frac{Q^{\mathrm{SS}}}{\rho n^2 D^5} \tag{D.16}$$

with D the propeller diameter and n the rotational velocity of the propeller in revolutions per second.

Finally, the isolated propeller efficiency is obtained from:

$$\eta^{\mathrm{SS}} = \frac{J}{2\pi}\frac{C_T^{\mathrm{SS}}}{C_Q^{\mathrm{SS}}} \tag{D.17}$$

Appendix E

Additional Numerical Results

This appendix presents additional numerical results which serve as background material to the results discussed in Part II of this report. The results related to the propeller performance are given in Section E.1, while the additional data for the computed propeller noise emissions is presented in Section E.2.

E.1 Powered Propeller Performance

This section presents additional results related to the computations of the propeller performance. First, the effects of the freestream velocity on the isolated propeller performance are discussed (Subsection E.1.1). Subsequently, the separate thrust and torque contributions due to the change in the dynamic pressure and the angle of attack in the pylon wake region observed in the installed configuration are evaluated (Subsections E.1.2 and E.1.3).

E.1.1 Effects of the Freestream Velocity on the Propeller Performance

Because of Reynolds number effects the propeller performance is expected to be a function of the freestream velocity. When the freestream velocity is increased, the propeller blade sections' Reynolds numbers increase. As a result, the boundary layer over the blades becomes thinner, resulting in a larger effective camber hence larger overspeeds. This leads to increased lift production, which directly translates into increased thrust. The drag coefficient should decrease with increasing Reynolds number. However, because of the increased lift it is not known beforehand whether the torque will increase or decrease with increasing freestream velocity. To verify whether the numerical method is capable of simulating the Reynolds number effect, the isolated propeller performance was computed for four freestream velocities: 15, 19, 26, and 30 m/s. The resulting propeller performance results are shown in Figure E.1.

From Figure E.1 it is observed that the computed results indeed show the expected trends. Although the differences are small, the thrust coefficient consistently increases with increasing freestream velocity over the entire advance ratio range. Comparison of the data obtained at freestream velocities of 19 and 30 m/s shows that increases in the thrust coefficient of in between two and ten percent are observed, with the relative difference increasing with increasing advance ratio. Although difficult to see in Figure E.1 because of the lower absolute levels, the trend in the relative increase of the torque coefficient with increasing velocity is similar to that observed for the thrust coefficient. Again increases of about two to ten percent are observed when comparing the data computed at freestream velocities of 19 and 30 m/s.

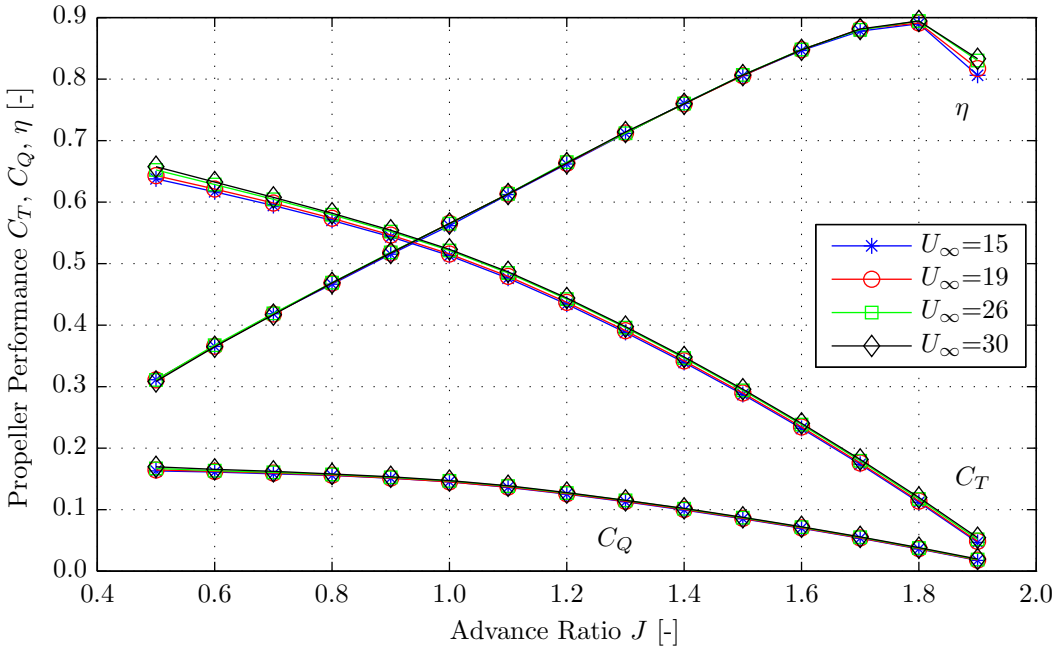

Figure E.1: Propeller performance diagram: effects of the freestream velocity. Isolated configuration, $U_\infty = [15, 19, 26, 30]$ m/s, $0.5 \leq J \leq 1.9$, with rotation correction.

E.1.2 Unsteady Lift and Drag Due to Dynamic Pressure Effects

As discussed in Paragraph 7.2.2.2, the change in the dynamic pressure in the pylon wake is accounted for by correcting the steady-state lift and drag responses. The resulting changes in the lift and drag coefficients are plotted in Figures E.2 and E.3 versus the polar angle ϕ.

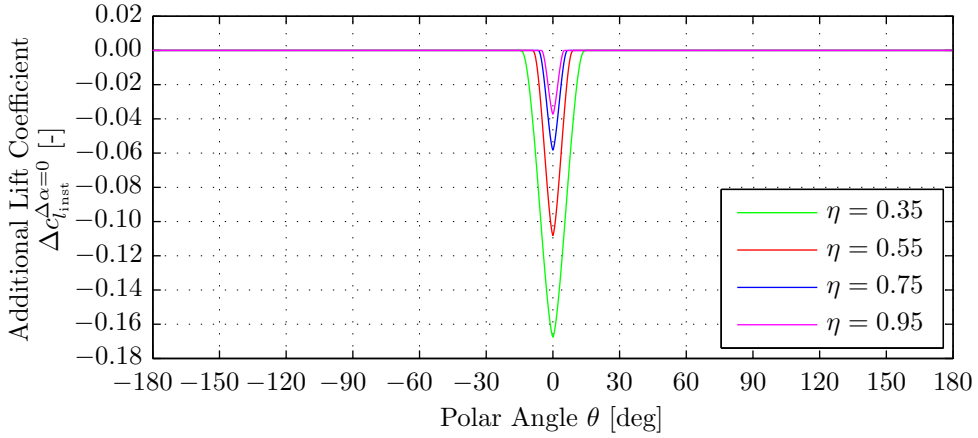

Figure E.2: Change in lift coefficient due to change in dynamic pressure in the pylon wake at various radial stations $\eta = r/R$. Installed configuration, $U_\infty = 19$ m/s, $J = 0.9$, extended pylon.

The change in the lift coefficient due to the reduction in the dynamic pressure in the pylon wake region presented in Figure E.2 shows that the peak of the additional lift coefficient at $\phi = 0°$ becomes increasingly negative with decreasing radial coordinate. This is explained by considering the lower rotational velocity of the inboard blade sections, as a result of which the relative effect of the constant velocity deficit in the pylon wake region is larger than at the outboard stations. Also, the steady-state lift coefficients used as the starting point of the computation are larger at the inboard sections, thereby further increasing the differences in the additional lift coefficient at the various radial stations.

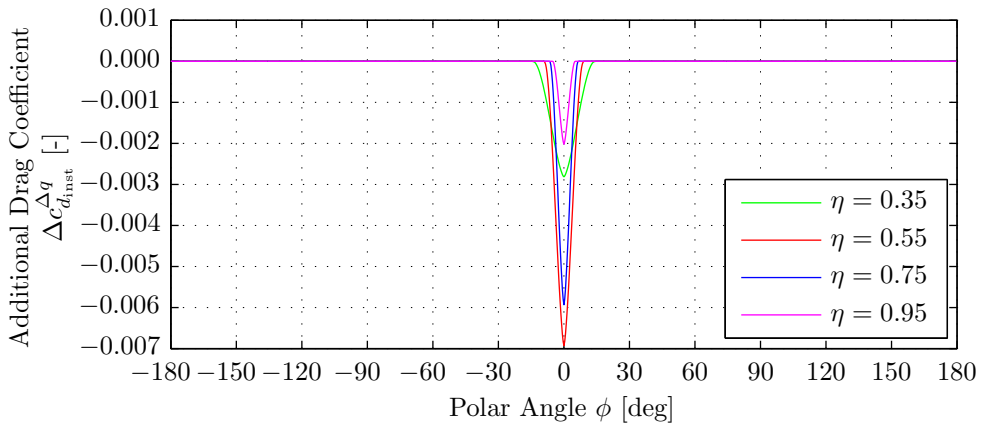

Figure E.3: Change in drag coefficient due to change in dynamic pressure in the pylon wake at various radial stations $\eta = r/R$. Installed configuration, $U_\infty = 19$ m/s, $J = 0.9$, extended pylon.

The additional drag coefficient resulting from the lower dynamic pressure in the wake of the pylon shows a different pattern than observed in the lift coefficient data. Figure E.3 shows that the change in the drag coefficient is largest around the semi-span of the blade (radial stations $\eta = 0.55$ and $\eta = 0.75$). This is explained by the fact that for the considered operating point the computed steady-state drag coefficients are much larger at the radial stations around the semi-span because of the gradual onset of stall in this region. Therefore, although the effect of the change in the dynamic pressure in the wake region is stronger on the inboard part of the blade, the computed absolute change in the drag coefficient at the stations around the semi-span is larger than for the more inboard stations.

E.1.3 Unsteady Lift Due to Angle of Attack Effects

The change in the lift response due to the increased angle of attack in the pylon wake region was determined using Sears' theory. Figure E.4 presents the additional lift coefficient computed using Equation (7.18) versus the polar angle ϕ for the same range of radial stations as considered before. Note that the effects of the change in the angle of attack on the drag coefficient were neglected and thus are not further discussed below.

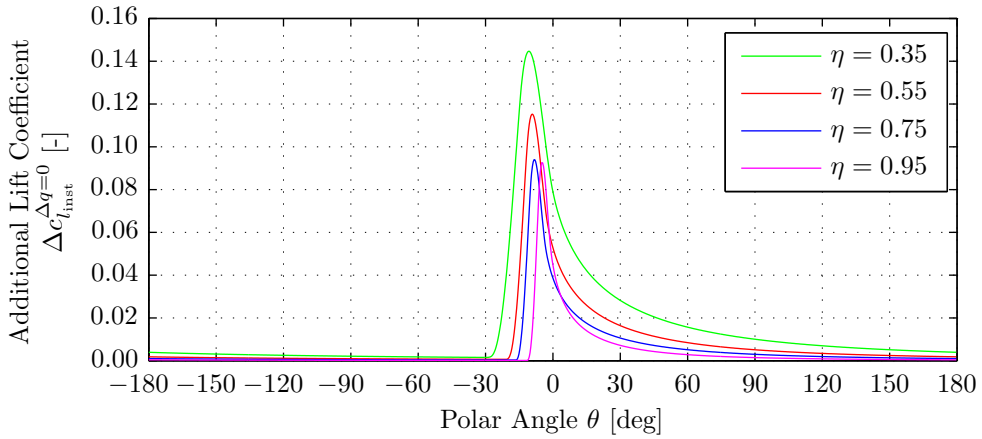

Figure E.4: Change in lift coefficient due to change in angle of attack in the pylon wake at various radial stations $\eta = r/R$. Installed configuration, $U_\infty = 19$ m/s, $J = 0.9$, extended pylon.

Figure E.4 shows that the effect of the change in the angle of attack in the pylon wake region on the lift response of the propeller blades is most pronounced for the inboard stations. This is again explained from the fact that the velocity deficit in the pylon wake region relative to the local effective velocity is largest for the inboard stations. Also, it is observed that the profiles of the additional lift coefficient are steeper for the outboard blade sections, which is as expected considering that the wake region is spread out over a larger range of polar angles for the inboard sections than for the outboard stations.

Furthermore, it is also observed from Figure E.4 that the phase shift between the peak of the additional lift coefficient response and the peak of the gust profile (located at $\phi = 0°$) increases with decreasing radial coordinate. For all radial coordinates, the peak occurs before the actual peak in the gust profile, which might be a surprising result. However, this behavior can be explained by considering the selected approach in which the Sears function is used to compute the unsteady lift response.

Considering the incompressible case, the Sears function is defined by Equation (7.14). The corresponding vector diagram in the complex plane for reduced frequencies ranging from zero up to and including ten is presented in Figure E.5.

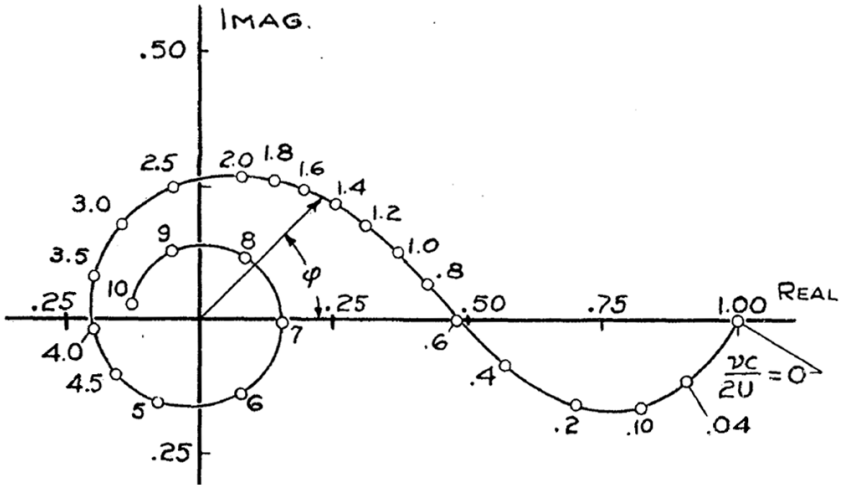

Figure E.5: Vector diagram of the incompressible Sears function. Reproduced from [58].

Figure E.5 shows that the Sears function spirals around the origin, with the amplitude (distance from the origin to the point of interest) decreasing with increasing reduced frequency (indicated here by the variable $\frac{\nu c}{2U}$). Furthermore, the lift response first lags behind the gust velocity vector (phase angle $\varphi < 0$), after which for reduced frequencies above around 0.6 the lift response leads the gust by an increasing phase angle φ.

Considering the characteristics of the Sears function plotted in Figure E.5 it is concluded that the unexpected behavior of the additional lift coefficient due to the change in the angle of attack can indeed be explained. At a freestream velocity of 19 m/s and an advance ratio of $J = 0.9$ the value of the reduced frequency at the $\eta = 0.75$ radial station is approximately equal to $0.16k$, with k the order of the gust harmonic. Clearly, for harmonic orders of four and higher the phase shift will be positive. Considering the large number of harmonic components present in the gust profiles (see Figure 9.4) it is concluded that part of the response does indeed fall in this region. In the end this could result in a positive phase shift of the entire lift

coefficient response. For reduced frequencies between approximately 4 and 7 again a negative phase shift is observed. As a result, the lift response profiles corresponding to the outboard blade sections, for which the higher harmonics of the gust profile still have significant values, show a smaller phase shift than observed at the inboard stations.

To gain additional insight in the unsteady lift response computed using Sears' theory the additional lift coefficient due to the change in the angle of attack was computed for different numbers of harmonic components. The corresponding results are presented in Figure E.6, in which for reference an equivalent steady solution ($\Delta c_l = 2\pi\Delta\alpha$) is also added.

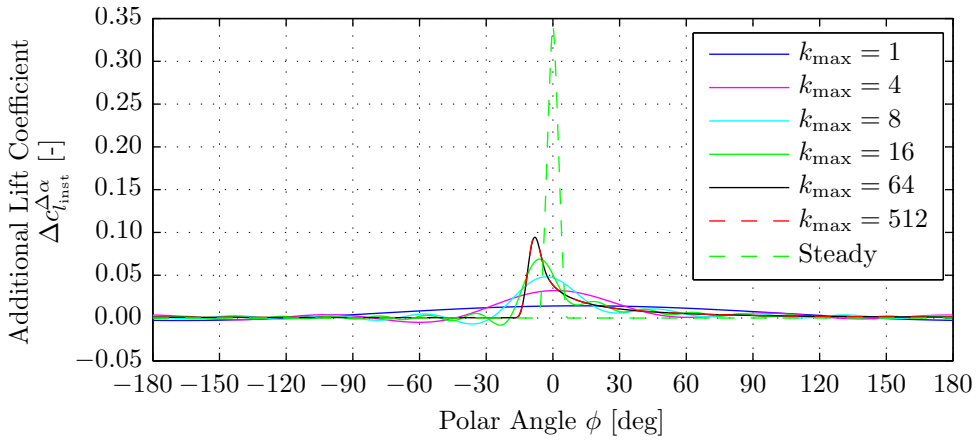

Figure E.6: Change in the lift coefficient due to the change in the angle of attack in the pylon wake region reconstructed using different numbers of harmonic components. Installed configuration, $U_\infty = 19$ m/s, $J = 0.9$, $\eta = 0.75$, extended pylon.

From Figure E.6 it is observed that the lift response starts leading the gust profile when the number of harmonics is increased, indicating that the positive phase shift is indeed a result of the high frequency contents in the gust profiles. Furthermore, it is seen that a relatively large number of harmonics is needed to properly reconstruct the lift coefficient response, with around 64 harmonics required for convergence of the solution. This is as expected considering the large number of harmonics required to characterize the gust profile.

E.2 Powered Propeller Noise Emissions

The additional powered propeller noise emission results are presented in separate subsections for the isolated, installed, and blown configurations (Subsections E.2.1, E.2.2, and E.2.3, respectively).

E.2.1 Isolated Configuration

The major noise results computed for the isolated configuration were presented in Section 10.2. The current subsection first discusses the effects of the definition of the lift and drag components on the computed noise levels (Paragraph E.2.1.1). Subsequently, the effects of the definition of the chordwise blade loading distributions is considered (Paragraph E.2.1.2). Then, a detailed discussion of the noise emissions' radiation efficiency at low freestream velocities is given (Paragraph E.2.1.3). Finally, a directivity analysis of the tonal noise components is presented (Paragraph E.2.1.4).

E.2.1.1 Effects of the Definition of the Lift and Drag Components

Whereas the lift and drag coefficients obtained from the performance computations are defined relative to the effective inflow velocity with induced effects taken into account, the noise computations require the input of the forces with respect to the local advance direction *without* induced effects. To obtain the correct force coefficients the original lift and drag coefficients could be rotated by the induced angle. In this way, the force coefficients c_{f_1} and c_{f_2} are obtained which can then be considered as the effective drag and lift coefficients which should be used in the noise computations. This was illustrated before in Figure 7.9.

However, as a result of the change of coordinate system the effective drag coefficient (now referred to as c_{f_1}) becomes unrealistically large since it also contains part of the original lift vector. Therefore, the loading noise due to drag is no longer simply related to the section's drag coefficient but also to a large extent to the lift coefficient, thereby complicating the analysis of the computed results. The loading noise term denoted 'loading due to drag' now would no longer correspond to the noise generated as a result of the actual drag force acting on the blade, but instead would be the result of the total force acting parallel to the local advance direction without induced effects.

An alternative method would be to substitute the original lift and drag coefficients computed using the lifting line method in the noise computations without modification. The effect of the selected definition of the force coefficients on the total SPL (defined as the combination of thickness, drag loading, and lift loading noise) is plotted versus the advance ratio in Figure E.7. The blue line labeled 'shifted' corresponds to the solution obtained after rotation of the original lift and drag coefficients by the induced angle. The red line labeled 'original' corresponds to the case for which the lift and drag coefficients obtained from the lifting line analysis are substituted directly into the noise prediction equations.

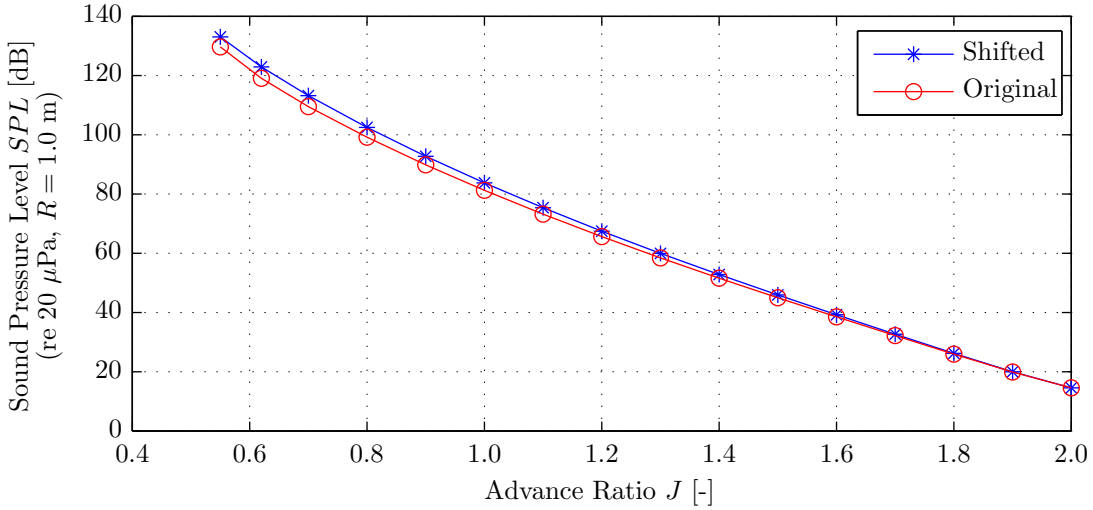

Figure E.7: Effect of the definition of the reference directions for the lift and drag forces on the total SPL. Isolated configuration, $U_\infty = 50$ m/s, $0.5 \leq J \leq 1.9$, $\theta = 90°$.

Figure E.7 shows that the difference between the total SPL computed using the two possible definitions for the force coefficients increases with decreasing advance ratio. This is as expected considering the increase in the induced angle observed with decreasing advance ratio. The maximum difference between the sound pressure levels shown in Figure E.7 is about 4 dB, occurring at the lowest advance ratios.

To increase insight in the differences between the noise levels predicted using the two different definitions of the force coefficients, Figure E.8 presents the evolution of the SPL due to drag and lift loading as a function of the advance ratio for both definitions. The solution obtained after rotation of the force coefficients corresponds to the lines labeled F_1 and F_2, while the results computed using the original lift and drag coefficients are indicated by D and L.

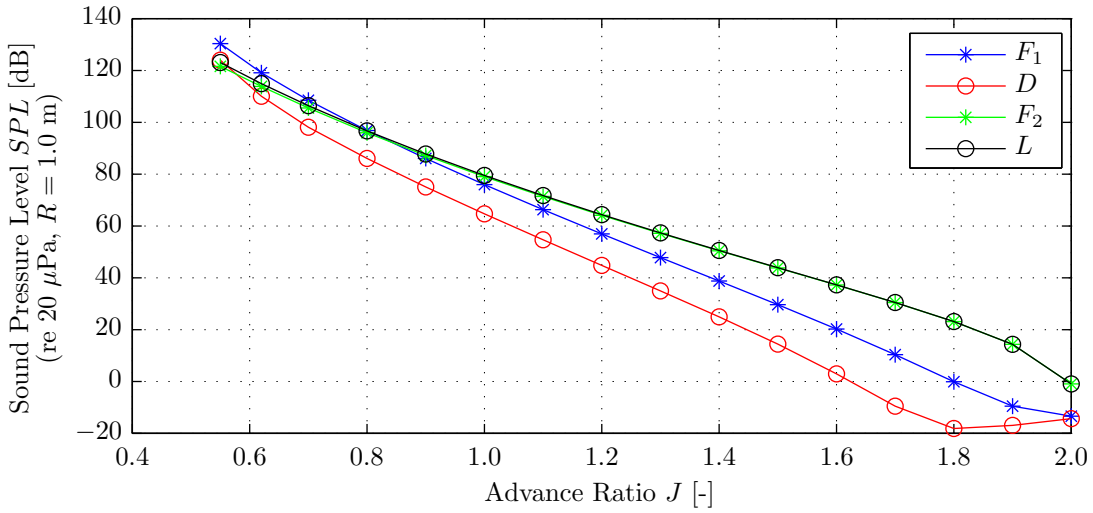

Figure E.8: Effects of the definition of the reference direction for the lift and drag forces on the SPL due to lift and drag loading. Isolated configuration, $U_\infty = 50$ m/s, $0.5 \leq J \leq 1.9$, $\theta = 90°$.

From Figure E.8 it is observed that when changing the definition of the force coefficients from the effective advance direction to the advance direction without induced effects, the loading noise due to lift remains approximately constant. This is as expected considering that the change in the lift coefficient resulting from the change in the reference direction will be relatively small. The noise related to the drag coefficient on the other hand changes significantly after rotation with the induced angle. Therefore, it can be stated that the change in the overall SPL observed in Figure E.7 results from a change in the loading noise due to drag. It is observed that in general the change in the drag loading noise due to the rotation with the induced angle decreases with increasing advance ratio. This might be the result of the decreasing lift-to-drag ratio observed when decreasing the advance ratio. The higher the lift-to-drag ratio, the larger the relative contribution of the original lift force to the newly defined drag force. However, because of the low absolute levels of the noise due to drag at high advance ratios the change in the overall SPL (i.e. the combination of thickness and loading noise) only starts to become pronounced in the lower advance ratio range.

Based on the previous discussion it is concluded that the choice of the definition of the lift and drag forces has a clear impact on the sound pressure levels computed using the propeller noise prediction method. It was decided to select the approach in which the original lift and drag coefficients are shifted with the induced angle. In this way the force coefficients used in the computations are defined in the same direction as used in the derivation of the equations. Furthermore, the correct thrust and torque are maintained when the shift is performed, thereby remaining closer to the physics of the actual problem. After the transformation of the lift and drag coefficients the two loading noise components should no longer be seen as the resultants of lift and drag. Instead, they should be considered as the loading noise resulting from the forces F_1 and F_2, with F_1 defined parallel to the local advance direction without

induced effects (i.e. analogous to drag) and F_2 perpendicular to it (i.e. analogous to lift). Taking into account the assumption made in the noise computation method that the blade sections move in the local advance direction without consideration of induced effects, it should be questioned whether the method is applicable at low advance ratios for which the induced angle is large.

E.2.1.2 Effects of the Definition of the Chordwise Blade Lift Distribution

The equations used to compute the harmonic propeller noise emissions require the input of the chordwise blade load distributions. The blade load distributions f_{D} (drag) and f_{L} (lift) are used to compute the chordwise loading parameters Ψ_{D} and Ψ_{L}, which represent the effects of chordwise noncompactness (interference of noise emissions from various source locations along the blade chord). For simplicity, so far all results presented in this report were obtained assuming a uniform lift distribution. To assess whether the use of this simplified lift distribution introduces large inaccuracies in the resulting solutions, the noise computations were also performed with a more realistic chordwise lift distribution obtained using XFOIL for the blade section at $\eta = 0.75$ at an angle of attack of 6 degrees and a Reynolds number of $3.0 \cdot 10^5$. The resulting lift distribution is depicted in Figure E.9, which for reference also contains the uniform distribution assumed previously. Considering that the effects of the definition of the chordwise lift distribution increase with the tip Mach number, it was decided to perform the comparison for the analysis point characterized by the highest tip Mach number considered in the numerical evaluations. Hence, the operating point at a freestream velocity of 50 m/s and an advance ratio of $J = 0.55$ was selected, corresponding to a tip Mach number of 0.85.

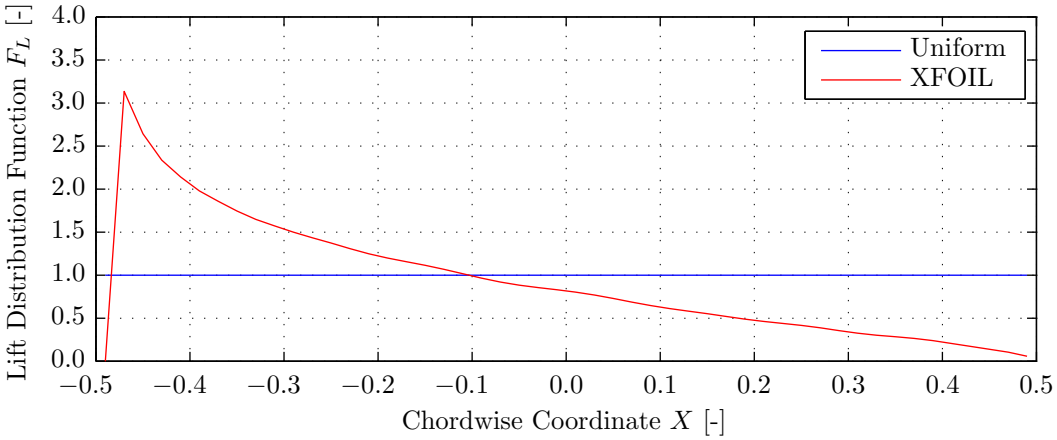

Figure E.9: Different loading distributions used to assess the effect of the chordwise lift distribution on the SPL due to loading in the F_2 direction.
Isolated configuration, $U_\infty = 50$ m/s, $J = 0.55$, $M_{\mathrm{t}} = 0.85$, $\theta = 90°$.

Figure E.9 shows that the lift distribution obtained from XFOIL is much more peaky than the uniform distribution assumed previously. The distribution computed using XFOIL was substituted into the analytic noise prediction routine, after which the computed SPL due to the loading noise resulting from the force F_2 was computed for the full range of axial directivity angles θ. The same chordwise lift distribution was used for all radial stations. The resulting sound pressure levels are plotted in Figure E.10, which also contains the corresponding results obtained using the uniform lift distribution.

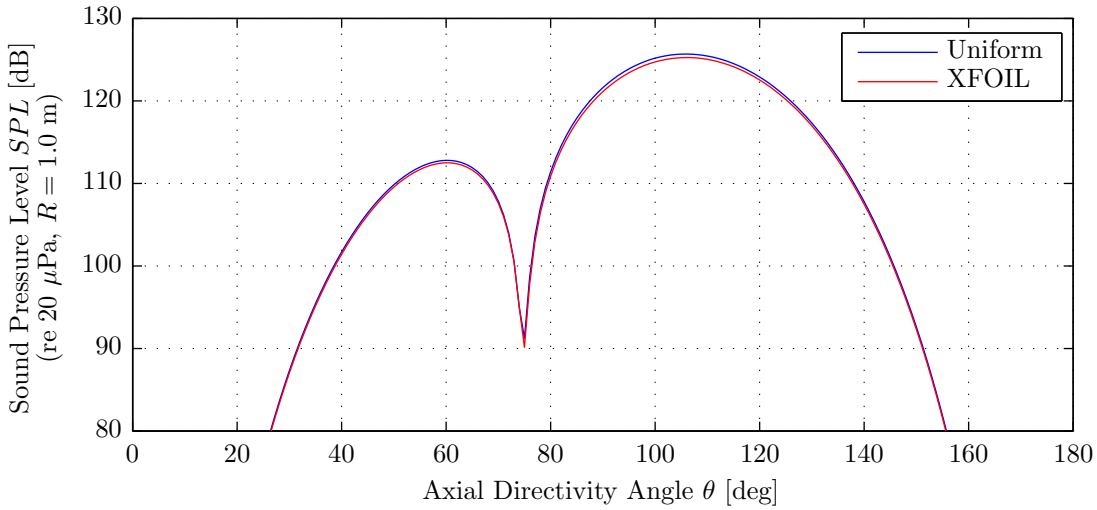

Figure E.10: Effects of the definition of the loading distribution on the SPL due to loading by the force in the F_2 direction. Isolated configuration, $U_\infty = 50$ m/s, $J = 0.55$, $M_t = 0.85$.

From Figure E.10 it is observed that the differences between the sound pressure levels computed using the uniform and non-uniform chordwise lift distributions are very small. The difference at the axial directivity angle at which the maximum SPL is obtained ($\theta = 105°$) is about 0.5 dB. As mentioned previously, it should be noted that the influence of the choice of the chordwise lift distribution function becomes larger with increasing tip Mach number. This is a result of the fact that higher tip Mach numbers lead to larger values of the chordwise wave number k_x, hence increased noncompactness effects. The comparison depicted in Figure E.10 showed that even at the highest tip Mach number considered in the numerical evaluations discussed in this report ($M_t = 0.85$) the effects of noncompactness are very small. Therefore, it is concluded that the maximum error introduced by the use of a uniform chordwise lift distribution will be within 0.5 dB for all operating points considered in the propeller noise computations. Since this difference is considered small relative to the expected accuracy of the method it was decided to use a uniform loading distribution in all computations discussed in this report.

E.2.1.3 Radiation Efficiency Versus the Tip Mach Number

The results presented in Figure 10.4 showed that the computed sound pressure levels for the isolated propeller are a strong function of the tip Mach number and that unexpectedly low sound pressure levels are obtained in the low tip Mach number range. Inspection of the equations used to compute the harmonics of the propeller noise emissions (see Subsection 7.3.1) learns that it is possible that the inadequate predictions at low freestream velocities result from the combination of a high blade number ($B = 8$) and low tip Mach numbers. In Equation (7.39) the radiation efficiency of the harmonic components is governed by the Bessel function of the first kind of order mB and argument $mB\eta M_t \sin\theta$ [49]. The typical behavior of Bessel functions of the first kind with order not equal to zero is to peak at arguments slightly larger than the order and to diminish towards zero for smaller arguments. Since relatively speaking the initial part around zero becomes longer when the order of the Bessel function is increased, an increase in the blade number typically results in a reduction of the radiation efficiency. Combined with small tip Mach numbers this effect might however become stronger than expected, resulting in underpredictions of the propeller noise levels.

To illustrate this, Figure E.11 shows the behavior of the Bessel function of order mB and argument $\zeta = mB\eta M_t \sin\theta$. The results are plotted for the first harmonic ($m = 1$) and a radial station at 75% of the blade span ($\eta = 0.75$). Three different blade numbers were used ($B = [2, 4, 8]$), while two tip Mach numbers were considered ($M_t = [0.3, 0.7]$). The function values corresponding to a tip Mach number of $M_t = 0.3$ are indicated by the asterisks, while the open circles correspond to the values obtained after substitution of a tip Mach number of $M_t = 0.7$. The axial directivity angle was set to $\theta = 90°$.

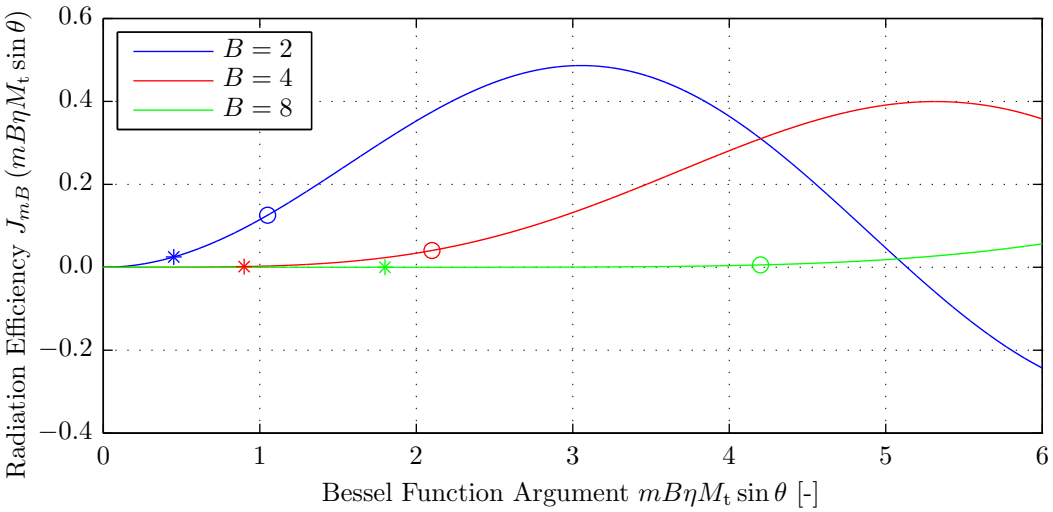

Figure E.11: Behavior of the Bessel function of the first kind of order mB and argument $mB\eta M_t \sin\theta$ for different blade numbers B.
Isolated configuration, $m = 1$, $\eta = 0.75$, $B = [2, 4, 8]$, $M_t = [0.3, 0.7]$, $\theta = 90°$.

Figure E.11 confirms the expected behavior of the Bessel function term. With increasing order (hence increasing blade number at constant harmonic order m) the peak shifts towards higher arguments, while the initial flat region becomes increasingly long. As a result, when the tip Mach number is low the relative magnitude of the Bessel function evaluated for the larger blade number is smaller than that computed for the smaller blade number. With increasing tip Mach number the argument of the Bessel function becomes increasingly large while the order remains the same, thereby making the effect of the blade number on the radiation efficiency increasingly less pronounced. The values indicated by the markers in Figure E.11 are summarized in Table E.1. The values of the Bessel function term multiplied with the blade number and the blade number squared are also added, as explained later.

Table E.1: Function values of the Bessel term in Equation (7.39).
$m = 1$, $\eta = 0.75$, $B = [2, 4, 8]$, $M_t = [0.3, 0.7]$, $\theta = 90°$.

B	mB	M_t	ζ	$J_{mB}(\zeta)$	$B \cdot J_{mB}(\zeta)$	$B^2 \cdot J_{mB}(\zeta)$
2	2	0.3	0.45	$2.5 \cdot 10^{-2}$	$5.0 \cdot 10^{-2}$	$1.0 \cdot 10^{-1}$
		0.7	1.05	$1.3 \cdot 10^{-1}$	$2.5 \cdot 10^{-1}$	$5.0 \cdot 10^{-1}$
4	4	0.3	0.90	$1.6 \cdot 10^{-3}$	$6.6 \cdot 10^{-3}$	$2.6 \cdot 10^{-2}$
		0.7	2.10	$4.0 \cdot 10^{-2}$	$1.6 \cdot 10^{-1}$	$6.5 \cdot 10^{-1}$
8	8	0.3	1.80	$9.8 \cdot 10^{-6}$	$7.8 \cdot 10^{-5}$	$6.2 \cdot 10^{-4}$
		0.7	4.20	$5.7 \cdot 10^{-3}$	$4.5 \cdot 10^{-2}$	$3.6 \cdot 10^{-1}$

Table E.1 shows that the function values computed for $B = 8$ are several orders of magnitude smaller than those computed for the smallest blade number ($B = 2$). The values of $J_{mB}(\zeta)$ for $B = 4$ fall in between the values obtained for $B = 2$ and $B = 8$. It should be noted that apart from the influence of the Bessel term all noise harmonics are multiplied with the blade number, thereby partially offsetting the computed reduction in the radiation efficiency at the higher blade numbers. For the thickness noise even the square of the blade number is used. For the tip Mach number of 0.7 the differences between the function values are strongly decreased after multiplication with the blade number. However, even after multiplication with the blade number or blade number squared the differences are still very large at the tip Mach number of 0.3. This then explains why for the current propeller the computed noise emissions at tip Mach numbers below around 0.3 are surprisingly low.

To confirm the previous observations, Figure E.12 displays the values of $J_{mB}(\zeta)$, $BJ_{mB}(\zeta)$, and $B^2 J_{mB}(\zeta)$ versus the tip Mach number for the three blade numbers as considered before.

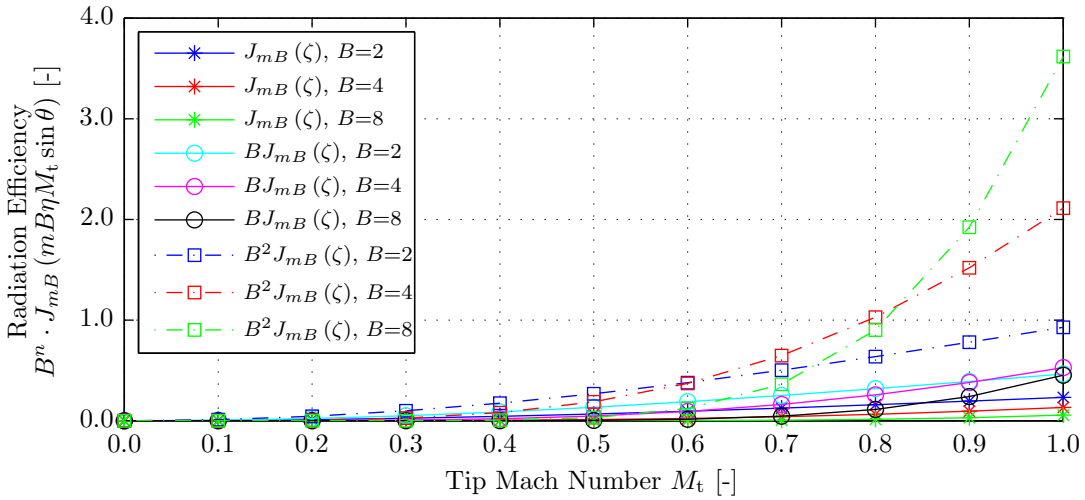

Figure E.12: Radiation efficiency as a function of the tip Mach number for different blade numbers B. Isolated configuration, $m = 1$, $\eta = 0.75$, $B = [2, 4, 8]$, $M_t = [0.3, 0.7]$, $\theta = 90°$.

Figure E.12 indeed shows that the behavior of the Bessel function term is such that for high blade numbers and low tip Mach numbers the radiation efficiency is very low. Comparing the results obtained for blade numbers of two and eight it is concluded that the adopted theory for the prediction of harmonic propeller noise in the isolated configuration underpredicts the noise of propellers with many blades operating at low tip Mach numbers.

E.2.1.4 Tonal Noise Directivity Analysis

Figure E.13 depicts the noise directivity in the axial direction for the same measurement point as shown before in Figure 10.1. However, now not the total sound pressure level (summed over all harmonics) is shown, but instead the sound pressure levels of the different harmonic components present in the signal are plotted.

From Figure E.13 it is observed that the predicted tonal noise levels rapidly decay with increasing harmonic number. This is as expected considering the governing equations used to predict the noise emissions. Increasing the harmonic order leads to an increased order of the Bessel function discussed in Subsection E.2.1.3. Therefore, the effect of increasing harmonic order on the radiation efficiency of the noise emissions can be compared to the effect of increasing the blade number at constant harmonic order.

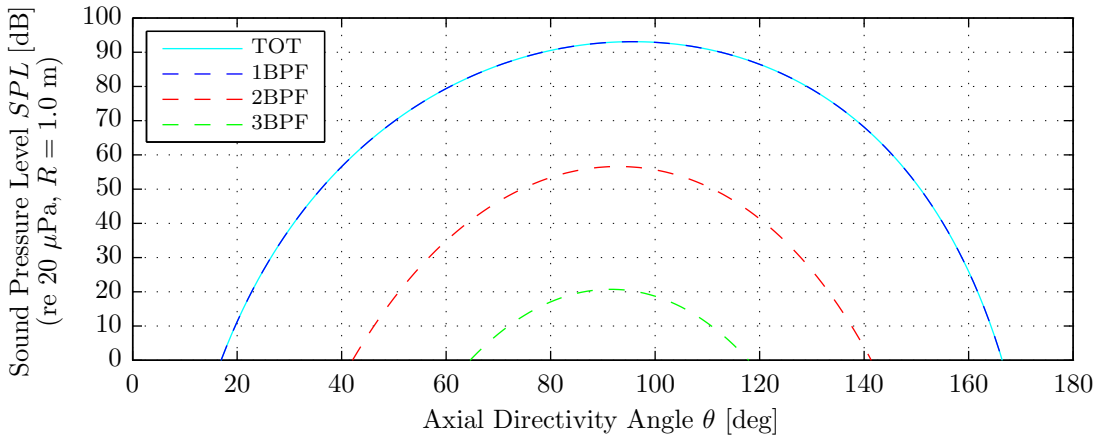

Figure E.13: Total SPL of the tonal noise components versus the axial directivity angle θ. Isolated configuration, $U_\infty = 50$ m/s, $J = 0.9$, $M_t = 0.53$.

E.2.2 Installed Configuration

The installed propeller noise emissions were discussed in Section 10.3. This part of the appendix presents the directivity patterns of the various noise components (Paragraph E.2.2.1). Subsequently, a directivity analysis of the tonal noise is discussed (Paragraph E.2.2.2).

E.2.2.1 Installed Propeller Noise Directivity Patterns

An example of the axial directivity of the installed propeller noise emissions is presented in Figure E.14. The results were obtained for a freestream velocity of 50 m/s, an advance ratio of $J = 0.9$, and a circumferential directivity angle of $\phi = 90°$.

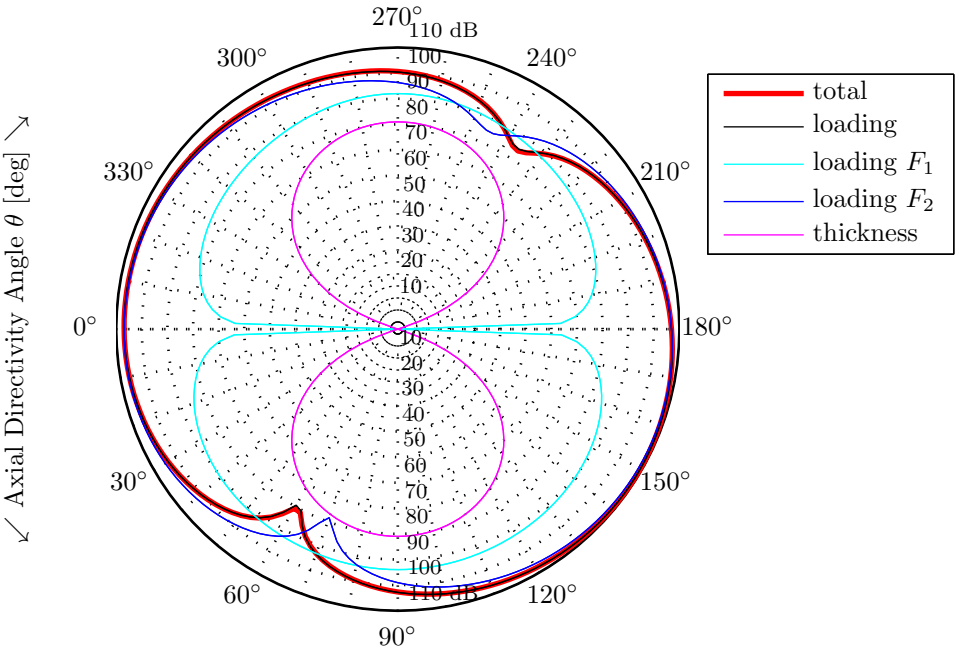

Figure E.14: Sound pressure level (re 20 μPa, $R = 1.0$ m) versus the axial directivity angle θ. Installed configuration, $U_\infty = 50$ m/s, $J = 0.9$, $M_t = 0.53$, $\phi = 90°$.

Figure E.14 shows that in the installed configuration the sound pressure levels of the propeller noise emissions are of the same order over the entire range of directivity angles considered, except for the presence of two nodes of reduced intensity. At the current operating point

($U_\infty = 50$ m/s and $J = 0.9$) these two nodes occur at axial directivity angles of approximately $\theta = 60°$ and $\theta = 240°$. Based on the results obtained for other operating points it is concluded that the directivity angles at which the two nodes occur become larger with increasing tip Mach number. At the largest tip Mach numbers considered in the evaluations presented in this report ($M_t \geq 0.70$) the axial directivity pattern changes, with significantly higher sound pressure levels around the propeller plane ($\theta = 90°$) than in the forward and rear arcs. This is explained by the fact that for high tip Mach numbers the isolated propeller noise emissions dominate the installation effects near the propeller plane.

Apart from the distinct effects on the axial directivity of the propeller's noise emissions the installation of the upstream pylon also affects the circumferential directivity. Figure E.15 presents an overview of the circumferential directivity of the different noise components. A constant axial directivity angle of $\theta = 90°$ was selected, while the same operating conditions were used as considered in Figure E.14.

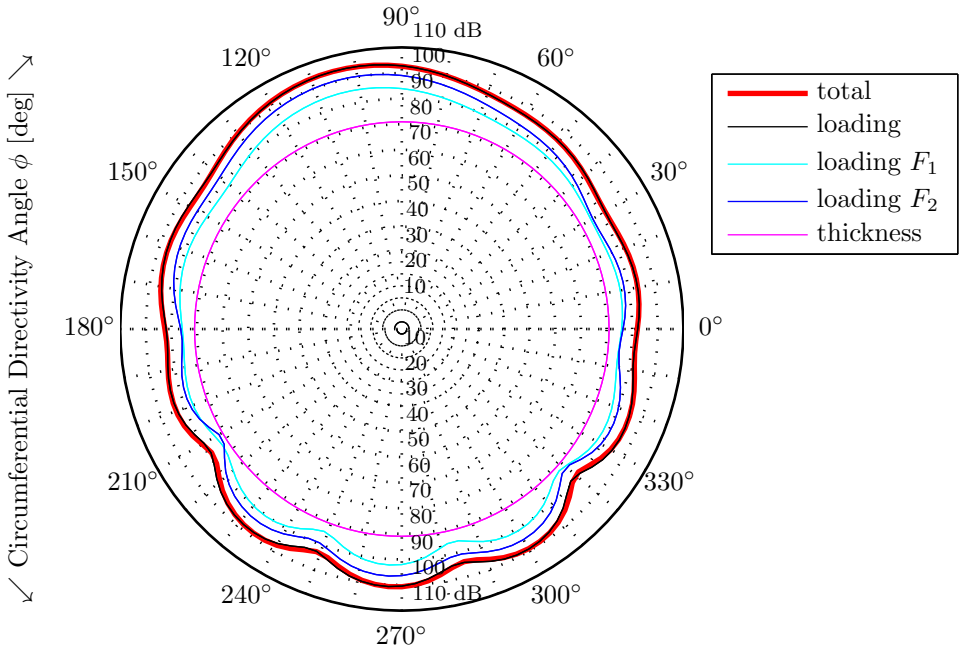

Figure E.15: Sound pressure level (re 20 μPa, $R = 1.0$ m) versus the circumferential angle ϕ. Installed configuration, $U_\infty = 50$ m/s, $J = 0.9$, $M_t = 0.53$, $\theta = 90°$.

The circumferential directivity pattern presented in Figure E.15 clearly shows a number of lobes in the circumferential direction due to the fluctuating forces on the propeller blades resulting from the installation effects. Inspection of the circumferential directivity of the separate components of the installed propeller noise emissions shows that the thickness noise is constant with ϕ, which is as expected since it is not affected by the installation effects. The directivity patterns of the loading noise terms due to F_1 and F_2 are comparable. This also corresponds to the expected results, since it was observed before that both loading noise components are mainly dominated by the contribution from the lift coefficient.

Analyses at different operating conditions showed that with increasing tip Mach number the lobes become less pronounced and the circumferential directivity pattern starts to become practically uniform (at $\theta = 90°$). Again, this is the result of the isolated propeller noise sources dominating the installation effects.

E.2.2.2 Tonal Noise Directivity Analysis

The sound pressure levels of the first four BPF harmonics in the installed propeller sound spectrum are presented in Figure E.16 as a function of the axial directivity angle θ. Again, the selected operating point was characterized by a freestream velocity of 50 m/s and an advance ratio of 0.9. The circumferential directivity angle was set equal to $\phi = 90°$.

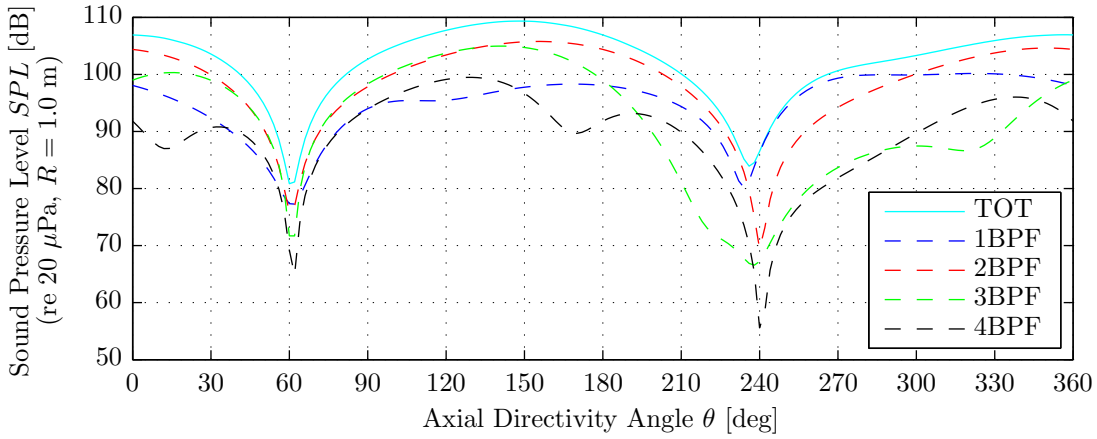

Figure E.16: Total SPL of the tonal noise components versus the axial directivity angle θ. Installed configuration, $U_\infty = 50$ m/s, $J = 0.9$, $\phi = 90°$.

Figure E.16 shows that at the considered operating point at most axial directivity angles the first four harmonics all contribute significantly to the total noise levels. Only around the axial directivity angle of $\theta = 240°$ the sound spectrum is dominated by a single tone (1BPF). Note that this region corresponds to the position where the installation effect is small as observed in Figure 10.6. At the other directivity angles in general the SPL of the 2BPF tone is largest, with the 3BPF tone being of equal magnitude in the $30° \leq \theta \leq 150°$ range.

Having discussed the axial directivity pattern of the harmonic components of the installed propeller noise, the circumferential directivity is considered. Figure E.17 presents an overview of the sound pressure levels of the first four BPF tones versus the circumferential angle ϕ. The same operating point is considered as used before: $U_\infty = 50$ m/s and $J = 0.9$.

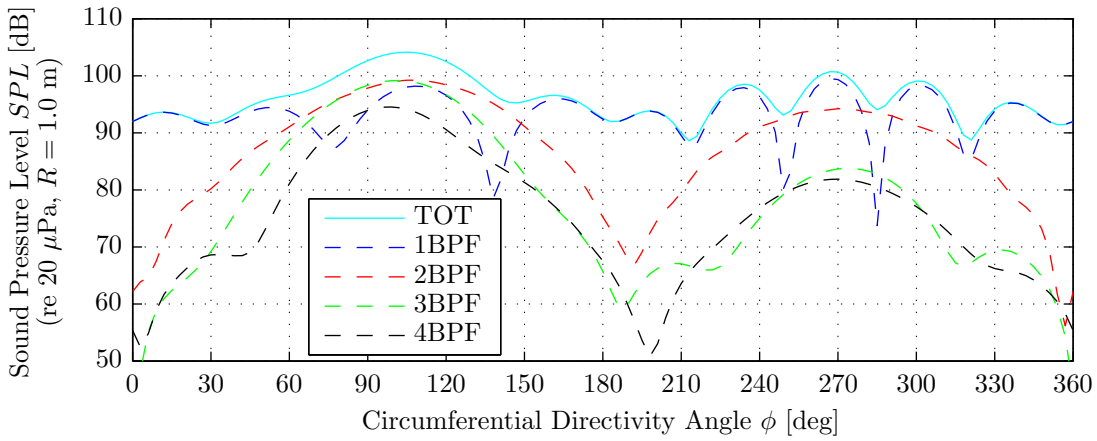

Figure E.17: Total SPL of the tonal noise components versus the circumferential directivity angle ϕ. Installed configuration, $U_\infty = 50$ m/s, $J = 0.9$, $\phi = 90°$.

The results depicted in Figure E.17 show that the lobes observed in the circumferential directivity pattern of the total SPL are mainly introduced by the 1BPF tone. The higher BPF multiples show more simple directivity patterns, with clear minima at circumferential directivity angles corresponding to the position of the pylon plane (around $\phi = 0°$ and $\phi = 180°$) and distinct maxima perpendicular to the pylon (around $\phi = 90°$ and $\phi = 270°$).

E.2.3 Blown Configuration

Section 10.4 discussed the results computed for the blown propeller noise emissions. This part of the appendix treats four additional topics. The directivity patterns of the various noise components are discussed first (Paragraph E.2.3.1), after which the effect of the tip Mach number on the noise emissions is assessed (Paragraph E.2.3.2). Finally, the sensitivity to the operating conditions and the directivity characteristics of the tonal noise emissions are presented (Paragraphs E.2.3.3 and E.2.3.4).

E.2.3.1 Blown Propeller Noise Directivity Patterns

A typical axial directivity polar plot of the noise emissions of the propeller in the blown configuration is shown in Figure E.18. The same operating point was considered as used in the presentation of the isolated and installed results: $U_\infty = 50$ m/s and $J = 0.9$. Furthermore, the circumferential directivity angle was fixed to $\phi = 90°$.

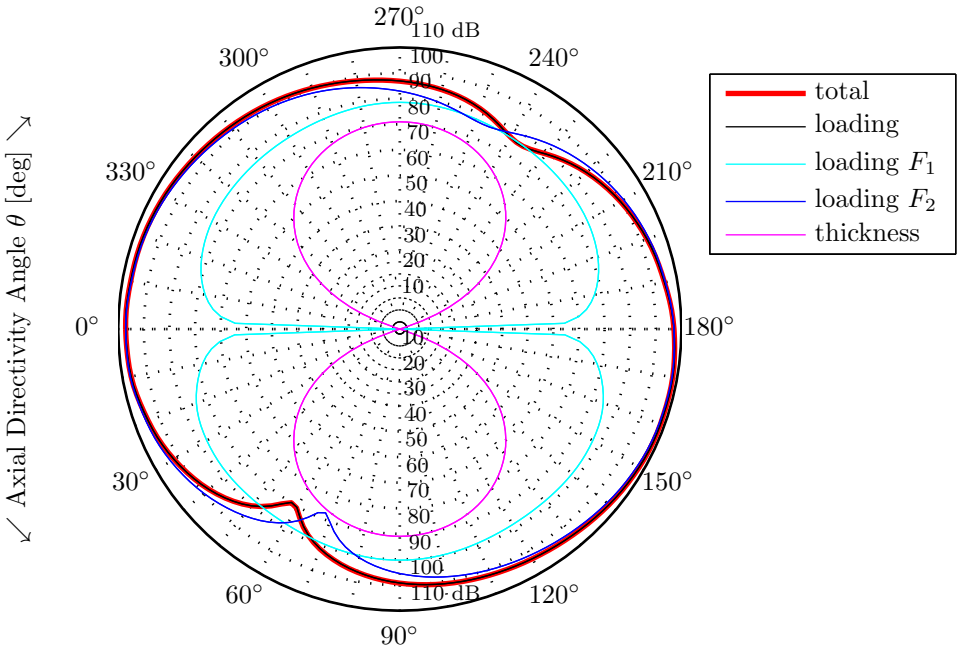

Figure E.18: Sound pressure level (re 20 μPa, $R = 1.0$ m) versus the axial directivity angle θ. Blown configuration, $U_\infty = 50$ m/s, $J = 0.9$, $M_t = 0.53$, $\phi = 90°$.

From Figure E.18 it is observed that, similarly as for the installed configuration, the loading noise due to F_2 dominates the sound spectrum corresponding to the blown propeller. This is a result of the contribution of the unsteady lift force associated with the changes in the dynamic pressure and the angle of attack in the pylon wake region. Apparently, the application of blowing does not fully eliminate the resulting load fluctuations. This is as expected considering the input blown wake profile, which was not completely uniform.

The unsteady blade loads also introduce a circumferential directivity pattern. Figure E.19 presents the SPL of the different components of the blown propeller noise emissions as a function of the circumferential angle ϕ. The same operating point was considered as used before ($U_\infty = 50$ m/s and $J = 0.9$), while the axial directivity angle was set to $\theta = 90°$.

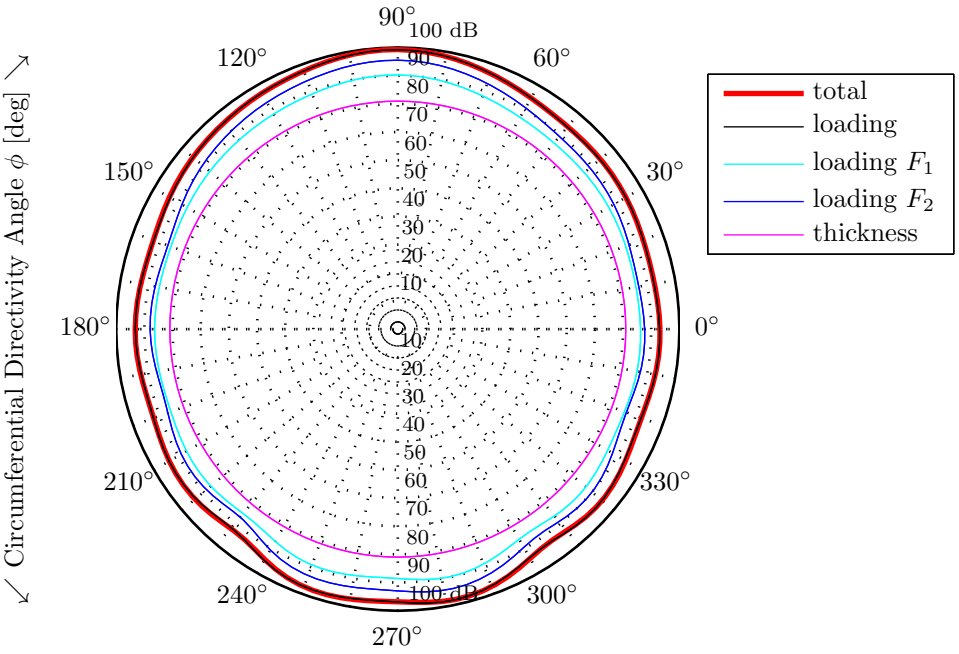

Figure E.19: Sound pressure level versus the circumferential angle ϕ. Blown configuration, $U_\infty = 50$ m/s, $J = 0.9$, $M_t = 0.53$, $\theta = 90°$.

Figure E.19 shows that the blown propeller noise emissions display a number of lobes in the circumferential direction. These are mainly the result of variations in the sound pressure levels due to the force in the F_2 direction, and hence also result from the fluctuating lift generated by the propeller blades.

E.2.3.2 Noise Emissions Versus Tip Mach Number and Freestream Velocity

Apart from the influence of the magnitude of the blade loads, the noise emissions are also strongly impacted by the value of the tip Mach number. Figure E.20 is presented to quantify the effects of the tip Mach number on the blown propeller noise emissions. The total sound pressure levels are plotted for $15 \leq U_\infty \leq 80$ m/s and $0.5 \leq J \leq 1.9$, while the axial and circumferential directivity angles were fixed to $\theta = \phi = 90°$. Note again that equal tip Mach numbers at different freestream velocities correspond to different advance ratios, hence different blade loading conditions.

Following the trends observed for the installed propeller, Figure E.20 shows that also in the blown configuration at constant tip Mach number the SPL increases with increasing freestream velocity, since along this direction the advance ratio increases hence the installation effects become more pronounced. Furthermore, it is observed again that for the region where the installation effects are dominant the sound pressure levels computed for the blown configuration are consistently lower than those obtained for unblown, installed conditions. Also, again kinks in the sound pressure level responses are recognized, corresponding to the tip Mach number for which the installed noise emissions become dominated by steady loading noise.

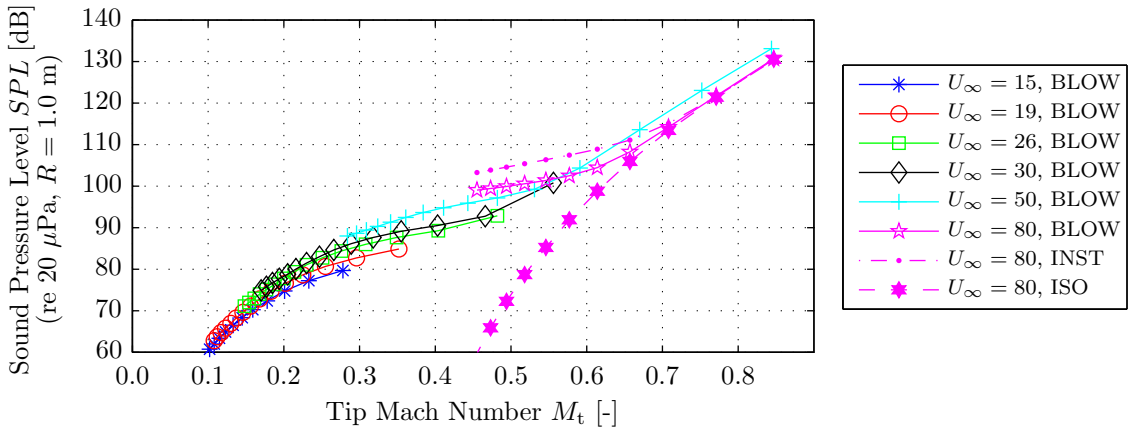

Figure E.20: Total SPL versus the tip Mach number. Blown configuration, $U_\infty = [15, 19, 26, 30, 50, 80]$ m/s, $0.5 \leq J \leq 1.9$, $\theta = \phi = 90°$.

E.2.3.3 Effects of the Propeller Operating Point on the Tonal SPL

Figure E.21 presents the sound pressure levels of the first four BPF tones versus the advance ratio for $U_\infty = 50$ m/s, $\theta = 90°$ and $\phi = 90°$.

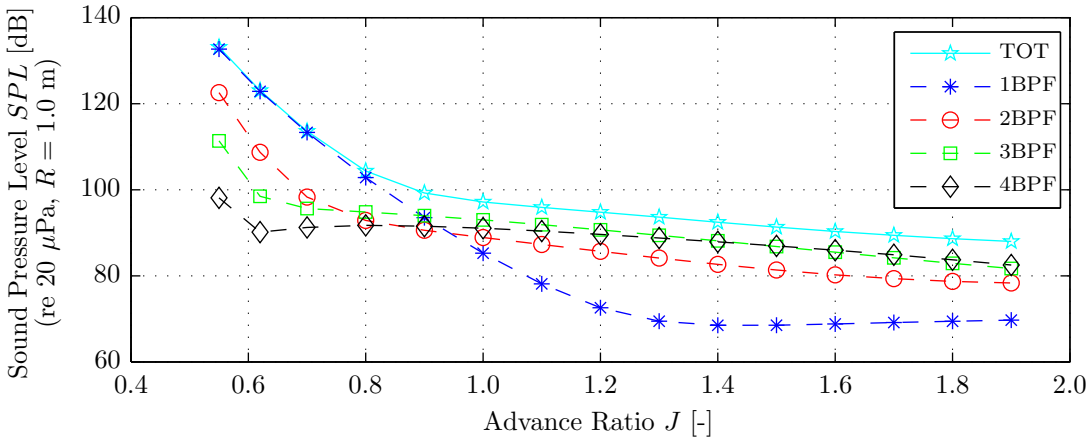

Figure E.21: Total SPL of the tonal noise levels versus the advance ratio. Blown configuration, $U_\infty = 50$ m/s, $0.5 \leq J \leq 1.9$, $\theta = \phi = 90°$.

Figure E.21 shows that in general the tonal noise levels increase with decreasing advance ratio as a result of the increased blade loads and tip Mach number. The SPL of the 1BPF tone however shows a small decrease for $1.4 \leq J \leq 1.9$, which is most likely the result of the increase in the frequencies of the gust profile corresponding to increasing tip Mach numbers. For advance ratios above approximately $J = 0.9$ the tones corresponding to the higher BPF multiples all have a higher sound pressure level than the 1BPF tone. This again is explained by considering the distribution of the unsteady lift coefficients over the different harmonics. At the lowest advance ratios strong increases in the SPL are observed for all BPF multiples. This is the result of a shift in the noise generating mechanism towards being dominated by the increased steady-state blade loads.

E.2.3.4 Tonal Noise Directivity Analysis

The sound pressure levels of the first four BPF tones are depicted in Figure E.22 as a function of the axial directivity angle θ. The circumferential directivity angle was set to $\phi = 90°$, while the selected operating point was characterized by $U_\infty = 50$ m/s and $J = 0.9$.

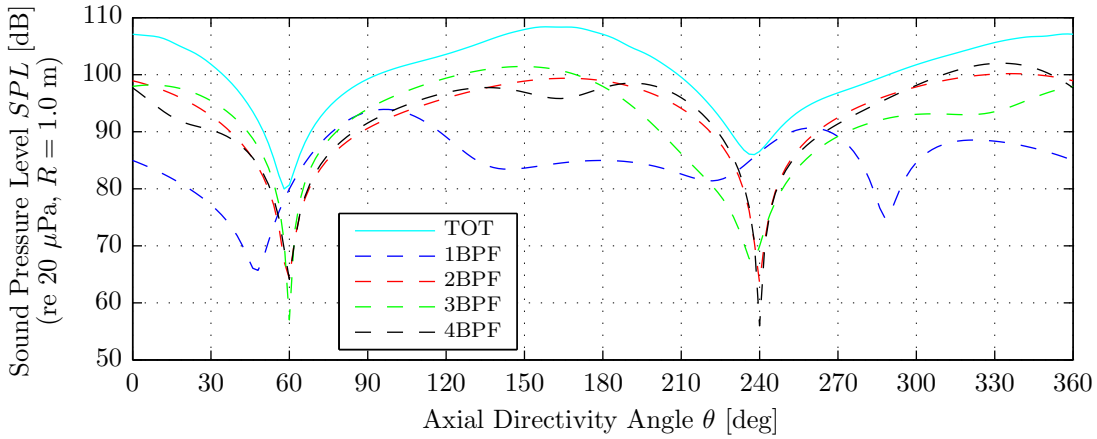

Figure E.22: Total SPL of the tonal noise components versus the axial directivity angle θ. Blown configuration, $U_\infty = 50$ m/s, $J = 0.9$, $\phi = 90°$.

Figure E.22 shows that in the blown configuration the 2BPF, 3BPF, and 4BPF tones dominate the 1BPF tone over the largest part of the axial directivity angle range. The differences are especially large for axial directivity angles close to the propeller axis, indicating that the unsteady lift response in the blown configuration is mainly present in the higher harmonics. This is confirmed by Figure 9.21 which showed the distribution of the Fourier coefficients of the unsteady lift response over the various harmonic numbers.

Figure E.23 depicts the circumferential directivity of the first four BPF tones for the same operating point as considered before, and an axial directivity angle of $\theta = 90°$.

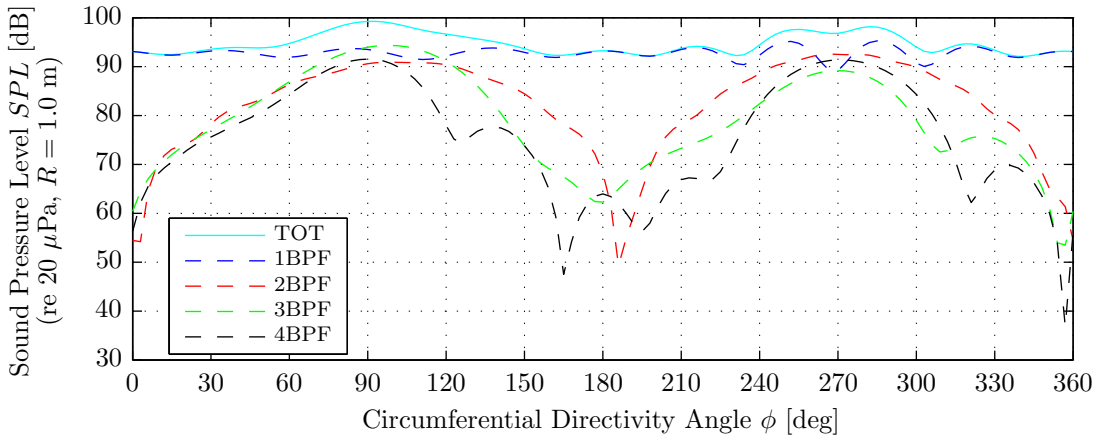

Figure E.23: Total SPL of the tonal noise components versus the circumferential directivity angle ϕ. Blown configuration, $U_\infty = 50$ m/s, $J = 0.9$, $\theta = 90°$.

Figure E.23 shows that in the propeller plane ($\theta = 90°$) the 1BPF tone remains approximately constant with the circumferential angle, hence mimicking the behavior observed in the isolated configuration. The higher BPF multiples on the other hand still show a distinct directivity pattern in the circumferential direction, which is as expected considering the distribution of the unsteady lift coefficient over the different harmonics. For the lower harmonics the magnitude of the Fourier coefficients is reduced more than for the higher harmonics, hence bringing the behavior of the 1BPF tone closer to the isolated case than that of the higher BPF multiples.

Appendix F

Additional Comparisons of Experimental and Numerical Results

This appendix presents additional results related to the comparison of the experimental and numerical results which were not treated in Chapter 11 of this report. The pylon wake profiles are considered first (Section F.1), followed by the propeller performance (Section F.2).

F.1 Pylon Wake Profiles

Section 11.1 only compared the computed and measured wake profiles for the extended pylon model. Below, the results for the default and sharp pylon models are presented and discussed in separate subsections. Note that only unblown results are considered.

F.1.1 Default Pylon Model

Figure F.1 displays the measured and computed velocity profiles in the wake of the default pylon. The corresponding values of the wake width and wake depth are summarized in Table F.1.

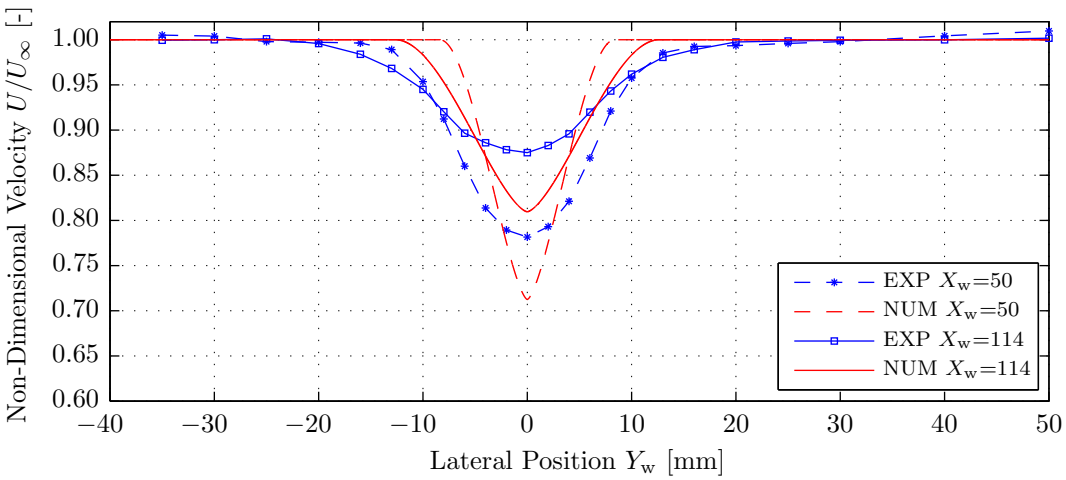

Figure F.1: Measured and computed wake profiles behind the default pylon model. $U_\infty = 26$ m/s, $X_w = [50, 114]$ mm.

Table F.1: Comparison of computed and measured wake width and depth for the default pylon. $U_\infty = 26$ m/s, $X_w = [50, 114]$ mm.

Data Set	$2b_w$ [mm]		$\Delta U_{max}/U_\infty$ [-]	
	$X_w = 50$ mm	$X_w = 114$ mm	$X_w = 50$ mm	$X_w = 114$ mm
Experimental	28	34	0.22	0.13
Numerical	15	21	0.29	0.19

From Figure F.1 and Table F.1 it is concluded that the measured wake profiles are much wider and less deep than the computed results. At an axial distance of 114 mm behind the default pylon's trailing edge the computed wake width is almost 40% smaller than the measured value, while the computed wake depth is approximately 50% larger. For the smaller axial spacing ($X_w = 50$ mm) comparable results are obtained.

The large differences between the measured and computed wake profiles for the default pylon are explained by returning to the discussion of the experimental results given in Section 3.2. There, it was concluded that the default pylon's wake is strongly influenced by separation from the model's thick trailing edge, leading to an increased wake decay rate compared to a situation in which the flow remains attached. Since the numerical method used to compute the wake profiles does not take into account any effects due to separation, the predicted wake decay is smaller than in real life and the resulting wake profiles are much more peaky than the measured profiles.

F.1.2 Sharp Pylon Model

Figure F.2 displays the velocity profiles obtained from the experimental and numerical analyses for the sharp pylon model, after which Table F.2 presents the wake widths and wake depths corresponding to the plotted data. Note that the position of the maximum velocity deficit in the measured pylon wake at an axial position of $X_w = 114$ mm occurs slightly left of the center of the pylon wake. This was explained before by a small misalignment of the wake traversing system.

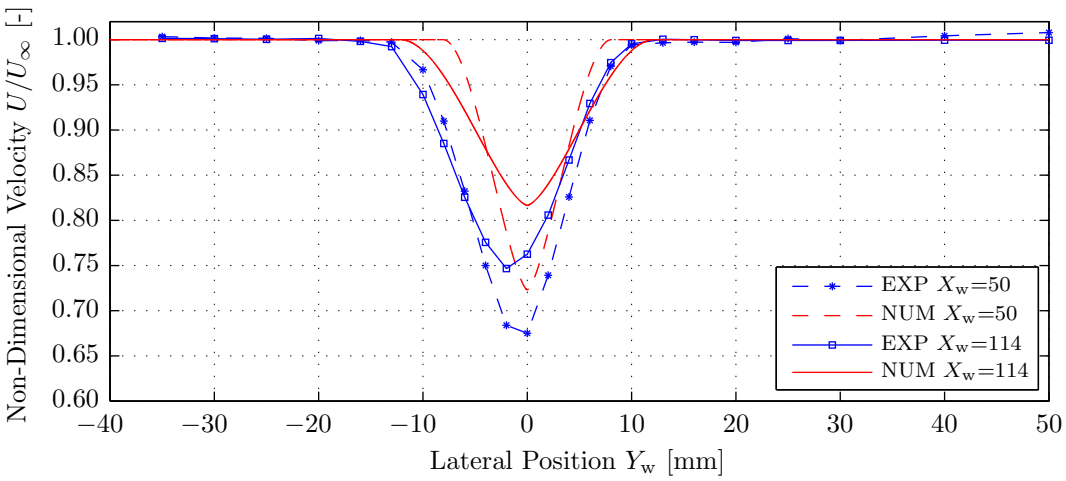

Figure F.2: Measured and computed wake profiles behind the sharp pylon model. $U_\infty = 26$ m/s, $X_w = [50, 114]$ mm.

Table F.2: Comparison of computed and measured wake width and depth for the sharp pylon. $U_\infty = 26$ m/s, $X_w = [50, 114]$ mm.

Data Set	$2b_w$ [mm]		$\Delta U_{max}/U_\infty$ [-]	
	$X_w = 50$ mm	$X_w = 114$ mm	$X_w = 50$ mm	$X_w = 114$ mm
Experimental	21	22	0.33	0.25
Numerical	14	20	0.28	0.18

The results presented for the sharp pylon model in Figure F.2 and Table F.2 are similar to those obtained for the extended pylon discussed in Section 11.1. The numerical method underpredicts the wake width by about 30% at $X_w = 50$ mm and 7% at $X_w = 114$ mm. Furthermore, the computed wake depth is approximately 15% smaller than the experimental value at 50 mm behind the pylon trailing edge, while at $X_w = 114$ mm a reduction of almost 30% is observed when comparing the computed value to the result obtained from the experiments.

F.2 Powered Propeller Performance

Section 11.2 presented a comparison of the measured and computed propeller performance for the isolated and installed configurations. A comparison between the blown propeller performance obtained from the experimental and numerical evaluations is presented in Figure F.3. The same operating conditions were considered as used for the comparisons of the isolated and installed results ($U_\infty = 26$ m/s and $0.5 \leq J \leq 1.9$). The blown results are presented for a blowing rate of $Q = 680$ L/min, with the numerical results computed for the blown wake profile obtained from the experimental pylon wake measurements.

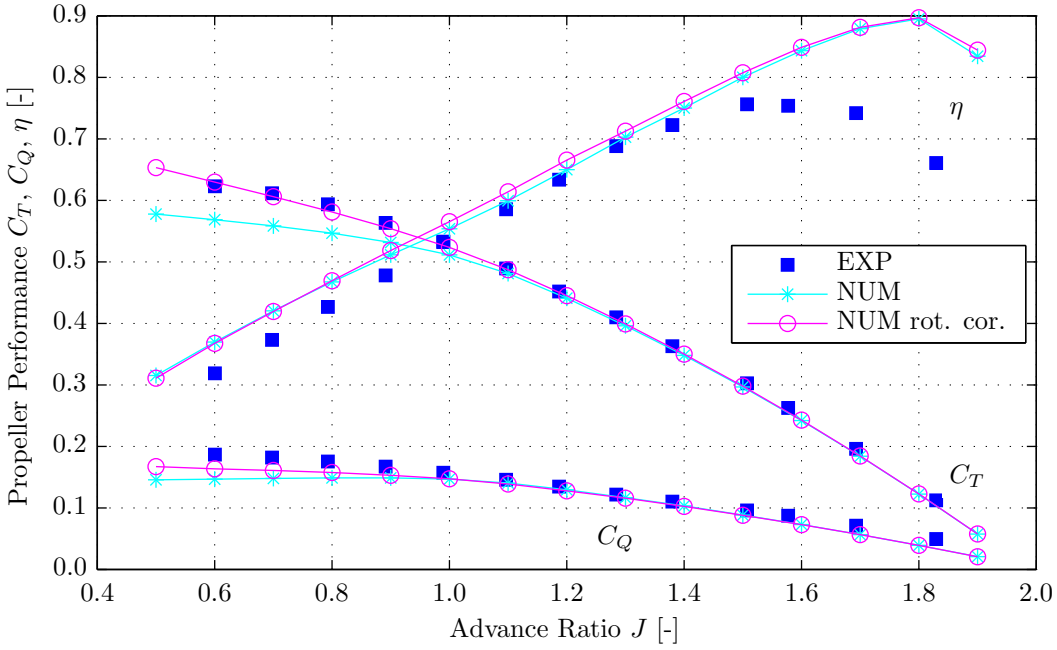

Figure F.3: Measured and computed propeller performance diagrams. Blown configuration, $U_\infty = 26$ m/s, $0.5 \leq J \leq 1.9$, $Q = 680$ L/min, $f_{cut} = 2,500$ Hz, extended pylon.

The results shown in Figure F.3 are similar to those observed for the installed configuration, and are therefore not discussed in detail here. In general, it can be stated that the effects of installation on the time-averaged thrust and torque coefficients is small. This is apparent in both the experimental and numerical data. It should be noted again that the experimental propeller performance results were characterized by a low signal quality, as a result of which the measured differences between the isolated and installed propeller performance were possibly the result of measurement variability.